Università degli Studi di Padova

DIPARTIMENTO DI FISICA E ASTRONOMIA GALILEO GALILEI
Sede Amministrativa: Università degli Studi di Padova

Corso di dottorato di ricerca in Astronomia, ciclo XXXI

The physics of the extended narrow-line region in active galactic nuclei

Dottorando
Enrico Congiu

Coordinatore
Chiar.mo Prof. Giampaolo Piotto

Supervisore
Dott. Stefano Ciroi

Anno Accademico 2017/2018

CONTENTS

ABSTRACT

L'*extended narrow-line region* (ENLR) è una delle strutture tipiche dei nuclei galattici attivi (AGN) più interessanti e meno studiate. È una struttura di gas, ionizzato dalla radiazione prodotta nelle regioni più interne dell'AGN. Il suo spettro e simile a quello di un'altra struttura tipica di questi oggetti, la *narrow-line region* (NLR). La differenza principale tra le due strutture è che l'ENLR ha una dimensione che supera il kiloparsec, alcune superano i 20 kpc, mentre la NLR è concentrata entro qualche centinaia di parsec dal nucleo.

In questo lavoro ho usato spettri e immagini (nella banda ottica e nel radio), per esaminare le proprietà di alcuni di questi oggetti caratterizzati dalla presenza di queste strutture particolari. Per prima cosa, ho usato spettri ad alta risoluzione e modelli di foto-ionizzazione e shocks per studiare le proprietà fisiche del gas in due oggetti con una nota ENLR: NGC 7212 e IC 5063. La risoluzione spettrale ha consentito di risolvere tutte le righe osservate, il cui profilo è risultato essere caratterizzato da picchi multipli e assimmetrie. Inoltre ho potuto analizzare le proprietà del gas in funzione della velocità dello stesso. In questo modo ho scoperto che, in entrambi gli oggetti, gli schock potrebbero contribuire in maniera consistente alla ionizzazione del gas che si muove ad alte velocità. Questa proprietà, combinata con la cinematica complessa che si evince dal profilo delle righe, potrebbe essere la prova dell'interazione tra i jet dell'AGN e il mezzo interstellare (ISM).

In seguito, ho iniziato a studiare la relazione tra l'ENLR e l'emissione radio estesa presente in molti AGN. Per prima cosa, ho cercato nuovi oggetti con emissione radio estesa in una nuova survey ottenuta con il VLA at 5 GHz di un campione di AGN appartenenti alla classe particolare delle *narrow-line Seyfert 1 galaxies* (NLS1s). Il primo risultato della survey, e probabilmente anche il più interessante, è stato la scoperta di un'emissione estesa con le caratteristiche di un *relic*, in Mrk 783, una NLS1 dell'universo vicino. Nuove immagini e spettri, acquisiti dopo la scoperta dell'emissione radio, hanno rivelato la presenza di una ENLR. La struttura di gas ionizzato è una dell più estese scoperte finora, si può tracciare l'emissione fino ad una distanza di 38 kpc dal nucleo, ed è allineata con la parte più estesa dell'emissione radio. Inoltre, la galassia ospite mostra segni di un recente merging con una compagna e potrebbe essere nelle prime fasi dell'interazione con una seconda sorgente vicina.

ABSTRACT

The extended narrow-line region (ENLR) is one of the most interesting and less studied structures typical of active galactic nuclei (AGN). It is made of gas, ionized by the radiation produced in the inner region of the AGN. Its spectral properties are similar to those of the narrow-line region (NLR), but the extension of ENLR is usually larger than 1 kpc (there are objects with ENLR larger than 20 kpc) while the NLR is often concentrated in a radius of some hundreds parsecs from the AGN.

In this work I used optical spectra and radio and optical images to investigate the properties of some of these peculiar structures. In particular, I firstly used high resolution spectra and models combining photo-ionization and shocks to study the physical conditions of the gas in the ENLR of two nearby sources, NGC 7212 and IC 5063. The spectral resolution of the data allowed to resolve all the observed lines, which show a complex profile characterized by multiple peaks, asymmetries and bumps. Moreover, it allowed me to investigate the behavior of the gas properties as a function of its velocity. In this way I discovered that, in both AGN, shocks might give an important contribution to the ionization of the gas moving at high velocities. This property, together with the complex kinematics of the gas, might be the result of the interaction between the AGN jets and the interstellar medium (ISM) of the galaxies.

Then, I started investigating the relation between extended optical emission and extended radio emission. For this reason, I looked for new extended radio structures in a VLA survey at 5 GHz of a sample of AGN belonging to the peculiar class of narrow-line Seyfert 1 galaxies (NLS1s). The first and most interesting result of this survey was the discovery of a very interesting radio emission, probably a relic, in Mrk 783, a nearby NLS1. An optical follow-up of the source revealed the presence of an ENLR. The structure is one of the largest discovered so far, with a maximum extension of 38 kpc just aligned with the most extended part of the radio emission. The host galaxy also shows signs of a recent merging with a companion, and it might be in the first stages of interaction with another nearby source.

INTRODUCTION

Active galactic nuclei (AGN) are known to be some of the most powerful emitters of the whole universe. The AGN class gather together objects showing a large variety of properties but that are all powered by the same engine: accretion of matter on a supermassive black hole. Even though the region where the powering processes take place is small compared to the dimension of a galaxy, the presence of an AGN can affect the properties of its host in a great variety of ways.

One of the most spectacular way in which an AGN can affect its host galaxy is the creation of extended emission regions which can be as large as the whole galaxy. The properties of these structures change depending on the part of the electromagnetic spectrum where they manifest themselves but, nevertheless, they all seem to be connected. Unfortunately extended emission regions are not as common as other AGN typical structures and they are observed only on a small number of objects.

The main purpose of this thesis is to study the properties of such extended emission regions at optical and radio wavelengths. The final goal is to shed some more light in the processes that take place in these regions, which can be fundamental in the so called AGN feedback, the effects that an AGN produces on its host. In the first chapter of this work I will summarize the properties of active galactic nuclei, focusing in particular on extended emission regions at optical and radio wavelengths. Since it is important to know the characteristics of the radiation we receive from this structures, in the second chapter I will shortly revise the dominant AGN emission processes in the regions of the electromagnetic spectrum I am interested in.

The main body of the work will be described in the following three chapters where I am going to report the result of the research I have been carrying on in the last three years. Chapter 3 will report the results of the study of high resolution optical spectra of two well known galaxies with extended emission line region. Chapter 4 will instead report the discovery of a kiloparsec scale radio emission region, one of the few of its kind, in a narrow-line Seyfert 1 galaxy, a peculiar class of AGN whose nature is still debated and that is rising more and more questions after the detection of γ-ray emission from one of them. Chapter 5 will present the analysis of new optical and radio data on this object which are rising even more questions with respect to the answer they are giving.

Finally, in the last chapter I will draw some conclusion from the overall results of my work.

1

ACTIVE GALACTIC NUCLEI

1.1 Brief history of AGN

Active galactic nuclei (AGN) are some of the most powerful objects in the universe and they are strong emitters at all wavelengths of the electromagnetic spectrum. However, the history of their discovery is mostly linked to the optical and radio band. AGN have been discovered in the early 1940s as galaxies characterized by a bright nucleus, whose spectrum showed several powerful emission lines (Seyfert, 1943). The galaxies studied in Seyfert (1943) where only six (NGC 1068, NGC 1275, NGC 3526, NGC 4051, NGC 4151, NGC 7469) and they became the basis of one of the most famous and common classes of AGN at low redshift: *Seyfert galaxies*. Seyfert already realized that not all the spectra were similar, but that some of them had really broad hydrogen permitted lines together with narrow forbidden lines, while some of them showed only a narrow component of both permitted and forbidden lines. But only with Khachikian & Weedman (1974) the modern classification in Seyfert 1 and Seyfert 2 objects was developed.

The nature of these objects was not clear from the beginning. The first and, probably, more natural hypothesis that could have been made at that time, was that the observed emission was produced by a large number of stars. Only sixteen years later Woltjer (1959) concluded that the emission produced in the inner parsecs of these objects would require a mass of a few of $10^8\,M_\odot$, too much to be produced only by simple stars. Salpeter (1964) and Zel'dovich (1964) finally proposed an accreting supermassive black hole as the engine powering AGN, which became the base of the modern description of AGN.

After the discovery of Seyfert galaxies, several other kinds of peculiar objects have been classified. At the same time of Seyfert's discovery, radio astronomy was still at its beginning, but in 1948 Bolton (1948) found several powerful radio emitters, optically identified in Bolton et al. (1949), among which there are the first radio galaxies ever identified: Centaurus A and Virgo A. In the following years of development of radio astronomy, one of the most important steps in the study of AGN was the 3C catalog (Edge et al., 1959). It was a catalogue of bright radio

sources at 159 MHz, that produced accurate positions for a large number of objects, allowing the research of their optical counterparts (Shields, 1999). Some of the 3C objects had a very small and point-like counterpart, with a spectrum characterized by strong optical unidentified emission lines. Because of the stellar-like appearance, they were known as quasi-stellar radio sources or quasars and they were thought to be peculiar stars (Shields, 1999). It took a few years to identify some of the lines in the spectrum of 3C 273 as high redshift hydrogen Balmer lines and to finally recognize these peculiar objects as distant galaxies (Schmidt, 1963).

It was now clear that all these objects were all linked together. They were all characterized by a spectrum with a strong optical continuum with a power-law shape and with prominent emission lines. Astronomers started to classify these objects according to their common features, while new classes of peculiar objects were being discovered (e.g. BL Lacs). All these efforts brought to the realization that all these astronomical sources were a different appearance of the same phenomenon and finally, in the early 90s, it was developed the so-called unified model of AGN, orderly described for the first time in the review paper by Antonucci (1993).

1.2 The unified model of AGN

The unified model of AGN (Antonucci, 1993) is still at the basis of the modern research on active galactic nuclei. The main point of this model is that only two types of AGN exist: radio-loud and radio-quiet. The classification among these two types of AGN has been defined by Kellermann et al. (1989) and it depends on the ratio R between the 5 GHz and B band flux of a source. If $R > 10$ the source is considered radio-loud, otherwise it is radio-quiet. Traditionally the radio-loudness of an AGN has been associated with the presence (or the absence) of a relativistic jet, even though with the discovery that radio quiet AGN can harbor a jet (e.g. Blundell et al., 2003) this association is becoming weaker and weaker (Padovani, 2017; Foschini, 2017).

According to the unified model, all the remaining properties of AGN can be explained by the luminosity of the sources and by the viewing angle. The luminosity can account for the quasar or Seyfert classification of a source, or for the Fanaroff-Riley classification (Fanaroff & Riley, 1974). The orientation of a source, instead, can explain the spectral properties of these objects.

Fig. 1.1 is a good representation of the unified model of AGN. The principal component of the engine is a **supermassive black hole** (SMBH) accreting matter from its surroundings. The accreting matter is orbiting in an **accretion disk** and it loses energy, getting close to the SMBH. The accretion disk has often been accredited as the source of the thermal emission known as the *big blue bump* (e.g. Shang et al., 2005). The SMBH and the accretion disk are surrounded by the so-called **corona**, a region filled with an electron plasma emitting X-rays via inverse Compton scattering of the photons produced closer to the SMBH (Haardt & Maraschi, 1991). Just outside the X-ray corona, there is the **broad-line region** (BLR), a region of highly ionized gas, distributed in clouds orbiting around the SMBH with velocities of the order of thousands km s^{-1}. The density of these clouds is relatively high, as it is possible to infer by the absence of broad forbidden lines in optical spectra (see Sec. 2.4.2). All these different structures compose the inner part of an AGN, which

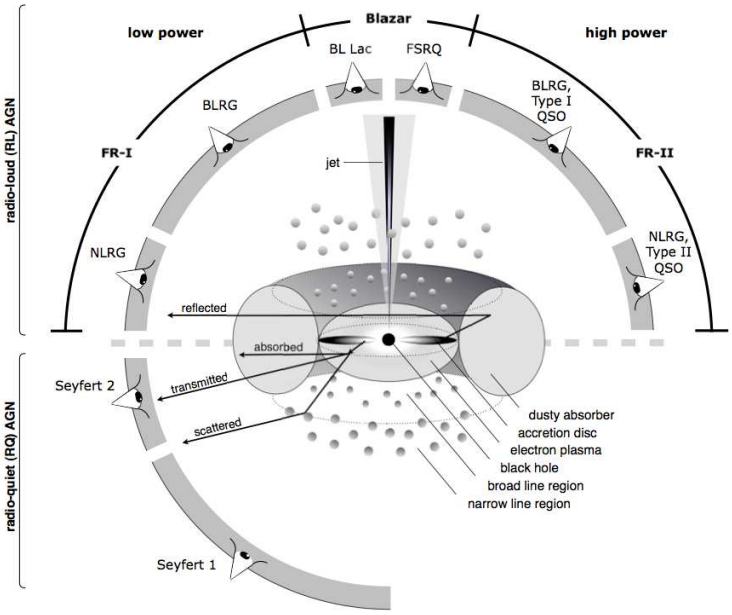

Figure 1.1: Scheme of the unified model of AGN from Beckmann & Shrader (2012).

is contained within a radius of $\sim 1\,\mathrm{pc}$ from the black hole (Beckmann & Shrader, 2012). In some AGN, a **relativistic jet** is launched in the region very close to the SMBH. The launching mechanism is still far to be fully understood, but the most accredited model to explain this process comes from Blandford et al. (1977), which says that the jet is launched by a strong magnetic field extracting energy from the rotation of the black hole itself.

This inner structure is enclosed in a region of dust rich gas, the **torus**, which is able to absorb almost all the soft X, ultraviolet, optical and near infrared incident radiation. Outside the torus, there is another region of ionized gas. Since it is more distant from the AGN with respect to the BLR, the gas clouds are characterized by a smaller rotational velocity and therefore they emit narrow lines (FWHM $\lesssim$ $1000\,\mathrm{km\ s^{-1}}$). Moreover, the electron density is much lower and the gas is able to emit forbidden lines. This region is known by the name **narrow-line region** (NLR).

The dimension of the NLR varies in each object, but it is usually between 100 pc and 1 kpc (Beckmann & Shrader, 2012). However, in some objects, it is possible to trace the strong emission lines typical of the NLR up to distances of the order of several kiloparsecs. In some exceptional cases, such as NGC 5252 (Tadhunter & Tsvetanov, 1989), Mrk 783 (Sec. 5), UGC 7342, NGC 5972 (Keel et al., 2012) and in another handful of objects, the size of this emission line region can be larger than 20 kpc. When the size of the NLR is larger than 1 kpc, the structure is often called **extended narrow-line region** (ENLR) or **extended emission line region** (EELR).

Among all the described components, the two most important structures needed to explain the AGN properties are the jet and the dusty torus. The jet is the main driver of radio emission in AGN and its presence should determine if an object is radio-loud or radio-quiet. The dusty torus instead, is what causes the difference

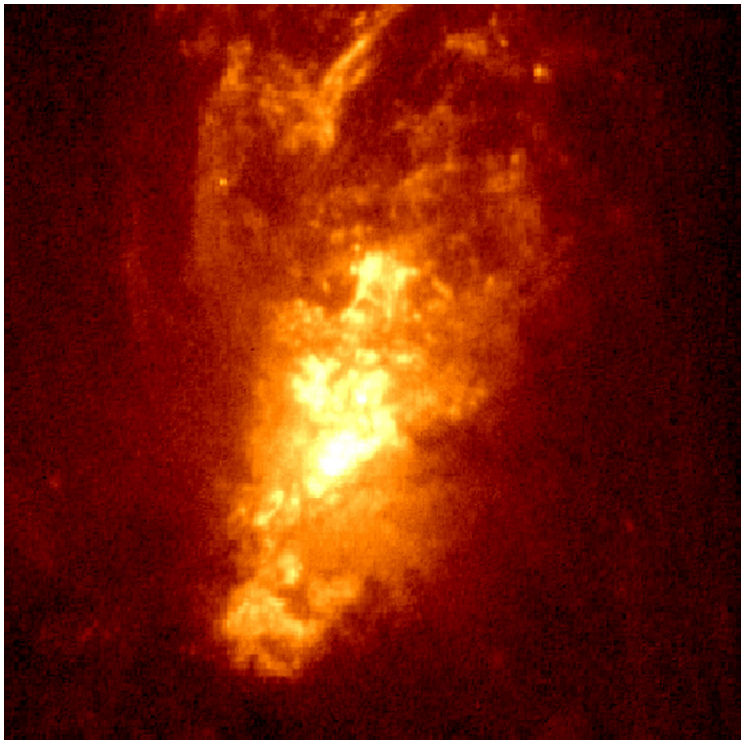

Figure 1.2: UV image of the ENLR of the famous Seyfert 2 galaxy NGC 1068. The image has been acquired with the Faint Object Camera (FOC) of the Hubble Space Telescope (HST). The image has been recovered from `https://www.spacetelescope.org/images/opo9407c/`

in the optical spectrum of the sources. The dust in the gas clouds composing the torus is able to completely hide the central part of the AGN to the observer located at high viewing angle with respect to the torus axis. In this situation, the BLR is not visible and the optical spectrum will be characterized only by the presence of the narrow lines produced in the NLR. AGN with this property are called Type 2 objects. Some example of this category of sources are Seyfert 2 galaxies, Narrow-line radio galaxies and Type 2 quasars. On the other hand, if the angle between the torus axis and the line of sight is small, the observer is able to see the innermost region of the structure. The BLR is directly visible from the observer and the permitted lines of the spectra show the broad component. Those sources are called Type 1 AGN and some examples are: Seyfert 1 galaxies, Broad-line radio galaxies, Type 1 quasars. At very small viewing angle, if a jet is present, the objects appear as blazars (see Fig. 1.1). The effects of orientation are observed not only in the optical spectrum but also in other bands of the electromagnetic spectrum, in particular the X-ray spectrum of an obscured (Type 2) and of an unobscured (Type 1) AGN are significantly different, and, for such reason, X-ray surveys have been used to detect and classify AGN.

1.3 The extended narrow-line region

The ENLR is a region of ionized gas that can be considered as a natural prosecution of the NLR when it reaches dimensions that overcome $\sim$ 1 kpc (Fig. 1.2). The main difference between the NLR and the ENLR is the observing frequencies of these structures. The NLR is observed in all AGN with emission lines, while the ENLR is observed only in a handful of objects, $\sim$ 50 of which are well studied and characterized at $z \leq 0.05$. Fortunately, the advent of new integral field spectrographs and relative surveys (e.g. MaNGA, Bundy et al., 2015) are giving a new pulse to the research and study of these structures (Husemann et al., 2014; He et al., 2018). The reason for this discrepancy might be a mix of observational biases (e.g. low surface brightness structures need long exposure times with large telescopes) and intrinsic reasons (e.g. gas distribution orientation of the AGN, etc.). Actually, in the sample described by Mulchaey et al. (1996a), a solid 79% of the observed galaxies (37 out of 47 objects) show resolved and extended line emission (Mulchaey et al., 1996b). Almost all of them are larger than 1 kpc and the unresolved ones are the most distant galaxies of the sample. This suggests that observational biases might be the principal reason for the low number of known ENLRs, combined with the difficulties in resolving them when the redshift starts to increase.

1.3.1 Spectral properties of the ENLR

Since the ENLR can be considered the natural prosecution of the NLR at large radii, the two structures are characterized by similar spectral and physical properties.

Their spectra show strong, not variable, narrow permitted and forbidden lines, with velocities of the order of 400–500 km s^{-1} (Bennert et al., 2004). The ENLR lines can be a little narrower with respect to that of the NLR, but usually at distances greater than some kiloparsecs from the active nucleus. This property has been used by early authors (e.g. Unger et al., 1987) to distinguish an NLR from an ENLR, even though nowadays this distinction is becoming less and less applied.

Several studies that analyzed both multiwavelength observations and ionization models (e.g. Kraemer & Crenshaw, 2000; Kallman & Bautista, 2001) proved that the gas is mostly photo-ionized by the AGN. The fact that the ionization is produced by the AGN is proved by the wide range of ionization degrees observed in both the NLR and the ENLR. It is the result of a strong ultraviolet spectrum, much stronger than the typical continuum emitted by young and hot stars (Osterbrock & Ferland, 2006). The temperature of the gas, as measured by the ratio of particular forbidden lines (see Sec. 2.4.2), is of the order of 10^4 K, much lower than in case of shock heated gas ($T \sim 5 \times 10^4$ K Osterbrock & Ferland, 2006). The presence of forbidden lines proves that the density is lower with respect to their critical density, and actual measurements show a typical range of 10^2–10^4 cm^{-3}.

1.3.2 Morphology

Most ENLR have a typical conical or bi-conical shape (e.g. Fig. 1.2), with the apexes of the cones pointing towards the AGN. This peculiar shape is mostly produced by the distribution of the ionizing light. The radiation originates in the inner part of the AGN, inside the dusty torus. Due to dust extinction, the ionizing photons can

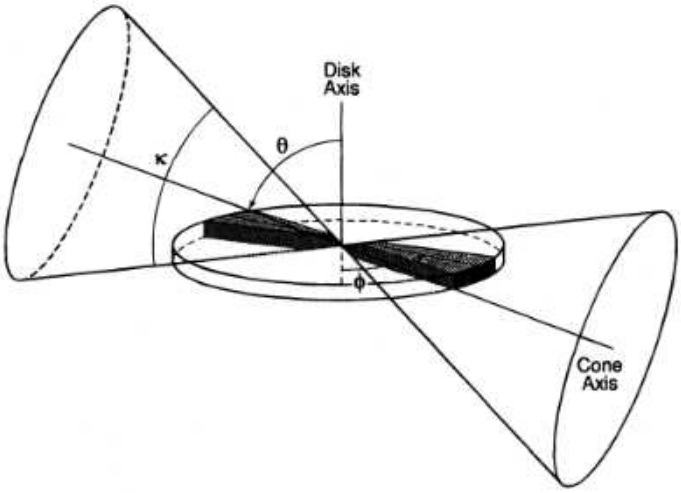

Figure 1.3: Bi-conical ionizing radiation field intersecting a thin disk of gas. The dark area represents the shape of the ENLR in this model. Figure from Mulchaey et al. (1996b).

escape only along the axis of the torus. Therefore, the radiation is collimated, and it assumes the bi-conical shape that is then observed in the distribution of the ionized gas. For this reason, the existence of ENLRs has always be considered one of the major proof of the validity of the unified model (Wilson & Tsvetanov, 1994; Schmitt et al., 2003b; He et al., 2018).

The shape of the ENLR is not determined only by the shape of the ionizing radiation field. Several other factors actually contribute in the determining its morphology. The most important one is the distribution of the gas in the host galaxy. Mulchaey et al. (1996b) studied the effects of the gas distribution simulating the morphologies produced by a bi-conical radiation field combined with a spherical or a disk-shaped gas distribution. The result is that when a disk-shaped distribution produces an ENLR (i.e. the inclination of the cone axis is sufficiently high) the resulting shape is that of a bi-cone (Fig. 1.3). This happens both if the line of sight is inside the cone (Type 1 AGN) or outside the cone (Type 2 AGN).

On the hypothesis of a spherical gas distribution, the ENLR is always produced, since the radiation field always intercepts the gas, but the shape changes according to the AGN type. While Type 2 objects maintain the bi-conical shape, in Type 1 objects the ENLR should assume a halo-like shape. The comparison of the models with the observations is consistent with a thin disk model for most objects. But, a consistent number of halo-like ENLR have been observed indiscriminately for Type 1 and Type 2 objects. This inconsistency is linked mostly to the low spatial resolution of the images which allows confusing small conical ENLR with halo-like ENLR. In fact, more recent works with higher resolution data (e.g. Schmitt et al., 2003a,b; Fischer et al., 2013) confirmed that the morphology of the ENLR is consistent with a disk-shaped gas distribution.

However, a property valid in both gas distributions is that the ENLR of Type

1 sources is always smaller with respect to that of Type 2 Sources. Even though this property has not been confirmed by Mulchaey et al. (1996b) comparison of the models with observations, subsequent studies (e.g. Schmitt et al., 2003b) confirmed that the ENLR of type 1 AGN is smaller, on average, of that of Type 2 sources.

There are exceptions to this rule. Several Type 1 objects (e.g. NGC 4151 Pogge, 1989; Evans et al., 1993) show large and bi-conical ENLR. The collimation by a disk-like BLR has been proposed by Evans et al. (1993) to explain these exceptions.

An interesting property of the ENLR gas that has been shown by high spatial resolution images of several ENLRs is that the gas is concentrated in clouds, clumps and filaments (e.g. Tadhunter & Tsvetanov, 1989; Mulchaey et al., 1996a,b; Schmitt et al., 2003a,b), instead of being smoothly and continuously distributed.

1.3.3 The origin of the gas

Up until now, the ionized gas forming the ENLR has always be considered as the gas of the host galaxy disk. While in some cases this might be true (e.g. Fischer et al., 2017), there are several authors that hypothesize other origins for the ENLR gas. AGN are often characterized by the presence of fast outflows of gas in several different phases, from the cold molecular one to the warm ionized gas (Baldwin et al., 1987; Hutchings et al., 1998; Crenshaw et al., 2000; Crenshaw & Kraemer, 2000; Dasyra et al., 2015; Morganti et al., 2015, 2018). These outflows usually have a bi-conical shape (Pogge, 1988; Schmitt et al., 1994; Fischer et al., 2013) and they might be able to move gas from the nuclear regions to external regions of a galaxy, producing the ENLR.

Another interesting possibility is that the gas is brought in the host galaxy through episodes of merging (Veilleux et al., 1999; Ciroi et al., 2005; Di Mille, 2007; Cracco et al., 2011). It is now widely accepted that when a galaxy merges with a gas rich companion the newly accreted gas is able to trigger the active phase in the nucleus of the main galaxy (Sanders et al., 1988; Hong et al., 2015). However, not all the gas involved in the merging arrives in the nucleus but most of it is redistributed in the galaxy and it can be ionized by the AGN radiation producing the ENLR. This process can be the cause of the presence of ENLR also in early-type galaxies where the gas is expected to be almost absent or in directions not corresponding to that of the galactic disk.

It is not easy to investigate the origin of the ENLR gas. The spectrum of the ENLR is often characterized by emission lines with disturbed profiles. Multiple peaks, asymmetries and bumps observed in high-resolution spectra (Ozaki, 2009; Morganti et al., 2007; Congiu et al., 2017c) are evidence of a disturbed kinematics of the gas, which can be produced by each one of the previously mentioned mechanisms with the addition of the interaction of the interstellar medium (ISM) with the AGN jets. However, several authors (e.g. Unger et al., 1987; Fischer et al., 2017, 2018) noticed that, usually, only the inner kiloparsec of the ENLR seems to be perturbed while the remaining part has a kinematics that can be attributed to that of the galaxy disk. These properties are compatible with the ENLR being mostly composed by the gas of the galactic disk ionized by the AGN while the inner kiloparsecs is disturbed either by gas outflows or by a jet which is expanding in the dense ISM of the galaxy nucleus.

1.4 Kiloparsec scale radio emission region

Models suggest that the clouds of the ENLR are accelerated via radiation or wind pressure (Crenshaw et al., 2000; Crenshaw & Kraemer, 2000). But there are several proofs that the ENLR is aligned with radio structures, i.e. jets, suggesting that there might be a correlation between the ionized gas and the relativistic plasma (e.g. Unger et al., 1987; Wilson & Tsvetanov, 1994; Falcke et al., 1998; Schmitt et al., 2003a,b; Morganti et al., 2007; Husemann et al., 2013). In particular, jets might expand in the ISM clearing the path for the radiation. This will make it easier for the radiation to escape from the NLR and to reach more distant gas (Wilson & Tsvetanov, 1994). During this process, the jets interact with the ISM producing shocks and turbulent motion of the gas (e.g. Cracco et al., 2011; Contini, 2013; Congiu et al., 2017c). I will now describe the principal properties of the radio extended emission in AGN, focusing in particular on the so-called kiloparsec scale radio emission region (KSR). Then I will describe the relationship between the KSR and the ENLR.

1.4.1 Principal properties

Radio emission is not uncommon in AGN. Kellermann et al. (2016) estimated from 5 GHz observation of low redshift ($0.2 < z < 0.3$) quasi-stellar objects (QSO), that almost 20% of them can be considered radio-loud (RL), while the other are considered radio-quiet(RQ). In particular, Kellermann et al. (2016) classified these objects considering RL all the sources with $L_{5_GHz} > 10^{23}\,\mathrm{W\,Hz^{-1}}$, even though the usual classification is based on the ratio between the flux density at 5 GHz and in the optical B-band $R = \frac{S_{5\,\mathrm{GHz}}}{F_B}$ (Kellermann et al., 1989). According to this classical classification a source is considered RL if $R > 10$.

However, the therm *radio-quiet* does not mean a complete absence of radio emission. Almost all AGN emit at radio wavelengths, but the sensitivity of modern instruments is not enough to observe the emission in some RQ sources (Kellermann et al., 2016). Nevertheless, it must be pointed out that the emission of RQ seems to be often related to star formation processes happening in the host galaxy, more than to the AGN itself.

RL quasars often show extended bipolar structures (Fig. 1.4, top panel). They are caused by relativistic jets launched by the AGN and they can terminate in radio lobes whose extension can surpass hundreds of kpc (e.g Fanaroff & Riley, 1974; Perley et al., 1979; Bridle et al., 1994). On the other hand, RQ-AGN, such as Seyfert galaxies and LINERs usually show compact nuclear emission (Singh et al., 2015a). Only occasionally, RQ-AGN show extended radio emission, whose dimension is usually smaller than ~ 10 kpc (Fig. 1.4, bottom panel). As it has been already introduced, most of the extended emission in RQ-AGN seems to be produced by star formation (Baum et al., 1993; Kellermann et al., 2016). However, several of them show resolved morphologies similar to jets (Baum et al., 1993; Colbert et al., 1996; Morganti et al., 1999; Gallimore et al., 2006; Singh et al., 2015a,b). Detailed studies of single objects revealed that Seyfert galaxies, probably the most common class of nearby RQ AGN, are characterized by a morphology of the radio emission consisting in a bright core and one or two jets with relative lobes. The morphology, therefore, is very similar to the structures observed in RL-AGN, but on much smaller scales

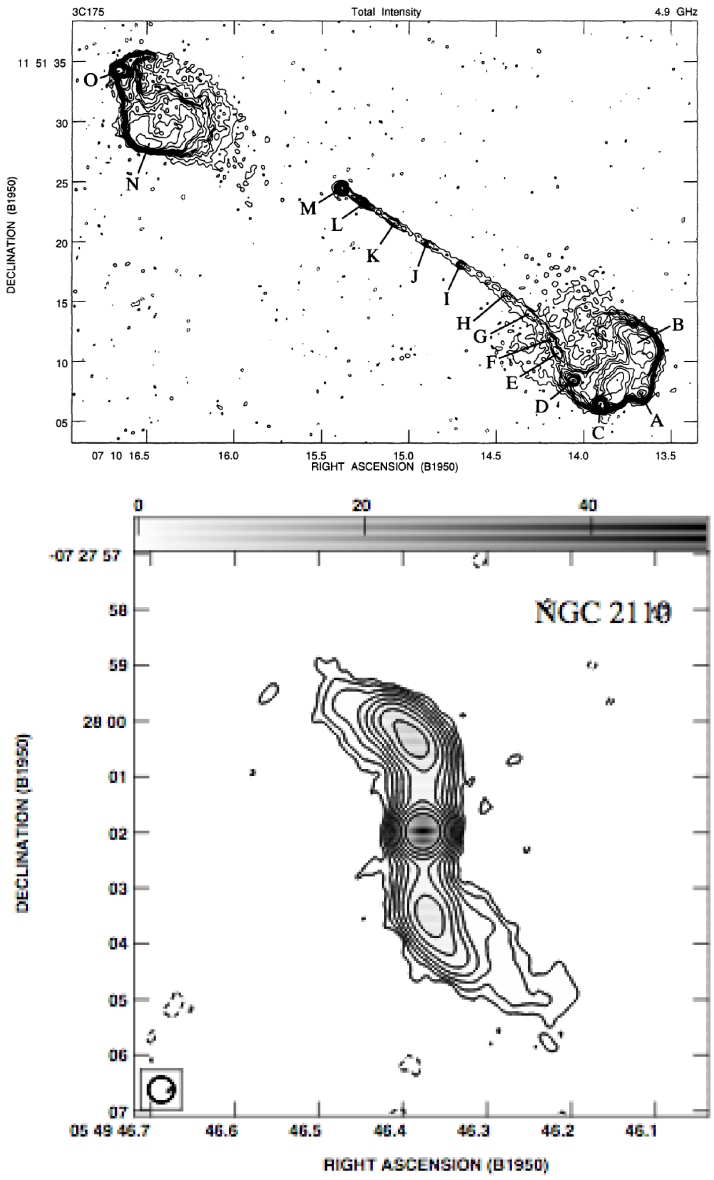

Figure 1.4: **Top:** VLA 5 GHz map of the radio galaxy 3C 175 from Bridle et al. (1994). It is possible to observe both the collimated jet emission and the terminal radio lobes. The extension of the source is > 300 kpc **Bottom:** VLA 1.4 GHz map of NGC 2110 from Mundell et al. (2009). The maximum extension of this source is ~ 1 kpc.

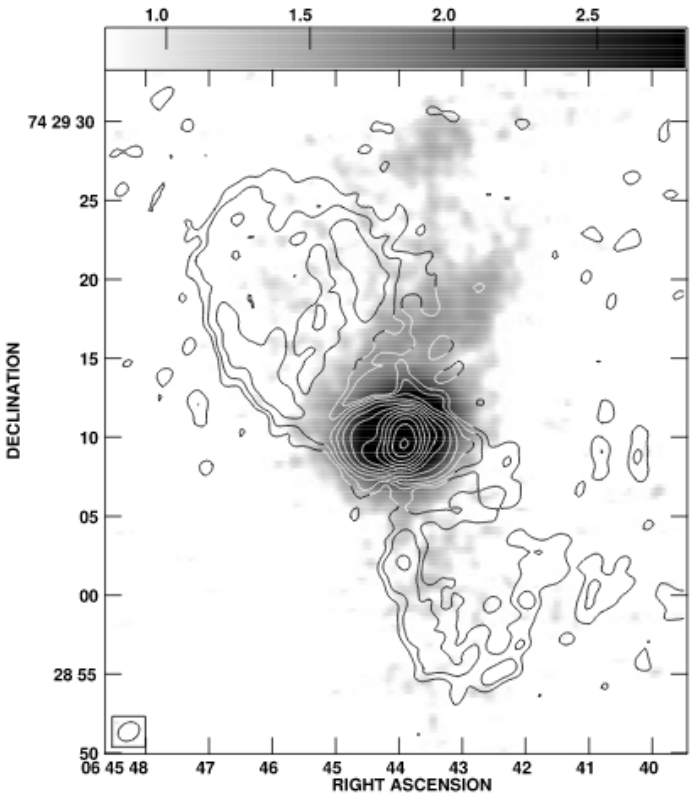

Figure 1.5: VLA 5 GHz contours of Mrk 6 superimposed to an HST [O III] image of the same source from Kharb et al. (2006).

(parsec scales vs kiloparsec or megaparsec) (e.g. Wrobel, 1984; Ulvestad et al., 1987; Morganti et al., 1999; Kukula et al., 1999; Momjian et al., 2003; Kharb et al., 2006).

The origin of extended radio emission both in RL and RQ-AGN (when it is not produced by star formation) is related to the presence of jets. However, we just saw that there is a huge difference between the extension of radio structures in the two classes of objects. A possible reason for this difference seems related to the properties of the ISM of the objects (Whittle & Wilson, 2004; Gallimore et al., 2006; Schawinski et al., 2011; Singh et al., 2015b). RL AGN with huge extended radio emission are usually found in gas-poor early-type galaxies. In this case, the jet does not need to dig its way out of the galaxy in a dense ISM. As a consequence, it preserves most of its energy and it can expand up to several hundred kpc or more. On the other hand, RQ-AGN seem to be located in gas-rich late-type galaxies. Their jets seem to be distorted by their interaction with a much denser ISM, which makes them lose more energy and stopping their expansion at much shorter scales.

1.4.2 KSR and ENLR

As it has already been mentioned, several works found that the position angle (PA) of the ENLR is often aligned with the PA of the KSR (e.g. Unger et al., 1987; Wilson & Tsvetanov, 1994; Capetti et al., 1996; Falcke et al., 1998; Schmitt et al., 2003a,b;

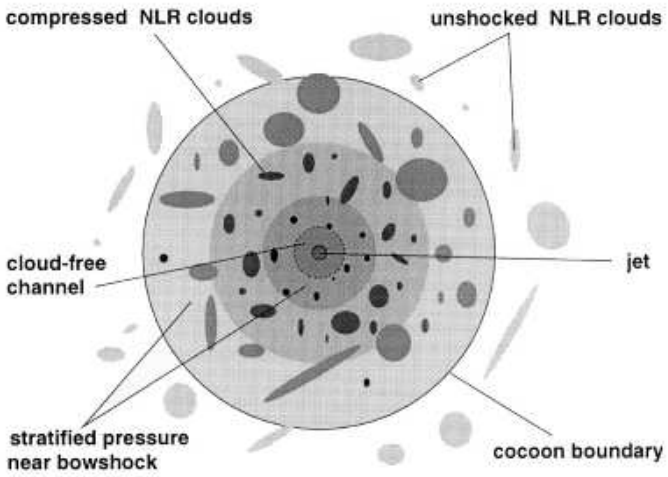

Figure 1.6: Scheme from Steffen et al. (1997) illustrating the interaction between the jet and the ISM of the NLR.

Morganti et al., 2007; Husemann et al., 2013) (Fig. 1.5). This happens for most ENLR known so far, therefore there must some kind of connection between the two extended structures. Just after the first observations of these structures, Wilson & Tsvetanov (1994) hypothesized that the morphology and position of the ENLR must have been a consequence of the action of the jet plasma. When the jet expands into the ISM it creates a path for the ionizing radiation, produced in the inner part of the AGN, to reach more distant gas with respect to that of the NLR. This hypothesis has been confirmed a few years later by Capetti et al. (1996) who found, for a small sample of Seyfert galaxies, a perfect correspondence between the position and the morphology of the optical and radio extended emission. For example, in their sample, the presence of radio lobe is always coupled with the shell-like emission line structures, while linear jet radio structures like in Mrk 3 are accompanied by similar morphologies of the ENLR.

Also, the kinematics of the ENLR might be the consequence of the interaction between the jet and the ionized gas. When the jet pushes the ISM, it creates shocks which can cause turbulent motion in the gas clouds, heat it and contribute to its ionization (e.g. Steffen et al., 1997; Morse et al., 1998; Rodríguez-Ardila et al., 2005; Contini et al., 2012; Congiu et al., 2017c) (Fig. 1.6).

The totality of the process through which the AGN interacts with its host galaxy is called AGN feedback. AGN feedback is usually divided in two types, according to the effect on star formation. It is considered positive when it produces an enhancement of the star formation, while it is negative when the result is a hampering of this process. This interplay between the AGN and the host galaxy can happen in two ways: via the interaction of the interstellar medium radiation pressure and wind, the so-called radiative mode, or via interaction between its jets and the ISM, the so-called kinetic mode. Fabian (2012) published a complete review of this argument.

The ENLR is the perfect place to study AGN feedback since both feedback mode can be active in this region. The main ionizing mechanism of the gas is photoionization by the AGN continuum, which can also influence the gas kinematics via

radiation pressure (radiative feedback). On the other hand, the presence of jets interacting with the ISM is the driver of the kinetic feedback. Therefore, investigating the properties of the gas of the ENLR can help to shed light on this still poorly known processes.

2

EMISSION PROCESSES IN AGN

AGN emission spans over the complete electromagnetic spectra, starting from the lowest observable radio frequencies to the highest energies of the γ-rays. Several processes, divided among continuum processes such as synchrotron emission, thermal emission, inverse Compton emission, and atomic and molecular transitions, both permitted and forbidden, contribute to this ultra wide band emission. In this chapter, I will describe the main processes characterizing AGN emission in the radio and optical bands.

2.1 Synchrotron emission

Synchrotron emission is one of the main mechanism of continuum emission in AGN, especially in radio-loud ones. It is classified as a non-thermal process, because the particles involved in the process usually are not in thermodynamical equilibrium. Synchrotron emission is the dominant emission mechanism in the radio region of an AGN broad band spectrum, also called spectral energy distribution (SED), but it can be responsible for a significant amount of emission up to optical and UV wavelengths, especially in peculiar classes of AGN such as blazars. Synchrotron emission occurs when charged particles, usually electrons, are accelerated in a magnetic field. If the electron has a velocity component perpendicular to the magnetic field, it starts spiraling because of the Lorentz force. The energy emitted by a single electron is a function of its energy, of the magnetic field strength B and of the angle between the field and the direction of motion of the particle.

To calculate the spectrum emitted by a population of electrons it is possible to start considering a single electron with charge e, rest mass m and Lorentz factor:

$$\gamma = \frac{1}{\sqrt{1 - \frac{v^2}{c^2}}}. \tag{2.1}$$

This section is partially extracted from Beckmann & Shrader (2012).

The electron is traveling with velocity $\mathbf{v}$ through a uniform and static magnetic field $\mathbf{B}$. The force acting on the electron is:

$$\frac{d}{dt}(\gamma m\mathbf{v}) = \frac{e}{c}(\mathbf{v}\times\mathbf{B}), \tag{2.2}$$

and, because of the cross product, it is always perpendicular to the motion of the particle. This means that the magnitude of its velocity v and the Lorentz factor γ are constant. The force is also perpendicular to the direction of the magnetic field, which implies that $v_\parallel$, and consequently $v_\perp$ ($v^2 = v_\parallel^2 + v_\perp^2$), is constant. The final result is that the electron motion will be a combination of a circular motion with constant radius r_g around the magnetic field lines and a motion at constant velocity ($v_\parallel$) along the field lines. The radius r_g is called gyroradius and it is defined as:

$$r_g = \frac{v_\perp \gamma mc}{eB}. \tag{2.3}$$

From the gyroradius it is possible to define the frequency of the circular motion, the Larmor frequency:

$$\nu_g = \frac{eB}{2\pi\gamma mc}, \tag{2.4}$$

and the angular gyrofrequency $\omega_g = 2\pi\nu_g$. The total luminosity produced by the acceleration process can be derived from the following equation (Rybicki & Lightman, 1986):

$$L = \frac{2e^2}{3c^3}\gamma^4\left[\left(\frac{d\mathbf{v}_\perp}{dt}\right)^2 + \gamma^2\left(\frac{d\mathbf{v}_\parallel}{dt}\right)^2\right], \tag{2.5}$$

considering that $d\mathbf{v}_\parallel/dt = 0$, the acceleration is perpendicular to the velocity, and that $d\mathbf{v}_\perp/dt = \omega_g\mathbf{v}_\perp$, because the electron follows a circular motion. Since $v_\perp = v\sin\beta$, where β is the pitch angle, v is the magnitude of its velocity, and assuming an isotropic distribution of particle velocities during the integration over the angles, the final synchrotron luminosity is:

$$L = \frac{4e^4B^2\gamma^2v^2}{9c^5m^2}. \tag{2.6}$$

This formula has been derived considering the case of an electron. However, it can be used also to describe the synchrotron emission of a positron, same mass but different sign of the charge, or of a proton, different mass and different charge sign. However it is clear that since $L \propto m^{-2}$ the lighter is the emitting particle, the more luminous is the emission if the particle velocity is the same in all cases. Since $m_p \sim 1836 \cdot m_e$, the emission of a proton would be a factor $\sim 10^{-7}$ lower with respect to the emission of an electron (or positron) moving at the same speed, and so the latter is by far a more efficient emitter. This consideration is important when discussing the nature of the particles producing synchrotron emission in relativistic jets. To produce the same luminosity a jet made of protons should be significantly faster than a jet of electrons or positrons, which is the reason why electron powered jets seem more plausible.

If only the case of electron or positrons is considered, the formula can be simplified further:

$$L = \frac{4}{3}\sigma_t \frac{v^2}{c}\gamma^2 U_B, \tag{2.7}$$

where $U_B = B^2/8\pi$ is the magnetic energy density and σ_t is the Thomson cross-section:

$$\sigma_t = \frac{8\pi}{3}\left(\frac{e^2}{mc^2}\right)^2. \tag{2.8}$$

If the electron is highly relativistic ($v \sim c$) the synchrotron luminosity is a function only of the Lorentz factor and of the magnetic energy density.

An important property of the synchrotron radiation is that it is not emitted isotropically. Because of relativistic beaming effects, the radiation is concentrated in a narrow cone pointed towards the motion of the particle (Fig. 2.1). The opening angle of the cone ϕ is a function of the γ factor of the particle, in particular $\phi \propto \gamma^{-1}$. This produces a lighthouse effect and the observer will detect radiation only when the cone is pointing towards the line of sight. The emission will be a short pulse of duration $\Delta t \sim 0.5\gamma^{-2}\omega_g^{-1}$, and the observed frequency will then be:

$$\nu \sim \Delta t^{-1} \sim \gamma^2 \nu_g = \frac{\gamma^3 v}{2\pi r_0}, \tag{2.9}$$

where r_0 is the gyroradius in the non-relativistic approximation ($\gamma \sim 1$). If the radiation emitted by the electron is averaged over the entire rotation it will appear concentrated in a solid angle pointed towards the direction of the motion parallel to the magnetic field.

The effective synchrotron spectrum emitted by an electron requires complex calculations to be derived (Rybicki & Lightman, 1986), but it is found that, averaging over the orbit, it is a continuum spectrum strongly peaked at the frequency $0.29\nu_c$ where ν_c is the critical frequency:

$$\nu_c = \frac{3}{2}\gamma^3 \nu_g \sin\beta. \tag{2.10}$$

The power per unit frequency of the spectrum is given by:

$$L(E,\nu) = \frac{\sqrt{3}e\gamma^2 B \sin\beta}{mc^2}\frac{nu}{\nu_c}\int_{\nu/\nu_c}^{\infty} K_{5/3}(\xi)d\xi, \tag{2.11}$$

where $K_{5/3}$ is the modified Bessel function of order 5/3.

2.1.1 Synchrotron emission of a particle plasma

Up until now only the synchrotron emission of a single particle in a magnetic field has been studied. In astrophysical sources this is unlikely to happen. In general the observed emission is produced by a large number of particles at the same time.

In order to compute the spectrum of an electron plasma, it is possible to assume that the energy is all emitted at the critical frequency ν_c. This is possible because the spectrum of a single particle is sharply peaked below this frequency (Fig. 2.2). Therefore:

$$\nu \sim \nu_c \sim \gamma^2 \nu_g = \left(\frac{E}{mc^2}\right)^2 \nu_g. \tag{2.12}$$

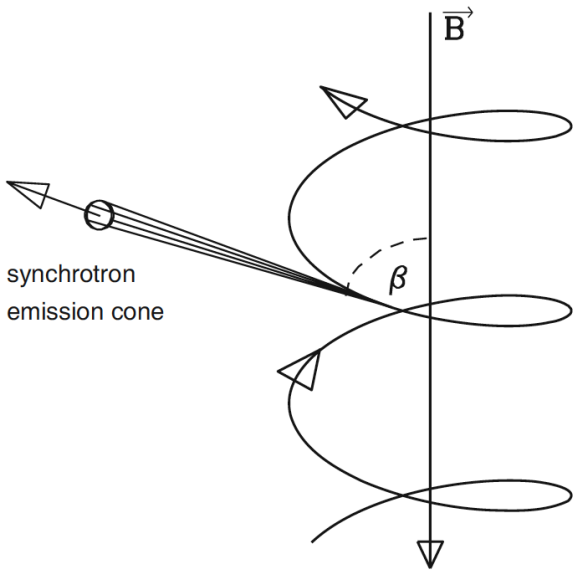

Figure 2.1: Scheme of synchrotron emission by a relativistic electron with pitch angle β from Beckmann & Shrader (2012). The emission is beamed in the direction of motion and forms a cone with opening angle $\phi \sim \gamma^{-1}$. If the emission is averaged over the entire rotation, it will be concentrated inside a solid angle pointing in the forward direction (top of the figure).

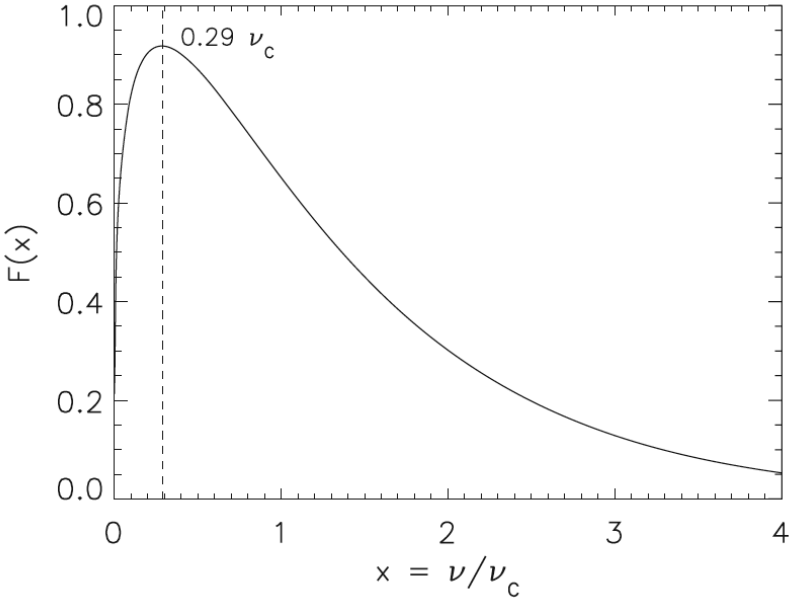

Figure 2.2: Synchrotron spectrum of a single particle from Beckmann & Shrader (2012). The total power $F(x)$ is in unit $x = \nu/\nu_g$.

It is easy to see that the frequency of the emission directly depends on the energy of the electron, therefore, on the electron energy distribution. If it is considered that the electrons have a continuum distribution of energy in the interval E_1–E_2 the total emissivity of the emission is:

$$\epsilon(\nu) = \int_{E_1}^{E_2} L(E,\nu) n(E) dE \tag{2.13}$$

where $n(E)dE$ is the number density of the electron in the energy interval between E and $E + dE$. The energy distribution is often a power-law, and it can be written in the following way:

$$n(E)dE = kE^{-p}dE, \tag{2.14}$$

where k is the normalization of the power-law, p is the index and they are both constant. If $p > 0$, as it typically happens in astrophysical sources, Eq. 2.14 means that the number of electrons decreases at higher energies. Integrating Eq. 2.13 assuming the power-law in Eq. 2.14, it is possible to obtain the synchrotron emissivity. The luminosity emitted per unit volume and unit time is:

$$\epsilon(\nu) = \frac{\sqrt{3}e^3}{2mc^2}\left(\frac{3e}{4\pi m^3 c^5}\right)^{\frac{p-1}{2}} k\left(B\sin\beta\right)^{\frac{p+1}{2}} \nu^{\frac{1-p}{2}} G\left(\frac{\nu}{\nu_{c1}}, \frac{\nu}{\nu_{c2}}, p\right) \tag{2.15}$$

where ν_{c1} and ν_{c2} are the critical frequencies at energies E_1 and E_2, while $G\left(\frac{\nu}{\nu_{c1}}, \frac{\nu}{\nu_{c2}}, p\right)$ is a function that is reduced to:

$$G\left(0, \infty, p\right) = \frac{2^{\frac{p-3}{2}}}{3}\left(\frac{3p+7}{p+1}\right)\Gamma\left(\frac{3p-1}{12}\right)\Gamma\left(\frac{3p+7}{12}\right), \tag{2.16}$$

where Γ is the gamma function, when $\nu_{c1} \ll \nu \ll \nu_{c2}$. Eq. 2.15 does not depend on ν, therefore:

$$\epsilon(\nu) \propto \nu^{\frac{1-p}{2}}. \tag{2.17}$$

Usually the quantity $\alpha_R = \frac{p-1}{2}$ is called radio spectral index. The slope of the radio spectrum is directly connected to the slope of the electron energy distribution. In the case of some of the brightest radio sources in the Universe, flat-spectrum radio quasars (FSRQ), the radio continuum has a spectral index $\alpha_R \sim 0.5$, produced by an electron energy distribution $n(E) \propto E^{-2}$. The spectrum can have a high frequency cut-off that depends on the critical frequency of the most energetic electrons.

2.2 Thermal emission

Synchrotron emission is probably the dominant continuum emission process in a large part of the AGN SED, in particular at low frequencies. However, in the IR-optical-UV range the continuum emission of most classes of AGN is dominated by thermal processes such as black body radiation. In the IR band most of the emission is produced by dust via thermal emission, while in the optical and UV range some AGN show an excess of emission with respect to the underlying power law produced by the synchrotron process, the so-called *big blue bump*.

This section is partially extracted from Robson (1996) and Beckmann & Shrader (2012).

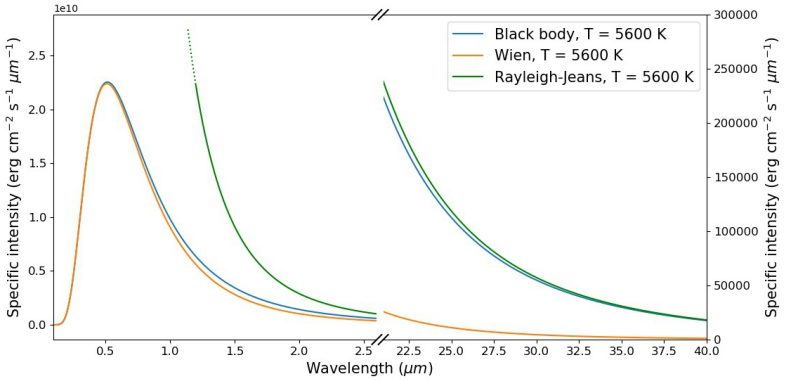

Figure 2.3: Black body spectrum and traditional approximations at high and low energies. The blue line represents the black body emission at a temperature T = 5600 K. The green line is the Rayleigh-Jeans approximation for $h\nu/kT << 1$, while the orange line is the Wien approximation for $h\nu/kT >> 1$. Both approximations are measured for T = 5600 K. The left panel shows the high energy end of the spectrum, while the right panel is a zoom in on the low energy tail, where the Rayleigh-Jeans approximation is valid.

The big blue bump is particularly interesting for two main reasons: its high energy UV radiation is important for the ionization of the gas and it has often been associated with thermal radiation from the accretion disk of the AGN.

For this reason, even though thermal processes are usually associated with stars more than with AGN, the following section will summarize the main characteristics of some thermal emission processes.

2.2.1 Black body radiation

Black body emitters are probably the most common emitters of the whole Universe. A black body is a body in thermal equilibrium with its surroundings and it is a perfect absorber, and emitter, of radiation. The emission of a black body is isotropic and it is not polarized. A black body is a theoretical construct and it is almost impossible to build in the laboratory. However, stars are a reasonable approximation of black bodies and they can be treated in this way for most common applications.

The main property of a black body radiator is its peculiar spectrum which depends only on the temperature of the black body and on none of its other properties. The shape of the spectrum is well described by the so-called *Planck's law*:

$$B_\nu(T) = \frac{2h\nu^3}{c^2} \frac{1}{\exp\left(\frac{h\nu}{kT}\right) - 1}, \tag{2.18}$$

where h is the Planck constant, c is the speed of light, k is the Boltzmann constant and T is the temperature of the black body. In Eq. 2.18, $B_\nu(T)$ is expressed as a function of the frequency, but it is easy to write the Planck's law as a function of wavelengths considering that:

$$B_\nu d\nu = B_\lambda d\lambda. \tag{2.19}$$

To better understand the properties of this curve it is useful to consider two limits. For low frequencies, where $h\nu/kT \ll 1$, the equation can be simplified to:

$$B_\nu(T) = \frac{2h\nu^2 kT}{c^2} \tag{2.20}$$

which is the so-called Rayleigh-Jeans approximation. Eq. 2.20 says that all black bodies at low frequencies can be approximated by a power law with index $\alpha = 2$. On the other extreme of the frequency range, for $h\nu/kT \gg 1$, the Wien approximation applies:

$$B_\nu(T) = \frac{2h\nu^3}{c^2} \exp\left(-\frac{h\nu}{kT}\right) \tag{2.21}$$

which says that the spectrum drops rapidly with an exponential cutoff. Fig. 2.3 shows the spectrum of a black body with a temperature of T = 5600 K and the two above mentioned approximations.

From the two approximations, it is clear that when $h\nu/kT \sim 1$ the black body spectrum has a maximum and it is possible to prove that this peak depends only on the temperature of the body. In particular the relation is:

$$\lambda_{max} T = K, \tag{2.22}$$

where K is a constant. Eq. 2.22 is called Wien Displacement Law. This is a really useful relation because it can be used to estimate the temperature of a black body (e.g. a star) from a relatively easy measure of the wavelength of its peak.

The last fundamental property of the black body radiation is its Luminosity. Integrating Eq. 2.18 over the frequency it is possible to obtain the energy flux radiated by a black body:

$$F = \sigma T^4. \tag{2.23}$$

This equation is called Stefan-Boltzmann law and confirm that most of the properties of the black body emission are related to the temperature of the black body itself. It is easy to calculate the radiated luminosity of the black body from Eq. 2.23:

$$L = 4\pi r^2 F = 4\pi r^2 \sigma T^4, \tag{2.24}$$

which depends only on the dimension of the source and on its temperature. Luminous objects can either be hot, large or both.

2.3 Free-free emission

Free-free emission, also called *thermal bremsstrahlung* from the German word for "braking radiation", is the continuum radiation emitted by charged particle (usually electrons) scattered by an ion. During this process, a charged particle interacts with an ion and as a consequence of the interaction it changes its path, it is accelerated, emitting radiation (Fig. 2.4). The name free-free radiation comes from the fact that the charged particle moves from a free state to another free state with lower energy and it is not bound to the ion in any moment of the process. Free-free radiation is typical of hot plasma in non-relativistic conditions.

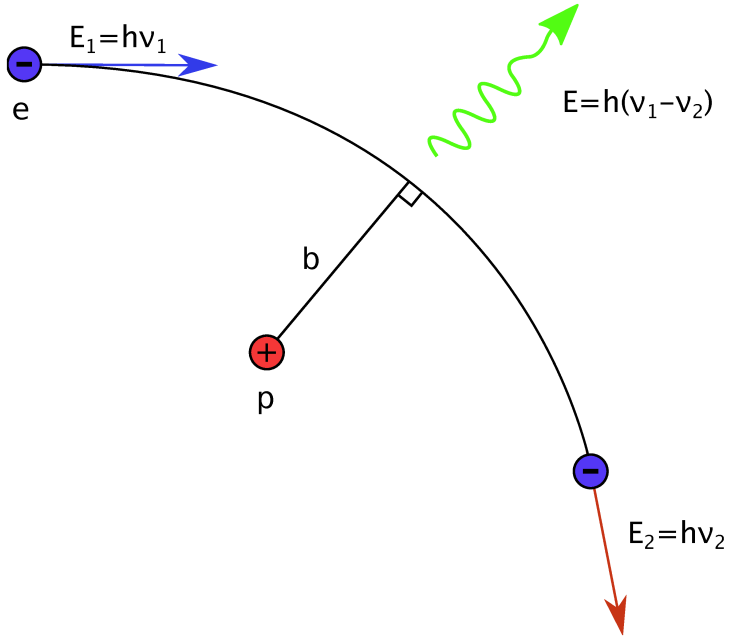

Figure 2.4: Scheme of the production of free-free radiation by an electron with energy $E_1 = h\nu_1$ interacting with a stationary proton. After the interaction the electron goes away with an energy $E_2 = h\nu_2$ after emitting a photon with an energy $E = h(\nu_1 - \nu 2)$.

To describe this emission process an ion with charge Ze and a free electron will be considered. Since the mass of the ion is always several orders of magnitude larger with respect to the mass of the electron, it is possible to consider the ion being at rest in every moment of the scattering, and the electron the only particle accelerated in the process. Considering the electron at a distance d from the ion, with d changing with time with the electron motion, the acceleration felt by the electron is:

$$a = \frac{F}{m} = \frac{Ze^2}{md^2} \approx \frac{Ze^2}{mb^2}, \tag{2.25}$$

where it has been considered that the majority of the acceleration is produced when the electron is at the minimum distance b from the ion. This value b is called the impact parameter. It is possible to calculate the luminosity emitted as a function of the distance (de Young, 2002):

$$L(d) = \frac{2Z^2e^6}{3c^3m^2d^4}. \tag{2.26}$$

$L(d)$ strongly depends on the distance with d^{-4}, therefore the most of the emission is produced when the electron is close to the ion, at a distance $d < \sqrt{2}b$. Moreover, the longer the electron stays close to the ion, the more it is accelerated. The time that the electron spend close to the ion is easy to calculate in the non-relativistic case and it is simply $\Delta t = 2b/v$, where v is the relative velocity of the electron with respect to the ion. It is possible to use this last equation with Eq. 2.26 to derive the

energy released by a single electron during the scattering:

$$E(b,v) = \frac{4Z^2e^6}{3c^3m^2b^3v}, \tag{2.27}$$

where it has been considered that most of the energy is produced when $d \sim b$. The maximum of the energy is produced also at a particular frequency, which is related to the time Δt. This frequency can be expressed as $\omega_{max} = \pi/\Delta t = \pi v/2b$ and it can be used to recover the energy emitted per unit frequency:

$$E(b,v) = \frac{8Z^2e^6}{3\pi c^3m^2b^2v^2}. \tag{2.28}$$

Once calculated the emission of a single electron, it is possible to calculate the emission of the whole plasma which will depend on the number of scattering events per unit time $N = n_i\sigma v$, where n_i is the ion density and $\sigma = \int 2\pi b db$ is the cross-section for the scattering. Not all the impact parameter b will produce a significant amount of emission, but only those for which the electron is close enough, $b \lesssim v/\omega$. It is also convenient to assume that the change in direction of the electron is small, in order to have $\Delta v \lesssim v$. Such conditions allow to obtain some b_{min} and b_{max} and, assuming an electron density n_e it is possible to measure the emissivity

$$\epsilon(v) = \frac{16Z^2e^6n_en_i}{3c^3m^2v} \ln\frac{b_{max}}{b_{min}}. \tag{2.29}$$

The quantity $\epsilon(v)$ is clearly a function of velocity, therefore to obtain the total emissivity of the plasma a velocity distribution must be assumed. In most astrophysical cases, free-free emission is produced in plasma where the electron velocity distribution can be described by a Maxwell-Boltzmann distribution, and this is why free-free emission is usually considered a thermal emission. Integrating Eq. 2.29 considering this velocity distribution and a minimum and maximum velocity of the particles, it is possible to obtain:

$$\epsilon(v) = \frac{16Z^2e^6n_en_i}{3c^3m^2}\bar{g}_{ff}\frac{4\pi^2}{\sqrt{3}}(2\pi)^{-3/2}\sqrt{\frac{m}{kT}}\exp\left(\frac{-mv_{min}^2}{2kT}\right). \tag{2.30}$$

The new parameter $\bar{g}_{ff}$ is called Gaunt factor and it is a quantum mechanical correction of the $\ln(b_{max}/b_{min})$ expression. For the integration it has been considered that $v_{max} = \infty$ while v_{min} must be large enough that $\frac{1}{2}mv^2 = h\nu$ in order to produce the photon. Finally, the total luminosity per unit volume is:

$$L = \frac{32\pi Z^2e^6}{3c^3m^2}\bar{g}_\nu\sqrt{\frac{2\pi mkT}{3h^2}}n_en_i. \tag{2.31}$$

The luminosity is proportional to the density of the plasma and it also increases with $\sqrt{T}$. The free-free emission is an efficient cooling process.

2.4 Emission lines

Optical AGN spectra are often characterized by strong emission lines which are emitted by several different atoms or ions. Such lines are fundamental to study the properties of the gas in the different AGN structures. The identification of the lines and the measurement of their observed wavelengths is an easy way to estimate the redshift of the AGN, the width of the line and its general profile is a proxy of the gas internal motion, and their relative strength is fundamental to investigate the physical condition of the emitting gas.

Each emission line corresponds to the transition of an electron between two energy levels in the same atom. These transitions are governed by the law of quantum mechanics and they usually must satisfy what are called the selection rules for electric dipole emission:

- $\Delta S = 0$
- $\Delta L = 0, \pm 1$ and $L = 0 \not\to L = 0$
- $\Delta J = 0, \pm 1$ and $J = 0 \not\to J = 0$
- $\Delta l = \pm 1$

where S is the total spin quantum number, L is the orbital quantum number, J is the total angular momentum quantum number and finally l is the orbital quantum number of the single electron.

In an atom, the only electron that can move between levels is one of those in the outermost incomplete shell. These valence electrons spend most of their time in the level with the minimum possible energy allowed by the Pauli exclusion principle[1]. When the electrons are in this level, it is said that the atom is in the ground state, while when one of them is on a higher energy level the atom is in an excited state. In order to emit a photon, the atom must be in an excited state and the transition must be towards the ground state or to another excited state with a lower energy.

The strength of a transition between two levels (let us call them level 1 and level 2) is determined by the probability that an excited atom will emit a photon per unit time in that transition. This transition probability is also called the *Einstein coefficient for spontaneous emission* A_{21} and it is defined by the following relation:

$$A_{21} = \frac{64\pi^4 \nu_{12}^3}{3hc^3 g_2} S_{21} \tag{2.32}$$

where S_{21} is the so called *line strength* and g_2 is the statistical weight of the level 2, $g_i = 2J_i + 1$. A_{21} is measured in s^{-1} and it is the inverse of the mean time that an electron spend on level 2 before moving to level 1 emitting a photon. From Eq. 2.32 it is possible to see that the transition probability is strongly dependent on the frequency of the transition itself, so if there are multiple possible transitions for the electron the one with the highest frequency (or the shortest wavelength) is preferred.

This section is partially extracted from Barbieri (1999), Dopita & Sutherland (2003), Osterbrock & Ferland (2006) and La Mura (2018).

[1]The Pauli exclusion principle says that no fermions can exist in an atom with exactly the same quantum numbers.

The transitions respecting the selection rules usually have high probabilities, $A_{21} \sim 10^8$–$10^9\,\mathrm{s}^{-1}$ and they are called *permitted transitions*.

As it has been previously said, to emit a photon, the atom must be in an excited state. One of the possible mechanisms to excite an atom is the photoexcitation. When an atom is placed in an electromagnetic field with energy density $U(\nu_{12})$, where ν_{12} is the frequency of the transition, there is a probability for the atom to absorb one photon and jump to an excited state. This transition probability is defined as $B_{12}U(\nu_{12})$ where $B(\nu_{12})$ is called the *Einstein coefficient for absorption*. However, in the same situation, an atom can also be deexcited into a lower level with a probability $B_{21}U(\nu_{12})$ emitting a photon which is a copy of the incoming one. This process is called stimulated emission and B_{21} is the *Einstein coefficient for stimulated emission*. B_{21} is defined by:

$$A_{21} = \frac{8\pi h\nu_{21}^3}{c^3} B_{21}. \tag{2.33}$$

B_{12} and B_{21} are linked by the following relation:

$$g_2 B_{21} = g_1 B_{12}. \tag{2.34}$$

This equation means that absorption and stimulated emission are competing between each other, and that the relative importance of the first with respect to the other depends on the amount of atom in level 2 and level 1. In usual astrophysical conditions the dominant process is absorption, stimulated emission become dominant only in peculiar cases such as in masers.

The concept of permitted transitions has already been introduced. But if there are permitted transition there should be also *forbidden transitions*. These are all the observed transitions where the electron should not be allowed to perform the jump, according to the electric dipole selection laws. However, in astrophysical optical spectra, it is possible to observe multiple lines which cannot be related to permitted transition and that must be the result of an electron deexciting through a forbidden transition. In AGN, in particular, these often are the strongest lines and they typically are associated with elements heavier than He. On the other hand, typical permitted lines observed in these objects are *recombination lines* such as those of the hydrogen Balmer series.

In the following section the properties of recombination lines and of forbidden lines and their importance in active galactic nuclei will be shortly described.

2.4.1 Recombination lines

The easiest atom to look for when describing spectroscopic transitions are those ions where there is a single electron orbiting around a nucleus of charge Z. Since this is the situation always happening in a hydrogen atom, where a single electron is bounded to a single proton, this class of ions is called *Hydrogenic ions*. For simplicity, the hydrogen atom will be considered in the following discussion.

In the low-density limit, the vast majority of the lines produced by hydrogen is the consequence of a recombination process, when a free electron get captured by a nucleus (typically a free proton). Other processes such as stimulated emission and ionization or excitation from excited states are negligible. The recombination can happen only in two ways:

- a direct recombination to the ground level,
- a recombination to an excited level followed by a transition cascade to the ground state.

From observations, it is clear that the emitting gas is in statistical equilibrium because the emission lines do not rapidly change as expected in the opposite case. Statistical equilibrium means that the populations of the levels are constant, and therefore for each leaving electron there should be another electron which arrives to populate the level:

$$N_n \sum_{m=1}^{n-1} A_{nm} = \sum_{m=n+1}^{\infty} A_{mn} N_m + N_p N_e \alpha_{0n}(T_e). \tag{2.35}$$

The left part of the equation represents the electrons leaving the level downward, where N_n is the number density of atoms in the level n and A_{nm} is the Einstein coefficient for spontaneous emission. The right part represents the electrons arriving at level n. The first term is the number of electrons arriving from upper levels via photon emission, with the same meaning of the symbols as in the left part of the equation, while the second term is the number of electrons directly recombining to level n. Here N_p and N_e are the densities of protons and electrons respectively (the hydrogen case has been considered here) and $\alpha_{0n}(T_e)$ is the coefficient of direct recombination to level n as a function of electron temperature T_e[2].

In thermodynamic equilibrium, which happens when every energy exchange process is perfectly balanced by its own inverse, it is possible to use the Saha equation to describe the ionization state of the gas and the Boltzmann equation to describe the population of the levels:

$$\frac{N_p N_e}{N_1} = \left(\frac{2\pi m_e kT}{h^2}\right)^{3/2} \exp(-h\nu_0/kT) \tag{2.36}$$

$$\frac{N_n}{N_1} = \frac{2n^2}{2} \exp(-\chi_n/kT) \tag{2.37}$$

where m_e is the electron mass, k is the Boltzmann constant, h is the Planck constant and χ_n is the excitation energy of the level n with respect to the ground state.

Combining the previous equation it is possible to obtain the density of atoms in the level n as:

$$N_n = N_p N_e n^2 \left(\frac{h^2}{2\pi m_e kT}\right)^{3/2} \exp\left(-\frac{h\nu_0 - \chi_n}{kT}\right) \tag{2.38}$$

In general, the thermodynamic equilibrium cannot be assumed, but the results are still valid if the right part of the equation is multiplied by a coefficient b_n called the departure coefficient from the thermodynamic equilibrium. It is possible to substitute Eq. 2.38 in Eq. 2.35 obtaining:

[2]The electron temperature is defined as the temperature of the Maxwell-Boltzmann distribution used to describe the velocity distribution of the electrons

$$b_n \sum_{m=1}^{n-1} A_{nm} = \sum_{m=n+1}^{\infty} \frac{m^2}{n^2} b_m A_{mn} \exp\left(\frac{\chi_m - \chi_n}{kT}\right) + \alpha_{0n}(T_e) \left(\frac{2\pi m_e kT}{h^2}\right)^{3/2} \exp\left(-\frac{h\nu_0 - \chi_n}{kT}\right) \quad (2.39)$$

Solving this equation is not trivial, but it allows to find the values for the b_i coefficient for each level. Once b_i is known, it is possible to use Eq. 2.38 to find the population of the level n and therefore the intensity I_ν^L for each line:

$$I_\nu^L = F_{nm}(T_e) \int_0^{r*} N_p N_n dr, \quad (2.40)$$

where all the line properties are grouped in the function F_{nm}.

Up until now, only the so called Case A has been considered, where the gas is optically thin in all the emission lines. However, this only happens in very diffuse nebulae which are extremely difficult to observe because of their low surface brightness. A more realistic condition observed in nebulae, and also in AGN, is the Case B. Case B happens when the optical depth in the Lyman series is so high that the series is optically thick. Typical values of the optical depths for Lyα are around $\tau \approx 10^4$ (Osterbrock & Ferland, 2006), meaning that the mean free path of a Lyα photon is so short that it is almost immediately reabsorbed by another atom. This is true not only for Lyα but for all the Lyman lines, even though the optical depth changes with the line. Moreover, every time that a Lyman photon with energy higher than that of Lyα is absorbed and emitted, there is some finite probability that the emitting transition is decomposed in 2 or more transitions emitting lower energy photons. For example, a Lyβ photon can be decomposed in a Lyα+Hα, a Lyγ in a Lyα+Hβ or Lyα+Hα+Paα and so on. In Case B, therefore, all the Lyα photons are emitted and absorbed almost instantaneously and can be ruled out from the sums of Eq. 2.39. Apart from this exception, the equations are the same and it is possible to measure, with accurate precision, the flux of each hydrogen lines in both cases.

Hydrogen recombination lines are important in AGN because they are some of the strongest lines which can be observed from the BLR. They are therefore fundamental to investigate the properties of the gas in this particular region. Unfortunately, they are not strongly variable as a function of temperature or density of the gas, they cannot be used to directly measure these quantities. Moreover, the gas conditions are quite different from those assumed in Case A and Case B calculations, therefore other processes besides recombination might contribute to the statistical balance and it is more difficult to have precise flux values. However, they trace the kinematics of the gas and the number of ionizing photons, making them fundamental in the study of the BLR structure.

On the other hand, it is possible to say that the gas in the NLR can be well approximated by the Case B scenario. Precise line ratios can be calculated and a comparison with the observed values can be used to estimate important quantities such as dust extinction.

2.4.2 Forbidden lines

Some of the strongest emission lines observed in optical spectra are not recombination lines but forbidden lines (e.g. [O III]λ5007, [N II]λ6584, [S II]$\lambda\lambda$6717, 6731)[3]. As it was already introduced, forbidden transitions are transitions that do not follow the selection rules presented in Sec. 2.4 for the electric dipole. However, they are allowed in another approximation, the *magnetic dipole approximation*.

The main difference between permitted and forbidden lines is that the coefficient of stimulated emission of the latter is several order of magnitudes smaller with respect to that of permitted transitions. There are two direct consequences of this:

- the mean lifetime of the excited level is longer ($\Delta t \approx A_{nm}^{-1}$);
- the Einstein coefficient of absorption is low (Eq. 2.33, 2.34).

Therefore, the ion cannot be excited by photoexcitation and once it is excited via another process, the electron can stay in the excited state for times of the order of seconds or minutes before moving to another level via photon emission.

The mechanism usually involved in the excitation of these ions is *collisional excitation*. The ion is excited via collision with a charged particle, usually electrons and in some cases protons. In this case, the exchange of energy and momentum is not limited by the selection rules because the colliding particle can be used to balance the transition. It must be considered that the collision between an ion and a particle can populate an excited level, but it can also depopulate it, if the electron stays in the excited state for a long enough time. For this reason, forbidden lines can be emitted only in a range of electron densities where the maximum density corresponds to the density where collisional deexcitation completely balance collisional excitation. This value depends on the mean lifetime of the level, since the longer it is, the easier the excited ions can be involved in a collision before emitting a photon.

The efficiency of the collisional excitation depends on the *collisional cross-section*. Considering again an atom with a ground state and a single excited state (1 and 2 respectively), the cross-section is defined by:

$$\sigma_{12}(E) = \left(\frac{h^2}{8\pi m_e E}\right)\left(\frac{\Omega_{12}}{g_1}\right) \tag{2.41}$$

where Ω_{12} is the *collision strength*, a quantity that does not depend on the energy of the transition and that it is symmetric with respect to the lower and upper state, $\Omega_{12} = \Omega_{21}$.

It is possible to derive some interesting properties of forbidden lines with this two level model. Let us consider the equilibrium between collisional excitation and radiative depopulation in the low-density limit:

$$R_{12} = A_{21} N_2, \tag{2.42}$$

where R_{21} is called the rate of population of the upper level per unit volume through collisional excitation:

$$R_{12} = N_e N_1 \alpha_{12}. \tag{2.43}$$

[3]To visually discern between permitted and forbidden lines, the name of the emitting ion in the latter is traditionally wrapped in square brackets.

In this equation, α is the collisional excitation coefficient. Using Eq. 2.43 in Eq. 2.42 and expanding α_{12} the equilibrium equation became:

$$N_2 = N_e N_1 \beta A_{21}^{-1} T^{-1/2} \left(\frac{\Omega_{12}}{g_1}\right) \exp\left(\frac{-E_{12}}{kT}\right), \tag{2.44}$$

where $\beta = [(2\pi\hbar^4)/(km_e^3)]^{1/2}$ is a constant. The flux of the emission line is just the product of the number of transition per unit of time and the energy of each photon:

$$F_{12} = \chi_1 N_e^2 \beta E_{12} T^{-1/2} \left(\frac{\Omega_{12}}{g_1}\right) \exp\left(\frac{-E_{12}}{kT}\right). \tag{2.45}$$

In this equation $N_1 = \chi_1 N_e$ with χ_1 the number fraction of the ion at level 1. This equation is important because it shows the dependence of the flux of the line from the gas temperature. At low temperatures, the line rapidly fades because the exponential is the dominant term, while at high temperatures $T^{-1/2}$ dominates and the line slowly fades. In the high-density limit, the level population are set by the Boltzmann equation and the flux of the line is:

$$F_{12} = \chi_1 N_e E_{12} A_{21} \left(\frac{g_2}{g_1}\right) \exp\left(\frac{-E_{12}}{kT}\right). \tag{2.46}$$

The dependence on the electron density N_e changes from N_e^2 to N_e, which implies that a *critical density* n_c exists. n_c represent the density where the collisional and radiative depopulation equally contribute to the depopulation of the excited level, $A_{21}N_2 = R_{21}$. R_{21} is the rate of depopulation through collisional deexcitation. After some calculation results that:

$$n_c = \frac{A_{21} g_2 T^{1/2}}{\beta \Omega_{12}}. \tag{2.47}$$

From Eq. 2.47 it is possible to see that n_c depends on A_{12} and Ω_{12} and therefore each transition has a different critical density. The presence or the absence of a peculiar emission line can, therefore, be used to roughly estimate the electron density of an astrophysical gas. The best example is the case of the BLR of an AGN. No broad forbidden lines are seen in the spectra of this region, meaning that the density is significantly higher with respect to the highest critical density, i.e. [O III]λ5007 ($n_c \approx 10^6\,\mathrm{cm}^{-3}$ Osterbrock & Ferland, 2006). In the high-density regime the line fades as n_c/n_e, therefore the density should be at least higher than $10^8\,\mathrm{cm}^{-3}$ to completely avoid level depopulation via photon emission. There are not forbidden lines that can be used to estimate an upper limit, but in the UV range is it possible to observe a broad C III]λ1909 line, which arises from a semi-forbidden transition[4]. Also semi-forbidden lines have a critical density and $n_c \approx 10^{10}\,\mathrm{cm}^{-3}$ for C III]λ1909, meaning that the density of the BLR gas should be between 10^8 and $10^{10}\,\mathrm{cm}^{-3}$.

Tree-level atom Even though the two levels model can be useful to derive some properties of forbidden lines, the physics of most of the observed lines can be better

[4]Semi-forbidden transition are transitions that are possible only in the electric quadrupole approximation.

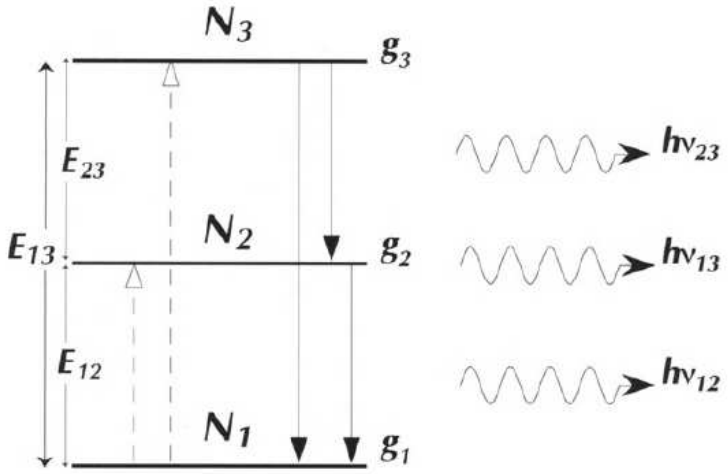

Figure 2.5: Three-level system in the low-density limit, e.g. [O III] (Dopita & Sutherland, 2003).

described by the three-level atom. The levels involved in the transitions often have the same principal quantum number, but they have been split in energy by quantum mechanic effects such as spin-orbit interaction, which are not described here.

The population of the levels can be recovered considering the equations of the statistical equilibrium:

$$\begin{aligned} N_1 C_{13} + N_2 C_{23} &= N_3(C_{31} + C_{32} + A_{32} + A_{31}), \\ N_1 C_{12} + N_3(C_{32} + A_{32}) &= N_2(C_{23} + C_{21} + A_{21}), \\ N_1 + N_2 + N_3 &= 1. \end{aligned} \tag{2.48}$$

While the A_{nm} coefficients are the usual spontaneous emission coefficients, the terms C_{nm} are called collision rates. If $n > m$ the rate represents collisional deexcitation, vice versa it represents collisional excitation. In the first two equations of Eq. 2.48, the left part represents the number of electrons arriving at the level n, the right part the electron leaving. The last equation is just a normalization, which says that the number densities of ions on a certain level are expressed as a fraction of the total ion density. This system of equations can be solved in all cases if the C_{nm} and A_{nm} coefficients are known, but it is useful to consider only two approximations: the low-density limit (collisional deexcitation coefficients negligible) and the limit where the energy difference between the upper two levels is negligible with respect to the difference between the ground level and the excited ones.

In the simple low-density limit (Fig. 2.5), the collisional deexcitation coefficients are negligible, as anticipated. Moreover, it is possible to assume two more simplifications. First, the upper level can be collisionally excited only from the ground level, because the mean lifetime of the middle level is too short for the ion to be further involved in a collision. Second, the number of electrons moving from the upper level to the middle one via photon emission is negligible with respect to the collisional excitation of the level, because the emission coefficient is small and it depends on

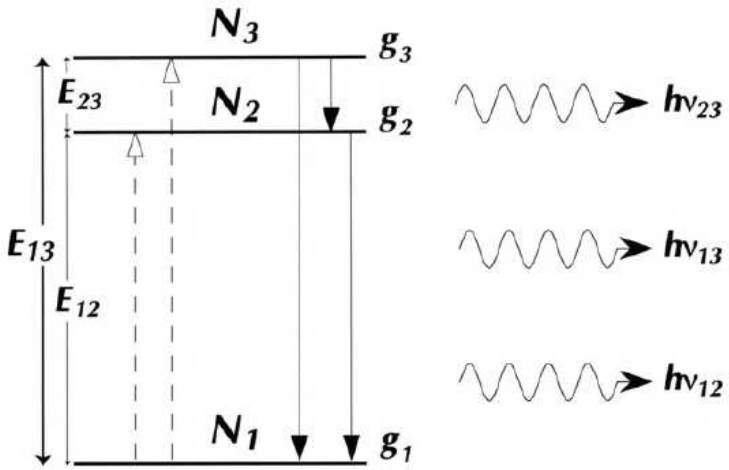

Figure 2.6: Three-level system in the $E_{32} \ll E_{21}$ approximation, e.g. [S II] (Dopita & Sutherland, 2003).

ν^3 (Eq. 2.33). The equations now are:

$$\begin{aligned} N_1 C_{13} &= N_3(A_{32} + A_{31}), \\ N_1 C_{12} &= N_2 A_{21}, \\ N_1 + N_2 + N_3 &= 1, \end{aligned} \tag{2.49}$$

and it is easy to derive $N_3 = N_1 C_{13}/(A_{32} + A_{31})$ and $N_2 = N_1 C_{12}/A_{21}$. Recalling that the flux of the line is just the energy of the line times the number of transitions per unit time, it is possible to recover the flux ratio between the two lines:

$$\begin{aligned} \frac{F_{32}}{F_{21}} &= \frac{E_{32}}{E_{21}} \frac{A_{32} C_{13}}{(A_{32} + A_{31}) C_{12}} \\ &= \frac{E_{32}}{E_{21}} \frac{A_{32} \Omega_{13}}{(A_{32} + A_{31}) \Omega_{12}} \exp\left(\frac{-E_{23}}{kT}\right) \end{aligned} \tag{2.50}$$

where the collisional rate has been expressed as a function of the collision strength, and E_{nm} is the energy difference between level n and m. The line ratio is clearly dependent on the temperature, and this is the reason why the ratio between lines rising from this combination of levels can be used to measure the temperature of the gas.

Common ions that have transitions approximated by this model are [O III], [O I], [N II]. Even though in this real ions the ground level is split in a triplet, the splitting is so small that it is possible to use the three-level approximation. Unfortunately, the line arising from the $3 \to 2$ transition in these systems is usually faint and it can be observed only in very high quality spectra.

The second approximation assumes that $E_{32} \ll E_{21}$ (Fig. 2.6). In this case, it is possible to neglect radiative transitions between the upper levels and the system in

Eq. 2.49, considering a low-density, becomes:

$$\begin{aligned} N_1 C_{13} &= N_3 A_{31}, \\ N_1 C_{12} &= N_2 A_{21} \\ N_1 + N_2 + N_3 &= 1. \end{aligned} \tag{2.51}$$

If A_{32} can be neglected, also Eq. 2.50 can be simplified:

$$\frac{F_{31}}{F_{21}} = \frac{E_{31} A_{32} N_3}{E_{21} A_{31} N_2} = \frac{E_{31} C_{13}}{E_{21} C_{12}} \sim \frac{\Omega_{13}}{\Omega_{12}} \exp\left(\frac{-E_{23}}{kT}\right) \sim \frac{\Omega_{13}}{\Omega_{12}} = \frac{g_3}{g_2}. \tag{2.52}$$

If E_{32} is negligible, the exponential can be neglected and $E_{31} \approx E_{21}$. in the high-density limit, on the other hand, the population of the level is described by the Boltzmann law, therefore $N_3/N_2 = g_3/g_2$. The flux ratio becomes:

$$\frac{F_{31}}{F_{21}} = \frac{E_{31} A_{32} N_3}{E_{21} A_{31} N_2} = \frac{A_{31} g_3}{A_{21} g_2}. \tag{2.53}$$

Eq. 2.52 and Eq. 2.53 show that the line ratio tends to a limit both at low and high density and that the two limits are different. Moreover, the limits do not depend on temperature, therefore it is possible to use the ratio between the two lines as a proxy of the gas electron density. Typical lines used to this aim are [O II]$\lambda\lambda 3726, 3729$ and [S II]$\lambda\lambda 6716, 6731$.

2.5 Shocks

Shocks are a peculiar emission mechanism and they are not as evident in the spectrum of AGN as the other mechanisms previously described. However, their presence is a well-established property of AGN (e.g. Dopita, 1995) and they are used to explain a wide variety of situations, starting from emission line ratios (e.g. Dopita & Sutherland, 1995; Dopita, 2000; Contini et al., 2002; Congiu et al., 2017c), to jet knots and polarization (e.g. Lister & Homan, 2005; Beckmann & Shrader, 2012). Shocks are also one of the main ways for the AGN to interact with its own host galaxy, since a jet expanding in the ISM produces shocks (Dopita, 2000; Fragile et al., 2017).

Shocks are able to both ionize the ISM during its passage, but radiative shocks also produce a large amount of radiation which contribute to the photo-ionization of the gas. A shock can be considered as a sharp discontinuity in some of the properties of the gas, in particular ρ, P and v, density, pressure and velocity. It is convenient to use a reference system moving with the shock front. The shock motion is usually steady, therefore the reference system is moving at a constant speed. It is also possible to describe the motion as a one-dimensional flow with the velocity components perpendicular to the shock front, and the quantity ahead and behind the shocks will be identified with the numbers 0 and 1 respectively. In these conditions, in every instant the conservation of mass and momentum across the shock front applies and it is possible to write:

$$P_0 + \rho_0 v_0 = P_1 + \rho_1 v_1, \tag{2.54}$$

$$\rho_0 v_0 = \rho_1 v_1. \tag{2.55}$$

This section is extracted from Dopita & Sutherland (2003) and Osterbrock & Ferland (2006).

In most conditions, it is also possible to assume an adiabatic compression of the gas, therefore the equation of state becomes $P = K\rho^\gamma$ and it can be used to recover a third equation:

$$\frac{v_0^2}{2} + \frac{\gamma}{\gamma - 1}\frac{P_0}{\rho_0} = \frac{v_1^2}{2} + \frac{\gamma}{\gamma - 1}\frac{P_1}{\rho_1}. \tag{2.56}$$

γ is the adiabatic index of the gas, and in most astrophysical cases, where the gas is mostly monoatomic hydrogen, its value is 5/3. Equation 2.54, 2.55 and 2.56 are the so called Rankine-Hugoniot conditions at the shock front and they relate the condition of the gas ahead and behind the shock. To solve the equations it is usually assumed that the quantity ahead the shock (ρ_0 and P_0) are known and the ratios ρ_1/ρ_0 and P_1/P_0 are derived as a function of the Mach number of the shock front. The Mach number M is defined as:

$$M = \frac{|v_0|}{c_0} \tag{2.57}$$

where c_0 is the sound speed in the undisturbed gas:

$$c_0 = \sqrt{\frac{\gamma P_0}{\rho_0}}. \tag{2.58}$$

The Mach number, therefore, is the ratio between the velocity of the gas and the speed of sound. The interesting limits for this number are 2: if $M \to 1$ the shock is considered a weak shock, a small disturbance in the gas propagating at the speed of sound; if $M \to \infty$ the shock is a strong shock propagating at supersonic speed. From the previous equation it is possible to calculate the ratio of densities and pressures behind and ahead of the shocks:

$$\frac{P_1}{P_0} = \frac{2\gamma}{\gamma + 1}M^2 - \frac{\gamma - 1}{\gamma + 1}, \tag{2.59}$$

$$\frac{\rho_1}{\rho_0} = \frac{(\gamma + 1)M^2}{(\gamma - 1)M^2 + 2}. \tag{2.60}$$

In the weak shock limit, both ratios tend to 1, while for $M \to \infty$ the ratios of pressures tends to ∞, but the ratio of densities depends on the kind of shocks: $\rho_1/\rho_0 \to 4$ for an adiabatic shock, $\rho_1/\rho_0 \to \infty$ for an isothermal shock. As a first approximation, in common astrophysical nebulae the temperature of the gas is driven by radiative processes and it is the same ahead and behind the shock, therefore the shock can often be considered isothermal.

In an actual shock the temperature just behind the shock rises significantly, but all the energy is radiated away efficiently and the gas cools rapidly, in such a way that relatively close to the front the temperature is the same of the gas ahead of the shock.

2.5.1 Radiative structure of shocks

In the previous section, it has been introduced the concept of isothermal shocks in astrophysical sources. It has also been said that there is a small region behind the shock front which is characterized by a high temperature where the gas is able

to cool rapidly. It is in this region that most of the interesting radiative processes happens.

The structure of this region depends on the velocity of the shock, and therefore on the energy transported. Just after the shock front, the various components of the plasma relax towards equipartition of energy in the so called *equipartition zone* and all the plasma components can be described by the same temperature. Just after that, there is a region called the *ionization zone*, where the lowly ionized gas coming from the pre-shock region suddenly increases its ionization degree because of the high temperature. If the shock is fast enough, the plasma reaches a status of *collisional ionization equilibrium*, where collisional ionization and recombination are in equilibrium, before entering in the following zone, the *cooling zone*. In this region, the gas rapidly cools, almost isobarically, and the density increases. During the cooling, the plasma emits extreme UV photons which are able to ionize hydrogen, and if it is hot enough it can also produce X-rays. When the temperature of the gas decreases to around 10^4 K, the hydrogen starts to be able to absorb the incoming UV radiation. Since the radiation is isotropic, half of it is able to cross the shock front and it can be absorbed by the pre-shock hydrogen which can be fully ionized if the velocity of the shock is higher than $120\,\mathrm{km\ s^{-1}}$. This is important because if the plasma entering the shock is already fully ionized the structure of the shock changes.

Moving downstream the shock, to the region where the UV photons have been completely absorbed, the plasma is finally able to continue cooling and recombining. The cooling, in all its phases, happens via emission of lines or continuum. At the beginning, where the temperature reaches its highest value, the emission is mostly in the UV range. Several permitted lines or semi-forbidden lines of abundant ions such as C II, C III, N V, O IV are emitted. When the temperature cools optical lines start to become dominant. The ions are mostly collisionally excited, so forbidden emission lines of [O I], [O II], [O III], [S II] dominates the spectrum, together with hydrogen Balmer lines. In particular, the flux in the Balmer lines strongly depends on the shock velocity and their ratio can be used to estimate this quantity.

3

IC 5063 AND NGC 7212

This chapter is extracted from Congiu et al. (2017b)

This chapter describes the first work I carried on during my PhD. It is focused on the study of known extended narrow-line regions (ENLRs) in two Seyfert 2 galaxies of the nearby universe: IC 5063 and NGC 7212. I analyzed high-resolution spectra to investigate how the main properties of the ENLR depend on the gas velocity. I divided the emission lines in velocity bins and I calculated several line ratios. Diagnostic diagrams and SUMA composite models (photo-ionization + shocks), show that in both galaxies there might be evidence of shocks significantly contributing to the gas ionization at high $|V|$, even though photo-ionization from the active nucleus remains the main ionization mechanism. In IC 5063 the ionization parameter depends on V and its trend might be explained assuming a hollow bi-conical shape for the ENLR, with one of the edges aligned with the galaxy disk. On the other hand, NGC 7212 does not show any kind of dependence. The models show that solar O/H relative abundances reproduce the observed spectra in all the analyzed regions. They also revealed a high fragmentation of the gas clouds, suggesting that the complex kinematics observed in these two objects might be caused by interaction between the ISM and high-velocity plasma components, such as jets.

3.1 Introduction

Active galactic nuclei (AGN) are among the most luminous objects of the Universe and they have been intensively studied, in the last decades, because they are characterized by many important astrophysical processes. Some nearby AGN, typically Seyfert 2 galaxies (~ 50 up to $z \sim 0.05$, Netzer, 2015), are characterized by conical or bi-conical structures of highly ionized gas, whose apexes point the galaxy nucleus, the *ionization cones*. The extension of optical emission (which is usually traced with

the [O III]λ5007 line) is of the order of kiloparsecs and in the most extended ionization cones it can be traced up to 15–20 kpc (Mulchaey et al., 1996a,b; Schmitt et al., 2003a). The presence of ionization cones was already predicted by the Unified Model (Antonucci & Miller, 1985; Antonucci, 1993) which affirms that the core of the AGN is surrounded by a dusty torus that absorbs part of the radiation coming from the nucleus. However, the radiation emitted along the torus axis can escape and ionize the surrounding gas, forming the narrow-line region (NLR). When the host galaxy contains enough gas and the NLR is not absorbing completely the ionizing photons, it is possible to observe the ionization cones (Evans et al., 1993). Due to its extension, this region of ionized gas is also called extended narrow-line region (ENLR)[1].

Both the NLR and the ENLR are characterized by spectra with narrow permitted and forbidden emission lines, with a typical full width at half maximum (FWHM) between 300 and 800 km s^{-1}. The presence of several forbidden lines indicates that the electron density of both regions is low, typically $n_e \sim 10^2$ – 10^4 cm^{-3}. High-resolution images of nearby galaxies with ionization cones (e.g. Schmitt et al., 2003a) reveal the presence of substructures, such as gaseous clouds and filaments. Medium and high-resolution spectra show line profiles characterized by asymmetries, bumps and multiple peaks (e.g. Dietrich & Wagner, 1998; Ozaki, 2009), indicating very complex kinematics. These internal gas motions are expected to produce shock-waves, which can further influence the properties of the NLR/ENLR (see e.g. Contini et al., 2012).

There are several possible causes of the complex kinematics of these structures. For example, the interaction between jets and the interstellar medium (ISM) of the galaxy, as suggested by the fact that the cone axis and the radio-jet axis, if present, are often aligned (Unger et al., 1987; Wilson & Tsvetanov, 1994; Nagar et al., 1999; Schmitt et al., 2003a). Another possibility is that the gas of the ENLR is the result of an episode of merging which brought new material toward the center of the host galaxy (Veilleux et al., 1999; Ciroi et al., 2005; Di Mille, 2007; Cracco et al., 2011). The third possibility is the presence of fast outflows (400 – 600 km s^{-1}) which involve different kinds of gas, from the cold molecular one to the warm ionized one (Baldwin et al., 1987; Morganti et al., 2015; Dasyra et al., 2015). It is worth noting that the radio-jet – ISM interaction could cause these outflows (Tadhunter et al., 2014; Morganti et al., 2015; Dasyra et al., 2015).

Trying to distinguish among these causes it is clearly not an easy task. Data indicate that most AGN hold a NLR, while, up to $z \sim 0.05$, very few of them show an ENLR (Netzer, 2015). The morphology of Seyfert galaxies up to $z \sim 1$ is almost unperturbed, suggesting that the gravitational interactions, when it occurs, must be minor merger events (Cisternas et al., 2011). Besides, most of Seyfert galaxies are classified as radio-quiet (Singh et al., 2015a) with compact radio emission, even though recent studies found that kiloparsec scale emission might be more common than expected (e.g. Gallimore et al., 2006; Singh et al., 2015a). In spite of that, the kinematics of both NLR and ENLR is often characterized by radial motions (e.g. Morganti et al., 2007; Ozaki, 2009; Cracco et al., 2011; Netzer, 2015), suggesting that the ionized gas is not simply driven by the gravitational potential of the host

[1] I consider the ENLR as a natural extension of the NLR beyond 0.8–1 kpc

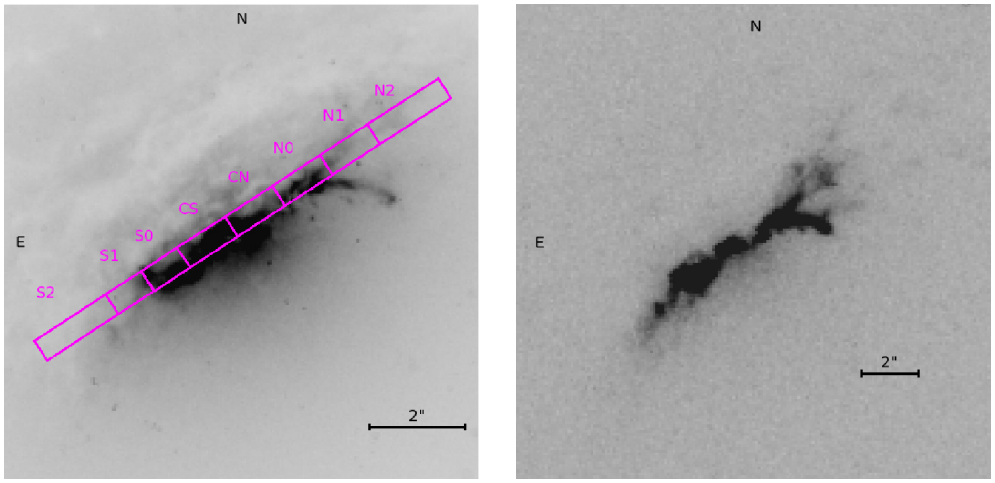

Figure 3.1: Left: Image of the Seyfert galaxy IC 5063 taken with the F606W filter of the Wide Field and Planetary Camera 2 (WFPC2) of the Hubble Space Telescope (HST). In purple are shown the position of the slit and the regions from which the one-dimensional spectra were extracted. **Right:** Image taken with the FR533N filter of the WFPC2. The images were recovered from the Hubble Legacy Archive (HLA).

galaxy.

Within this picture, I chose to carry out a pilot study of the physical properties of the NLR/ENLR gas as a function of velocity by comparing the intensities and profiles of emission lines analyzed in medium and/or high-resolution spectra. I am well aware that this is a relatively unexplored field due to the need of observing nearby AGN with large diameter telescopes, in order to have simultaneously good spectral and spatial resolution and high signal-to-noise ratio (SNR) spectra. Nevertheless, this first test showed that with a resolution $R \sim 10000$ it is possible to highlight structures in the line profiles, such as multiple peaks and asymmetries, which are usually missed in low-resolution spectra. Moreover, the lines seem to be intrinsically broad, therefore a further increase of the resolution will probably not improve the separation between the gaseous components.

In Ozaki (2009) the author developed a method to investigate the emission line profile in high-resolution spectra. Ozaki analyzed medium resolution data of the archetypal Seyfert 2 galaxy NGC 1068, dividing the emission lines in velocity bins, according to the morphology of the [O III]λ5007 profile, and analyzing the properties of the gas in each one of them in order to study their variation as a function of velocity. In this work, I adapted and applied this method to medium resolution echelle spectra of two nearby Seyfert 2 galaxies with ENLR: IC 5063 and NGC 7212. Both of them show extended ionization cones and are observable from the southern hemisphere. I used the strongest optical lines to directly measure the physical properties of the gas such as density, extinction, ionization degree. Then, I calculated the gas physical conditions and element abundances through detailed modeling of the line ratios. I adopted the code SUMA (Contini et al., 2012) which accounts for the coupled effect of photo-ionization and shocks (see Sec. 3.4.5).

Table 3.1: Principal characteristics of MagE observations.

Name	Exp. time (s)	PA (deg)	Slit (arcsec)	Dispersion (Å px^{-1})	Seeing (arcsec)	Date
IC 5063	2400	123	0.5	0.29	1.1	2010-05-31
NGC 7212	6000	16	0.5	0.28	1.1	2010-05-31

From left to right: 1) name of the object, 2) total exposure time, 3) Position angle of the slit during the observations, 4) slit width, 5) dispersion of the spectra, 6) seeing of the observations, as measured from the close standard star observed during the night , 7) date of observations.

In Sec. 3.2 I present the observations and the sample, in Sec. 3.3 I describe the data reduction, in Sec. 3.4 I show how I analyzed the data and the results obtained and in Sec. 3.5 I summarize our work.

In this chapter, the following cosmological parameters have been assumed: $H_0 = 70\,\mathrm{km\ s^{-1}\,Mpc^{-1}}$, $\Omega_{m,0} = 0.3$ and $\Omega_{\Lambda,0} = 0.7$ (Komatsu et al., 2011).

3.2 Sample and observations

In this work, I studied two nearby Seyfert galaxies with known ENLR: IC 5063 and NGC 7212 (Tab. 3.2). I analyzed archival spectra of these sources observed with the MagE (Magellan Echellette) spectrograph mounted at the Nasmyth focus of the Clay telescope, one of the two 6.5m Magellan telescopes of the Las Campanas Observatory (Chile). MagE is able to cover simultaneously the complete visible spectrum (3100 – 10000 Å) with a maximum resolution R = 8000 or $\sim 37.5\,\mathrm{km\,s^{-1}}$(Marshall et al., 2008). The spatial scale of the instrument is $0.3\,\mathrm{arcsec\,px^{-1}}$.

Both galaxies were observed with multiple exposures of 1200 s each with the $0.5''$ slit. Additional spectra were also acquired to perform data reduction (night-sky and calibration lamp spectra). The spectrophotometric standard HR5501 was observed each night to carry out the flux calibration. The details of the observations are reported in Table 3.1. While IC 5063 spectrum has been analyzed for the first time in this work, the NGC 7212 data were previously published in Cracco et al. (2011).

3.2.1 IC 5063

IC 5063 (Fig. 3.1) ($z = 0.01135$) is a lenticular galaxy classified as a Seyfert 2 (Morganti et al., 2007). Table 3.2 lists some of the principal properties about the object as reported by the NASA/IPAC Extragalactic Database (NED)[2]. It is one of the most radio-loud Seyfert 2 galaxies known, its radio luminosity is 2 orders of magnitude larger than that of typical Seyfert galaxies (Morganti et al., 1998). IC 5063 is characterized by a complex system of dust lanes aligned with the major axis of the galaxy. It also shows a strong IR emission (Hough et al., 1987) and a very broad component of Hα in polarized light (Inglis et al., 1993), likely a sign of an obscured broad line region (BLR).

The ENLR was discovered by Colina et al. (1991), who found a very extended region of ionized gas ($\sim 22\,\mathrm{kpc}$, $H_0 = 50\,\mathrm{km\ s^{-1}\,Mpc^{-1}}$) at position angle $PA =$

[2] `https://ned.ipac.caltech.edu/`

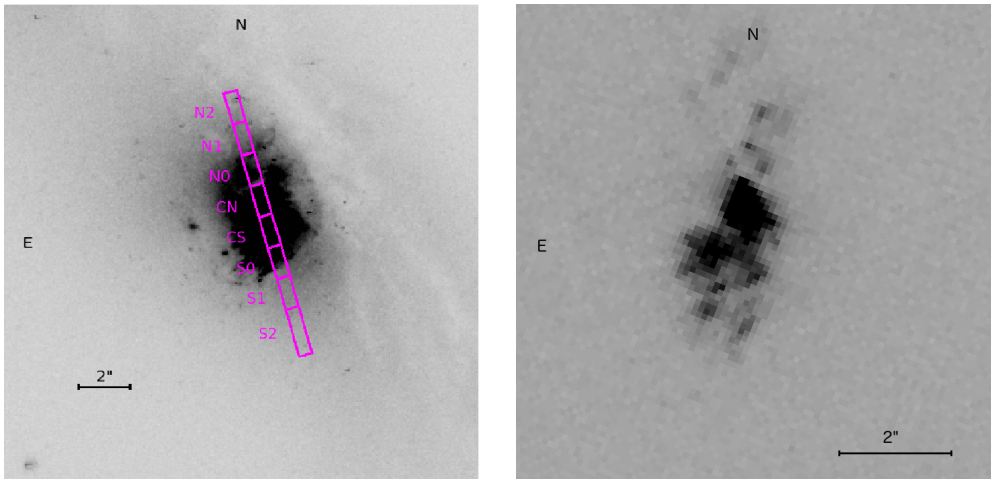

Figure 3.2: Left: Image of the Seyfert galaxy NGC 7212 taken with the F606W filter of the WFPC2 of the HST. In purple are shown the position of the slit and the regions from which the one-dimensional spectra were extracted. **Right:** Image taken with the FR533N filter of the WFPC2. The images were recovered from the HLA.

123°, with a peculiar X shape and an opening angle of about 50°. They supposed that the ENLR is the result of a quite recent merging between an elliptical galaxy and a small gas-rich spiral galaxy. Morganti et al. (2007) traced [O III]$\lambda\lambda$4959, 5007 and Hα emission lines up to a distance of about 15–16 arcsec (3.5–3.8 kpc) from the nucleus in a direction very close to the two resolved radio jets, PA = 117°. The authors found signs of fast outflows, with velocities of about 600 km s^{-1} in all the gas phases.

Similar velocities were also found several years earlier by Morganti et al. (1998) who discovered fast outflows in the neutral gas of the galaxy studying the H I line at 21 cm. These outflows were the first of their kind discovered in a galaxy and they were deeply studied in the following years (Morganti et al., 2007; Tadhunter et al., 2014; Morganti et al., 2015). The authors explained them as gas accelerated by fast shocks caused by the radio jets plasma expanding in the ISM.

3.2.2 NGC 7212

NGC 7212 (Fig. 3.2) is a nearby spiral galaxy ($z = 0.02663$) belonging to a system composed by three interacting objects. Some of its characteristics are reported in Table 3.2. It was classified as Seyfert 2 by Wasilewski (1981). Later Tran (1995), who studied some Seyfert 2 galaxies in polarized light, found an elongated NLR in NGC 7212 with the axis aligned with a structure of highly ionized gas at PA = 170°. Then, Falcke et al. (1998) discovered the presence of a diffuse and extended NLR also in non-polarized light, in a compatible direction with the previously found elongated structure, but without the well-defined shape typical of ionization cones. They also discovered a radio-jet aligned with this ENLR and they suggested that the two structures are interacting.

The existence of the ionization cones was finally confirmed by Cracco et al. (2011)

Table 3.2: Principal properties of the observed galaxies from the NED.

Name	RA (h:m:s)	Dec (d:m:s)	z	B (mag)	A(V) (mag)	Morph.
IC 5063	20:52:02	−57:04:08	0.01135	12.89	0.165	S0
NGC 7212	22:07:01	10:13:52	0.02663	14.78[1]	0.195	Sab

[1]Muñoz Marín et al. (2007)
From left to right: 1) name of the object, 2) right ascension and 3) declination, 4) redshift of the source, 5) B-band magnitude, 6) galactic extinction from Schlafly & Finkbeiner (2011) reported by the NED, 7) morphological classification.

through integral field spectroscopy observations. This structure extends from the nucleus to about $3 - 4$ kpc in both directions and it is almost aligned with the optical minor axis of the galaxy (PA = 150°). Cracco et al. (2011) discovered clear asymmetries in the emission lines of the ENLR, a sign of the presence of radial motions of the gas. This property, together with a possible sub-solar metallicity, induced the authors to suggest that the ENLR gas in NGC 7212 has been accreted through the interaction of the active galaxy with the other members of the system. In addition, Cracco et al. (2011) found quite high [N II]/Hα and [S II]/Hα ratios, especially in the region of interaction between NGC 7212 and one of the companion galaxies. This suggested that the ionization mechanism of the gas is a combination of photo-ionization from a non-thermal continuum and shocks (Contini et al., 2012).

3.3 Data Reduction

I performed the data reduction using IRAF 2.15[3] (Image Reduction and Analysis Facility). After subtracting the bias from all the images, I extracted the spectrum of each dispersion order using the `strip` option of the `apall` task and I processed each extracted spectrum (from now on also called apertures) following a standard long-slit reduction. I used a Th–Ar lamp for wavelength calibration and the standard star HR5501 for flux calibration and telluric correction.

The final goal of the data reduction was to obtain one-dimensional (1D) spectra of different regions of the galaxies. In this analysis, it is essential to have straight and aligned spectra, to extract the emission of the same region at all wavelengths. Therefore, I first rectified the two-dimensional spectra using the tasks `identify` and `reidentify` to trace the central peak of each spectrum along the spatial direction. Secondly, I applied the correction to the images with `fitcoords` and `transform`. Then I used `xregister` to align all the apertures.

After that, I divided the 2D spectra of the galaxies into regions, looking for the best trade-off between a good SNR in all spectra and a good spatial sampling of the extended emission. For this reason, the dimension of each one of them can vary between 3 and 5 pixels. I used, as a reference, the Hα emission line (Fig. 3.3). Then, I summed up the flux of each region to obtain 1D spectra. The names and the positions of the extracted regions are shown in Table 3.3. The final SNR ratio on the continuum at 5500 Å (rest-frame wavelength) varies from SNR $\sim$ 25 in the CN

[3]http://iraf.noao.edu

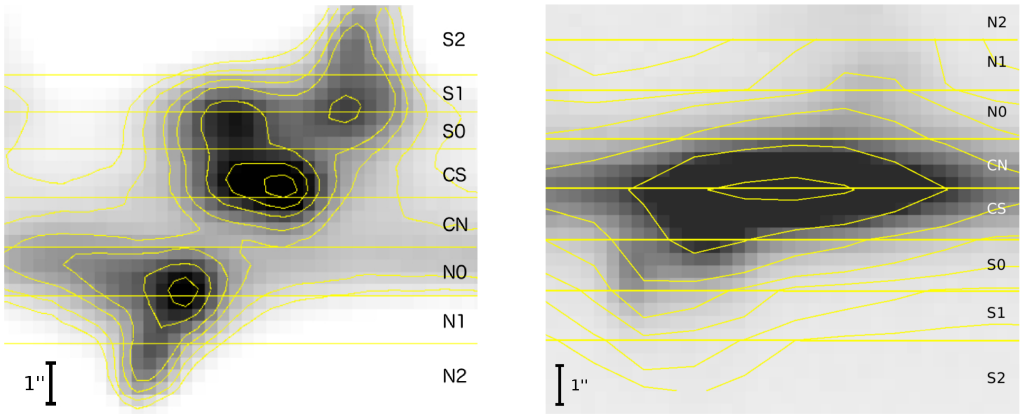

Figure 3.3: The figure show the division in regions of the MagE spectra of IC 5063 (left) and NGC 7212 (right). For both objects the Hα region of the spectrum is shown with contours to highlight the features of the emission lines.

Table 3.3: Projected distances in arcseconds and parsecs of the regions from the nucleus of the galaxy, recessional velocities measured from the spectra and velocity corrections from STARLIGHT.

	IC 5063				NGC 7212			
Region	R (arcsec)	R (pc)	V (km s^{-1})	ΔV (km s^{-1})	R (arcsec)	R (pc)	V (km s^{-1})	ΔV (km s^{-1})
N2	4.50	1044	3328	−38.51	4.50	2408	8062	−44.02
N1	3.00	696	3337	−14.58	3.00	1605	8016	4.11
N0	1.80	417	3357	−28.78	1.80	963	8074	−55.91
CN	0.60	139	3364	−19.01	0.60	321	7963	−38.77
CS	0.60	139	3380	−15.52	0.60	321	7916	−59.07
S0	1.65	382	3417	−28.51	1.80	963	7799	54.31
S1	2.55	591	3438	−40.09	3.00	1605	7703	137.68
S2	3.90	904	3448	−23.02	-	-	-	-

region of IC 5063 to SNR $\sim$ 18 in the N2 region. Even though the observing time of NGC 7212 is more than twice that of IC 5063, the spectra of this galaxy have a generally lower SNR. The highest SNR is found in the CN region (SNR $\sim$ 20) while the lowest is SNR $\sim$ 4.5 and it is measured in the N2 region.

3.3.1 Subtraction of the stellar continuum

The galaxy continuum is a combination of several components: the stellar continuum, the AGN continuum and the nebular continuum, which is mainly due to hydrogen free-free and free-bound emission. AGN emission is negligible in Seyfert 2 galaxies because the AGN is obscured by the dusty torus (e.g. Beckmann & Shrader, 2012) and the nebular continuum is estimated to be at least one order of magnitude fainter than the observed stellar emission (Osterbrock, 1989). Therefore, for the purposes of the work, the main component of the galaxy continuum is the stellar continuum. To obtain reliable line flux measurements it is important to subtract

this component from the spectra, mainly because of the typical stellar absorption features (e.g. hydrogen Balmer lines) which can fall at the same wavelength of emission lines, modifying their observed flux.

One of the best methods to subtract this component is to use STARLIGHT (Cid Fernandes et al., 2005; Mateus et al., 2006; Cid Fernandes et al., 2007). STARLIGHT is a software developed to fit the stellar component of galaxy spectra using a linear combination of simple stellar populations spectra, taking into account both extinction and velocity dispersion.

To work properly, STARLIGHT needs spectra with fixed characteristics: they have to be corrected for Galactic extinction, they must be shifted to rest frame and they must also have a $1\,\text{Å}\,\text{px}^{-1}$ dispersion. I corrected for Galactic extinction with A(V) = 0.165 and A(V) = 0.195 (Schlafly & Finkbeiner, 2011) for IC 5063 and NGC 7212 respectively (Table 3.2). I then shifted the spectra to rest-frame wavelengths. It is not easy to do accurate redshift measurements on these objects because the emission lines are broad and they sometimes show multiple peaks. For this reason I averaged the values obtained from some of the deepest stellar absorptions: the Mg I triplet (λ5167, λ5177, λ5184 Å) and the Na I doublet (λ5889, λ5895 Å). In the most external regions of the galaxies, where the SNR of the continuum was too low to detect those lines, I used the strongest peak of some emission lines such as Hβ or [O III]λ5007. The obtained recessional velocities are shown in Table 3.3. To estimate the errors on the velocity measurements, I calculated the accuracy of the wavelength calibration comparing the position of the sky lines with respect to the expected position. I obtained $\sigma = 0.2\,\text{Å}$, which corresponds to $\sigma_V = 10\,\text{km s}^{-1}$. However, STARLIGHT can independently measure small velocity shifts from the rest frame spectra ($< 500\,\text{km s}^{-1}$) during the fit. This allows to fine tune the velocity correction, especially where emission lines are used. The fine-tuning is very important because I needed to remove every single velocity component due to galaxy rotation to study the kinematics of the gas.

Once applied the listed corrections, I ran STARLIGHT using 150 spectra of stellar populations with 25 different ages (from 10^6 to $1.8 \times 10^8\,\text{yr}$) and 6 different metallicities (from $Z = 10^{-4}$ to $Z = 5 \times 10^{-2}$) to obtain the spectrum of the stellar component and the velocity correction. In the regions where the SNR was too low to obtain a good fit of the continuum, I used the results of the software to correct the velocity measurements but I subtracted the stellar continuum fitting it with a polynomial function, using IRAF `splot` task. This happened principally in the faintest NGC 7212 spectra, i.e. hose of the N2, N1 and S2 regions (SNR $\sim$ 4–8).

3.3.2 Deblending

Because of their intrinsic width, some prominent spectral lines are partially overlapped (e.g. Hα and [N II]$\lambda\lambda$6548, 6584; [S II]$\lambda\lambda$6716, 6731). These lines are essential to study the gas properties: Hα is used in the diagnostic diagrams (Baldwin et al., 1981; Veilleux & Osterbrock, 1987) and to measure the extinction coefficient, the ratio between the [S II]$\lambda\lambda$6716, 6731 doublet is used to estimate the electron density. Therefore, to measure their fluxes, especially on the line wings, I had to deblend them. To perform the deblending I adapted to this case the method developed by Schirmer et al. (2013). They assumed that if Hα and Hβ are produced by the very

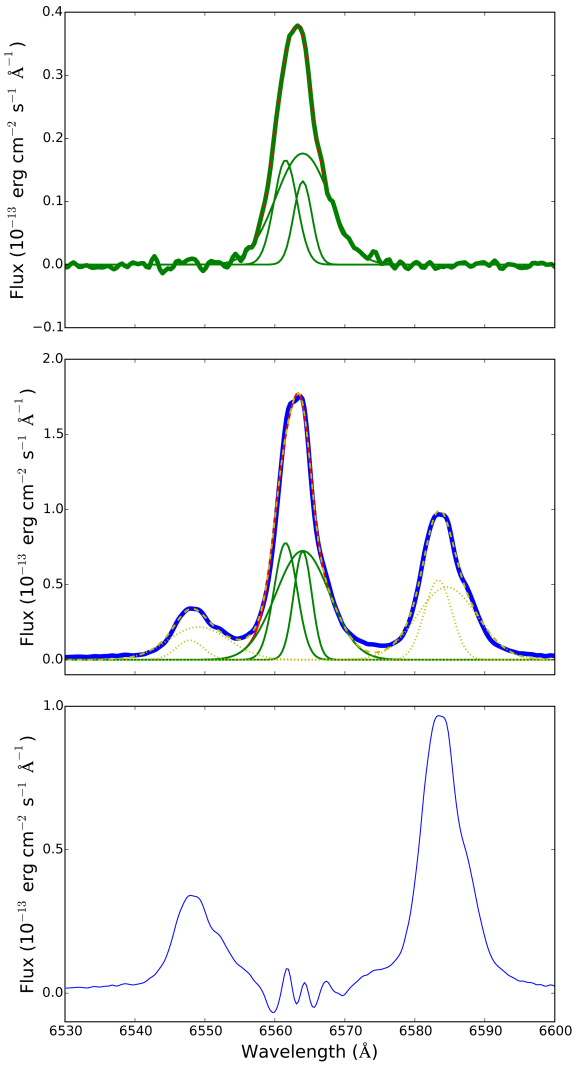

Figure 3.4: The deblending process of Hα + [N II] in the CS region of IC 5063. The top panel shows Hβ shifted to Hα wavelength and fitted with 3 Gaussians (the thin curves). The middle panel shows the best fit of Hα + [N II]. The thin solid curves are the Gaussians fitting Hα and the dotted ones are the functions fitting the [N II] doublet. In the bottom panel there is the result of the subtraction of the Hα fit from the spectrum.

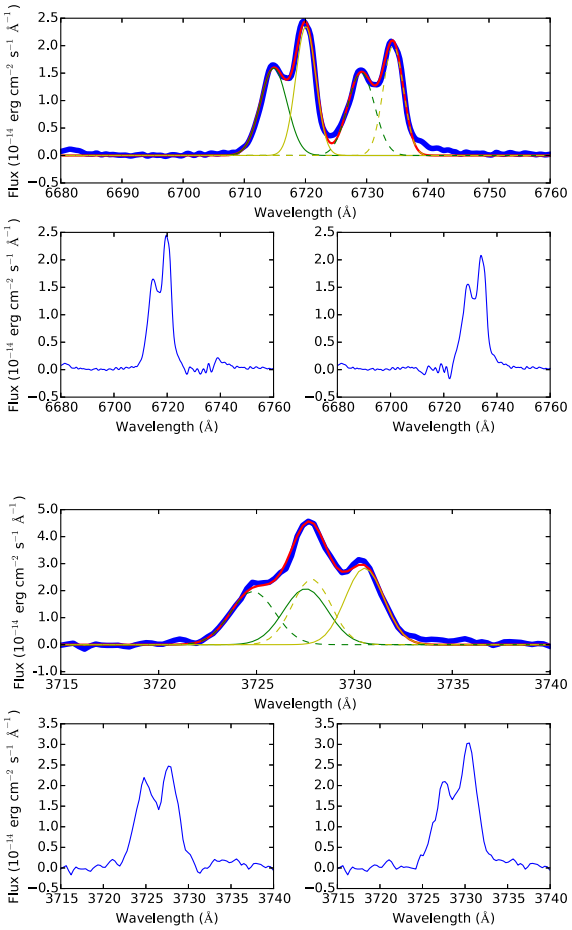

Figure 3.5: The final results of the deblending process for the [S II] doublet (top) and [O II] doublet (bottom) of the CS region of IC 5063. For each doublet is shown the original spectrum, with the fitting functions, and the two lines after the deblending. The continuous lines represent the functions with the free parameters ([S II]λ6716 (top), [O II]λ3729 (bottom)), the dashed lines represent the functions fitted with the constraints ([S II]λ6731 (top),[O II]λ3726 (bottom)). The original spectrum is shown in blue, the fitted spectrum is shown in red, the green Gaussians are the main components of each line, the yellow ones are their secondary components.

same gas, they must have the same profile, except for extinction effects. Therefore, they multiplied Hβ for a constant factor in order to match the Hα peak intensity, they subtracted the multiplied Hβ from the Hα+ [N II] group, obtaining only the [N II] doublet emission. To recover the final Hα line they subtracted the doublet from the original spectrum, after removing the residuals of the previous subtraction, due to intrinsic noise and to the assumption of constant extinction in the whole line.

To deblend Hα from [N II] I wrote a *python 2.7* script, modifying this process in the following way. I first shifted Hβ to the wavelength of Hα and I fitted it with 2 or 3 Gaussians, trying to reproduce the line profile and selecting the result showing the minimum residual. Then, I fitted Hα with the same number of functions, keeping the same FWHM and the same relative positions but varying their intensities. In this way, I considered that the extinction could change in each kinematic component. To get a better result I also fitted the [N II] doublet using 2 Gaussians for each line. Then, I subtracted the Hα fit from the spectrum, obtaining the [N II] doublet and I removed the residuals (Fig. 3.4). Finally, I subtracted again the [N II] doublet from the original spectrum, obtaining the final Hα line. I used the same process to remove [S III]λ6310 from [O I]λ6300 in the regions where the [S III] line was strong enough to be detected.

To deblend the [S II] doublet and the [O II]$\lambda\lambda$3726, 3729 doublet I further modified the method. I started deblending the [S II] doublet because their separation in wavelength is ~ 14 Å and they are usually partially resolved. To fit these lines I assumed that they have the same profile, except for the intensity, because they are emitted by the same gas but their ratio is influenced by the electron density. I reproduced each line with 2 or 3 Gaussian functions, depending on the quality of the spectrum. To reduce the number of free parameters, I fitted the [S II]λ6716 line letting all the parameters free to vary and I fixed the position and the width of the Gaussians for the [S II]λ6731 line with respect to the corresponding quantities for the [S II]λ6716 line, according to the theoretical properties of the doublet ($\Delta\lambda = 14.3$ and same FWHM). Fig. 3.5 (top) shows the result of the deblending of these lines for the CS region of IC 5063.

The [O II] lines are much closer to each other (~ 2.5 Å) and it is not possible to deblend them without using any reference line. I adopted the [S II] doublet as a reference because, considering only the ions showing strong emission lines in our spectra, it has the closest ionization potential to that of the [O II] (Table 3.4). Therefore, I can suppose that their emission comes from spatially close regions and I can assume for them a similar profile. The two doublets also depend on the electron density in a similar way (see Osterbrock & Ferland, 2006). Therefore, I measured the ratio between the central intensity of each component in the two lines of the [S II] fit and I used those ratios to put constraints on the Gaussians used to fit the [O II] doublet. After that, I proceeded as before, fitting one line and constraining the parameters of the second one. However, since the [O II] lines are almost totally overlapped, in several spectra it was not possible to use the same number of Gaussians used to fit the [S II] doublet. In these cases, I applied the process using only 2 Gaussians and refitting the [S II] lines. Fig. 3.5 (bottom) shows the final result after the deblending of the [O II] doublet in the CS region of IC 5063.

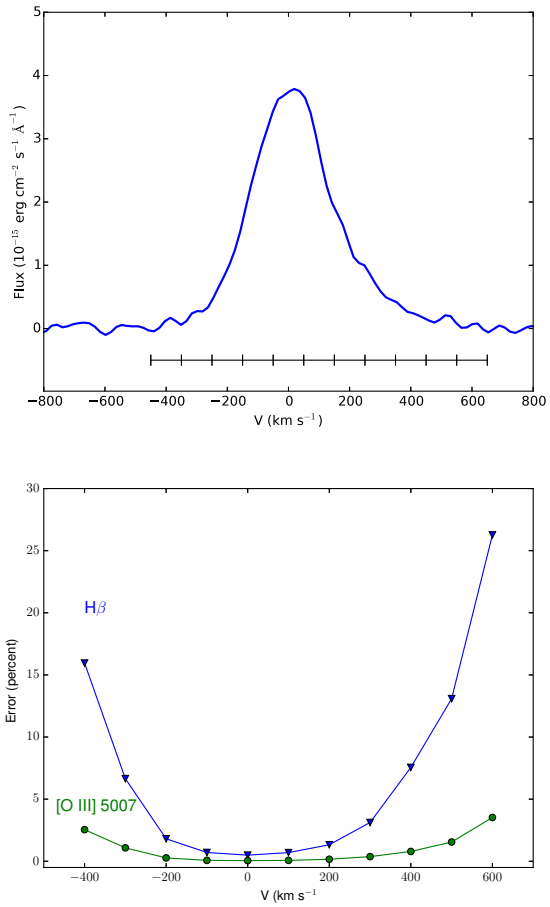

Figure 3.6: **Top:** Plot of Hβ taken from the spectrum of the CS region of IC 5063. In the lower part of the figure the adopted velocity bins are shown. **Bottom:** Profile of the relative error in Hβ and [O III]λ5007 in the same region.

3.4 Data Analysis and Results

I divided all the line profiles in velocity bins (Fig. 3.6) and I measured the fluxes inside them, as done by Ozaki (2009). While this author took into account the morphology of the profile of the brightest emission line ([O III]λ5007) for each region, I preferred to adopt a less arbitrary method and to use a fixed width of 100 km s^{-1} which is about three times the theoretical instrumental velocity resolution (R $\sim$ 37.5 km s^{-1}). I performed the measurement using an IRAF script. To take into account the different line widths in different regions, I assumed the velocity bins of Hβ as a reference for the other emission lines. This choice was based on the need of calculating flux ratios, deriving physical parameters and plotting diagnostic diagrams. To this aim, it is essential to have good measurements of Hβ flux in each bin. Being Hβ one of the weakest lines I am interested in, high-velocity bins that can be observed only in strong lines have been lost. I also measured the total flux of each line, to compare the velocity dependent results to the average properties of

Table 3.4: Measured emission lines and energy of the ion. The lower value represents the energy needed to produce the ion, the higher value the energy needed to further ionize it.

Ion	Wavelength (Å)	E (eV)
[O II]	3727	13.6 – 35.1
[O III]	4363	35.1 – 54.9
[Ar IV]	4711	40.9 – 59.8
[Ar IV]	4740	40.9 – 59.8
H I	4861	-
[O III]	4959	35.1 – 54.9
[O III]	5007	35.1 – 54.9
[O I]	6300	– 13.6
H I	6563	-
[N II]	6584	14.5 – 29.6
[S II]	6717	10.4 – 23.3
[S II]	6731	10.4 – 23.3
[O II]	7319	13.6 – 35.1
[O II]	7330	13.6 – 35.1

the gas.

Fig. 3.6 (bottom) shows the behavior of the relative error on the flux as a function of velocity in two lines (Hβ and [O III]λ5007) of the CS region of IC 5063. To estimate the error I used the following equation:

$$\frac{\Delta I}{I} = \frac{rms}{I_0} \tag{3.1}$$

where I is the bin flux and ΔI its error, rms is the root mean square of the continuum measured near the line and I_0 is the central peak of the bin. The error increases, as expected, in the line wings both in a weak line (Hβ) and in a strong line ([O III]λ5007). In Hβ I have a maximum error of $\sim$ 25 percent of the flux in the line wings, while in [O III]λ5007 the error is much lower ($\sim$ 4 percent). A similar behavior is expected for all the measured lines.

I first estimated the local extinction by using the Balmer decrement and assuming a theoretical Hα/Hβ ratio of 2.86. To recover the visual extinction A(V), I applied the CCM (Cardelli–Clayton–Mathis) extinction law (Cardelli et al., 1989). I measured A(V) both for each velocity bin and for the total line flux and I corrected the measured fluxes of all the lines.

Then, I studied the mechanisms responsible for heating and ionizing the gas in the different regions of both galaxies directly from diagnostic diagrams (Baldwin et al., 1981; Veilleux & Osterbrock, 1987). Penston et al. (1990) empirical relation was adopted to determine the ionization parameter, while the physical parameters such as temperature and density of the emitting gas were obtained from the characteristic line ratios. Finally, to have a more complete picture of the physical parameters and abundances of the elements throughout the regions, I carried out a detailed modeling of the spectra accounting for both the photo-ionization from the active center and for shocks.

3.4.1 Diagnostic Diagrams

With the extinction corrected fluxes, I proceeded to plot the diagnostic diagrams. I used four different diagrams: three are the traditional BPT diagrams from Baldwin et al. (1981) and Veilleux & Osterbrock (1987) which compare the [O III]λ5007/Hβ ratio to [O I]λ6300/Hα, [N II]λ6584/Hα and [S II]$\lambda\lambda$6716, 6731/Hα. The fourth one is a less used diagram developed by Baldwin et al. (1981) which involves the [O II]$\lambda\lambda$3726, 3729/[O III]λ5007 ratio to evaluate the ionization degree of the gas and a ΔE parameter which combines the previous ratios to discern between different ionization mechanisms (Eq. 3.2, 3.3, 3.4, 3.5, where x = ([O II]λ3726 + [O II]λ3729)/[O III]λ5007):

$$\Delta E_1 = \log\left(\frac{[\mathrm{O\,III}]\lambda5007}{\mathrm{H}\beta}\right) + \log\left(0.32 + x\right) - 0.44; \tag{3.2}$$

$$\Delta E_2 = \frac{1}{2}\left[\log\left(\frac{[\mathrm{N\,II}]\lambda6584}{\mathrm{H}\alpha}\right) - \log\left(\frac{x}{x + 1.93}\right) + 0.37\right]; \tag{3.3}$$

$$\Delta E_3 = \frac{1}{5}\left[\log\left(\frac{[\mathrm{O\,I}]\lambda6300}{\mathrm{H}\alpha}\right) + 2.23\right]; \tag{3.4}$$

$$\Delta E = \frac{1}{3}\left[\Delta E_1 + \Delta E_2 + \Delta E_3\right]. \tag{3.5}$$

In the first three diagrams, I used the functions defined by Kewley et al. (2001) to discern between H II regions and power-law ionized regions and the function from Kewley et al. (2006) to divide the latter into Seyfert-like emission regions and LINER-like emission regions. I used the ΔE vs. [O II]$\lambda\lambda$3726, 3729/[O III]λ5007 diagrams to investigate the influence of shock-waves in ionizing the NLR/ENLR gas. The error bars were calculated using Eq. 3.1 and applying error propagation for all the diagnostic ratios. Fig. 3.7 shows an example of diagnostic diagrams for the N0 region of IC 5063 and the S0 region of NGC 7212. The diagrams of the other regions are shown in Appendix (Fig. B.1–B.3). Fig. 3.8 also shows the same diagnostic diagrams calculated using the total flux of the lines for each region. From these plots it is possible to see that all the points lie in the AGN region. Moreover, the majority of the points in the log([O III]λ5007/Hβ) vs log([O I]λ6300/Hα) and in the log([O III]λ5007/Hβ) vs log([S II]$\lambda\lambda$6716, 6731/Hα) diagrams are located to the left of the diagram, which is the area usually occupied by Seyfert galaxies (Kewley et al., 2006). In the ΔE vs log([O II]$\lambda\lambda$3726, 3729/[O III]λ5007) the points are located on the side of the diagram occupied by clouds ionized by a power-law continuum. This means that the main ionization mechanism in the NLR/ENLR of both galaxies is the photo-ionization by the active nucleus. However, it must be noticed that in most diagrams the points are not randomly distributed but they follow a well-defined trend. The points corresponding to high values of $|V|$ tend to have a lower [O III]λ5007/Hβ ratio but a higher ratio between low ionization lines and Hα. For this reason, some points are located close to the LINER region (e.g. Fig. 3.7). This behavior might be explained as a consequence of shocks, which affect the spectrum lowering the ionization degree of the gas (low [O III]λ5007/Hβ ratio) and increasing the number of ions in a low ionization state (high [O I]λ6300/Hα, [N II]λ6584/Hα and [S II]$\lambda\lambda$6716, 6731/Hα). This is in agreement with the ΔE vs.

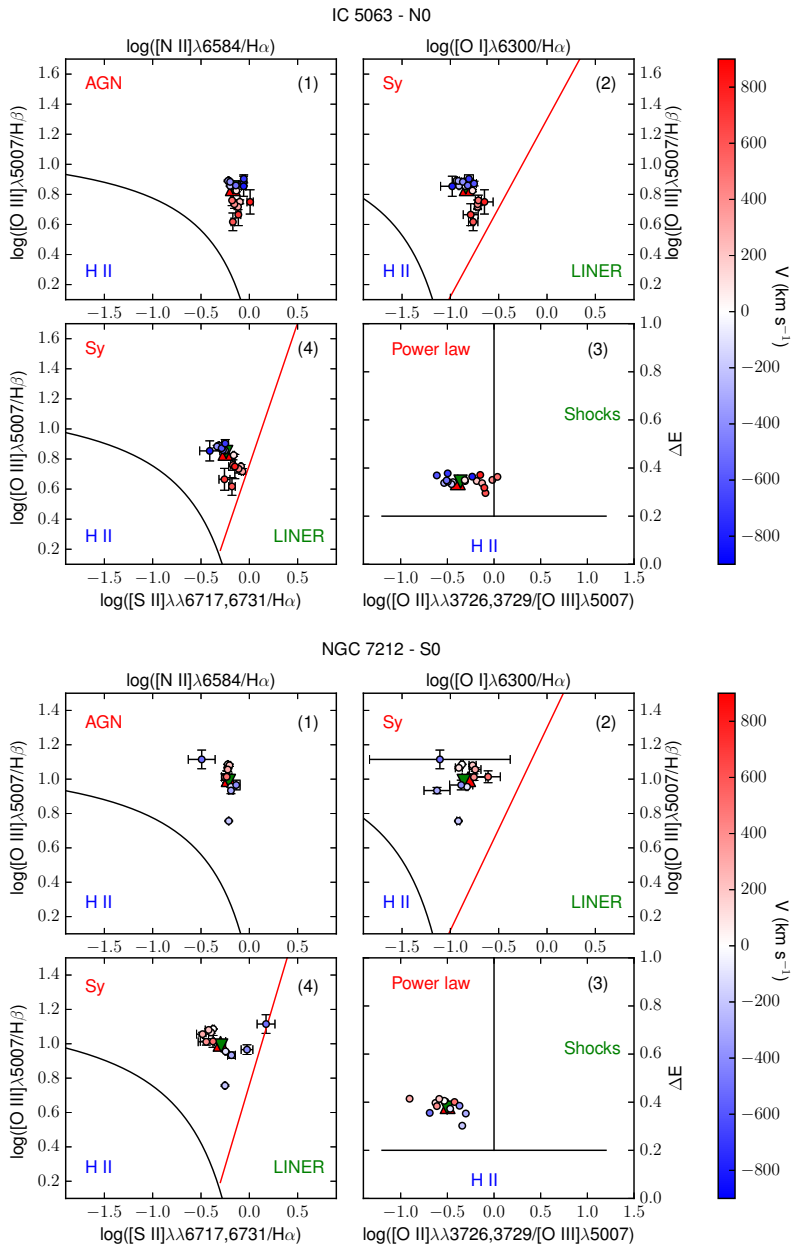

Figure 3.7: Diagnostic diagrams of the N0 region of IC 5063 (top) and of the S0 region of NGC 7212 (bottom). In each plot, I show, from the top left panel clockwise: (1) log([O III]Hβ) vs log([N II]/Hα), (2) log([O III]/Hβ) vs log([O I]/Hα), (3) ΔE vs log([O II]/[O III]), (4) log([O III]/Hβ) vs log([S II]/Hα) (Baldwin et al., 1981; Veilleux & Osterbrock, 1987). The green triangles represent the line ratios calculated with the total line flux in each region. The color bar shows the velocity of each bin. The black curves in (1), (2), (4) divide power-law ionized regions (top) and H II regions (bottom). The red lines divide Seyfert-like regions (left) and LINER-like regions (right) (Kewley et al., 2006). The black lines in (3) divide H II regions (bottom), power-law ionized region (left) and shock ionized regions (right) (Baldwin et al., 1981).

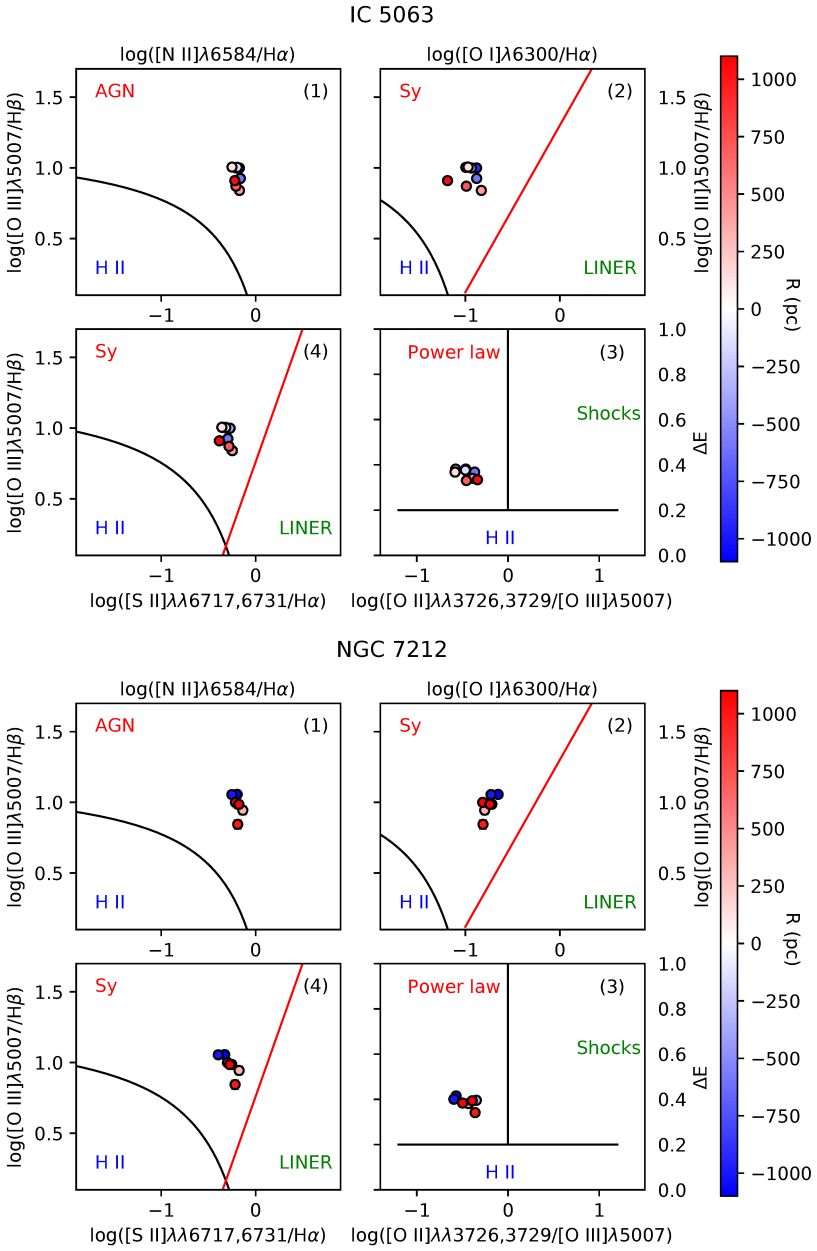

Figure 3.8: Diagnostic diagrams of IC 5063 (top) and NGC 7212 (bottom) calculated with the total flux of the lines. In each plot I show, from the top left panel clockwise: (1) log([O III]Hβ) vs log([N II]/Hα), (2) log([O III]/Hβ) vs log([O I]/Hα), (3) ΔE vs log([O II]/[O III]), (4) log([O III]/Hβ) vs log([S II]/Hα) (Baldwin et al., 1981; Veilleux & Osterbrock, 1987). The color bar shows the distance from the nucleus of each region. The error bars are smaller than the size of the points. The black curves in (1), (2), (4) divide power-law ionized regions (top) and H II regions (bottom). The red lines divide Seyfert-like regions (left) and LINER-like regions (right) (Kewley et al., 2006). The black lines in (3) divide H II regions (bottom), power-law ionized region (left) and shock ionized regions (right) (Baldwin et al., 1981).

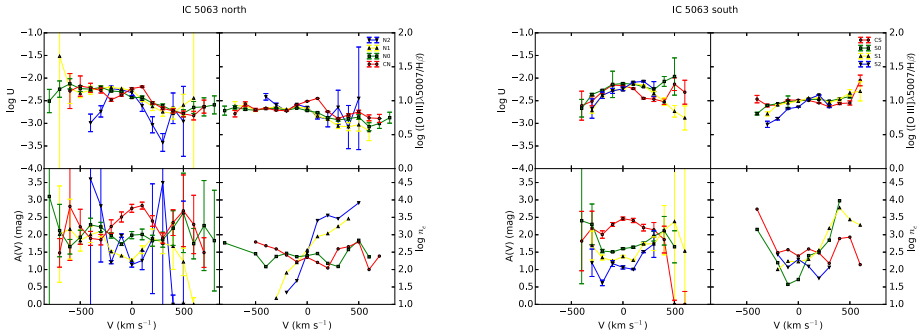

Figure 3.9: Left: From the top left panel, clockwise: ionization parameter, $\log([O\,III]\lambda5007/\mathrm{H}\beta)$, electron density ($\mathrm{cm}^{-3}$) and extinction coefficient (mag) as a function of velocity for the northern regions of IC 5063. **Right:** same quantities for the southern regions of IC 5063.

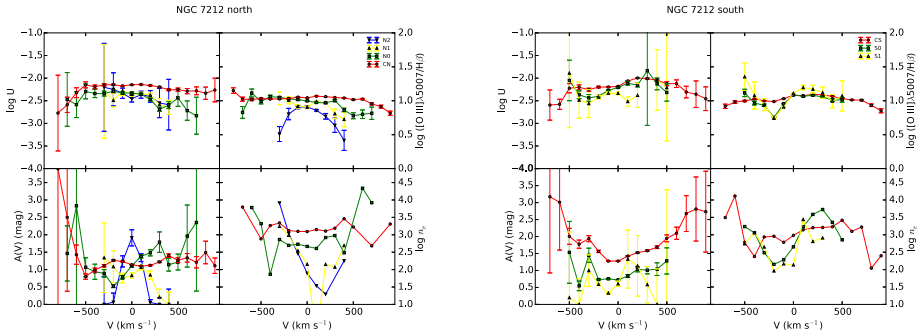

Figure 3.10: Left: From the top left panel, clockwise: ionization parameter, $\log([\mathrm{O\,III}]\lambda5007/\mathrm{H}\beta)$, electron density ($\mathrm{cm}^{-3}$) and extinction coefficient (mag) as a function of velocity for the northern regions of NGC 7212. **Right:** same quantities for the southern regions of NGC 7212.

[O II]$\lambda\lambda3726, 3729$/[O III]$\lambda5007$ where the points corresponding to those bins are close to the shocks side of the plot. Moreover, gas moving at a relatively low speed does not show any sign of shocks. Most of the line flux is contained within these bins, therefore, when the diagnostic ratios are calculated using the whole flux of the lines almost no sign of shock-ionized gas is observed. In fact, analyzing the diagnostic diagrams in Fig. 3.8, it is possible to see that both in IC 5063 and NGC 7212 all the points are clustered in the Seyfert region of the plots, without any peculiar behavior. This does not mean that there is no contribution by shocks at low V, but that it is negligible with respect to photo-ionization.

3.4.2 Ionization parameter and extinction

The ionization parameter, defined as the number of ionizing photons reaching a cloud per number of electrons in the gas, can be used to estimate the ionization

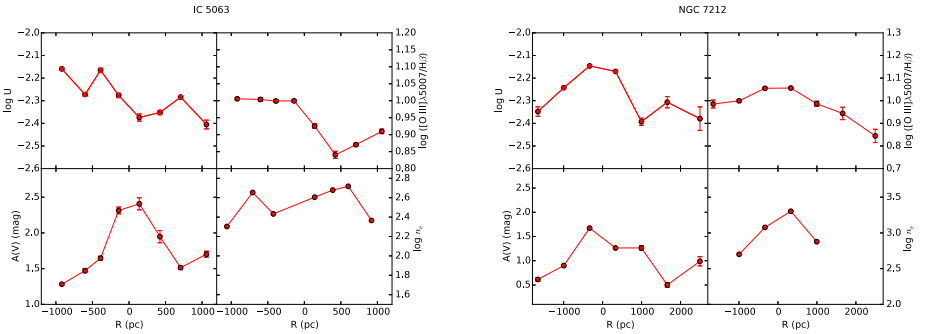

Figure 3.11: From the top left panel, clockwise: ionization parameter, $\log([\mathrm{O\,III}]\lambda5007/\mathrm{H}\beta)$, electron density ($\mathrm{cm}^{-3}$) and extinction coefficient (mag) as a function of the distance from the galactic nucleus for IC 5063 (left) and NGC 7212 (right).

degree of the gas. For an isotropic source, it is defined as :

$$U = \frac{Q}{4\pi r^2 c n_e} \,, \tag{3.6}$$

where Q is the total number of ionizing photons emitted by the source, r is the distance of the cloud from the ionizing source, c is the speed of light and n_e is the electron density. To estimate this parameter I used the empirical relation from Penston et al. (1990):

$$\log U = -2.74 - \log\left(\frac{[\mathrm{O\,II}]\lambda\lambda3726,3729}{[\mathrm{O\,III}]\lambda5007}\right) \,. \tag{3.7}$$

The main problem of this relation is that the $[\mathrm{O\,II}]\lambda\lambda3726,3729/[\mathrm{O\,III}]\lambda5007$ ratio strongly depends on the extinction correction. To check the reliability of the obtained values I compared the $\log U$ vs velocity (V) and $\log U$ vs distance from the nucleus (R) plots with similar plots involving the $[\mathrm{O\,III}]\lambda5007/\mathrm{H}\beta$ ratio. Even if this ratio is not a real ionization parameter, it is sensitive to the ionization degree of the gas and it has the advantage to be independent from the extinction correction, because the two lines are close in wavelength. When the two diagrams are compatible, the extinction correction applied to the fluxes is reliable.

Fig. 3.9 and Fig. 3.10 show the plots of $\log U$, $\log([\mathrm{O\,III}]\lambda5007/\mathrm{H}\beta)$, A(V) and n_e as a function of velocity. Similar plots obtained with the total flux of the lines are shown in Fig. 3.11.

The behaviors of $\log U$ and $\log([\mathrm{O\,III}]/\mathrm{H}\beta)$ are often similar. This confirms the overall reliability of the extinction correction, even though the error bars on A(V) increase rapidly with $|V|$. Almost all the differences between the two plots can be explained as an effect of errors in measuring A(V) at high $|V|$ due to a low SNR in $\mathrm{H}\beta$ wings. An example is the region N2 of IC 5063 (Fig. 3.9 left, blue solid line): the behavior of $\log U$ reflects perfectly that of the extinction.

In IC 5063, A(V) usually shows a peak at low velocities, then it decreases and the error bars are compatible with a flat trend. The A(V) vs distance (R) plot is similar, I found a maximum extinction of 2.4 mag in the CN region and then A(V)

progressively decreases at increasing R. In NGC 7212 I observed the same behavior of the A(V) vs R plot, but the extinction is generally 1 mag lower. The high A(V) values of IC 5063 are expected because the target shows a large dust lane crossing the whole galaxy, that is also aligned with the ENLR. The A(V) vs. V plots show that the extinction is almost constant at all velocities.

In principle, U (eq. 3.7) is not expected to be dependent on velocity because there is not a direct link between these two quantities. However, if the clouds are accelerated by radiation pressure and ionized by a continuum which is attenuated by an absorbing medium with varying column density, $\log U$ is expected to depend on the gas velocity (Ozaki, 2009). This kind of behavior is observed in some regions of our galaxies. In Fig. 3.9 it is possible to see that in the CN, N0 and N1 regions of IC 5063, the ionization parameter decreases of about one order of magnitude between $V = -600\,\mathrm{km\ s^{-1}}$ and $V = 500\,\mathrm{km\ s^{-1}}$. On the basis of the results from Kraemer & Crenshaw (2000) and Ozaki (2009), this might mean that the blueshifted gas is irradiated directly by the AGN, while the redshifted gas is ionized by an attenuated continuum. In the S0, S1 and S2 regions $\log U$ increases in the opposite direction, from $V = -400$ to $V = 200\,\mathrm{km\ s^{-1}}$. The velocity range is quite narrow because at higher $|V|$ the effect of the extinction correction dominates with respect to the real behavior of the ionization parameter. However, the fact that in these regions, the ionization increases with V is clearly confirmed by the $\log([\mathrm{O\,III}]/\mathrm{H}\beta)$ vs V plot.

Ozaki (2009) linked the ionization parameter dependence on velocity to the geometry of the ionization cones. If the ionization cones have a hollow bi-conical shape and one of their edges is aligned to the galaxy disk, such as in NGC 1068 (Cecil et al., 2002; Das et al., 2006), this edge should be irradiated by a continuum attenuated by the dust present in the disk while the rest of the cone should be excited by the non-absorbed continuum. Therefore, if the line of sight intercepts the ionization cone at the proper angle, it is possible to see the velocity dependence of the ionization parameter.

This explanation seems to be in contrast with what said in the previous section. However, it is possible for the two phenomena to coexist. The attenuation of the continuum contributes to decreasing the ionization degree of the gas, also seen in the diagnostic diagrams, while the presence of shocks causes the points in the ΔE diagram to get close, and often to cross, the shock-power law threshold (Fig. B.1).

The geometrical shape of the ionization cones of IC 5063 is not known but, combining our results with Ozaki's conclusions, the behavior of the ionization parameter is likely the result of a hollow bi-conical shape. This shape could be explained as the effect of the radio-jet expanding in a clumpy medium and forming a cocoon around it, which drives away the gas from the jet axis (Morganti et al., 2015; Dasyra et al., 2015) .

In NGC 7212, U can be considered independent from the velocity in every region. All the small deviations from a constant value are related to variations of the extinction. This might mean that the three-dimensional shape of the ionization cones is different from that of IC 5063, or that our line of sight intercepts the object at a different angle. The only region with a peculiar behavior is N2 (Fig. 3.10). In this region, $\log U$ and $\log([\mathrm{O\,III}]/\mathrm{H}\beta)$ are quite different. U slightly decreases from $V = -300$ to $V = 400\,\mathrm{km\ s^{-1}}$ while $\log([\mathrm{O\,III}]/\mathrm{H}\beta)$ has a parabolic shape. A possible reason might be the low SNR of Hβ wings which causes an overestimation of

its flux at high velocities and an underestimation of the $\log([\mathrm{O\,III}]/\mathrm{H}\beta)$ ratio.

These results are well in agreement with Cracco et al. (2011), who found $\log([\mathrm{O\,III}]/\mathrm{H}\beta) \sim 1$ in the whole ENLR. The observed scatter of the ionization parameter is compatible with an almost constant trend.

3.4.3 Temperature and densities

I was able to obtain, in most regions, the average temperature and density of the gas in two different ionization regimes. In particular, I used $[\mathrm{O\,III}]\lambda\lambda 4959, 5007$, $[\mathrm{O\,III}]\lambda 4363$ and $[\mathrm{Ar\,IV}]\lambda\lambda 4711, 4740$ for the gas with medium ionization degree, and $[\mathrm{O\,II}]\lambda\lambda 3726, 3729$, $[\mathrm{O\,II}]\lambda 7320$ and $[\mathrm{S\,II}]\lambda\lambda 6716, 6731$ for the gas in low ionization degree.

Unfortunately, some of the lines needed to estimate temperatures and densities were so faint that they could not be divided into velocity bins (e.g. $[\mathrm{O\,III}]\lambda 4363$, $[\mathrm{Ar\,IV}]\lambda\lambda 4711, 4740$). Therefore, I was forced to use the total flux of these lines and calculate the averaged temperature and density. Only with the $[\mathrm{S\,II}]\lambda\lambda 6716, 6731$ lines it was possible to estimate the density as a function of velocity.

I proceeded using iteratively the `temden` IRAF task until I obtained stable values for both temperature and density. Once reached the final results, I used the average temperature of the low ionization gas to attempt to calculate n_e from the [S II] lines in the velocity bins. All the results are shown in Fig. 3.9, 3.10 and 3.11.

Table 3.5 and Table 3.6 report temperature and densities obtained with the total flux of the lines. Due to the errors on the line ratios, what I really am interested in is the order of magnitude of these quantities. For this reason, I rounded off the measured values to the nearest hundreds K for the temperature and to the nearest multiple of 50 for the density. The observed temperature is of the order of 10000 K, a typical temperature in photo-ionized regions (Osterbrock & Ferland, 2006). In IC 5063 both temperature and density of the medium ionization gas are slightly higher than those of the low ionization gas, while for NGC 7212 the situation is less clear. NGC 7212 spectra had a lower SNR than IC 5063 ones, especially in the external regions, therefore it was not possible to measure the weak lines needed for the calculations. In this galaxy, it is worth noticing that the temperature of the low ionization gas measured in the central region of the galaxy is close to 15000 K. Following Roche et al. (2016), high temperatures of the low ionization gas might be a hint of jet-ISM interaction.

To calculate the density in the regions where I could not directly measure the temperature, I used the typical value T = 10000 K for photo-ionized gas (Osterbrock & Ferland, 2006). The density measurement depends weakly on the temperature (Osterbrock & Ferland, 2006) and this value is close enough to the mean $T_{[\mathrm{O\,II}]}$ measured from Table 3.5 and 3.6 ($\sim$ 11800 K) that the difference is negligible for our purposes.

After that, I used the temperatures obtained with the [O II] lines (Table 3.5 and Table 3.6) to measure the electron density with the [S II] lines as a function of velocity. The results are shown in Fig. 3.9 and Fig 3.10. Typical values are $\log n_e([\mathrm{S\,II}]) = 2.0$–$3.0$, but, in some cases, I measured larger and smaller values, especially at high $|V|$ where the SNR is low and the effects of the deblending can affect the results. In some regions, the situation is not clear (e.g. N1 and N2 regions

Table 3.5: Temperature and electron density of the medium and low ionization gas of IC 5063. The temperatures are rounded off to the nearest hundred K, the electron density to the nearest multiple of 50. I used the [O II] doublet when it was not possible to measure n_e with the [S II] doublet.

Region	$T_{[O\,III]}$ (K) (K)	$n_{[Ar\,IV]}$ (cm^{-3}) (cm^{-3})	$T_{[O\,II]}$ (K) (K)	$n_{[S\,II]}$ (cm^{-3}) (cm^{-3})
N2	-	-	9100	2000
N1	12400	8500	7800	4500
N0	13600	1400	15500	250
CN	13700	12750	11100 [a]	250 [b]
CS	15200	3400	10700	400
S0	13800	6200	11700	500
S1	13300	3150	10900	500
S2	15300	4250	12400	250

[a] measured with n_e([O II])
[b] measured from the [O II] doublet

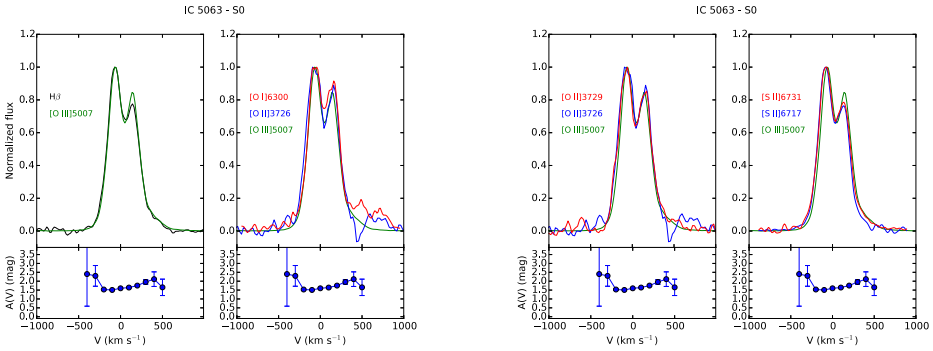

Figure 3.12: Comparison of the emission lines of the S0 region of IC 5063. The behavior of the extinction coefficient as a function of velocity is shown under each plot.

in IC 5063, Fig. 3.9) and these properties will be further investigated with SUMA simulations.

3.4.4 Line profiles

The analysis of the line profiles, on the basis of the emitting gas conditions estimated in previous sections, can provide detailed information on the kinematics and the distribution of the clouds. For each region I compared the profile of some of the brightest lines normalized to their peak emission, to study how they change. Fig. 3.12 and Fig. 3.13 show an example of the profile of the lines for the S0 region of IC 5063 and the CS region of NGC 7212 respectively. These figures show, from left to right, the comparison between: [O III]λ5007 and Hβ; [O I]λ6300, [O II]λ3726 and [O III]λ5007; [O II]λ3726, [O II]λ3729 and [O III]λ5007; [S II]λ6716, [S II]λ6731 and [O III]λ5007. All the other regions are shown in Fig. A.1–A.8 and Fig. A.9–A.15

Table 3.6: Temperature and electron density of the medium and low ionization gas of NGC 7212. The temperature are rounded off to the nearest hundred K, the electron density to the nearest multiple of 50. I measured n_e of the low ionization gas assuming T = 10000 K in the regions where it was not possible to measure the temperature.

Region	$T_{[O\,III]}$ (K) (K)	$n_{[Ar\,IV]}$ (cm^{-3}) (cm^{-3})	$T_{[O\,II]}$ (K) (K)	$n_{[S\,II]}$ (cm^{-3}) (cm^{-3})
N2	-	-	-	200 [a]
N1	-	-	-	150 [a]
N0	-	-	10800	750
CN	14800	5600	13000	2000
CS	15200	3100	14500	1200
S0	14000	2450	14200	500
S1	-	-	-	350 [a]

[a] measured with $T_{[O\,II]} = 10000$ K

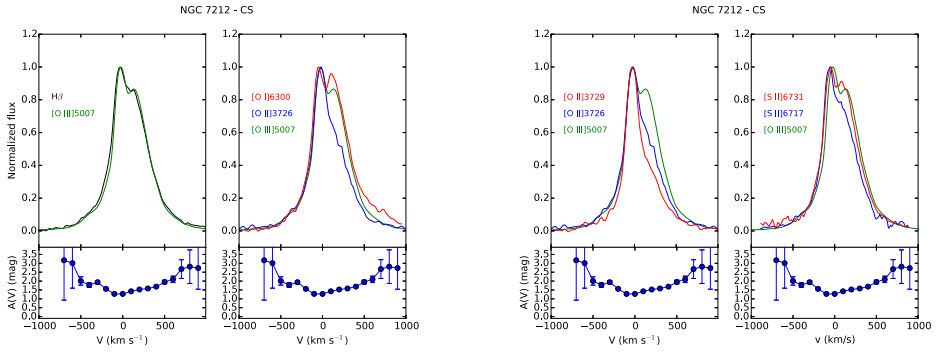

Figure 3.13: Comparison of the emission lines of the CS region of NGC 7212. The behavior of the extinction coefficient as a function of velocity is shown under each plot.

of the Appendix A. The A(V) profile measured in each region is reported under the corresponding panel, to evaluate if possible differences between the line profiles could be caused by extinction. I also used these plots to check the results of the deblending process, comparing the lines of the deblended doublets to the [O III]λ5007 to highlight potential differences.

The line profile can significantly change from region to region. In the external regions they are quite narrow and relatively smooth, but they often show a prominent blue or red wing (Fig. A.1, A.8). NGC 7212 shows broader and more disturbed profiles than IC 5063 in the external regions: the FWHM of the N2 region of NGC 7212 and IC 5063 are 300 km s^{-1} and 170 km s^{-1} respectively.

The spectra were all shifted to rest frame using stellar kinematics, but the main peak of each line is often shifted toward longer or shorter wavelengths of ~ 100 km s^{-1}. This is probably caused by bulk motions of gas, which has a different kinematics with respect to the stellar component of the galaxies.

In general, the complexity of the line profiles might be related to the interaction of jets with ISM, as better explained at the end of Sec. 3.4.5.4, considering the result of the composite modeling.

The direction of rotation of the galaxies can be easily inferred by the spectra in Fig. 3.3 and by the velocities measured in Tab. 3.3. IC 5063 shows blueshifted lines in the northern region of the spectrum and redshifted lines in the southern part. Therefore the galaxy is rotating clockwise, with a maximum rotational velocity of ~ 70 km s^{-1} (measured in the S2 region) with respect of the average velocity of the two CN and CS regions. On the other hand, NGC 7212 seems to rotate in the opposite direction, with the blueshifted lines observed in the southern regions of the spectrum and the redshifted ones on the northern. The largest rotational velocity is measured in the N2 region also for this object, and it consists of ~ 130 km s^{-1}.

3.4.4.1 IC 5063

IC 5063 shows an emission outside the nucleus (regions S0 and S1, Fig. 3.1, bottom panel) characterized by two well-resolved peaks, the first positioned at $V \sim -60$ km s^{-1} and the second at $V \sim 140$ km s^{-1}, which can be observed in all the emission lines (Fig. A.6 and A.7). Not even one of the peaks is positioned at $V = 0$ km s^{-1}, meaning that the kinematics of the gas is different from the one of the stellar component, as stated in the introduction of Sec. 3.4.4. A further analysis of the emission lines of the southern regions (CS, S0, S1, S2) shows a connection between their profiles. In the CS region, which represents the southern part of the nucleus (Fig. A.5), the emission lines are quite narrow and smooth, but there is a small asymmetry at $V \sim 180$ km s^{-1}. The maximum of the line is located at $V = 0$ km s^{-1}, even though the flat top of both [O III]λ5007 and Hβ makes the estimate relatively unreliable. In the next region (S0, Fig. A.6) the main peak is the one located at negative velocity, while the secondary is the one at $V \sim 140$ km s^{-1}. The situation changes in the S1 region (Fig. A.7), where the red peak becomes the strongest and the blue peak starts to weaken and it becomes a blue wing in the S2 region (Fig. A.8). In this region, the main peak is further shifted to the red, up to a velocity $V \sim 160$ km s^{-1}.

This evolution indicates the presence of two distinct kinematic components. The

blue one could be associated with an outflow, which is the dominant component of the nuclear emission, and then it starts to become weaker at higher distances from the nucleus. These two peaks correspond to the two narrow components found by Morganti et al. (2007) nearby the south-east hotspot. In each region the line profiles are very similar for all the considered lines except in S1. Here, all the lines show a secondary peak which is 10 to 20 percent stronger with respect to the same feature visible in [O III]λ5007 (Fig. A.7), with the exception of [O I]λ6300 which is very similar to the [O III] line.

On the other side of the galaxy, the line profiles do not show any secondary peak, but in the CN and N0 regions I observe a very broad component centered at $V \sim -300\,\mathrm{km\ s^{-1}}$ (FWHM$\sim 900\,\mathrm{km\ s^{-1}}$) which can be identified with the well known gas outflow of the galaxy west hotspot (e.g. Morganti et al., 2007, 2015; Dasyra et al., 2015). The stronger peak is positioned at $V \sim 100\,\mathrm{km\ s^{-1}}$, therefore the shift between the broad and narrow component is $\Delta V \sim 130\,\mathrm{km\ s^{-1}}$.

In the CN region, each line has a different shape (Fig. A.4). All the lines show clearly a narrow component and the broad asymmetric component of the outflow. The relative peak intensity of the two changes as a function of the line. The [O III]λ5007 is characterized by the weakest broad component, while the [S II]λ6716 has the strongest one. Finally, the N0 region (Fig. A.3) shows very similar profiles of Hβ and [O III]λ5007, but broader profiles of the low ionization oxygen and sulfur lines.

3.4.4.2 NGC 7212

NGC 7212 is characterized by a more complex gas kinematics. The emission lines are more asymmetric and disturbed. In the northern regions, there is a good agreement between the shape of all the studied lines, except for the N0 region (Fig. A.11) where the [O I]λ6300 is significantly narrower than the other oxygen lines. All the lines show a blue component which becomes weaker towards the external region of the galaxy. Both components are visible also in the central regions (CN and CS, Fig. A.12–A.13). It is interesting that the CS region is the first one clearly showing the presence of two peaks, separated by $\Delta V \sim 170\,\mathrm{km\ s^{-1}}$. The stronger peak is located at $V \sim -90\,\mathrm{km\ s^{-1}}$, while the fainter is located at $V \sim 80\,\mathrm{km\ s^{-1}}$. The peak is visible in all lines except in the [O II] doublet where it becomes an asymmetry. It is not clear whether this asymmetry is real or an effect of the deblending process which is not able to recover the secondary peak starting from the blended lines. Such a feature could be caused by a strong extinction of the weaker peak, but this is not confirmed by the A(V) profile. In the CS region, the dominant component becomes the blue one, while the red one is the fainter one. These two components are probably due to the presence of consistent outflows starting in the nucleus and moving towards the north side of the galaxy.

On the other hand, the southern regions are more peculiar. In the S0 region (Fig. A.14) the lines show very different profiles. Hβ has a double-peaked shape, with the stronger peak located at $V \sim -80\,\mathrm{km\ s^{-1}}$ and the fainter at $V \sim -200\,\mathrm{km\ s^{-1}}$ ($\Delta V \sim 120\,\mathrm{km\ s^{-1}}$), not visible in [O III]λ5007 which shows only a wing. The secondary peak is observed in the [S II] doublet but not in the oxygen lines. They have the blue bump, but its relative intensity changes: the [O II]λ3726 has the

strongest bump ($\sim 80\%$ of the peak intensity), followed by the [O I]λ6300 ($\sim 60\%$) and by the [O III]λ5007 ($\sim 40\%$). Finally, in the S1 region (Fig. A.15) Hβ and all the other low ionization lines (except [O II]λ3729) show an asymmetric profile with a blue-shifted peak ($V \sim -150\,\mathrm{km\ s^{-1}}$) and two bumps in the red part of the lines. On the other hand, [O III]λ5007 shows a peak at $V \sim -50\,\mathrm{km\ s^{-1}}$ and a relatively strong bump (> 80 percent of the peak intensity) in the velocity where the other lines have the peak.

Since this galaxy is merging with a companion, it is not possible to clearly determine the origin of the complex kinematics. The most probable scenario is that outflows are probably responsible for the multiple components observed in the inner region of the galaxy, while in the most external parts the action of jets, as in IC 5063, and the merging are probably both influencing the gas kinematics.

3.4.5 Detailed modeling of the observed spectra

Modeling the spectra by pure photo-ionization models gives satisfying results for intermediate ionization level lines. However, collisional phenomena can be critical in the calculation of the spectra emitted by high-velocity gas. The physical properties of the galaxies, such as the complex structure of the emission lines, the presence of merging and possible interaction between jets and ISM among others, suggested us to use a code which takes into account the effects of both photo-ionization and shocks.

The SUMA code (Contini, 2015, and references therein) simulates the physical conditions in an emitting gaseous cloud under the coupled effect of photo-ionization from the radiation source and shocks. The line and continuum emission from the gas are calculated consistently with dust-reprocessed radiation in a plane-parallel geometry. The main physical properties of the emitting gas and the element abundances are accounted for.

3.4.5.1 Input parameters

The parameters characterizing the shock are roughly suggested by the data, e.g. the shock velocity V_s by the velocity bin and the pre-shock density n_0 by the characteristic line ratios and by the pre-shock magnetic field B_0. I adopted $B_0 = 10^{-4}$ G, which is suitable to the NLR of AGN (Beck, 2012). Changes in B_0 are compensated by opposite changes in n_0. From these input parameters, the code produces a table of line fluxes with respect to Hβ that must then be compared with the observations. A fine tuning of the input parameter is performed iteratively in order to improve the results of the simulations. At the end of the process, the final input parameters can be considered an actual result of the simulations.

The ionizing radiation from a source, external to the emitting cloud, is characterized by its spectrum and by the flux intensity. The flux is calculated in 440 energy bands ranging between a few eV to keV. If the photo-ionization source is an active nucleus, the input parameter that refers to the radiation field is the power-law flux from the active center F in number of photons $\mathrm{cm^{-2}s^{-1}eV^{-1}}$ at the Lyman limit with spectral indexes $\alpha_{UV} = -1.5$ and $\alpha_X = -0.7$. It was found by modeling the spectra of many different AGN that these indexes were the most suitable, in general (see, e.g. Contini & Aldrovandi, 1983; Aldrovandi & Contini, 1984; Rodríguez-Ardila

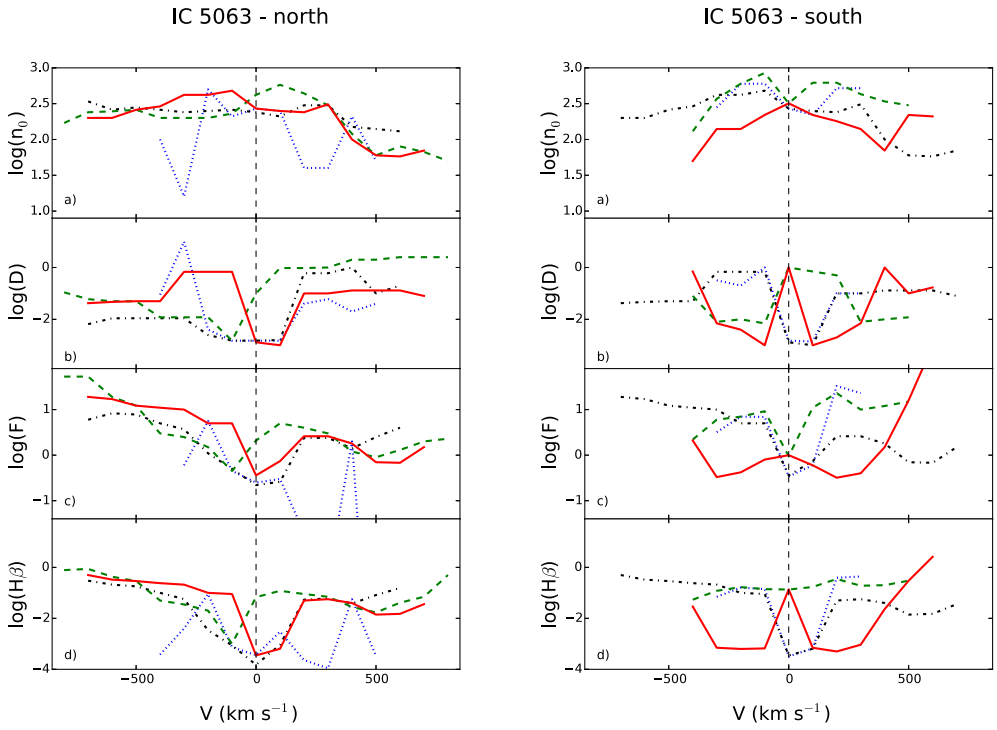

Figure 3.14: The final input quantities calculated by SUMA in the IC 5063 regions. From top to bottom: the pre-shock density n_0 is in cm^{-3}, the cloud geometrical thickness D is in 10^{18} cm, the power-law flux from the active center F is in 10^{10} photons $\mathrm{cm}^{-2}\mathrm{s}^{-1}\mathrm{eV}^{-1}$ at the Lyman limit, Hβ flux is in erg $\mathrm{cm}^{-2}\,\mathrm{s}^{-1}$. Left: north; right: south. Red solid line: CN (CS), green dashed: N0 (S0), black dash-dotted: N1 (S1), blue dotted line: N2 (S2).

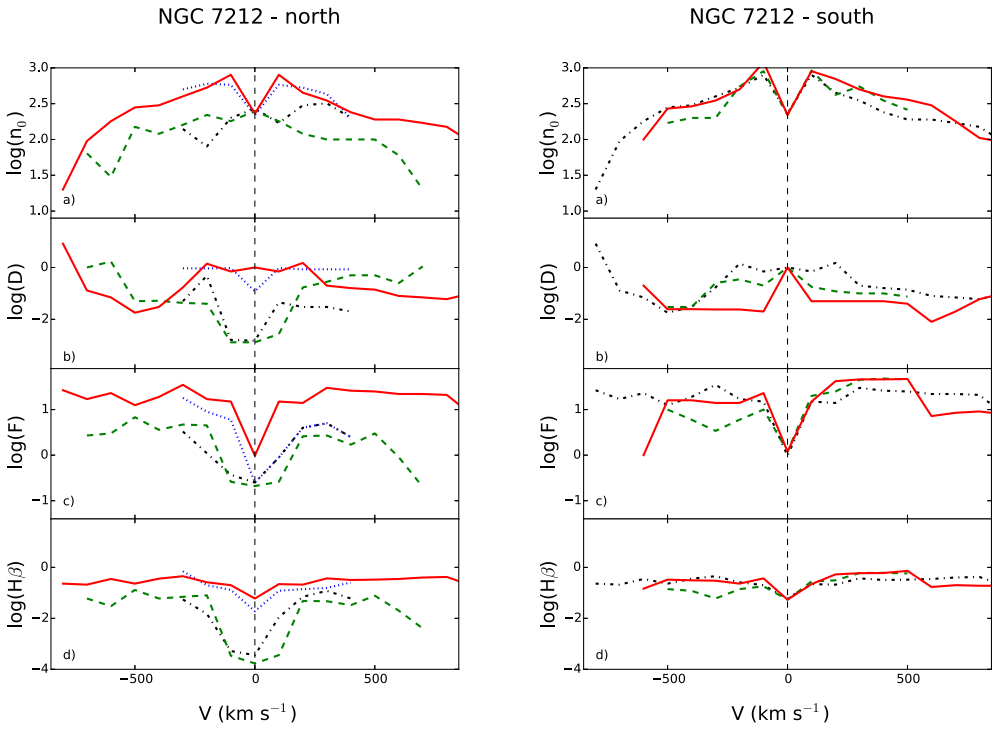

Figure 3.15: The final input quantities calculated by SUMA in the NGC 7212 regions. From top to bottom: the pre-shock density n_0 is in cm^{-3}, the cloud geometrical thickness D is in 10^{18} cm, the power-law flux from the active center F is in 10^{10} photons $\mathrm{cm}^{-2}\mathrm{s}^{-1}\mathrm{eV}^{-1}$ at the Lyman limit, Hβ flux is in erg $\mathrm{cm}^{-2}\,\mathrm{s}^{-1}$. Left: north; right: south. Red solid line: CN (CS), green dashed: N0 (S0), black dash-dotted: N1 (S1), blue dotted line: N2.

et al., 2005, and references therein). For UV line ratios of a sample of galaxies at $z > 1.7$, Villar-Martin et al. (1997) found that $\alpha_{UV} = -1$ provided a very good fit. The power-law in the X-ray domain was found flatter by the observations of local galaxies ($\alpha_X = -1$, e.g. Crenshaw et al., 2002; Turner et al., 2001). Nevertheless, for all the models presented in the following, I will adopt $\alpha_{UV} = -1.5$ and $\alpha_X = -0.7$, recalling that the shocked zone also contributes to the emission-line intensities. Therefore our results are less dependent on the shape of the ionizing radiation. In SUMA the ionizing continuum starts at 7.9 eV and ends at 5 keV and the switch between the α_{UV} and α_X happens at 260 eV. The relation between F and the ionization parameter U is the following:

$$U = \left(\frac{F}{nc(\alpha_{UV}-1)}\right)\left(E_H^{-\alpha_{UV}+1} - E_C^{-\alpha_{UV}+1}\right), \tag{3.8}$$

where E_H is H ionization potential and E_C is the high energy cutoff, n_e the density, α_{UV} the spectral index, and c the speed of light.

In addition to the radiation from the primary source, the diffuse secondary radiation created by the hot gas is also calculated, using 240 energy bands for the spectrum. The primary radiation source is independent but it affects the surrounding gas. In contrast, the secondary diffuse radiation is emitted from the slabs of gas heated by the radiation flux reaching the gas and, in particular, by the shock. Primary and secondary radiations are calculated by radiation transfer downstream.

In our model the gas region surrounding the radiation source is not considered as a unique cloud, but as an ensemble of filaments. The geometrical thickness of these filaments is another input parameter of the code (D) and it is calculated consistently with the physical conditions already described and element abundances of the emitting gas. D determines whether the model is radiation-bounded or matter-bounded. The abundances of He, C, N, O, Ne, Mg, Si, S, Ar, Fe, relative to H, are accounted for as input parameters. Previous results lead to O/H close to solar for most AGN and for most of the H II regions (e.g. Contini, 2017). I will conventionally define "solar" relative abundances $(\mathrm{O/H})_\odot = 6.6 - 6.7 \times 10^{-4}$ and $(\mathrm{N/H})_\odot = 9. \times 10^{-5}$ (Allen, 1976; Grevesse & Sauval, 1998) that were found suitable to local galaxy nebulae. Moreover, these values are included between those of Anders & Grevesse (1989) (8.5×10^{-4} and 1.12×10^{-4}, respectively) and Asplund et al. (2009) (4.9×10^{-4} and 6.76×10^{-5}, respectively).

The fractional abundances of all the ions in all ionization levels are calculated in each slab resolving the ionization equations. The dust-to-gas ratio (d/g) is an input parameter. Mutual heating and cooling between dust and gas affect the temperatures of gas in the emitting region of the cloud. Fig. 3.14 and Fig. 3.15 show the input parameter as a function of V used to model the observed spectra.

3.4.5.2 Calculation process

The code accounts for the direction of the cloud motion relative to the external photo-ionizing source. A parameter switches between inflow (the radiation flux from the source reaches the shock front edge of the cloud) and outflow (the flux reaches the edge opposite to the shock front). The calculations start at the shock front where the gas is compressed and thermalized adiabatically, reaching the maximum

temperature in the immediate post-shock region (eq. 3.9).

$$T \sim 1.5 \times 10^5 \left(\frac{V_s}{100\,\mathrm{km\ s^{-1}}} \right)^2 . \tag{3.9}$$

T decreases downstream by the cooling rate and the gas recombines. The downstream region is cut into a maximum of 300 plane-parallel slabs with different geometrical widths calculated automatically, in order to account for the temperature gradient. In each slab, compression (n_e/n_0) is calculated by combining the Rankine–Hugoniot equations for conservation of mass, momentum and energy throughout the shock front (Cox, 1972). Compression ranges between 4 (the adiabatic jump) and > 100, depending on V_s and B_0. The stronger the magnetic field, the lower the compression downstream, while a higher shock velocity corresponds to a higher compression.

In pure photo-ionization models, the density n_e is constant throughout the nebula. In models accounting for the shocks, both the electron temperature T_e and density n_e show a characteristic profile throughout each cloud (see for instance Fig. 3.16 left and right panels). After the shock, the temperature reaches its upper limit at a certain distance from the shock-front and remains nearly constant, while n_e decreases following recombination. The cooling rate is calculated in each slab by free-free (bremsstrahlung), free-bound and line emission. Therefore, the most significant lines must be calculated in each slab even if only a few ones are observed because they contribute to the temperature slope downstream.

The primary and secondary radiation spectra change throughout the downstream slabs, each of them contributing to the optical depth. In each slab of gas the fractional abundance of the ions of each chemical element is obtained by solving the ionization equations which account for photo-ionization (by the primary and diffuse secondary radiations and collisional ionization) and for recombination (radiative, dielectronic), as well as for charge transfer effects, etc. The ionization equations are coupled to the energy equation when collision processes dominate (Cox, 1972) and to the thermal balance if radiative processes dominate. The latter balances the heating of the gas due to the primary and diffuse radiations reaching the slab with the cooling due to line emission, dust collisional ionization and thermal bremsstrahlung. The line intensity contributions from all the slabs are integrated throughout the cloud. In particular, the absolute line fluxes referring to the ionization level i of element K are calculated by the term n_K(i) which represents the density of the ion X(i). I consider that n_K(i)=X(i)[K/H]n_H, where X(i) is the fractional abundance of the ion i calculated by the ionization equations, [K/H] is the relative abundance of the element K to H and n_H is the density of H (by number cm^{-3}). In models including shock, n_H is calculated by the compression equation in each slab downstream. So the element abundances relative to H appear as input parameters. To obtain the N/H relative abundance for each galaxy, I consider the charge exchange reaction $N^+ + H \rightleftharpoons N + H^+$. Charge exchange reactions occur between ions with similar ionization potential (I(H^+) = 13.54 eV, I(N^+) = 14.49 eV and I(O^+) = 13.56 eV). It was found that N ionization equilibrium in the ISM is strongly affected by charge exchange. This process as well as $O^+ + H \rightleftharpoons O + H^+$ are included in the SUMA code. The N^+/N ion fractional abundance follows the behavior of O^+/O so, comparing the [N II]/Hβ and the [O II]/Hβ line ratios with the data, the N/H relative abundances

can be easily determined (see Contini et al., 2012).

Dust grains are coupled to the gas across the shock front by the magnetic field. They are heated radiatively by photo-ionization and collisionally by the gas up to the evaporation temperature ($T_{dust} \geq 1500\,K$). The distribution of the grain radii in each of the downstream slabs is determined by sputtering, which depends on the shock velocity and on the gas density. Throughout shock fronts and downstream, the grains might be completely destroyed by sputtering.

The calculations proceed until the gas cools down to a temperature below $10^3\,K$ (the model is radiation bounded) or the calculations are interrupted when all the lines reproduce the observed line ratios (the model is matter bounded). In case that photo-ionization and shocks act on opposite edges, i.e. when the cloud propagates outwards from the radiation source, the calculations require some iterations, until the results converge. In this case, the cloud geometrical thickness plays an important role. Actually, if the cloud is very thin, the cool gas region may disappear leading to low or negligible low ionization level lines.

Summarizing, the calculations start in the first slab downstream adopting the input parameters given by the model. Then, it calculates the density, the fractional abundances of the ions from each level for each element, free-free, free-bound and line emission fluxes. It calculates T_e by thermal balancing or the enthalpy equation, and the optical depth of the slab in order to obtain the primary and secondary fluxes by radiation transfer for the next slab. Finally, the parameters calculated in slab i are adopted as initial conditions for slab i+1. Integrating the line intensities from each slab, the absolute fluxes of the lines and of bremsstrahlung are obtained at the nebula. The line ratios to a certain line (generally Hβ for the optical-UV spectrum) are then calculated and compared with the observed data, in order to avoid problems of distances, absorption, etc. The number of the lines calculated by the code (over 300) does not depend on the number of the observed lines nor does it depend on the number of input parameters, but rather on the elements composing the gas.

3.4.5.3 Grids of models

The input physical parameters are combined throughout the calculation of forbidden and permitted lines emitted from a shocked nebula. The initial ranges of the physical conditions in the gas are deduced, as a first guess, from the observed line ratios because they are more constraining than the continuum SED. Grids of models are calculated for each spectrum, modifying the input parameters gradually, in order to reproduce as close as possible all the observed line ratios. At each stage of the modeling process, if a satisfactory fit is not found for all the lines, a new iteration is initiated with a different set of input parameters. When one of the line ratios is not reproduced, I checked how it depends on the physical parameters and decided accordingly how to change them, considering that each ratio has a different weight. The input parameters are therefore refined by the detailed modeling of the spectra. The spectra of NGC 7212 and IC 5063 are rich in number of lines, therefore the calculated spectra are strongly constrained by the observed lines. They are different in each of the observed spectra, revealing different physical conditions from region to region. The models selected by the fit of the line spectrum are cross-checked by fitting the continuum SED. In the UV range the bremsstrahlung from the nebula

Table 3.7: Simulation for $V < 0$ of the S0 region of IC 5063. For each bin, there are the observed quantities and the results of the models. The first nine rows show the comparison between the observed and the synthetic spectra, the remaining rows show the input parameters of each model.

	bin 1		bin 2		bin 3		bin 4	
line	obs.	mod.	obs.	mod.	obs.	mod.	obs.	mod.
[O II]λ3727+	2.43	2.68	3.06	2.8	3.58	3.5	5.43	5.47
[Ne III]λ3869+	1.27	1.4	1.35	1.6	2.2	1.6	0.12	1.0
[He II]λ4686	0.15	0.37	0.12	0.3	0.02	0.28	0.0	0.2
[O III]λ5007+	12.97	13.0	12.0	12.0	11.4	11.1	8.98	8.88
[O I]λ6300,[S III]λ6310	0.32	0.46	0.3	0.3	0.41	0.46	0.53	0.4
Hα	2.86	2.9	2.86	2.9	2.86	2.9	2.86	2.96
[N II]λ6584	1.9	1.9	2.07	2.2	2.18	2.	3.22	3.86
[S II]λ6716	0.9	0.53	1.09	0.54	0.92	0.5	0.98	0.82
[S II]λ6731	0.8	1.1	0.9	1.1	1.0	1.0	0.72	1.3
V (km s^{-1})	-100	–	-200	–	-300	–	-400	–
V_s (km s^{-1})	–	100	–	170	–	300	–	400
n_0(cm^{-3})	–	850	–	600	–	370	–	130
D(10^{18} cm)	–	0.007	–	0.01	–	0.008	–	0.08
F (units[1])	–	9.2	–	7.	–	6.	–	2.2
O/H (10^{-4})	–	5.	–	6.6	–	6.6	–	6.1
N/H (10^{-4})	–	0.5	–	0.6	–	0.5	–	0.8
Ne/H(10^{-4})	–	0.7	–	1.	–	1.	–	0.7
S/H (10^{-4})	–	0.2	–	0.2	–	0.18	–	0.12
Hβ (erg cm^{-2} s^{-1})	–	0.14	–	0.168	–	0.12	–	0.054

[1] in 10^{10} phot cm^{-2}s^{-1}eV^{-1} at the Lyman limit ($\alpha_{UV} = -1.5$, $\alpha_X = -0.7$);

is blended with black body emission from the star population background. The maximum frequency of the bremsstrahlung peak in the UV – X-ray domain depends on the shock velocity. In the IR range dust reprocessed radiation is generally seen. In the radio range synchrotron radiation by the Fermi mechanism at the shock front is easily recognized by the slope of the SED.

I generally consider that the observed spectrum is satisfactorily fitted by a model when the strongest lines are reproduced by the calculation within 20 percent and the weak ones within 50 percent. The final gap between observed and calculated line ratios is due to observational errors both random and systematic, as well as to the uncertainties of the atomic parameters adopted by the code, such as recombination coefficients, collision strengths etc., which are continuously updated, and to the choice of the model itself. The set of the input parameters which leads to the best fit of the observed line ratios and continuum SED determines the physical and chemical properties of the emitting gas. As already introduced in Sec. 3.4.5.1, they are considered as the "results" of modeling (Table C.12).

3.4.5.4 Choice of NGC 7212 and IC 5063 parameters

I start modeling by trying to reproduce the observed [O III]$\lambda\lambda$5007, 4959/Hβ line ratio ($\lambda\lambda$5007, 4959, hereafter 5007+; the + indicates that the doublet 5007, 4959 is summed up), which is, in general, the highest ratio, by readjusting F and V_s (V_s, however, is constrained through a small range by the observed V). The higher

F, the higher the [O III]/Hβ and the [O III]/[O II] line ratios, as well as He II/Hβ. Moreover, a high F maintains the gas ionized far from the source, yielding enhanced [O I] and [S II] lines. These lines behave similarly because the first ionization potential of S (10.36 eV) is lower than that of O (13.61 eV). Then, I consider the [O II]$\lambda\lambda$3726, 3729 doublet (hereafter 3726+). If the flux from the active center is low ($F \leq 10^9$ ph cm^{-2}s^{-1}eV^{-1}), a shock-dominated regime is found, which is characterized by relatively high [O II]/[O III] (≥ 1). [O II] can be drastically reduced by collisional de-excitation at high electron densities ($n_e > 3000\,\mathrm{cm}^{-3}$).

The gas density is a crucial parameter. In each cloud, it reaches its upper limit downstream and remains nearly constant, while the electron density decreases following recombination. A high density, increasing the cooling rate, speeds up the recombination process of the gas, enhancing the low-ionization lines. Indeed, each line is produced in a region of gas at a different n_e and T_e, depending on the ionization level and the atomic parameters characteristic of the ion. The density n_e, which can be roughly inferred from the [S II]6716/6731 doublet ratio, is related with n_0 (the pre-shock density) by compression downstream (n_e/n_0), which ranges between 4 and ~ 100, depending on V_s and B_0. The [S II] lines are also characterized by a relatively low critical density for collisional de-excitation. In some cases, the [S II]6716/6731 line ratio varies from > 1 to < 1 throughout a relatively small region, since the [S II] line ratios depend on both the temperature and electron density of the emitting gas (Osterbrock & Ferland, 2006), which in models accounting for the shock are far from constant throughout the clouds. Thus, even sophisticated calculations which reproduce approximately the high inhomogeneous conditions of the gas lead to some discrepancies between the calculated and observed line ratios. Unfortunately, there are no data for S lines from higher ionization levels which could indicate whether the choice of the model is misleading or different relative abundances should be adopted. I recall that sulfur can be easily depleted from the gaseous phase and trapped into dust grains and molecules.

Finally, the results of the modeling are shown in Table C.1–C.32 of the Appendix C. I show here Table 3.7, as an example of a typical table. I can conclude that composite models are able to reproduce the observed spectra accurately, in particular they well reproduce the high [O I]/Hβ line ratios. For instance, the spectrum in Table C.9, corresponding to the emitting cloud in the CS region of IC 5063 (bin 4), shows V_s of ~ 400 km s^{-1}. The cloud moves outwards from the active center, therefore the photo-ionizing radiation reaches the edge opposite to the shock front. The profiles of T_e, n_e and of the O^{++}/O, O^{+}/O and O^{0}/O fractional abundances throughout the clouds are shown in Fig. 3.16. Reducing the shock velocity to $V_s = 50$ km s^{-1} and even lower I can simulate the case of pure photo-ionization. With these models, I can still obtain a good fit of [O III]/Hβ and [O II]/Hβ by increasing the pre-shock density and the photo-ionization flux. However, [O I]/Hβ will be lower than observed by a factor of ~ 10, indicating that the shock velocity constrains the spectra, particularly at high V_s.

Another interesting result of the modeling is the high fragmentation of matter which is revealed by the large range of geometrical thickness (D) used to model the spectra. This might be explained by the interaction between jets and ISM. The interaction causes shocks and it creates turbulence at the shock-front producing fragmentation of matter. These clouds move in a turbulent regime which can cause

the complex line profile described in Sec. 3.4.4.

3.4.6 The spectral energy distribution of the continuum

To cross-check the results obtained by the detailed modeling of the line spectra, I have gathered from the NED greythe data corresponding to the continuum spectral energy distribution (SED) of IC 5063 and NGC 7212. Fig. 3.17 shows the SED obtained from these data. Error bars are not shown for sake of clarity at frequencies $< 10^{17}$ Hz. I have selected some models which, on average, best reproduce the line ratios at different V_s (100, 300 and 600 km s^{-1}) and I have compared them with the data in Fig. 3.17. At $\nu > 10^{17}$ Hz the data are fitted by the power-law flux from the AGN. The flux is reprocessed by gas and dust within the clouds and it is emitted as free-free and free-bound (and line) at lower frequencies. The reprocessed radiation by dust grains appears in the IR. In the specific case of IC 5063 the model corresponding to low V_s and low F reproduces the data lower limit in the UV-optical range. Most of the data are nested inside the black body radiation flux corresponding to a temperature of T = 5000 K, which represents the background contribution of relatively old stars as, e.g. red giants and Mira. The near IR side of the IR bump is fitted by the black body re-radiation flux corresponding to $T = 200$ K. It represents emission from a large amount of warm dust produced in the stellar wind of red giant stars. Dust is heated collisionally and radiatively in the clouds. The grains are destroyed by sputtering at high V_s (> 200 km s^{-1}) throughout the shock front. Dust is heated to a maximum $T = 66$ K in the $V_s = 300$ km s^{-1} cloud and to a maximum of 90 K in the $V_s = 600$ km s^{-1} cloud, so the reprocessed radiation peaks at lower ν. In the radio ranges, the data at $\nu \geq 10^{10}$ Hz are fitted by the bremsstrahlung and reradiation by dust, while the data at lower ν ($< 10^{10}$) follow a power-law flux with spectral index = 0.75. It represents the synchrotron radiation flux created by the first-order Fermi mechanism at the shock front.

Interestingly, the same models are used to reproduce the continuum SED of both galaxies. In the far radio range of NGC 7212 self-absorption of the flux is evident. Unfortunately, the data for IC 5063 are lacking.

3.5 Concluding remarks

I studied the NLR/ENLR gas of two nearby Seyfert 2 galaxies: IC 5063 and NGC 7212. I analyzed high-resolution spectra to highlight the different kinematic components of the emission lines and to study the properties of the gas as a function of velocity. I produced diagnostic diagrams and I studied the ionization parameter and the physical conditions of the gas resulting from the line ratios. Finally I compared the observations to detailed models of the spectra, obtaining the following results:

1. The diagnostic diagrams show that the main ionization mechanism of the gas is photo-ionization from the power-law continuum produced by the AGN. However, high-velocity gas seems to lie closer to the LINER/shock region of the diagrams than low-velocity gas. This could suggest that there might be some contribution of shocks in the ionization of high-velocity gas.

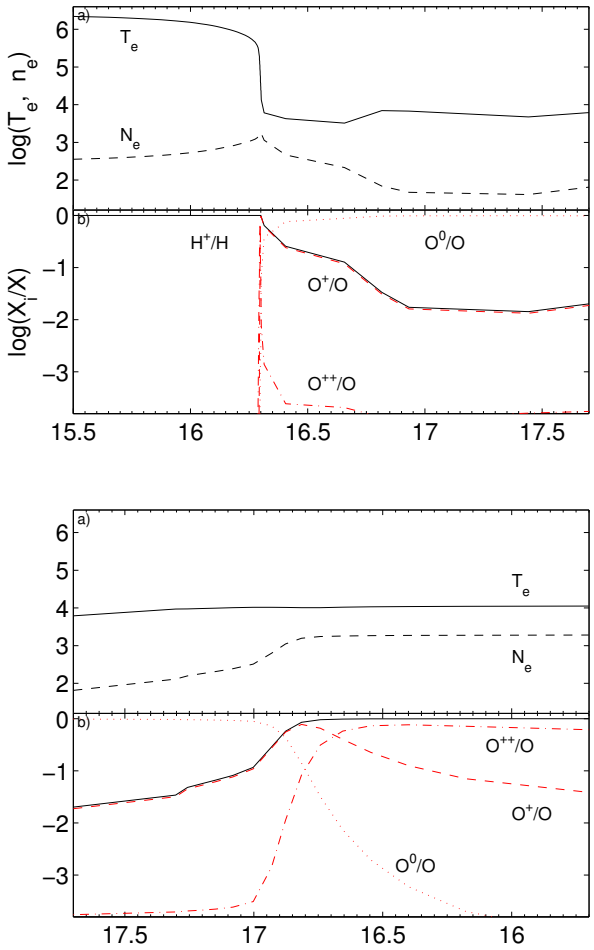

Figure 3.16: The emitting cloud is divided into two halves represented by the left and right diagrams. The top diagram shows the region close to the shock front (left edge) and the distance from the shock front on the X-axis scale is logarithmic. The bottom diagram shows the conditions downstream far from the shock front, close to the (right) edge reached by the photo-ionization flux which is opposite to the shock front. The distance from the illuminated edge is given by a reverse logarithmic X-axis scale. Top panels: the electron temperature and the electron density throughout the emitting cloud. Bottom panels: red lines: O^{++}/O (dot-dashed), O^{+}/O (dashed) and O^{0}/O (dotted); black solid lines: H^{+}/H.

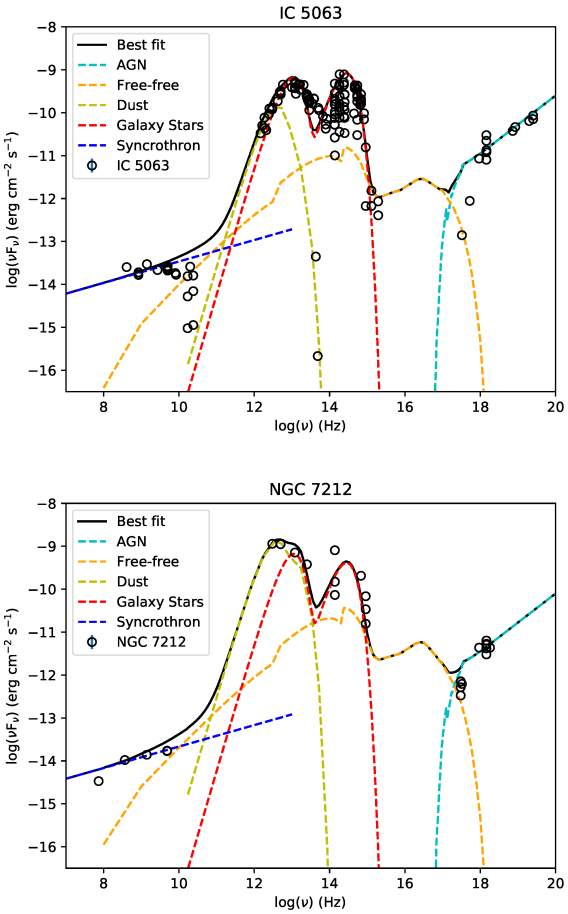

Figure 3.17: The continuum SED of IC 5063 (top) and NGC 7212 (bottom). Black circles: observed data described by the NED. For the sake of clarity, the error bars on the measurements are not shown in these plots. The cyan dashed line in the X-ray domain is the ionizing flux from the AGN. The orange dashed line is the combination of the bremsstrahlung radiation produced by the gas. This component is the sum of three models calculated with 1) $V_s = 100\,km\,s^{-1}$, $n_0 = 200\,cm^{-3}$, log(F) = 9.78, $D = 3 \times 10^{17}\,cm$, 2) $V_s = 300\,km\,s^{-1}$, $n_0 = 300\,cm^{-3}$, log(F) = 10, $D = 3{\times}10^{17}\,cm$ and 3) $V_s = 600\,km\,s^{-1}$, $n_0 = 200\,cm^{-3}$, log(F) = 10.3, $D = 2 \times 10^{16}\,cm$. For all models O/H=$6.6{\times}10^{-4}$, N/H=$5{\times}10^{-5}$ and Ne/H=10^{-4} and a solar metallicity for the other metals. The yellow dashed line is the radiation reprocessed by dust grains calculated consistently with the gas models described above. The red dacyanshed line is the emission due to the stellar component of the galaxy, modeled as two black bodies with temperature of $T = 2000$ and $T = 5000\,K$. The blue dashed line is the synchrotron radiation. The solid black line represent the best fitted model, corresponding to the sum of the different components.

2. In the CN, N0 and N1 regions of IC 5063, the ionization parameter decreases of about one order of magnitude between $V = -600\,\mathrm{km\ s^{-1}}$ and $V = 500\,\mathrm{kms}$, which means that the blueshifted gas is irradiated directly by the AGN, while the redshifted gas is ionized by an attenuated continuum. In the S0, S1 and S2 regions U increases in the opposite direction, from $V = -400$ to $V = 200\,\mathrm{km\ s^{-1}}$. The velocity range is quite narrow because at higher $|V|$ the effects of the extinction correction dominates with respect to the real behavior of the ionization parameter. The ionization increase with V is clearly confirmed by the $\log([O\,III]/\mathrm{H}\beta)$ vs V plot. This behavior of the ionization parameter might be explained assuming a hollow bi-conical shape of the ENLR with one of the edges aligned with the galaxy disk.

3. NGC 7212 shows an ionization parameter which does not depend on velocity. Therefore, it is not possible to say anything about the real geometrical shape of the ENLR.

4. The electron temperature and density are obtained from measured line ratios where possible (Table 3.5 and 3.6). A value of the density was also calculated for each bin by the detailed modeling of the spectra, which accounts also for the shocks (Table C.12 and Appendix C). The two results are typically in agreement and they are consistent with properties of photo-ionized gas.

5. The SUMA composite models results show that the O/H relative abundances are close to solar (Allen, 1976).

6. Analyzing the SED I noticed that, although the multiwavelength dataset is not complete, the power-law flux in the radio range created by the Fermi mechanism at the shock-front, the bremsstrahlung emitted by the gas downstream and the black-body fluxes corresponding to dust reprocessed radiation and to the old star population. Therefore, the Fermi mechanism and the bremsstrahlung radiation confirm the presence of shocks in both galaxies.

7. The analysis of the line profiles shows that the kinematics of both galaxies is quite complex. The profiles change significantly from region to region. In the nucleus of the galaxies, they are often relatively broad and characterized by multiple peaks and bumps. In the external regions, they become narrower but they usually show a red or blue wing. NGC 7212 lines are broader and more disturbed than IC 5063 lines, but they are characterized by less prominent wings. Those are all signs of gas in a turbulent regime.

8. The high fragmentation of the clouds derived by SUMA is an index of interaction between jets and ISM and it might also explain the complex gas kinematics.

9. The high temperatures that seem to characterize the low ionization gas of NGC 7212 might be explained by the jet-ISM interaction (Roche et al., 2016).

10. The main peak of the lines outside the nucleus is shifted towards longer or shorter wavelengths, depending on the observed region. It is a sign of consistent bulk motions of gas with respect to the galaxy stellar component.

11. The profile of the lines within each region does not change, with some exception due to variations in the ionization degree of the gas or difficulties in recovering the original shape of the lines during the deblending process.

Finally, I confirmed that this kind of analysis of the line profiles can be a powerful tool to investigate the properties of gas in such complex conditions. It can show gas properties that a standard analysis would miss, for example, the peculiar behavior of the ionization profile in IC 5063 and the shift of the points corresponding to high $|V|$ in the diagnostic diagrams, which can be associated with the presence of shocks. In particular, the latter cannot be easily observed, when the diagnostic diagrams are produced with the whole line flux, because the contribution of the high $|V|$ gas is negligible with respect to the whole line flux.

4

EXTENDED RADIO EMISSION IN MRK 783

This chapter is extracted from Congiu et al. (2017c)

During the second year of my PhD, I got the chance to start working on the data reduction and analysis of a Karl G. Jansky Very Large Array (JVLA) survey of a sample of narrow-line Seyfert 1 galaxies (NLS1s). I took the chance to look for promising objects to follow-up with optical imaging and spectroscopy in order to discover new extended narrow-line regions (ENLR). In this chapter, I present the analysis of the radio properties of the most promising object in the sample, Mrk 783. The galaxy is one of the few NLS1 showing extended emission of the order of 10 kpc at $z < 0.1$. This is intriguing, since the radio-loudness parameter R of this object is close to the threshold between radio-quiet and radio-loud active galactic nuclei (AGN). The radio emission is divided into a compact core component and an extended component, observed on both sides of the nucleus and extending from 14 kpc southeast to 12 kpc northwest. There is no sign of a collimated jet and the shape of the extended component is similar to those of some Seyfert galaxies. The properties of the emission are compatible with a relic produced by the intermittent activity cycle of the AGN.

4.1 Introduction

Narrow-line Seyfert 1 galaxies (NLS1s) are a puzzling class of active galactic nuclei (AGN), which were first classified by Osterbrock & Pogge (1985) according to their full width at half maximum (FWHM) of Hβ $< 2000\,\mathrm{km\,s^{-1}}$. However, despite the narrowness of Hβ, their ratio [O III]λ5007/Hβ < 3 and the presence of strong Fe II multiplets in the optical and UV spectrum indicate that these objects are type 1 AGN.

Radio-quiet[1] NLS1s (RQNLS1s) constitute 93% of the total population up to redshift 0.8 (Komossa et al., 2006) and 96.5% at z < 0.35 (Cracco et al., 2016). This means that radio-loud NLS1s (RLNLS1s) are relatively uncommon. The latter can be divided into two different classes according to their radio spectrum in the cm range. Flat-spectrum RLNLS1s (F-NLS1s, $\nu < 0.5$, $S_\nu \propto \nu^{-\alpha}$) probably have a relativistic jet pointed toward Earth and can produce γ-rays (Abdo et al., 2009a,b), while steep-spectrum RLNLS1s (S-NLS1s, $\nu > 0.5$,) often show an extended radio morphology and are likely misaligned F-NLS1s.

One of the most interesting possibilities concerning the nature of NLS1s is that they are young and evolving objects (Mathur, 2000). In particular, this appears to be true for RLNLS1s: F-NLS1s might be young flat-spectrum radio quasars (FSRQs) with a small black hole mass and S-NLS1s young radio galaxies (Foschini et al., 2015; Berton et al., 2016b). However, a preference for low inclination might also play a role (e.g., Shen & Ho, 2014; Peterson, 2011). Thus NLS1s are a somewhat heterogeneous group.

S-NLS1s have often been associated with compact steep-spectrum objects (CSS; Oshlack et al., 2001; Komossa et al., 2006; Gallo et al., 2006; Yuan et al., 2008; Caccianiga et al., 2014; Gu et al., 2015; Schulz et al., 2016; Berton et al., 2016b; Caccianiga et al., 2017), which are usually believed to be young and growing radio galaxies (Fanti et al., 1995). Only a handful of S-NLS1s were investigated in radio (Whalen et al., 2006; Antón et al., 2008; Doi et al., 2012; Richards & Lister, 2015; Doi et al., 2015; Gu et al., 2015; Caccianiga et al., 2017). RLNLS1s, indeed, have a lower observed jet power than FSRQs (Foschini et al., 2015) because of their low black hole mass (Heinz & Sunyaev, 2003; Foschini, 2014). Therefore, while F-NLS1s are relatively easy to find because their luminosity is enhanced by relativistic beaming, S-NLS1s are not as easily detectable.

To study the radio properties of NLS1s, a survey has been carried out with the Karl G. Jansky Very Large Array (JVLA) at 5 GHz in A configuration. The sample consists of 60 sources drawn from the papers by Foschini et al. (2015) and Berton et al. (2015), and it contains radio-quiet (but not radio-silent) NLS1s, F-NLS1s, and S-NLS1s. In this chapter, I report the detection of extended emission in one S-NLS1s, Mrk 783. This source is one of the few NLS1 showing such an extended emission at z < 0.1. In Sect. 4.2 I describe the source according to results published in the literature, in Sect. 4.3 I describe the data reduction I performed, in Sect. 4.4 I present our results, in Sect. 4.5 I discuss them and, finally, in Sect. 4.6 I provide a brief summary. Throughout this work, I adopt a standard ΛCDM cosmology, with a Hubble constant $H_0 = 70\,\mathrm{km\ s^{-1}Mpc^{-1}}$, and $\Omega_\Lambda = 0.73$ (Komatsu et al., 2011). Spectral indexes are specified with flux density $S_\nu \propto \nu^{-\alpha}$ at frequency ν.

4.2 Mrk 783

Mrk 783 ($\alpha = 13^\mathrm{h}\ 02^\mathrm{m}\ 58.8^\mathrm{s}$ $\delta{=}{+}16^\circ\ 24'\ 27''$) is a NLS1 galaxy first classified by Osterbrock & Pogge (1985) at $z = 0.0672$ (Hewitt & Burbidge, 1991) with a bolometric luminosity of the AGN $L_\mathrm{bol} = 3.3 \times 10^{44}\,\mathrm{erg\,s^{-1}}$ (Berton et al., 2015). Its

[1]The radio loudness is defined by the parameter R, the ratio between the 5 GHz flux and the optical B-band flux (Kellermann et al., 1989). A source is considered to be radio-loud if R > 10 and radio-quiet if R < 10.

host galaxy was classified as a lenticular galaxy (Petrosian et al., 2007), but the SDSS image clearly shows the presence of a tidal tail, or a spiral arm, extended in the east direction.

The mass of the central black hole inferred from the broad Hβ line width is about 4.3×10^7 $M_\odot$ (Berton et al., 2015). Hβ shows a prominent red wing in the broad component, indicating a receding outflow with a velocity of $\sim 500\,\mathrm{km\ s^{-1}}$. This broad component is clearly visible in all the permitted lines of the optical spectrum. Conversely, narrow lines, and particularly [O III]λ5007, do not show any outflowing component and are well reproduced by a single Gaussian profile (Berton et al., 2016a).

Mrk 783 is a strong X-ray emitter that has been detected by ROSAT (Schwope et al., 2000), INTEGRAL (Krivonos et al., 2007), and Swift/XRT (Panessa et al., 2011). Panessa et al. (2011) reported a luminosity of $9.33 \times 10^{43}\,\mathrm{erg\,s^{-1}}$ between 20 and 100 keV and a photon index of 1.7 ± 0.2 between 0.3 and 100 keV. This is consistent with non-saturated Comptonization, which occurs in the accretion disk corona and not in relativistic jets.

In the last 30 years, the galaxy has been observed with several instruments and in several radio bands, for example, the WSRT at 1.4 GHz (Meurs & Wilson, 1981), VLA at 5 GHz (Ulvestad & Wilson, 1984; Ulvestad et al., 1995), and Green Bank telescope at 1.4 GHz (Bicay et al., 1995). However, no extended emission was ever found. Recently, Doi et al. (2013) observed the galaxy nucleus with the Very Long Baseline Array (VLBA) looking for extended emission near the core of the AGN. The image only shows a compact core, but the flux density recovered by the authors at 1.7 GHz is only 4% of the NRAO VLA Sky Survey (NVSS) flux density at 1.4 GHz ($S_\nu = 33.2$ mJy; Condon et al., 1998). This discrepancy means that the vast majority of the flux emitted by the galaxy is distributed in structures with relatively low brightness temperature, which could not be seen by the instrument. Another hint of the extended emission can be found in the Faint Images of the Radio Sky at Twenty-Centimeters survey (FIRST) image of the galaxy (Becker et al., 1995). The source is elongated along position angle (PA) 131° and shows a peak and a total flux density of 18.5 mJy and 28.72 mJy, respectively. At low frequencies, the TIFR Giant Metrewave Radio Telescope Sky Survey (TGSS; Intema et al., 2017) at 147 MHz reports a flux density of 89.2 ± 10.9 mJy.

Mrk 783 was classified as moderately radio-loud (Berton et al., 2015) or radio-quiet (Doi et al., 2013). The R parameter is indeed close to 10. Therefore, a different estimate of the optical magnitude or optical variability in the source could have provided two different classifications. This is not uncommon, as has been clearly shown by Ho & Peng (2001) and Kharb et al. (2014). However, the radio emission does not appear to be dominant over the optical magnitude as in classical radio galaxies.

4.3 Data reduction

The galaxy was observed on September 6th, 2015 with the JVLA at 5 GHz in A configuration with a bandwidth of 2 GHz, for a total exposure time of 10 minutes. The data were acquired as part of a larger survey of NLS1 galaxies with the main purpose of detecting extended radio emission on arcsecond scale (project code 15A-

283, P.I. Richards), and they are the first to be fully reduced and analyzed. For the analysis of the whole sample, see Berton et al. (2018).

I reduced and analyzed the data using the Common Astronomy Software Applications (CASA) version 4.5, the standard Expanded VLA (EVLA) data reduction pipeline, and the Astronomical Image Processing System (AIPS). The main calibrator was 3C 286. I split off the measurement set of the object from the main dataset, averaging over the 64 channels of each spectral window. After that, the object was cleaned using all the spectral windows and a natural weighting to create a first image. To improve the quality of the final map, I proceeded with iterative cycles of phase-only self-calibration of the visibilities. The results of the CASA self-calibration were not satisfactory because this self-calibration caused a general increase in the noise level of the maps. Therefore I tried to redo the self-calibration process using AIPS, which, indeed, significantly improved the quality of the final images. Once the presence of extended emission was confirmed, I returned to CASA and I proceeded with a second cleaning of the data to obtain the final images. In addition to the high-resolution image I produced another image, using a taper of $50\,\mathrm{k}\lambda$, to recover the highest possible fraction of the extended emission flux density. Fig. 4.1 shows the maps of the object before and after the application of the taper. The lower panels show the radio contours superimposed on a Sloan Digital Sky Survey (SDSS) optical image.

4.4 Results

The images in Fig. 4.1 clearly show a compact core and extended emission at PA= 131°, which is in agreement with the FIRST data. In the high-resolution image, the extended emission is observed only in the southeast region of the galaxy up to a projected distance of ~ 8 kpc. In the tapered image, instead, it is observed on both sides of the nucleus up to a projected distance of 14 kpc in the southeast and 12.5 kpc in the northwest direction.

I fitted the central component in the high-resolution image with a 2D Gaussian, using the fitting algorithm in the CASA viewer. I measured a peak flux density of 3.32 ± 0.04 mJy beam^{-1}, an integrated flux density $S_{\nu,\mathrm{c}} = 4.03 \pm 0.08$ mJy, and the size of deconvolved core axes 216 ± 21 (~ 280) and 173 ± 24 (~ 225) mas (pc) for the major and minor axis, respectively. The beam size is $0.45'' \times 0.40''$. With these values I calculated the core luminosity $L_{\mathrm{c}} = 2.3 \times 10^{39}\,\mathrm{erg\,s^{-1}}$ and I used the following equation to estimate the brightness temperature (Doi et al., 2013):

$$T_B = 1.8 \times 10^9 (1+z) \frac{S_{\nu,\mathrm{c}}}{\nu^2 \phi_{\mathrm{maj}} \phi_{\mathrm{min}}} \sim 7600\,\mathrm{K}, \tag{4.1}$$

where z is the redshift, ϕ_{maj} is the core major axis, and ϕ_{min} is the minor axis. This T_B is only a lower limit to the peak value because our measurement includes some extended emission. The real core emission as detected with VLBI is smaller and Doi et al. (2013) quote a peak value of $T_B > 7.7 \times 10^7$ K at 1.7 GHz. From the tapered image I measured a total flux density $S_{\nu,\mathrm{t}} = 18.85 \pm 0.03$ mJy ($L_{\mathrm{tot}} = 1.03 \times 10^{40}\,\mathrm{erg\,s^{-1}}$) and I obtained the flux density of the extended emission ($S_{\nu,e} = 14.82 \pm 0.1$ mJy, $L_{\mathrm{ext}} = 8.5 \times 10^{39}\,erg.s^{-1}$), after subtracting the JVLA core flux

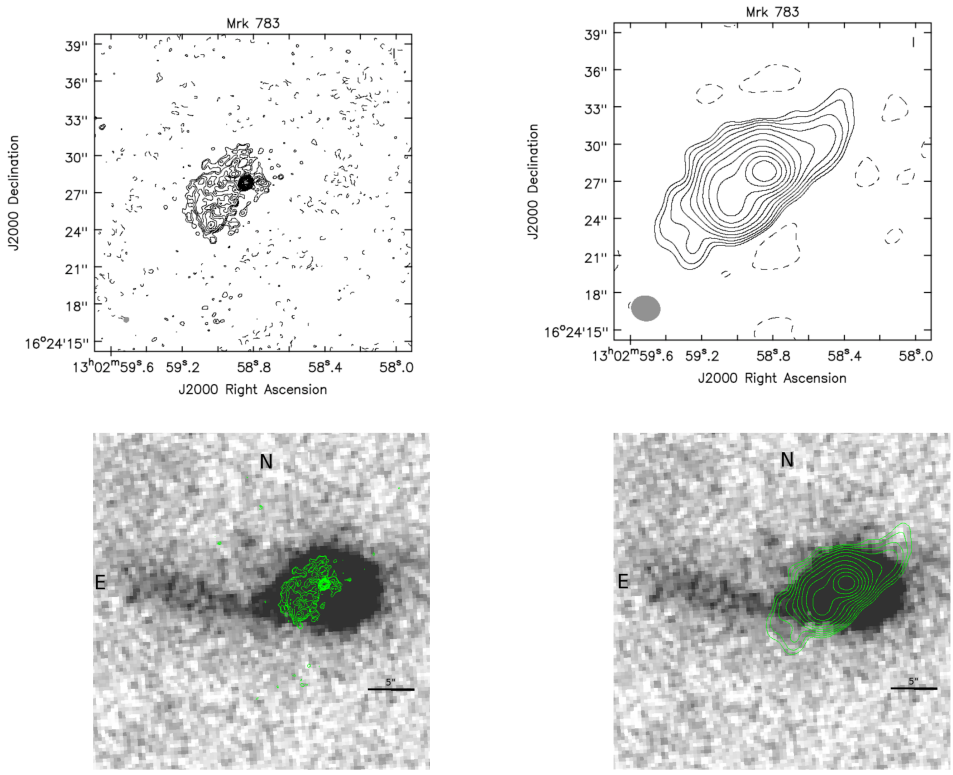

Figure 4.1: **Top:** VLA images with natural weighting of Mrk 783 at 5 GHz. The scale is 1.3 kpc arcsec^{-1}. *Left:* The high-resolution image is shown; the beam size is $0.45'' \times 0.40''$. The contour levels are separated by a factor $\sqrt{2}$ starting from 3σ with $\sigma = 0.011$ mJy. The dashed contours represent a -2σ value. *Right:* Image of the source with a Gaussian taper of 50 kλ is shown; the beam size is $2.00'' \times 2.33''$. The contour levels are separated by a factor $\sqrt{2}$ starting from 3σ with $\sigma = 0.039$ mJy. The dashed contours represent a -2σ value. **Bottom:** The same contours superimposed on a SDSS image of the galaxy in the g band.

Table 4.1: Fluxes of the galaxy in several radio and infrared bands.

Band	Flux density (mJy)	Notes	Reference
150 MHz	89.2	total	1
1.4 GHz	33.2	total	2
1.4 GHz	28.7	total	3
5 GHz	4.0	core	4
5 GHz	14.8	extended	4
5 GHz	18.9	total	4
60 μm	310.0	total	5
22 μm	65.9	total	6

(1) TGSS (Intema et al., 2017); (2) NVSS (Condon et al., 1998); (3) FIRST (Becker et al., 1995); (4) this work; (5) IRAS (Moshir & et al., 1990); (6) WISE (Wright et al., 2010).

density. To evaluate the relative importance of the core emission with respect to the total emission I measured the core dominance parameter (CD) as follows:

$$\mathrm{CD} = S_{\nu,\mathrm{c}}/(S_{\nu,\mathrm{t}} - S_{\nu,\mathrm{c}}) \sim 0.27. \tag{4.2}$$

The core flux is likely an upper limit, therefore the CD parameter is also an upper limit, meaning that the galaxy is not core dominated.

To better characterize the emission I measured the spectral indexes of the two components. I measured these components by dividing the spectral windows into two bins: the first centered at 4.7 GHz and the second at 5.7 GHz. Images were made at the two frequencies, adjusting the weighting of the visibilities using the ROBUST parameter in the AIPS task IMAGR so as to obtain similar beams; they were finally convolved with identical circular beams of size 0.45 arcsec. The spectral index images were made using task COMB after blanking total intensity values below 1.5 sigma. I obtained the following spectral indexes for the core component and the southern lobe, respectively: $\alpha_{\mathrm{c}} \sim 0.67 \pm 0.13$, $\alpha_{\mathrm{ext}} \sim 2.02 \pm 0.74$. The α_{ext} was estimated for the southeast lobe, avoiding the noisiest regions toward the north and east of the core.

4.5 Discussion

The VLA data revealed emission in a compact core as well as an extended component, which can be observed on both sides of the nucleus in the tapered image. The power at 5 GHz is $L_\nu = 2.1 \times 10^{30}\,\mathrm{erg\,s^{-1}Hz^{-1}}$, which is below the nominal $\sim 7 \times 10^{31}\,\mathrm{erg\,s^{-1}Hz^{-1}}$, the Fanaroff-Riley (FR) cutoff power. The CD (≤ 0.27) indicates that the emission is not core dominated and the steep spectral index of the core is different from those of highly beamed radio quasars and BL Lacs ($\alpha \sim 0$), but it is more similar to that of CSS sources ($\alpha \sim 0.5$). The extended component does not show any sign of a highly collimated jet, but it has a double-lobe shape

that resembles the radio emission of some Seyfert galaxies, such as NGC 6764 (Hota & Saikia, 2006) and Mrk 6 (Kharb et al., 2006).

Extended radio surveys of normal Seyfert galaxies and LINERs (e.g., Baum et al., 1993; Gallimore et al., 2006; Singh et al., 2015a) have discovered that kiloparsec-scale radio emission is not uncommon in these objects. The emission usually seems to have an AGN origin (Gallimore et al., 2006; Singh et al., 2015a), but, in some cases, star formation (SF) can contribute significantly (e.g., Baum et al., 1993). This could be true, indeed, in the case of NLS1 galaxies where the presence of SF (both in RQ and RL objects) has often been reported in the literature (e.g., Sani et al., 2010; Caccianiga et al., 2015). The very red mid-IR colors ($W3-W4=2.6$) measured by the Wide-field Infrared Survey Explorer (WISE) of Mrk 783 and its strong emission at 60 μm measured by the InfraRed Astronomical Satellite (IRAS) (310 mJy) seem to support this hypothesis. In order to evaluate the impact of this possible SF on the observed radio emission, I computed the parameter $q22$, defined as

$$q22 = \log(S_{22\,\mu\mathrm{m}}/S_{1.4\,\mathrm{GHz}}), \tag{4.3}$$

where $S_{22\,\mu\mathrm{m}}$ and $S_{1.4\,\mathrm{GHz}}$ are the WISE 22 μm flux density and the NVSS flux density, respectively. The resulting value ($q22 \sim 0.3$) is significantly lower than that usually observed in SF galaxies ($q22 > 1$; Caccianiga et al., 2015). This means that, even if all the observed mid-IR emissions were produced by the SF, the expected radio flux at 1.4 GHz would be much lower than the observed flux ($\sim$ 20 percent of the observed flux) . Considering that part of the IR emission is likely due to the AGN, I conclude that, even if present, the SF alone cannot explain the majority of the observed radio emission.

I compared our spectral indexes with results in the literature. Using TGSS, NVSS, and our flux densities (Tab. 4.1) I recovered a spectral index $\alpha \sim 0.44$. This is significantly flatter with respect to our measurements. A possible explanation for this discrepancy might be the presence of a break or a cutoff at 5 GHz. Furthermore, biases of the surveys toward extended emissions, for example, due to short integration time, might also cause an underestimate of the spectral index.

A possible explanation for the very steep spectral indexes observed in our VLA images might be that the observed emission is a relic. This could be supported by the absence of collimated structure in our images and in the high-resolution images from Doi et al. (2013). Relic emission has already been observed in some Seyfert galaxies (e.g., NGC 4235, Kharb et al., 2016) and they also show very steep spectra (e.g., Jamrozy et al., 2004; Kharb et al., 2016).

Czerny et al. (2009) found that in young radio sources with high accretion rates, radiation pressure instabilities of the accretion disk can result in intermittent activity of the radio jet. In their model, the activity phases last for $10^3 - 10^4$ yr and they are separated by periods of $10^4 - 10^6$ yr in which the radio jet is switched off. During the cycle, the previous activity period should manifest in the form of a relic extended emission that continues its expansion until the emitting cocoon cools down and recollapses. The maximum extension and cooling time of the cocoon depend on many factors, such as jet power and duration of the activity phase. In the case of NLS1, both quantities are considered relatively small, resulting in a very low detection rate of such emission in this class of AGN (Czerny et al., 2009; Foschini et al., 2015). Such extended emission might appear only if the central black hole

mass is in the higher part of the mass distribution (which spans between 10^6 to 10^8 $M_\odot$, e.g., Cracco et al., 2016), more precisely if $M_{BH} > 10^7$ $M_\odot$ the BH should produce the necessary jet power to make it escape from the central regions of the AGN (Doi et al., 2012). The mass of Mrk 783 black hole is 4.3×10^7 $M_\odot$ (Berton et al., 2015), therefore it belongs to the objects that in principle could produce the extended emission. Some of the properties of the emission, such as its size and the absence of a collimated jet, might suggest that the galaxy has been observed in one of its quiescent phases not long after the switching off of the radio jet.

It is worth noting that the large-scale structure of the radio emission in the tapered image has an S-like shape, which is typical of precessing radio jets (Ekers et al., 1978; Parma et al., 1985). Precessing jets could arise in binary black hole systems (e.g., Roos et al., 1993; Romero et al., 2000; Rubinur et al., 2017) or result from accretion disk instabilities (Pringle, 1996; Livio & Pringle, 1997). In the latter case, it might be consistent with a scenario of episodic activity described previously. The resemblance to the case of Mrk 6 is strong (Kharb et al., 2006).

Another possible explanation of why I observe such steep spectral indexes might be that there is a strong interaction between a jet and interstellar medium of the galaxy. This could cause shocks and magnetic field amplification, leading to greater radiative losses and steep spectra.

This source might represent one of the few examples of the elusive parent population of F-NLS1s, i.e., S-NLS1s, Mrk 783, which lies at the edge of the RQ/RL division. The same is true for another S-NLS1 with extended emission, Mrk 1239 (Doi et al., 2015). This might indicate that more sources of this kind could be found among RQ objects. Very few RQNLS1s show detectable jets or diffuse radio emission (Berton et al., 2016a). This is partly because they are by definition faint in the radio regime, but some objects that fit the RQ definition show non-thermal core emission when observed with high sensitivity (Giroletti & Panessa, 2009).

Another hypothesis regarding the parent population of F-NLS1s is based on a different assumption about NLS1s nature. Some authors believe that the narrowness of permitted lines is not due to the low black hole mass, but instead to a flat BLR observed pole-on (e.g., Decarli et al., 2008). Mrk 783, however, shows extended emission on both sides of the core, hence it likely has a non-negligible inclination. In this case then, the low black hole mass estimate should not be significantly affected by any BLR flattening, although this might happen in other objects (Shen & Ho, 2014).

To better understand the nature of this object, simultaneous radio observations at different frequencies are needed to study the spectral energy distribution (SED) of the emission. In particular, it is fundamental to investigate the reason of such a difference between our spectral indexes and what I found from data in the literature. Also, images with an intermediate spatial resolution between our data and the data from Doi et al. (2013) (e.g., from e-MERLIN) could be useful to investigate the presence of an intermediate scale radio jet.

4.6 Concluding remarks

In this chapter, I presented the first results of a survey of NLS1s carried out with the JVLA at 5 GHz in A configuration. In particular, I reported the detection of

extended emission in the S-NLS1 Mrk 783. I found a compact core and extended emission that, in the tapered image, is observed on both the southeast and northwest sides of the galaxy nucleus, up to a maximum projected distance of 14 kpc. I excluded star formation as the dominating cause of the extended emission owing to the low value of the IR-to-radio flux ratio ($q22$). The latter, together with the morphology of the emission, indeed suggests an AGN origin. At the same time, in the high-resolution image (Fig. 4.1) I could not find any sign of a large-scale collimated jet and Doi et al. (2013) did not find any small-scale jets. These facts, and the very steep measured spectral indexes, led me to hypothesize that the extended emission might be a relic and that the source might be in a quiescent period of its activity cycle, which is in agreement with the theoretical model by Czerny et al. (2009) and the young age scenario for NLS1s (Mathur, 2000). Further observations are needed both in radio and in other bands to confirm these results and to investigate the nature of this object in more detail.

5

OPTICAL ANALYSIS OF MRK 783

In this chapter, I will report the results of the optical follow-up of Mrk 783, the NLS1 galaxy with radio extended emission analyzed in the previous chapter. I acquired new spectroscopic data in order to investigate the presence of an extended narrow-line region (ENLR) aligned with the radio emission.

The new data revealed the presence of an ENLR with a maximum size of 38 kpc, well above the typical size of these extended structures at $z < 0.1$. The diagnostic diagrams confirm that the gas is ionized by the AGN continuum, at least in the inner kiloparsecs where all the emission lines were detected.

The analysis of the spectra, together with new and archival broad-band images, suggests that the galaxy recently merged with a companion and that it might be in the first stages of the interaction with another companion source located ~ 100 kpc away.

5.1 Introduction

The extended narrow-line region (ENLR) is one of the most puzzling and less studied structures observed in active galactic nuclei (AGN). It is a region of highly ionized gas that can have an extension, usually traced thanks to optical emission lines, of the order of tens of kiloparsecs (e.g. Stockton & MacKenty, 1987; Tadhunter & Tsvetanov, 1989; Keel et al., 2012).

ENLRs are observed both in Type 1 and Type 2 AGN (mainly in Seyfert galaxies), even though they seem to have different properties in the two samples. In Seyfert 2s the ENLR is usually characterized by a conical or bi-conical shape with the apexes pointing toward the nucleus of the galaxy (for this reason ENLRs are often called *ionization cones*), while Seyfert 1s usually show more compact and halo-like structures (Schmitt et al., 2003a,b).

This behavior can be explained thanks to the Unified Model of AGN (Antonucci, 1993; Urry & Padovani, 1995). According to this model, the core of the AGN is surrounded by a dusty torus, which is able to absorb part of the ionizing radiation produced in the inner region of the nucleus. The radiation, therefore, can escape

only along the torus axis and photo-ionize the surrounding gas, creating the NLR. If the ionizing radiation can escape the NLR and it finds gas at larger radii it will produce the ENLR.

Since Type 1 AGN are observed close to face-on, the line of sight falls inside the cone, producing the halo-like shape observed in these objects, while in Seyfert 2s the AGN is observed almost edge-on, allowing the observation of the full extension of the structure and its conical shape (Schmitt et al., 2003a,b). This property makes ionization cones one of the best proxy to measure the inclination of the AGN with respect to the line of sight (Fischer et al., 2013; Marin, 2014).

The second factor influencing the presence and the shape of the ENLR is the galactic scale gas distribution. A spherical distribution of host galaxy gas would allow the formation of ionization cones only on Type 2 AGN, while a disk distribution would allow to observe these shapes also in Type 1 objects (Mulchaey et al., 1996b; Schmitt et al., 2003b). Ionization cones are, indeed, observed in several Type 1 AGN (e.g. NGC 4151, Pogge (1988); Mrk 79, Schmitt et al. (2003a)). New results from He et al. (2018) suggest that 30–40% of AGN with ENLR are Type 1 objects.

The ENLR is often characterized by a spectrum with complex lines profile showing double peaks or asymmetries (Dietrich & Wagner, 1998; Morganti et al., 2007; Ozaki, 2009; Congiu et al., 2017b), produced by the presence of several kinematic components in the gas. In some galaxies, outflows of gas with velocities of 400 – 600 km s^{-1} have been observed in several gas phases (from the cold molecular gas to the warm ionized one) inside the ionization cones (e.g. IC 5063, Baldwin et al., 1987; Morganti et al., 1998, 2007; Dasyra et al., 2015; Morganti et al., 2015). Moreover, ionization cones seem to be often aligned with the radio jets of the AGN (Unger et al., 1987; Nagar et al., 1999; Schmitt et al., 2003a,b) and in some case it has been proved that shocks can be important in the ionization of the ENLR gas (Congiu et al., 2017b; Rodríguez-Ardila et al., 2017). All these properties might be explained as the result of the interaction between the ISM of the galaxy and the radio jet of the AGN (e.g. Unger et al., 1987; Tadhunter et al., 2014; Congiu et al., 2017b; Rodríguez-Ardila et al., 2017).

With this mind, soon after the discovery of a kiloparsec scale radio emission in the narrow-line Seyfert 1 (NLS1) galaxy Mrk 783 (Congiu et al., 2017c), I started an optical follow-up of the source which brought to the discovery of a very extended optical emission at the same position angle (PA) of the radio emission. As mentioned in the previous chapter of this work, NLS1s are a peculiar class of Type 1 AGN, classified for the first time by Osterbrock & Pogge (1985). They are characterized by narrow permitted emission lines, full width at half maximum (FWHM) of Hβ < 2000 km s^{-1}, [O III]λ5007/Hβ ratio < 3 (Osterbrock & Pogge, 1985) and strong iron multiplets indicating that they are type 1 AGN (Goodrich, 1989). The analysis of new spectra of Mrk 783 (Congiu et al., 2017a) revealed that the strongest optical emission lines can be traced up to $\sim 30''$ from the nucleus, which corresponds to a projected size of ~ 38 kpc, making this ENLR one of the most extended discovered so far at $z < 0.1$.

In this chapter, I present a detailed analysis of several spectra and images of Mrk 783 to characterize the properties of the emission, and of the host galaxy in general, and to study the relation between the ENLR and the extended radio emission.

In Sec. 5.2 I will describe the target, Mrk 783 while in Sec. 5.3 I will present new and archival observations. In Sec. 5.4 I will present a qualitative analysis of all the data, while Sec. 5.5 will focus on a more quantitative and detailed analysis of the spectra. Finally, in Sec. 5.6 I will discuss the results that will be summarized in Sec. 5.7. In this work, I adopt the following cosmological parameters: $H_0 = 70\,\mathrm{km\ s^{-1}\,Mpc^{-1}}$, $\Omega_{m,0} = 0.27$ and $\Omega_{\Lambda,0} = 0.73$ (Komatsu et al., 2011).

5.2 Mrk 783

Mrk 783 ($\alpha = 13^{\mathrm{h}}\ 02^{\mathrm{m}}\ 58.8^{\mathrm{s}}$ δ=+16° 24′ 27″) is a NLS1 galaxy firstly classified by Osterbrock & Pogge (1985) at $z = 0.0672$ (Hewitt & Burbidge, 1991). The AGN is characterized by a bolometric luminosity $L_{bol} = 3.3 \times 10^{44}\,\mathrm{erg\,s^{-1}}$ and the supermassive black hole (SMBH) has a mass of $\sim 4.3 \times 10^7\,\mathrm{M_\odot}$ (Berton et al., 2015). The host has been classified as a lenticular galaxy by Petrosian et al. (2007).

The object has been observed several times in the radio band and it was detected in all the major surveys (FIRST, NVSS), but only recently Congiu et al. (2017c) discovered a kiloparsec scale radio emission thanks to a VLA snapshot survey carried out at 5 GHz in A configuration (Berton et al., 2018). The maximum extension of the radio emission has been measured, in the tapered image, to be 14 kpc and it is located along PA = 131° (Congiu et al., 2017c). Due to the very steep in-band spectra indexes measured from the VLA images, the authors hypothesized that the extended emission is a relic due to the intermittent activity of the AGN.

On VLBI scale the object has been studied by Doi et al. (2013) with the VLBA at 1.7 GHz. Mrk 783 appears as a point-source, without any extended emission, and with a brightness temperature of 7.7×10^7 K, a sign of the non-thermal origin of this emission.

5.3 Observations

In order to investigate the presence of the extended optical emission associated with the KSR in this galaxy, I proposed new spectroscopic and imaging observations. The main purpose of the former was to detect and characterize the property of the putative ENLR and of the environment in which the galaxy resides. The latter were proposed to get a better insight into the morphological properties of the source and to identify eventual companion galaxies.

5.3.1 Spectroscopy

The galaxy has been observed two times with the Low Dispersion Survey Spectrograph - 3 (LDSS-3) of the Magellan telescopes. All the observations have been performed in long slit mode, with the $1'' \times 4'$ "center" slit and the VPH-All. This combination of slit and dispersion element allows to cover almost the whole optical wavelength range (4250 – 10000 Å) with a good sensitivity. The galaxy was observed twice at position angle PA = 131°, with the slit parallel to the radio emission, and once at PA = 90°, in order to observe the secondary nucleus that will be mentioned and analyzed in Sec. 5.4.1 and following.

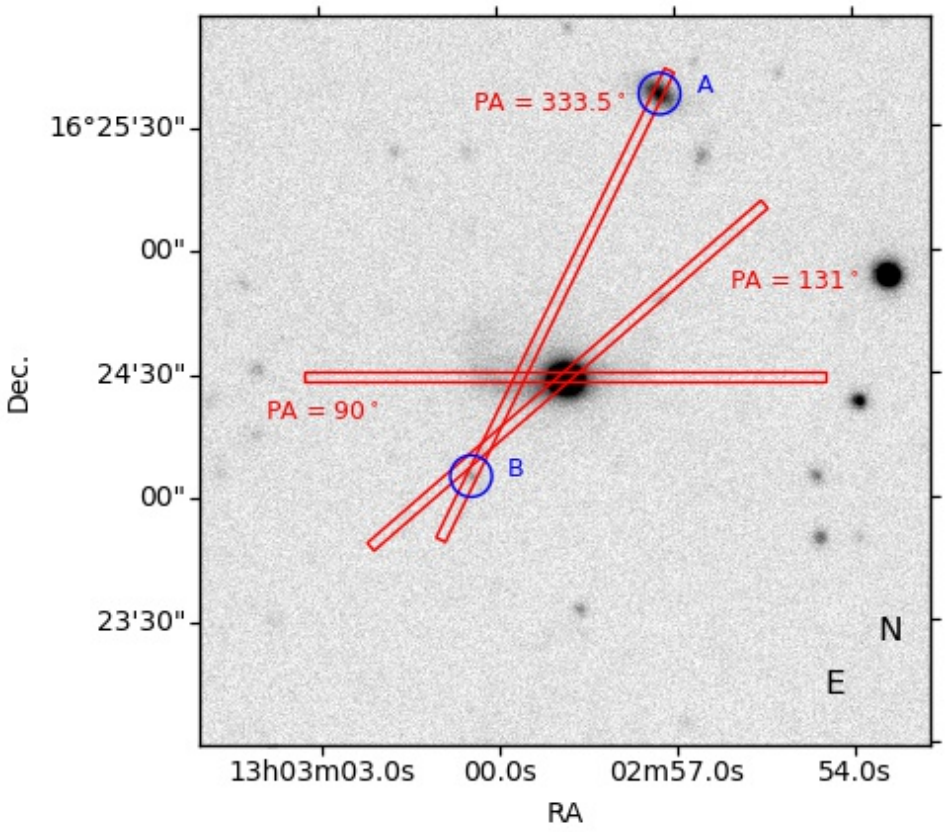

Figure 5.1: Image of Mrk 783 acquired with the Copernico telescope of the Asiago Astronomical Observatory with a g filter. In the image is shown the position of the slit during the spectroscopic observations and the position of the sources A and B observed with TNG. The spectra at PA = 90° and 131° were observed with LDSS-3@Magellan, while the spectrum at PA = 333.5° was acquired with DOLORES@TNG. Only one of the two PA = 131° spectra is shown in the figure, since the only difference is that in the second spectrum the position of the nucleus on the slit has been shifted, in order to avoid the slit support covering part of the extended emission.

Table 5.1: Details of spectroscopic observations.

Date	PA	Slit width	Exp. (arcsec)	Time (s)	$\Delta\lambda$ (Å)	RMS (Å)	Standard	Instrument
2017-02-22	131°	1.0	3	3600	8.2	0.87	LTT 4816	LDSS-3
2017-06-09	90°	1.0	3	3600	7.9	1.50	EG 274	LDSS-3
	131°	1.0	3	3600	7.9	0.52	EG 274	LDSS-3
2018-06-11	333.5°	1.0	3	2700	10.04	-	-	DOLORES

From left to right: (1) date of the observation, (2) position angle, (3) width of the slit in arcseconds, (4)number of exposures per pointing, (5) total exposure time, (6) resolution of the spectrum measured from the calibration lamp spectrum, (7) error on the wavelength calibration measured on the sky lines, (8) standard star used for flux calibration, (10) instrument used.

A fourth spectrum has been acquired with the DOLORES spectrograph of the Telescopio Nazionale Galileo (TNG) using the 1.0″ slit and the LR-B grism. This configuration allows to obtain a low-resolution spectrum (R $\sim$ 600) of the whole optical wavelength range. As it is possible to see from Fig. 5.1, this last spectrum is not centered on the galaxy itself, but it has been acquired in order to study two putative companions of the AGN. In particular, I wanted to measure the redshift of J1302+1625 and J1303+1624 (source A and B respectively, in Fig. 5.1), to investigate the possibility of the two objects being part of a group with Mrk 783

The reduction of the spectra obtained with both instruments was performed with standard IRAF[1] tasks. The spectra have been trimmed, corrected for bias and flat-field and wavelength calibrated using the spectra of a HeNeAr lamp (LDSS-3) or a HgNe lamp (DOLORES). LDSS-3 spectra have also been flux calibrated using two different standard stars for the two runs: LTT 4816 and EG 274. Since the main goal of the TNG spectrum was to measure the redshift of the two sources, no spectroscopic standard star has been observed. To obtain the final data the different exposures for each spectrum have been combined and the sky contribution has been subtracted from the spectra.

Before the subtraction, I used the calibration lamp spectra and some sky emission lines to estimate the resolution of the science data and the reliability of the wavelength calibration. While LDSS-3 spectra are quite well calibrated, unfortunately the sky lines of DOLORES spectrum show a systematic shift of ~ 5 Å. This must be ascribed to the fact that the calibration lamp has been observed as part of the daylight calibration plan, and not immediately after the science observation. I tried to improve this calibration using the sky lines as a reference for the calibration process. But, since the available sky lines in the spectrum are only a few and they are quite close together, the new calibration was no reliable. Tab. 5.1 summarizes the properties of the observations.

5.3.2 Imaging

Mrk 783 has been observed in all the available bands (*ugriz*) by the Sloan Digital Sky Survey (SDSS). In particular, for this work I considered the images of the Data

[1] http://iraf.noao.edu/

Table 5.2: Details of imaging observations.

Instrument	Filter	Exp.	Exp. time (s)	Seeing (arcsec)	SB limit (mag)	Date
SDSS	u	1	54	1.4	23.5	2005-06-01
SDSS	g	1	54	1.2	24.7	2005-06-01
SDSS	r	1	54	1.1	24.1	2005-06-01
SDSS	i	1	54	1.0	23.5	2005-06-01
SDSS	z	1	54	0.9	22.0	2005-06-01
AFOSC	g	12	7200	2.6	26.1	2018-04-18

From left to right: (1) Telescope or instrument, (2) filter, (3) number of exposures per pointing, (4) total exposure time, (5) average seeing, (6) 3σ surface brightness limit of the image (7) date of observation.

Release 7[2]. The g-band image of Mrk 783 has a measured 3σ surface brightness limit of $\sim 24.7\,\mathrm{mag\,arcsec^{-2}}$. In order to better detect faint structures, such as tidal tails or spiral arms that seems to be present in the SDSS images, I also acquired a new g-band data with the Copernico telescope of the Asiago Astronomical Observatory (Fig. 5.1). The galaxy has been observed for a total exposure time of 2 hr divided into 12 single 600 s exposures. The new data have been corrected for bias and flat-field with standard IRAF tasks. Then the scientific images have been astrometrized. The seeing during the observations was highly variable, therefore, before the combination, they were all convolved with a Gaussian kernel in order to obtain a uniform seeing corresponding to the worst seeing value. Also, an airmass correction has been applied during this phase. Tab. 5.2 shows a summary of the properties of the above-mentioned images.

5.4 Preliminary Analysis

5.4.1 Two-dimensional spectra

The first LDSS-3 spectrum of Mrk 783 was acquired on February 2017. The position of the slit has been chosen in order to be aligned with the axis of the radio emission discovered in Congiu et al. (2017c), since its purpose was to verify the presence of optical radio emission aligned with the radio structure.

This spectrum revealed, indeed, extended emission in all the strongest emission lines ([O III]λ5007 in particular, Fig. 5.2, panel a) on both sides of the AGN. The [O III]λ5007 line can be traced up to a distance of $\sim 25''$ from the nucleus of the galaxy, which corresponds to a projected distance of ~ 32 kpc. In this spectrum, the emission stops sharply, because of the presence of an interruption of the slit. For this reason, another spectrum of the source at the same PA has been acquired, taking care to position the galaxy in such a way to avoid the slit support.

The Hβ region of the new spectrum is shown in Fig. 5.2 (panel b). As expected, the emission is slightly more extended and it reaches $\sim 30''$ (~ 38 kpc) from the nucleus. It is interesting to notice that, in both spectra, the emission is not continu-

[2] `https://classic.sdss.org/dr7/`

ous but, moving from the AGN outward, it gets fainter and then it re-brights. One possibility for this behavior might be that the most extended emission is produced by a nearby source. From Fig. 5.1 it is possible to see that there actually is a faint source close to that position, source B (J1303+1624). J1303+1624 should have been outside the slit during the observations of both spectra, but it is possible that some imprecision during the pointing caused this source to fall inside it. This is the reason why this source was included in the TNG observations described in Sec. 5.4.3. However, if the whole emission belongs to the ENLR of Mrk 783 a projected size of ~ 38 kpc would make this ENLR one of the most extended observed so far at low redshift.

The spectrum in the panel c of Fig. 5.2 shows the Hβ region of the last LDSS-3 spectrum, acquired at PA = 90°. Extended emission can be observed, on both sides of the nucleus, also at this position angle. The size of the emission in this direction is smaller, but the [O III]λ5007 line can be traced up to a distance of ~ 17.5 arcsec (~ 23 kpc) from the nucleus. In this case, the emission is continuous. An interesting property that can be observed in panel c of Fig. 5.2 is that there seems to be a second continuum 1.5 arcsec west with respect to the AGN, that can be better appreciated in Fig. 5.3. These last figures show the distribution of light along the slit in a single dispersion element.

5.4.2 Morphology and color

The galaxy has been classified as a lenticular galaxy by Petrosian et al. (2007). However, a quick look analysis of the SDSS images (e.g. Fig. 5.4) revealed the presence of a faint extended structure on the east side of the nucleus, possibly a spiral arm or a tidal tail. Fig.5.5 shows the g, r and i-band images of Mrk 783 in units of surface intensity (counts cm^{-2} s^{-1}). Superimposed on the images there are contours of iso-intensity which starts from $3\sigma_{sky}$, where σ_{sky} is the RMS of the background. The images show that the faint structure observed in the RGB image is real, even though is barely over the 3σ detection limit.

Fig. 5.5 also shows that there seems to be a light excess ~ 1.5 arcsec west of the AGN, in the position corresponding to the second continuum observed in Fig. 5.2 and 5.3. This excess becomes more prominent moving towards redder wavelengths, i.e. the shape of the contours deviate from an ellipse more in the r and i images than in the g image.

Fig. 5.6 shows a $g-r$ image of the galaxy. The AGN has a blue color ($g-r \simeq -1$) while the other structure has a red color ($g-r \simeq 1$), confirming that the secondary structure is redder than the AGN. A $g-r$ color $\simeq 1$ is typical of stars with a temperature between 4000 and 5000 K i.e. K type stars (Fukugita et al., 2011). It is, therefore, possible that this light excess might be originated by an over-concentration of K stars. The images have not been corrected for Milky Way extinction, but according to the calibration of Schlafly & Finkbeiner (2011) it is of the order of 0.09 mag in the g-band and 0.07 mag in r-band, therefore it will not particularly influence these results.

The origin of this concentration is puzzling. A possibility is that this structure is the nucleus of a galaxy that merged with Mrk 783. In this scenario, the faint extended structure on the east side of the nucleus would be a tidal tail produced by

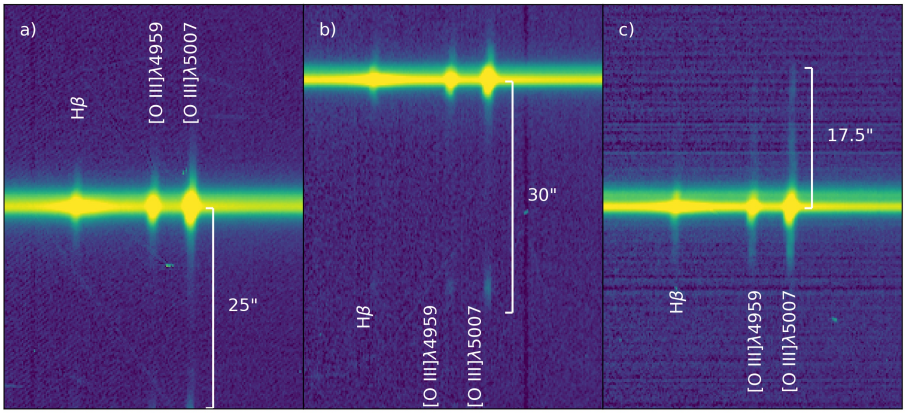

Figure 5.2: **Panel a)** Hβ region of February LDSS-3 spectrum at PA = 131°. It is possible to observe that all the three lines visible in this wavelength range (Hβ, [O III]λ4959 and [O III]λ5007) show extended emission that can be traced up to $\sim$ 25 arcsec from the nucleus of the galaxy in the lower part of the image. The emission ends sharply because of an interruption of the slit. A less extended emission is present also on the other side of the nucleus. In this spectrum, northwest is up and southeast is left. **Panel b)** Hβ region of June LDSS-3 spectrum at PA = 131°. The galaxy has been moved upward in the slit and the observed emission is slightly more extended, reaching $\sim$ 30 arcsec. The orientation of the spectrum is the same as in the previous panel. **Panel c)** Hβ region of June LDSS-3 spectrum at PA = 90°. Extended emission is observed on both sides of the nucleus also at this PA, with the upper part reaching $\sim$ 17.5 arcsec from the AGN. In this spectrum, west is up and east is down.

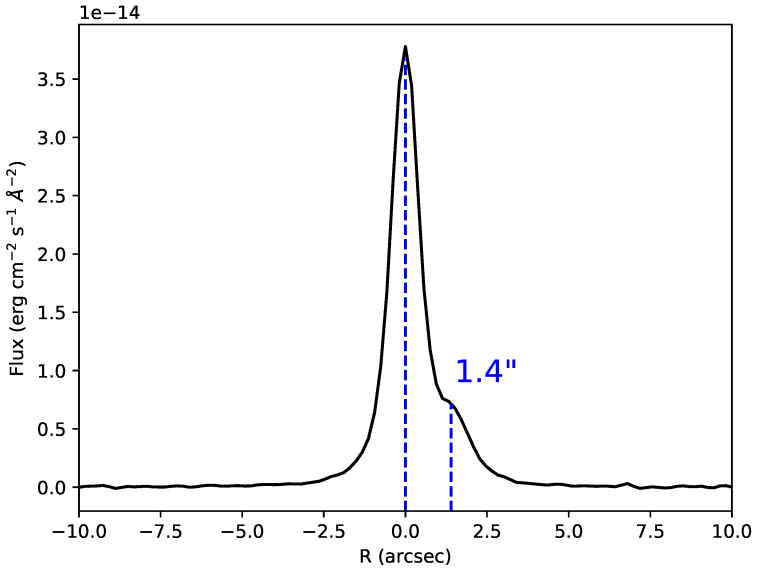

Figure 5.3: Flux distribution along the slit of the spectrum in the right panel of Fig. 5.2. A single dispersion element has been considered for this plot.

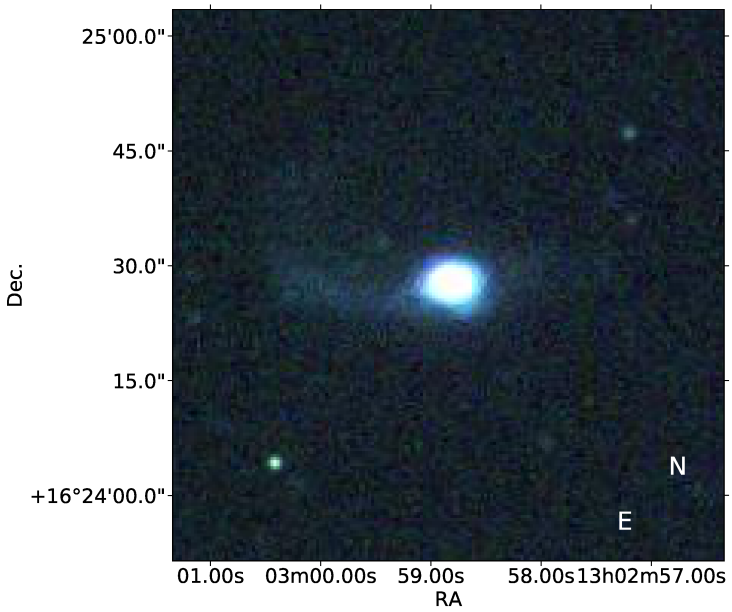

Figure 5.4: Left: RGB image created from the g, r and i SDSS images.

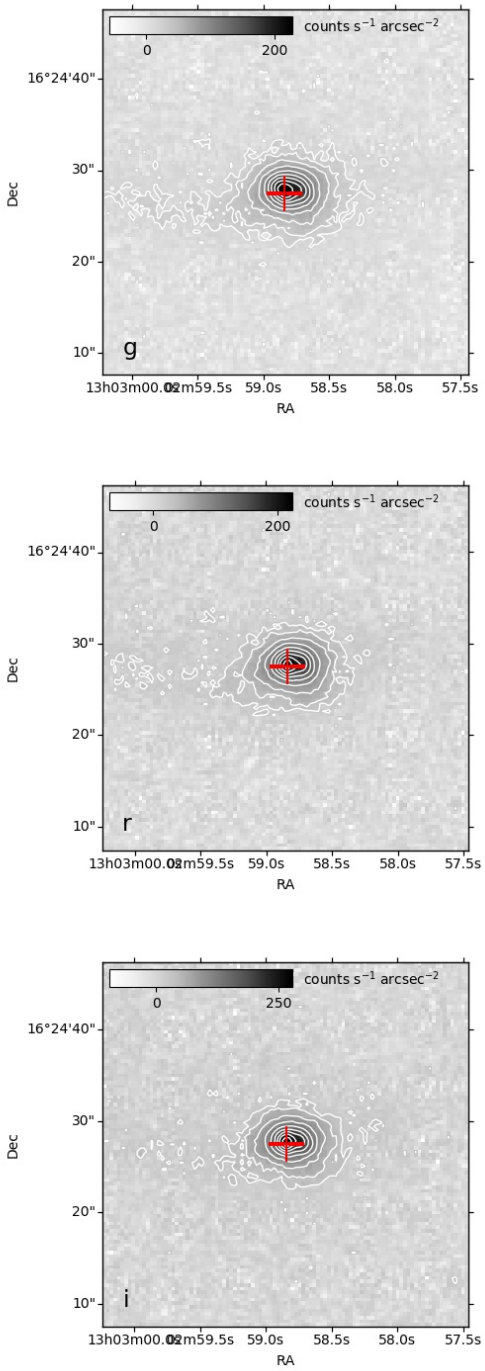

Figure 5.5: Left: SDSS g-band image of Mrk 783. **Center:** SDSS r-band image of Mrk 783. **Center:** SDSS i-band image of Mrk 783. Each image is in units of specific intensity (counts $\mathrm{cm}^{-2}\,\mathrm{s}^{-1}$). The contours are defined as $3(2^n)\sigma_{sky}$, where σ_{sky} is the RMS of the background and $n \geq 0$. The red cross marks the coordinates of the center of the galaxy as reported by the NED.

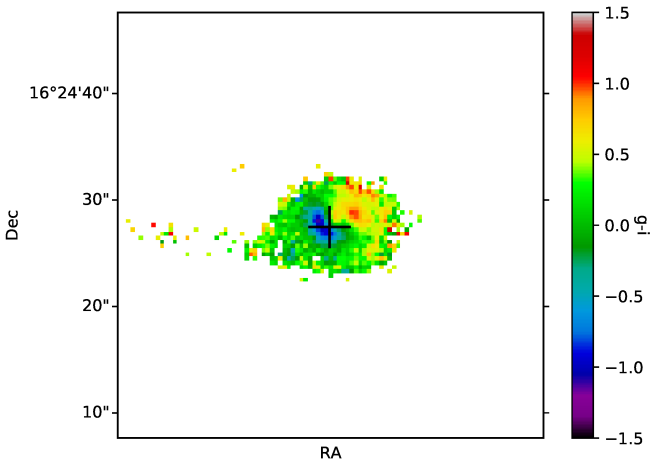

Figure 5.6: $g - r$ image of Mrk 783. The black cross marks the NED coordinates of the object. It is possible to see how the galaxy is sharply divided into two regions. On the left, the AGN has a negative color while the second point-like structure has a positive color. The difference in color between the two sides is ~ 2 mag.

the interaction. This will also explain the presence of a single extended structure. If the extended structure were a spiral arm, there should have been another similar arm on the other side of the galaxy, since the minimum number of spiral arms in a galaxy is 2 (D'Onghia, 2015). However, also the opposite situation is possible, where the stellar structure is the real nucleus of Mrk 783 and the AGN has been accreted as a result of the interaction.

Another possible scenario is that the supermassive black hole was kicked out of the galaxy nucleus during a merging episode. These events are rare but not impossible since such scenario has been predicted by numerical simulations and some candidates have already been discovered (for a review see Komossa, 2012). Considering the possibility of a merging event as a possible origin of the secondary structure, it should be noticed that the merging might have also been the trigger of the AGN activity (Hong et al., 2015).

An alternative possibility is that the stellar structure is a star-forming region. In this case, the red color of this region might be due to dust extinction, more than by the presence of old stars. The presence of star formation in Mrk 783 is strongly suggested by the red WISE color $W3 - W4 = 2.6$ and by the spectral energy distribution (SED) of the galaxy (Fig. 5.7). The SED has been fitted with an AGN template from Polletta et al. (2007) (the BQSO template in particular) and of a star-forming galaxy (M 82). FIRST and NVSS data, together with Congiu et al. (2017c) measurements have been used to constrain the synchrotron emission. The main result of the analysis is that the infrared region of the SED seems to be dominated by star formation. The estimated star formation rate is of $\sim 10 - 20\,\mathrm{M}_\odot\,\mathrm{yr}^{-1}$.

To discern between these scenarios is not an easy task. A detailed analysis of

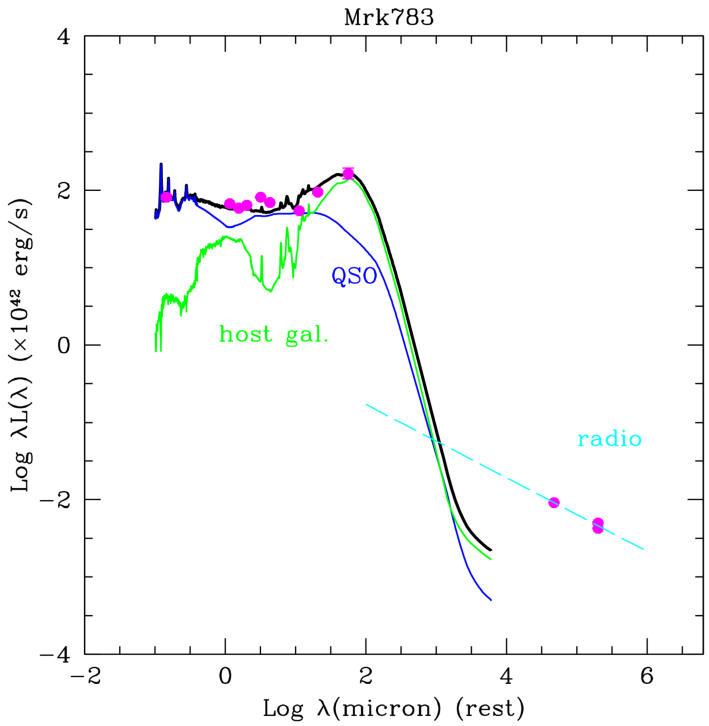

Figure 5.7: SED of Mrk 783 in the visible, infrared and radio band. The flux measurements have been recovered from the NED, with the exception of the 5 GHz flux that comes from Congiu et al. (2017c). The solid line represents the best fitting model, composed by an AGN template (BQSO template from Polletta et al. (2007) with $A(V) = 0.3$, in blue) and a starburst template (M 82, in green). The cyan dashed line is the power-law contribution of the jet.

the kinematics of the central regions of the galaxy might reveal where is located its center of mass. In such a way it will be possible to understand which one between the AGN and the secondary structure[3] is the real nucleus of the galaxy. The kinematics might also reveal if one of the two structure has been accreted in a merging event or if they both belong to the galaxy. In the first case the kinematics of the accreted structure should be disturbed with respect to the kinematics of the host galaxy itself, while in the second case there should not be any difference.

5.4.3 Environment

In the previous section, I discussed how the galaxy might have been merged with a companion. However, the probability of a merging event is higher if the merging galaxies are located in a group composed by multiple objects (Kampczyk et al., 2013). For this reason, I decided to investigate the vicinity of Mrk 783 to look for other objects that might be gravitationally connected to the target.

Mrk 783 seems quite isolated but there is at least one galaxy, J1302+1625 (source A in Fig. 5.1), that might be close enough. No redshift measurement is available for this object and for this reason the TNG spectrum has been acquired. During this observation the slit was positioned in order to observe also J1303+1624 (source B in Fig. 5.1) since it was close enough to the slit during the LDSS-3 observations to be related to the extended emission observed in panel a) and b) of Fig. 5.2 (see Sec. 5.4.1).

The distance of source J1302+1625 and J1303+1624 from the nucleus of Mrk 783 are ~ 73 arcsec and ~ 32 arcsec respectively, corresponding to a projected distance of ~ 100 and ~ 42 kpc at Mrk 783 redshift. Therefore, if their redshift is similar to that of Mrk 783 they would be close enough to be gravitationally connected. Unfortunately, as it has been mentioned in Sec. 5.3.1, the absolute wavelength calibration of the TNG spectrum is not reliable. However, part of the extended emission of Mrk 783 fell inside the slit during the observation and its spectrum can be used as a reference to estimate the redshift of the two sources (Fig. 5.1).

Both J1302+1625 and J1303+1624 has been detected. J1302+1625 spectrum shows a continuum emission and some emission lines ([O III]λ4959, [O III]λ5007, Hα). This is in agreement with the disk-like morphology observed in SDSS and AFOSC images. On the other hand, J1303+1624 shows a faint featureless continuum, in agreement with SDSS classification of the object as a star. Moreover, since the lines produced in Mrk 783 ENLR are clearly detected, if J1303+1624 were the origin of the most extended emission in panel a) and b) of Fig. 5.2 lines should have been detected also in this spectrum. This confirms that all the extended emission observed in Fig. 5.2 belongs to Mrk 783.

Fig. 5.8 shows the spectra of the three object. They all have been normalized at 5100 Å. Mrk 783 and J1302+1625 show the same emission lines at the same position. To have a precise measurement of the wavelength of the [O III]λ5007 line I fitted it in each object with a Gaussian function, using a Monte Carlo algorithm to evaluate the error on the position. The result is that the line in Mrk 783 is at 5347.6 ± 0.4 Å while in J1302+1625 is at 5348.3 ± 0.4 Å. The difference between the two wavelengths of the two line is ~ 0.7 Å (~ 50 km s^{-1}). This confirms that the

[3]For the sake of simplicity, I will call this structure the secondary nucleus from now on.

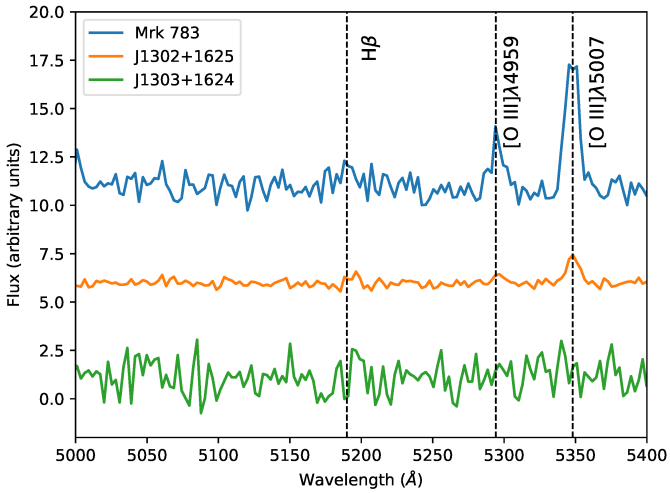

Figure 5.8: Hβ region of the TNG spectra. In blue is shown the spectrum of Mrk 783, in orange the spectrum of J1302+1625 and in green the spectrum of J1303+1624. The vertical dashed lines show the position of the principal emission lines observed in this wavelength range. I assumed as a reference the position of Mrk 783 lines. All the spectra have been normalized at 5100 Å and the blue and orange spectra have been shifted for the sake of clarity. It is possible to see that the emission lines of Mrk 783 and source A are well aligned, while source B does not show any feature in this wavelength range.

Table 5.3: Main properties of the companion sources of Mrk 783.

Source	Name	Type	RA (hh:mm:ss)	Dec (dd:mm:ss)	g (mag)	Distance (arcsec)
A	J1302+1625	Galaxy	13:02:57.20	+16:25:37.1	18.7	72.7
B	J1303+1624	Star	13:03:00.42	+16:24:04.3	21.70	32.3

From left to right: (1) Source name in Fig. 5.1, (2) name of the source, (3) SDSS classification of the source, (4) right ascension, (5) declination, (6) g-band magnitude measured from AFOSC image, (7) distance in arcsecond from the AGN.

vicinity of the two objects is not just a projection effect. Tab. 5.3 shows the main properties of J1302+1625 and J1303+1624.

The observation of another galaxy at a distance of 100 kpc from Mrk 783 confirms that the object is part of a (small) group of galaxies. Actually, the two objects are close enough that they might be already interacting, even though the undisturbed morphology of J1302+1625 suggests that the interaction is still in the early phases.

Since the probability of merging are higher in groups (Kampczyk et al., 2013) the scenario described above where the properties of Mrk 783 are the result of a merging event is even more plausible now, even though a final confirmation will require better data and a more detailed analysis.

5.5 Spectral Analysis

5.5.1 Spectra Extraction and Line Fitting

To better analyze the properties of the LDSS-3 spectra as a function of the distance from the AGN, I divided each two-dimensional spectra in 1 arcsec bins and I extracted one-dimensional spectra from each one of them showing emission lines. All the spectra have been corrected for galactic extinction using the standard CCM extinction law (Cardelli et al., 1989), with $R = 3.1$ and the absorption in the V band $A(V)$ provided by the NASA/IPAC Extragalactic Database[4] (NED) and extracted from Schlafly & Finkbeiner (2011). A correction for telluric absorption has also been applied, since Hα falls close to one of the major telluric absorption.

An accurate measurement of the emission line flux, especially for the Balmer lines, usually requires a subtraction of the underlying stellar continuum, since stellar absorption might significantly contribute to the line flux. This process is not needed in the nucleus of type 1 AGN since the AGN continuum dominates over the stellar continuum and the influence of stellar absorption is negligible, as it is clearly shown in Fig. 5.9. No absorption lines are seen in this region, and the continuum shape is typical of AGN, with the blue end brighter than the red end. On the other hand, outside the nucleus the stellar emission is the dominant continuum source and an accurate subtraction should be performed.

However, to obtain reliable results this procedure must be performed on high signal-to-noise ratio (SNR) spectra. Since the SNR of the continuum is low in

[4]https://ned.ipac.caltech.edu/

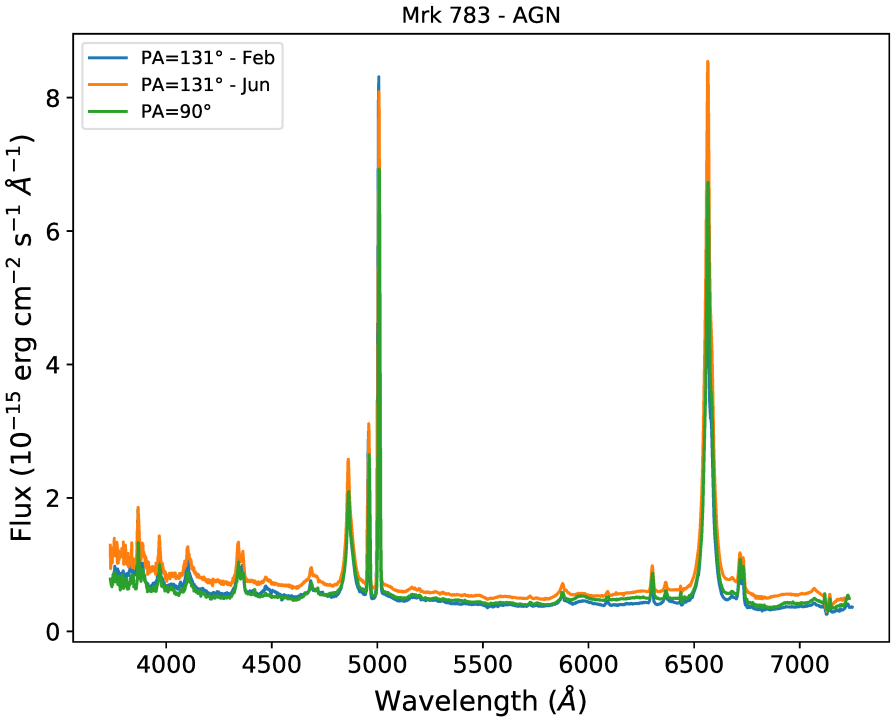

Figure 5.9: One-dimensional spectrum of the nucleus of Mrk 783 extracted from all the three LDSS-3 spectra.

most of the bin extracted from the LDSS-3 spectra uncontaminated by the AGN (SNR$<$ 10), I decided to not perform the stellar continuum subtraction.

After the extinction correction, I measured the flux of the most prominent emission lines of all spectra. I used a Monte Carlo algorithm to measure the flux, wavelength and dispersion of each emission line with errors. Since the resolution of the instrument is relatively low ($\sim$ 500 km s^{-1}) most of the line are not resolved and they can be fitted with a single Gaussian function. Close to the AGN, where the Balmer lines start to get broad, I used two or three Gaussian components to fit them. In these cases, I used one Gaussian to fit the narrow component and one or two Gaussians for the broad component.

During the line fitting procedure, I had to pay particular attention to the Hα and [N II] doublet, since they are very close. To obtain a better result I fitted the three lines simultaneously using one component for each line of the [N II] doublet and one, two or three components for Hα, according to the profile shape. To reduce the number of free parameters I constrained the narrow components to have all the same width. In the very nucleus of the galaxy, I also had to fit the [S II] doublet simultaneously with the Hα group, because the broad components of Hα were so large to be partially blended with the doublet. Also, in this case, I reduced the number of free parameters forcing the width of the narrow lines to be the same. Fig. 5.10 shows an example of the deblending process in the nucleus of Mrk 783.

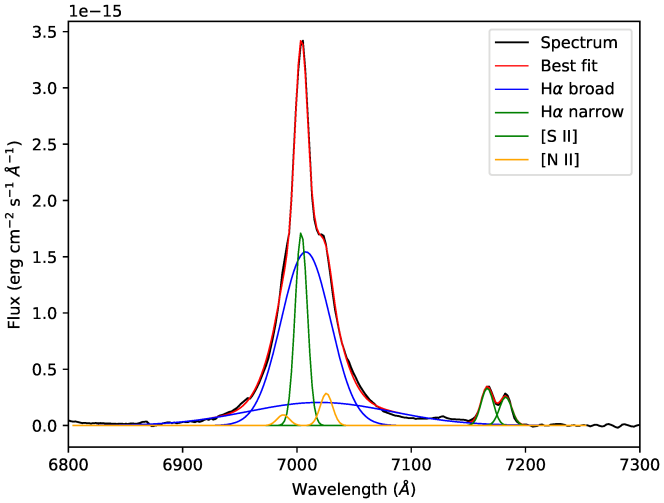

Figure 5.10: Example of the fit of the Hα group in the nucleus of Mrk 783. In particular this is the one-dimensional spectrum of the nucleus extracted from February LDSS-3 spectrum.

5.5.2 The nuclear spectrum

All the three spectra of Mrk 783 acquired with the LDSS-3 spectrograph have been centered on the AGN. There are some small differences between the three spectra, probably because of the different conditions of the sky during the observations. For these reasons, the spectra have not been combined to produce a single spectrum of the nucleus but they will be examined separately in the following sections. Fig. 5.9 shows the AGN spectrum extracted from each one of the LDSS-3 spectra. There are some small differences between the three spectra, probably due to the different sky condition or by a small error in positioning the AGN inside the slit. However, to check the classification of the AGN as a NLS1 I will only consider one of the spectra. Since the spectra are very similar and there is not any advantage in choosing one over the others, in this section I will always refer to the February spectrum at PA = 131°.

As stated in Sec. 5.1, the spectrum of an AGN must satisfy three requirements to be classified as a NLS1: 1) $FWHM(\mathrm{H}\beta) < 2000\,\mathrm{km\ s^{-1}}$, 2) [O III]$\lambda$5007/H$\beta < 3$ (Osterbrock & Pogge, 1985) and 3) Strong Fe II multiplets or presence of [Fe VII]λ6087 and [Fe X]λ6375 lines (Goodrich, 1989). Mrk 783 shows a $FWHM(\mathrm{H}\beta) \sim 1500\,\mathrm{km\ s^{-1}}$ and a flux [O III]λ5007/H$\beta \sim 1.5$, that are well below Osterbrock & Pogge (1985) limits. On the other hand, the object shows little Fe II emission (there is only some trace of the 5190 Å multiplet), but it shows both the [Fe VII]λ6087 line and the [Fe X]λ6375 (blended with the [O I]λ6363 line) and other high ionization Fe lines (Fig. 5.11). Therefore the classification of Mrk 783 as a NLS1 can be confirmed.

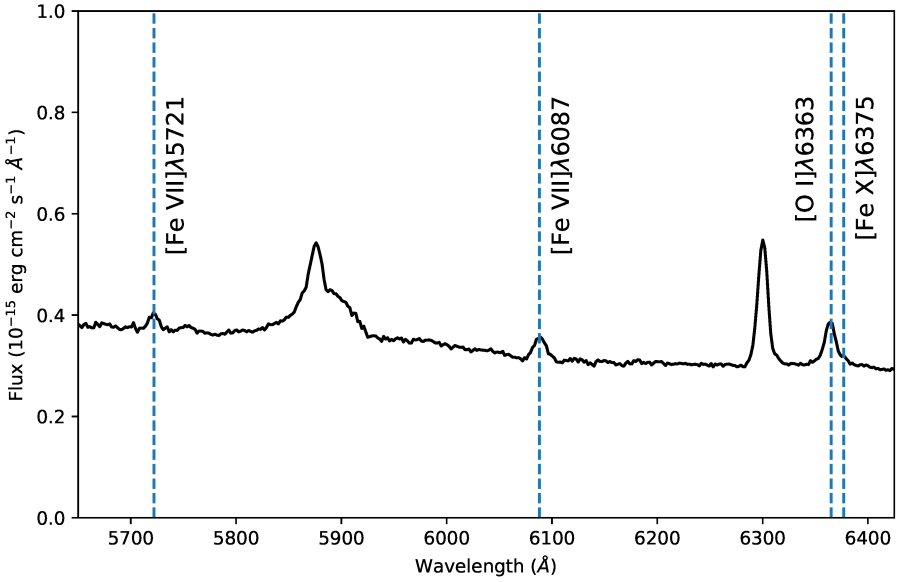

Figure 5.11: February LDSS spectrum between 5650 and 6425 Å. The dashed lines show the position of [Fe VII]λ5721, [Fe VII]λ6087, [Fe X]λ6375,[O I]λ6363.

5.5.3 Kinematics

From the position of the lines measured from the spectra, I was able to produce, for each observation at each PA, a velocity vs radius plot. In almost all the one-dimensional spectra it has been possible to measure the velocity of both the narrow Hα component and [O III]λ5007 and the results of the measurements are shown in Fig. 5.12. Since the inclination of the galaxy is not known, it is not possible to correct velocities and distances, and all the values reported in this work are projected quantities.

From these plots, it is possible to see that the kinematics of the gas seems significantly disturbed at all distances from the nucleus. In particular, at PA = 90° the gas velocity decreases of $> 100\,\mathrm{km\ s^{-1}}$ between $r \simeq 7\,\mathrm{kpc}$ and $r \simeq 15\,\mathrm{kpc}$. Then it starts to rise again up to velocities similar to those before the drop. A similar feature can be observed also on the other side of the rotation curve, even though the drop and rise are significantly faster. On the other hand, the velocity curves at PA = 131° are flatter with respect to the velocity curve of the other position angle, but there are faster variations. Nevertheless, the main trend seems to indicate the presence of rotation of the gas, with a $\Delta v \simeq 200\,\mathrm{km\ s^{-1}}$ at PA = 131° and PA $\Delta v \simeq 300\,\mathrm{km\ s^{-1}}$ at PA = 90°. The difference of amplitude of the velocity curve is probably due to the inclination of the galaxy. The spectrum at PA = 90° is probably closer to the major axis of the galaxy with respect to the spectra at PA = 131°.

In general, the kinematics of Hα and [O III]λ5007 is quite similar, most of the differences between the kinematics of the two lines are inside the error bars. In the top and center plots is evident the absence of emission between the main body of

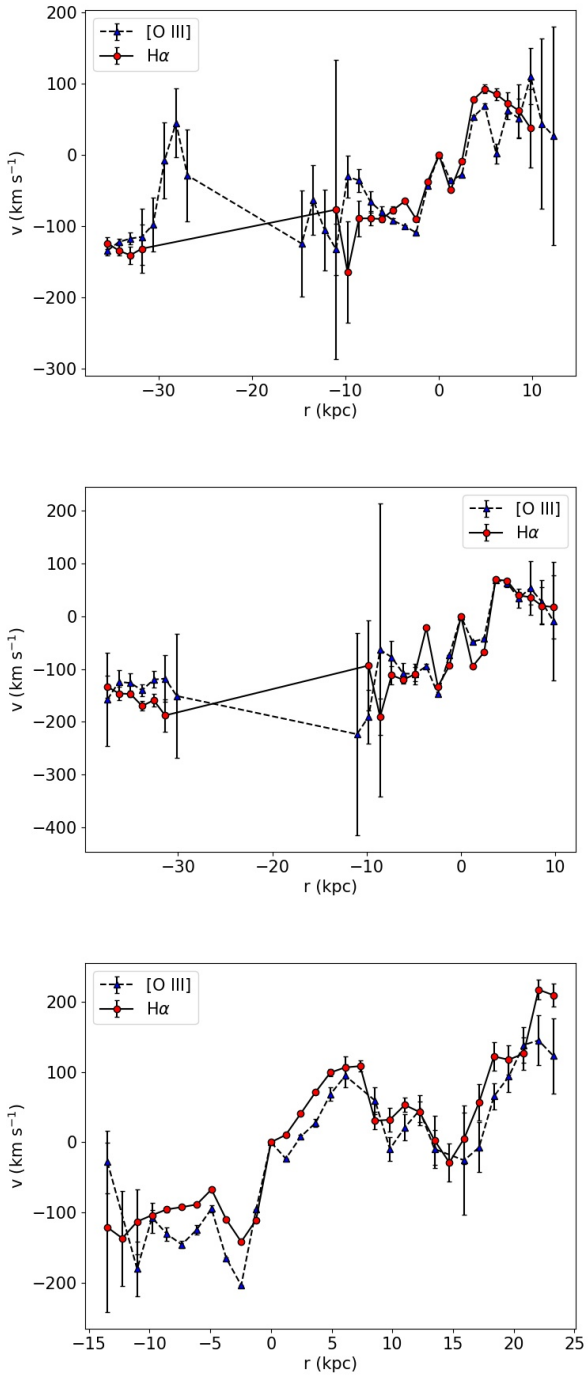

Figure 5.12: Velocity vs distance from the nucleus maps for, from top to bottom: February PA = 131° spectrum, June PA = 131° spectrum and June PA = 90° spectrum. Blue triangles represent [O III]λ5007 velocities, the red dots are Hα velocities. The error bars represent 1σ errors. The absence of error bars means that they are smaller than the size of the point. The velocity of the central spectrum has been considered as the systemic velocity of the galaxy.

the galaxy and the most extended region of the emission, which was already visible in Fig. 5.9.

No peculiar features are observed in the position of the secondary nucleus of Sec. 5.4.2, so it is not possible to determine which one between the AGN and the secondary nucleus sits in the dynamical center of the galaxy. Without integral field data or narrow filter images of the source to map the gas distribution, it is difficult to have a better insight on the kinematical properties of this object.

A merging event might be able to explain the disturbed kinematics. The kinematical signature of an event of this type might be visible up to a time of 0.2−0.4 GHz from the event (Hung et al., 2016), therefore the merger must be relatively recent if we can still observe its effect on the gas kinematics.

Also, the presence of a relativistic jet digging in the ISM might be able to influence the gas kinematics. The radio emission discovered by Congiu et al. (2017c) means that a jet might have been active in this galaxy. The structure is aligned with PA = 131°, but there are no traces of radio emission at PA = 90° where the largest features are observed. Moreover, the extension of this structure is of the order of 10 kpc, so it cannot be responsible for features at larger distances from the nucleus. Therefore, if a relativistic jet has been active (or is still active) in this object it could have produced the features observed in the inner region at PA = 131°, but it cannot be responsible for what is happening at PA = 90°.

Up until now, the gas kinematics is, hence, another piece of evidence in support of a merging event. If this is the correct scenario, the kinematics also helped constraining the age of the event, limiting the maximum age of the merging at 0.4 Gyr.

5.5.4 Line ratios

The extended emission has been considered, so far, the ENLR produced by the AGN. However, in Sec. 5.4.2 it has been discussed that the SED of Mrk 783 seems to have an infrared excess produced by a star formation rate of $\sim 10\,M_\odot\,yr^{-1}$. So, it is possible that part of the gas is ionized by young stars and not by the AGN.

To test this possibility it is possible to use the so-called *diagnostic diagrams*, diagrams comparing ratios between strong forbidden lines and nearby narrow Balmer lines (Baldwin et al., 1981; Veilleux & Osterbrock, 1987). In particular, there are three different diagnostic diagrams that are used to this aim: log[O III]λ5007/Hβ vs log[N II]λ6584/Hα, log[O III]λ5007/Hβ vs log[O I]λ6300/Hα and log[O III]λ5007/Hβ vs log[S II]$\lambda\lambda$6717, 6731/Hα.

In order to better classify the emission, I tried to produce all three diagrams for each spectrum. However, while Hα and [O III]λ5007 have been detected in the vast majority of the spectra, all the other lines are fainter and they are often missing. For example, in Fig. 5.13 it is possible to see the flux distribution of some of the emission lines used in the diagnostic diagrams. Lines such as Hβ and [N II]λ6584 are detected only in the inner part of the galaxy. The main consequence of this is that it will not be possible to investigate with diagnostic diagrams the ionizing source of the most extended structures.

Fig. 5.14 shows the aforementioned diagnostic diagrams for the three LDSS-3 spectra. The plots show that the main ionization mechanism of the gas is photoionization by the AGN. So, at least for the inner $\sim$ 8 kpc the extended emis-

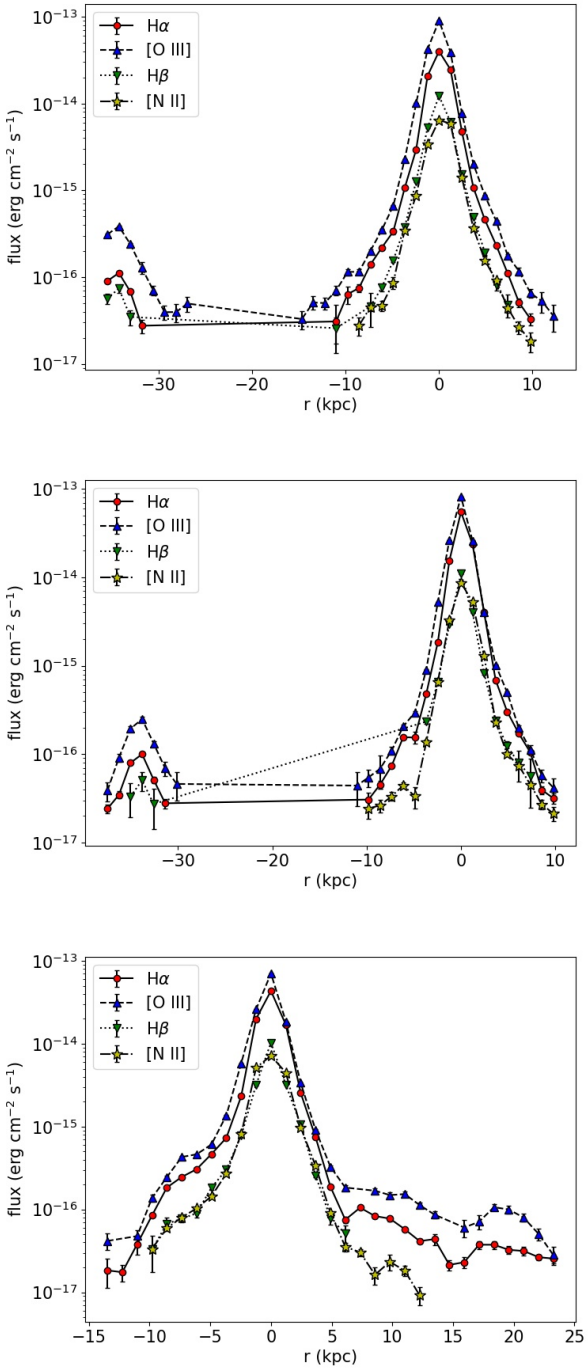

Figure 5.13: Line flux vs distance from the nucleus plot for each LDSS-3 spectrum. From top to bottom: February PA = 131°, June PA = 131° and June PA = 90°. The error bars represent 1σ errors. Where they are not present they are smaller than the size of the corresponding point.

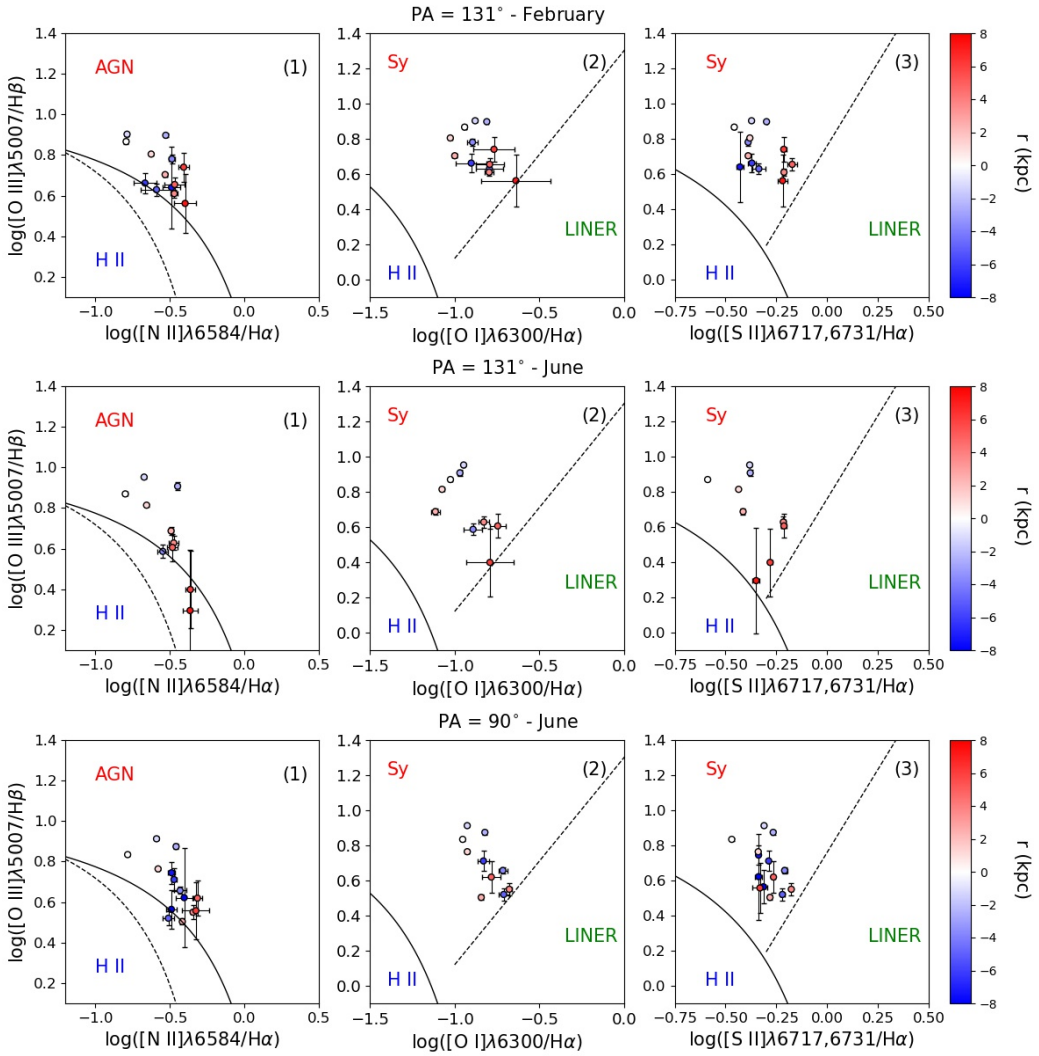

Figure 5.14: Diagnostic diagrams for the LDSS-3 spectra. From top to bottom February PA = 131°, June PA = 131° and June PA = 90°. For each spectrum, the left panel is the log[O III]λ5007/Hβ vs log[N II]λ6584/Hα diagram, the central panel is the log[O III]λ5007/Hβ vs log[O I]λ6300/Hα diagram while the right panel is the log[O III]λ5007/Hβ vs log[S II]$\lambda\lambda$6717, 6731/Hα. The color bar shows, for each point, the distance from the nucleus of the corresponding spectrum. In each panel, the solid curve is the Kewley et al. (2001) relation dividing AGN from star-forming regions, the dashed curve is the Kauffmann et al. (2003) line for pure star formation while the dashed lines are the Kewley et al. (2006) relations dividing Seyfert galaxies from LINERs. The error bars represent 1σ errors on the line ratios. Where they are absent, the dimension of the bars is smaller than the size of the corresponding point.

sion actually is the ENLR of the AGN. However, there are some points in the log[O III]λ5007/Hβ vs log[N II]λ6584/Hα diagram that are located in the region between Kewley et al. (2001) and Kauffmann et al. (2003) lines. This means that there might be some star-forming regions contributing to the ionization of the ISM. It is interesting to notice that the position of the points in the diagnostic diagrams of the two PA = 131° spectra are quite different, meaning that probably they are observing slightly different regions because of a slightly different alignment.

In the analysis of these plots, it must be considered that the subtraction of the stellar continuum has not been performed. This might produce an overestimate of the diagnostic ratios, at least in some spectra. Therefore, it is possible that the subtraction of the stellar continuum might move some other points in the mixed region or shift some of the points already in this region into the H II one. However, the global results should not change much, and the AGN is the main ionizing source of the gas, at least up to a distance of the order of ~ 10 kpc.

From Fig. 5.13 it is possible to see that, at PA = 131° the limiting lines are the low ionization forbidden lines ([N II], [S II] and [O I]) while at PA = 90° is Hβ the missing line at high distances from the nucleus. Therefore, it is still possible to use the log[O III]λ5007/Hβ ratio to estimate the ionizing source of some of the most distant regions at PA = 131° and log[N II]λ6584/Hα in the remaining spectrum. A log[O III]λ5007/H$\beta > 0.6$ guarantees a classification as AGN in two out of three diagnostic diagrams while log[N II]λ6584/Hα should be greater than -0.5 to tentatively classify the region at least as a mixed ionization zone in the left panels of Fig. 5.13. In order to classify a region as ionized by the AGN with only the log[N II]λ6584/Hα ratio, the measured value should be greater than -0.1.

Fig. 5.15 shows the above-mentioned plots. From the top and middle panels, it is possible to see that most of the regions at PA = 131° are ionized by the AGN also at high distances from the nucleus, since most of the points are above the log[O III]λ5007/H$\beta = 0.6$ limit. On the other hand, in the bottom panel no points fell above the log[N II]λ6584/H$\alpha = -0.1$ limit, and most of them are in the section of the plot enclosed between the two limits. However, it is clear from the diagnostic diagrams in Fig. 5.14 that low [N II]λ6584/Hα values do not mean that the region cannot be ionized by the AGN, but only that this ratio is not sufficient to realistically estimate the ionizing source of the gas.

5.6 Discussion

The data analyzed in this work have been acquired as a follow up of the source after the discovery of a peculiar kiloparsec-scale radio emission region (KSR) (Congiu et al., 2017c). The main question is, therefore, if there is a connection between the KSR and the ENLR of Mrk 783. An important clue of a connection is that the most extended part of the ENLR has been found perfectly aligned with the most extended lobe of the radio emission. According to Wilson & Tsvetanov (1994), it seems that the relativistic jet launched by the AGN is able to clear the path of the ionizing radiation in the ISM. This might be what happened in Mrk 783. Even though the radio emission is a relic, as suggested in (Congiu et al., 2017c), the original radio jet might have been able to clear the path for the radiation, allowing it to reach larger distances with respect to what happens in other ENLR. However, the size of the KSR

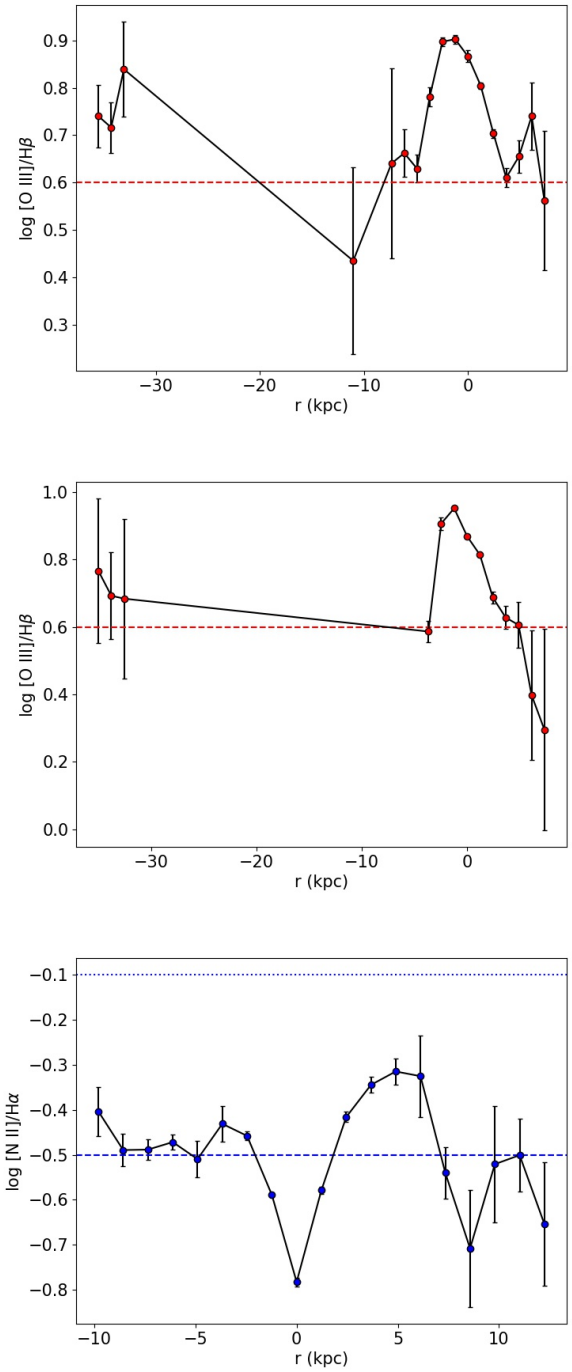

Figure 5.15: **Top:** log[O III]λ5007/Hβ vs distance from the nucleus plot for February PA = 131° spectrum. The dashed line represents the 0.6 limit. **Middle:** same plot as the previous panel for June PA = 131° spectrum. **Bottom:** log[N II]λ6584/Hα plot for June PA = 90° spectrum. In this plot, the dashed line represents the −0.5 limit for mixed ionization and the dotted line is the −0.1 limit for AGN ionization. As in the diagnostic diagrams, the error bars represent 1σ error on the line ratios. Absent bars means that they are smaller than the size of the point.

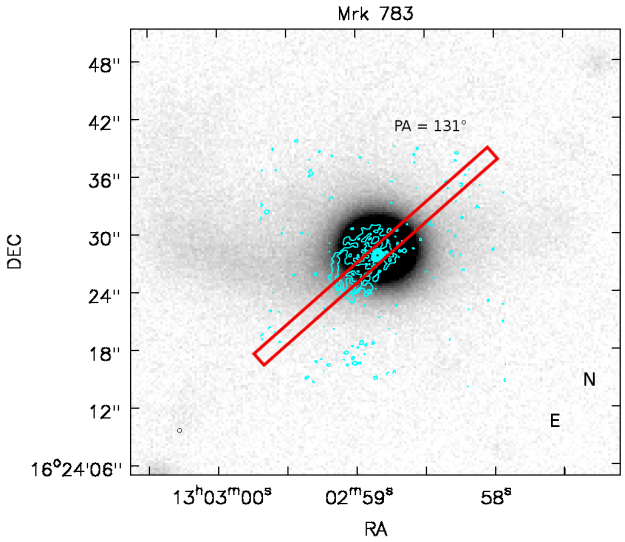

Figure 5.16: VLA 5 GHz contours from the natural weighted image of Congiu et al. (2017c) superimposed to the Asiago g band image of Mrk 783. The position of the slit during LDSS-3 observations at PA = 131° is shown.

is less than half the extension of the ENLR at the same position angle. Fig 5.16 shows how the bulk of the radio emission is located inside the nucleus of the galaxy, even though the jet might have been able to dig in the densest part of the ISM. Fig 5.16 also shows how the emission on the north-west side of the nucleus is not visible in the natural weighted image, in agreement with the fact that the optical emission in that region is less extended. On the other hand, no particularly extended radio emission is observed at PA = 90°, while the ENLR there reaches a size of 17.5 arcsec. Since the morphology of the ENLR is not known, it is not possible to definitively confirm that the axes of the two extended regions are aligned. Narrow-band images or integral field spectra would be necessary to investigate this topic.

Besides the relation with the radio emission, the data analyzed in this work confirmed that Mrk 783 is a very peculiar object. Firstly, the ENLR observed in this source, with a maximum size of ~ 38 kpc, is one of the largest discovered so far in the nearby universe and it is located in a Type 1 object, which are believed to host smaller ENLR (Schmitt et al., 2003b) with respect to Type 2 objects. There are a few sources with similar ENLR sizes UGC 7342 and NGC 5972 (37 and 33 kpc respectively Keel et al., 2012) but ENLRs larger than 30 kpc are usually observed only in objects at $z > 0.1$ (e.g. Stockton & MacKenty, 1987; Humphrey et al., 2010; Sun et al., 2018).

Both UGC 7342 and NGC 5972 show a disturbed morphology and UGC 7342 is an ongoing merger. Since the gravitational interaction produced during a merger influences the gas distribution, it is possible that it can create the conditions needed to produced larger ENLR than in stable systems.

The analyzed data show several properties of Mrk 783 suggesting that it recently merged with another object. The extended structure observed in the SDSS

and AFOSC images resemble the tidal tails observed in interacting systems like the Antennae galaxies. A secondary nucleus is observed and in Sec. 5.4.2 several scenario for its origin has been analyzed and most of them involve a merging episode. Finally, the complex kinematics shown in Fig. 5.12 might be a consequence of the merging event, meaning that the episode happened no more than $\sim 0.4\,\mathrm{Gyr}$ ago, which is the limit after which the kinematical signature of a merging should be no longer observable. The spectral and spatial resolution of the data are not high enough neither to detect multiple kinematical components in a single region nor to investigate where is located the dynamical center of the galaxy, to identify which one between the AGN and the secondary nucleus is the real nucleus of the galaxy. However, there are several hints suggesting that Mrk 783 might have merged with a companion galaxy and the merging event could be the reason of the large extension of the ENLR.

In support of the merging hypothesis, there is also the discovery of the companion galaxy J1302+1625 $\sim 100\,\mathrm{kpc}$ away from the nucleus of Mrk 783 which proves that Mrk 783 is not an isolated object. The two galaxies are also close enough that they might be in the early phases of interaction.

It might also be possible that the merging event that produced the disturbed morphology of the object is also responsible for the ignition of the AGN. Merging events are now widely accepted as one of the few mechanisms that are able to bring gas close to the supermassive black hole of a galaxy, supplying it of the gas needed for the accretion (Sanders et al., 1988; Hong et al., 2015). Moreover, according to Mathur (2000), NLS1 resides in rejuvenated galaxies, that is galaxies where new gas has been accreted following a galaxy-galaxy merging.

The morphology of Mrk 783 ENLR, instead, is still unknown. The orientation of the cone and the gas distribution cannot be determined without, at least, a narrow band image of the [O III]λ5007 line emitted by the gas. One of the few things that can be observed from the spectra is that in each long slit spectra the emission is extended on both sides of the nucleus, but one side is always more extended than the other. The typical shape of the ENLR is that of a bi-cone (Pogge, 1988; Schmitt et al., 1994; Fischer et al., 2013) and usually, because of its inclination with respect to the galaxy disk, one of the sides is more extended than the other because of extinction due to the dust present in the disk. The light of the cone beyond the disk must cross a larger amount of gas and dust than the other cone, and it often results shorter (e.g. NGC 5643, Simpson et al., 1997) or, in some cases, absent (Wilson, 1996).

From the PA of the spectra, it is possible to give a rough estimate of the opening angle of the ionization cones. Assuming that the more extended part of the spectra at PA = 131° and PA = 90° belongs to the same cone, it is possible to estimate a minimum opening angle of $\sim 139°$, which is quite large but not outside the possible values found by He et al. (2018). On the other hand, if the more extended regions are part of opposite cones, the minimum opening angle is reduced to 41°.

Fig. 5.2 shows that the extended emission at PA = 131° is not continuous but it seems that the most extended emitting region is separated from the main galaxy. From the images it is not clear the nature of this emitting region, it can be both a single cloud or part of a faint tidal tail. A peculiar property of this region is the absence of emission lines of low ionization ions ([N II], [S II]), even though the SNR

of some of the extracted spectra is high enough for them to be detected. This might be an indication of the very high ionization of the gas in this particular region.

5.7 Concluding remarks

In this work, I analyzed new optical data of the NLS1 galaxy Mrk 783. The object shows an extended narrow line region with a maximum extension of $\sim 38\,\mathrm{kpc}$ projected. The position angle of the maximum extension of the ENLR corresponds to the position angle of the maximum extension of the KSR discovered by Congiu et al. (2017c). Diagnostic diagrams and other line ratios confirm that the ionizing source of the gas in most of the regions analyzed is the AGN itself.

The galaxy also shows peculiar spectral properties that require new data and a dedicated analysis to be properly studied. Its morphology is disturbed and a secondary nucleus is observed, probably the consequence of a quite recent merging, as suggested by the complex rotation curves observed from Hα and [O III]λ5007.

The object, therefore, is one of the most interesting AGN with ENLR discovered so far. Unfortunately, the data gathered up until now are insufficient to have a complete picture of the properties of Mrk 783. Narrow band images and integral field spectroscopy will be fundamental resources to improve our knowledge on this object. Understanding the relationship between the ENLR and the radio emission, the merging events and all the other properties of this galaxy will be of the uttermost importance to shed light on the feedback processes between the AGN and its host.

A wider study to detect and characterize other similar objects will be fundamental to understand if Mrk 783 is only a "lucky case" and what is its position in the class of NLS1 and AGN in general.

CONCLUSIONS

During my PhD, I investigated several aspects of the physics of the ENLR in nearby AGN. I used several techniques and observations at optical and radio wavelengths to have a better insight into the processes characterizing these regions.

In particular, my work has been focused on the study of three peculiar objects, IC 5063, NGC 7212 and Mrk 783. The first two were objects with a known ENLR while the ENLR of Mrk 783 was discovered as a consequence of one of the side projects I was working on during this three year period.

During my PhD I chose to study in details only a few objects instead that a large sample. The reasons for this were three: 1) even though the number of ENLR known is slowly increasing, up until now there are only a handful of objects with an ENLR at low redshift with respect to the number of AGN known, 2) the nature of the ENLR itself make the study of such objects extremely difficult, 3) there are only few data with the sufficient quality available. The fact that the ENLR is extended and resolved and that there are not two similar ENLRs make it extremely difficult to observe and analyze a large sample of this structures. Moreover, only a deep and dedicated analysis can discover the secrets beyond each one of these sources.

All the three galaxies I analyzed are characterized by extended radio emission. While this characteristic was well known for IC 5063 and NGC 7212, I discovered the KSR of Mrk 783 analyzing the data of a recent JVLA survey of NLS1 galaxies (see Ch. 4). This kind of relation between radio emission and ENLR has already been observed several times (e.g. Wilson & Tsvetanov, 1994; Schmitt et al., 2003a,b) and it is in agreement with the hypothesis that ENLR and relativistic jets (often the source of the radio emission) are connected (Wilson & Tsvetanov, 1994). A property suggesting that this relation might actually be true is the fact that at least two objects (IC 5063 and NGC 7212) show hints of the presence of shocks in the interstellar medium, which are often produced by the interaction of the jet with the galactic ISM. Mrk 783 data were not suitable to perform this kind of analysis.

Another important discovery I made about IC 5063 is that its ionization parameter depends on the velocity of the gas, which is proof that the ENLR of this object has a hollow bi-conical shape. This discovery has not been repeated in NGC 7212 and a similar study has not been possible for Mrk 783, because of the low resolution of the spectra and of the low SNR around the [O II]$\lambda\lambda$3726, 3729 doublet needed to study the ionization parameter.

On the other hand, the huge size of Mrk 783 ENLR is one of the main results of my work. With a maximum extension of $\sim$ 38 kpc this ENLR is one of the largest ENLR observed at low redshift. Mrk 783 shows a disturbed morphology and kinematics probably caused by a quite recent merging event. Since other two galaxies showing similar extensions (UGC 7342 and NGC 5972 Keel et al., 2012)

also shows evidence of recent merging, it is possible that the size of the ENLR is connected to the merging event. However, NGC 7212 that is in interaction with its companion galaxies does not show a particularly large ENLR (Cracco et al., 2011), therefore the relation between ENLR and interaction between galaxies deserves a more detailed investigation.

In this work, I also discovered the limit of traditional techniques in studying this kind of extended objects. Since most of the light produced in the ENLR is concentrated on narrow emission lines (in particular [O III]λ5007), these structures are difficult to detect in normal broad band images (e.g. Sun et al., 2018) while long slit spectra are more sensitive to line emission, but they lack the 2D spatial information that is fundamental to characterize the morphology and other properties of ENLRs. However, while instruments with narrow-band filters are becoming rarer and rarer, new efficient integral field spectrographs are becoming available to the astronomical community opening a new range of possibilities to study optical extended emission in nearby AGN.

On the other hand, I confirmed that extended radio emission can be used as a tracer of extended optical emission and this property should be exploited to search for new ENLRs. New public high resolution sky surveys such as the VLASS (VLA Sky Survey Hales, 2013), the LoTSS (LOFAR two meter sky survey Shimwell et al., 2017), the GLEAM (GaLactic and Extragalactic All-sky MWA Survey Hurley-Walker et al., 2017), as well as dedicated surveys will increase the number of known KSR in AGN that can be used to look for optical ENLRs. A detailed study of these new sample of ENLRs will be fundamental to finally discover how the AGN and its host galaxy interact and live together.

ACKNOWLEDGMENT

This work includes data gathered with the 6.5-m Magellan Telescopes located at Las Campanas Observatory, Chile. The STARLIGHT project is supported by the Brazilian agencies CNPq, CAPES and FAPESP and by the France–Brazi CAPES/-Cofecub program. This research has made use of the NASA/IPAC Extragalactic Database (NED) which is operated by the Jet Propulsion Laboratory, California Institute of Technology, under contract with the National Aeronautics and Space Administration. This study is based on observations made with the NASA/ESA Hubble Space Telescope and obtained from the Hubble Legacy Archive, which is a collaboration between the Space Telescope Science Institute (STScI/NASA), the Space Telescope European Coordinating Facility (ST-ECF/ESA) and the Canadian Astronomy Data Centre (CADC/NRC/CSA). The National Radio Astronomy Observatory is a facility of the National Science Foundation operated under cooperative agreement by Associated Universities, Inc. This research has made use of the NASA/IPAC Infrared Science Archive, which is operated by the Jet Propulsion Laboratory, California Institute of Technology, under contract with the National Aeronautics and Space Administration. This publication makes use of data products from the Wide-field Infrared Survey Explorer, which is a joint project of the University of California, Los Angeles, and the Jet Propulsion Laboratory/California Institute of Technology, funded by the National Aeronautics and Space Administration. GMRT is run by the National Centre for Radio Astrophysics of the Tata Institute of Fundamental Research. Funding for the Sloan Digital Sky Survey has been provided by the Alfred P. Sloan Foundation and the US Department of Energy Office of Science. The SDSS web site is http://www.sdss.org. SDSS-III is managed by the Astrophysical Research Consortium for the Participating Institutions of the SDSS-III Collaboration including the University of Arizona, the Brazilian Participation Group, Brookhaven National Laboratory, Carnegie Mellon University, University of Florida, the French Participation Group, the German Participation Group, Harvard University, the Instituto de Astrofisica de Canarias, the Michigan State/Notre Dame/JINA Participation Group, Johns Hopkins University, Lawrence Berkeley National Laboratory, Max Planck Institute for Astrophysics, Max Planck Institute for Extraterrestrial Physics, New Mexico State University, University of Portsmouth, Princeton University, the Spanish Participation Group, University of Tokyo, University of Utah, Vanderbilt University, University of Virginia, University of Washington, and Yale University. This work is based on observations made with the Copernico Telescope of the INAF-Asiago Observatory.

Bibliography

Abdo A. A., et al., 2009a, ApJ, 699, 976

Abdo A. A., et al., 2009b, ApJ, 707, 727

Aldrovandi S. M. V., Contini M., 1984, A&A, 140, 368

Allen C. W., 1976, Astrophysical Quantities

Anders E., Grevesse N., 1989, Geochim. Cosmochim. Acta, 53, 197

Antón S., Browne I. W. A., Marchã M. J., 2008, A&A, 490, 583

Antonucci R., 1993, ARA&A, 31, 473

Antonucci R. R. J., Miller J. S., 1985, ApJ, 297, 621

Asplund M., Grevesse N., Sauval A. J., Scott P., 2009, ARA&A, 47, 481

Baldwin J. A., Phillips M. M., Terlevich R., 1981, PASP, 93, 5

Baldwin J. A., Wilson A. S., Whittle M., 1987, ApJ, 319, 84

Barbieri C., 1999, Lezioni di astronomia. Astronomia. Testi e manuali, Zanichelli

Baum S. A., O'Dea C. P., Dallacassa D., de Bruyn A. G., Pedlar A., 1993, ApJ, 419, 553

Beck R., 2012, in Journal of Physics Conference Series. p. 012051 (arXiv:1112.1823), doi:10.1088/1742-6596/372/1/012051

Becker R. H., White R. L., Helfand D. J., 1995, ApJ, 450, 559

Beckmann V., Shrader C. R., 2012, Active Galactic Nuclei

Bennert N., Falcke H., Shchekinov Y., Wilson A. S., 2004, in Storchi-Bergmann T., Ho L. C., Schmitt H. R., eds, IAU Symposium Vol. 222, The Interplay Among Black Holes, Stars and ISM in Galactic Nuclei. pp 307–308 (arXiv:astro-ph/0404278), doi:10.1017/S1743921304002340

Berton M., et al., 2015, A&A, 578, A28

Berton M., Foschini L., Ciroi S., Cracco V., La Mura G., Di Mille F., Rafanelli P., 2016a, A&A, 591, A88

Berton M., et al., 2016b, A&A, 591, A98

Berton M., et al., 2018, A&A, 614, A87

Bicay M. D., Kojoian G., Seal J., Dickinson D. F., Malkan M. A., 1995, ApJS, 98, 369

Blandford R. D., McKee C. F., Rees M. J., 1977, Nature, 267, 211

Blundell K. M., Beasley A. J., Bicknell G. V., 2003, ApJ, 591, L103

Bolton J. G., 1948, Nature, 162, 141

Bolton J. G., Stanley G. J., Slee O. B., 1949, Nature, 164, 101

Bridle A. H., Hough D. H., Lonsdale C. J., Burns J. O., Laing R. A., 1994, AJ, 108, 766

Bundy K., et al., 2015, ApJ, 798, 7

Caccianiga A., et al., 2014, MNRAS, 441, 172

Caccianiga A., et al., 2015, MNRAS, 451, 1795

Caccianiga A., Dallacasa D., Antón S., Ballo L., Berton M., Mack K.-H., Paulino-Afonso A., 2017, MNRAS, 464, 1474

Capetti A., Axon D. J., Macchetto F., Sparks W. B., Boksenberg A., 1996, ApJ, 469, 554

Cardelli J. A., Clayton G. C., Mathis J. S., 1989, ApJ, 345, 245

Cecil G., Dopita M. A., Groves B., Wilson A. S., Ferruit P., Pécontal E., Binette L., 2002, ApJ, 568, 627

Cid Fernandes R., Mateus A., Sodré L., Stasińska G., Gomes J. M., 2005, MNRAS, 358, 363

Cid Fernandes R., Asari N. V., Sodré L., Stasińska G., Mateus A., Torres-Papaqui J. P., Schoenell W., 2007, MNRAS, 375, L16

Ciroi S., Afanasiev V. L., Moiseev A. V., Botte V., Di Mille F., Dodonov S. N., Rafanelli P., Smirnova A. A., 2005, MNRAS, 360, 253

Cisternas M., et al., 2011, ApJ, 726, 57

Colbert E. J. M., Baum S. A., Gallimore J. F., O'Dea C. P., Christensen J. A., 1996, ApJ, 467, 551

Colina L., Sparks W. B., Macchetto F., 1991, ApJ, 370, 102

Condon J. J., Cotton W. D., Greisen E. W., Yin Q. F., Perley R. A., Taylor G. B., Broderick J. J., 1998, AJ, 115, 1693

Congiu E., et al., 2017a, Front. Astron. Space Sci., 4, 27

Congiu E., et al., 2017b, MNRAS, 471, 562

Congiu E., et al., 2017c, A&A, 603, A32

Contini M., 2013, MNRAS, 429, 242

Contini M., 2015, MNRAS, 452, 3795

Contini M., 2017, MNRAS, 469, 3125

Contini M., Aldrovandi S. M. V., 1983, A&A, 127, 15

Contini M., Viegas S. M., Prieto M. A., 2002, A&A, 386, 399

Contini M., Cracco V., Ciroi S., La Mura G., 2012, A&A, 545, A72

Cox D. P., 1972, ApJ, 178, 143

Cracco V., et al., 2011, MNRAS, 418, 2630

Cracco V., Ciroi S., Berton M., Di Mille F., Foschini L., La Mura G., Rafanelli P., 2016, MNRAS, 462, 1256

Crenshaw D. M., Kraemer S. B., 2000, ApJ, 532, L101

Crenshaw D. M., et al., 2000, AJ, 120, 1731

Crenshaw D. M., et al., 2002, ApJ, 566, 187

Czerny B., Siemiginowska A., Janiuk A., Nikiel-Wroczyński B., Stawarz L., 2009, ApJ, 698, 840

D'Onghia E., 2015, ApJ, 808, L8

Das V., Crenshaw D. M., Kraemer S. B., Deo R. P., 2006, AJ, 132, 620

Dasyra K. M., Bostrom A. C., Combes F., Vlahakis N., 2015, ApJ, 815, 34

Decarli R., Dotti M., Fontana M., Haardt F., 2008, MNRAS, 386, L15

Di Mille F., 2007, PhD thesis, Univ. Padova

Dietrich M., Wagner S. J., 1998, A&A, 338, 405

Doi A., Nagira H., Kawakatu N., Kino M., Nagai H., Asada K., 2012, ApJ, 760, 41

Doi A., Asada K., Fujisawa K., Nagai H., Hagiwara Y., Wajima K., Inoue M., 2013, ApJ, 765, 69

Doi A., Wajima K., Hagiwara Y., Inoue M., 2015, ApJ, 798, L30

Dopita M. A., 1995, Ap&SS, 233, 215

Dopita M. A., 2000, Ap&SS, 272, 79

Dopita M. A., Sutherland R. S., 1995, ApJ, 455, 468

Dopita M. A., Sutherland R. S., 2003, Astrophysics of the diffuse universe

Edge D. O., Shakeshaft J. R., McAdam W. B., Baldwin J. E., Archer S., 1959, Memoirs of the Royal Astronomical Society, 68, 37

Ekers R. D., Fanti R., Lari C., Parma P., 1978, Nature, 276, 588

Evans I. N., Tsvetanov Z., Kriss G. A., Ford H. C., Caganoff S., Koratkar A. P., 1993, ApJ, 417, 82

Fabian A. C., 2012, ARA&A, 50, 455

Falcke H., Wilson A. S., Simpson C., 1998, ApJ, 502, 199

Fanaroff B. L., Riley J. M., 1974, MNRAS, 167, 31P

Fanti C., Fanti R., Dallacasa D., Schilizzi R. T., Spencer R. E., Stanghellini C., 1995, A&A, 302, 317

Fischer T. C., Crenshaw D. M., Kraemer S. B., Schmitt H. R., 2013, ApJS, 209, 1

Fischer T. C., et al., 2017, ApJ, 834, 30

Fischer T. C., et al., 2018, ApJ, 856, 102

Foschini L., 2014, International Journal of Modern Physics Conference Series, 28, 1460188

Foschini L., 2017, Frontiers in Astronomy and Space Sciences, 4, 6

Foschini L., et al., 2015, A&A, 575, A13

Fragile P. C., Anninos P., Croft S., Lacy M., Witry J. W. L., 2017, ApJ, 850, 171

Fukugita M., Yasuda N., Doi M., Gunn J. E., York D. G., 2011, AJ, 141, 47

Gallimore J. F., Axon D. J., O'Dea C. P., Baum S. A., Pedlar A., 2006, AJ, 132, 546

Gallo L. C., et al., 2006, MNRAS, 370, 245

Giroletti M., Panessa F., 2009, ApJ, 706, L260

Goodrich R. W., 1989, ApJ, 342, 224

Grevesse N., Sauval A. J., 1998, Space Sci. Rev., 85, 161

Gu M., Chen Y., Komossa S., Yuan W., Shen Z., Wajima K., Zhou H., Zensus J. A., 2015, ApJS, 221, 3

Haardt F., Maraschi L., 1991, ApJ, 380, L51

Hales C. A., 2013, preprint, (arXiv:1312.4602)

He Z., et al., 2018, MNRAS, 478, 3614

Heinz S., Sunyaev R. A., 2003, MNRAS, 343, L59

Hewitt A., Burbidge G., 1991, ApJS, 75, 297

Ho L. C., Peng C. Y., 2001, ApJ, 555, 650

Hong J., Im M., Kim M., Ho L. C., 2015, ApJ, 804, 34

Hota A., Saikia D. J., 2006, MNRAS, 371, 945

Hough J. H., Brindle C., Axon D. J., Bailey J., Sparks W. B., 1987, MNRAS, 224, 1013

Humphrey A., Villar-Martín M., Sánchez S. F., Martínez-Sansigre A., Delgado R. G., Pérez E., Tadhunter C., Pérez-Torres M. A., 2010, MNRAS, 408, L1

Hung C.-L., Hayward C. C., Smith H. A., Ashby M. L. N., Lanz L., Martínez-Galarza J. R., Sanders D. B., Zezas A., 2016, ApJ, 816, 99

Hurley-Walker N., et al., 2017, MNRAS, 464, 1146

Husemann B., Wisotzki L., Sánchez S. F., Jahnke K., 2013, A&A, 549, A43

Husemann B., Jahnke K., Sánchez S. F., Wisotzki L., Nugroho D., Kupko D., Schramm M., 2014, MNRAS, 443, 755

Hutchings J. B., et al., 1998, ApJ, 492, L115

Inglis M. D., Brindle C., Hough J. H., Young S., Axon D. J., Bailey J. A., Ward M. J., 1993, MNRAS, 263, 895

Intema H. T., Jagannathan P., Mooley K. P., Frail D. A., 2017, A&A, 598, A78

Jamrozy M., Klein U., Mack K.-H., Gregorini L., Parma P., 2004, A&A, 427, 79

Kallman T., Bautista M., 2001, ApJS, 133, 221

Kampczyk P., et al., 2013, ApJ, 762, 43

Kauffmann G., et al., 2003, MNRAS, 346, 1055

Keel W. C., et al., 2012, MNRAS, 420, 878

Kellermann K. I., Sramek R., Schmidt M., Shaffer D. B., Green R., 1989, AJ, 98, 1195

Kellermann K. I., Condon J. J., Kimball A. E., Perley R. A., Ivezić Ž., 2016, ApJ, 831, 168

Kewley L. J., Dopita M. A., Sutherland R. S., Heisler C. A., Trevena J., 2001, ApJ, 556, 121

Kewley L. J., Groves B., Kauffmann G., Heckman T., 2006, MNRAS, 372, 961

Khachikian E. Y., Weedman D. W., 1974, ApJ, 192, 581

Kharb P., O'Dea C. P., Baum S. A., Colbert E. J. M., Xu C., 2006, ApJ, 652, 177

Kharb P., O'Dea C. P., Baum S. A., Hardcastle M. J., Dicken D., Croston J. H., Mingo B., Noel-Storr J., 2014, MNRAS, 440, 2976

Kharb P., Srivastava S., Singh V., Gallimore J. F., Ishwara-Chandra C. H., Ananda H., 2016, MNRAS, 459, 1310

Komatsu E., et al., 2011, ApJS, 192, 18

Komossa S., 2012, Advances in Astronomy, 2012, 364973

Komossa S., Voges W., Xu D., Mathur S., Adorf H.-M., Lemson G., Duschl W. J., Grupe D., 2006, AJ, 132, 531

Kraemer S. B., Crenshaw D. M., 2000, ApJ, 544, 763

Krivonos R., Revnivtsev M., Lutovinov A., Sazonov S., Churazov E., Sunyaev R., 2007, A&A, 475, 775

Kukula M. J., Ghosh T., Pedlar A., Schilizzi R. T., 1999, ApJ, 518, 117

La Mura G., 2018, Lecture Notes for Astronomical Spectroscopy

Lister M. L., Homan D. C., 2005, AJ, 130, 1389

Livio M., Pringle J. E., 1997, ApJ, 486, 835

Marin F., 2014, MNRAS, 441, 551

Marshall J. L., et al., 2008, in Society of Photo-Optical Instrumentation Engineers (SPIE) Conference Series. p. 54 (arXiv:0807.3774), doi:10.1117/12.789972

Mateus A., Sodré L., Cid Fernandes R., Stasińska G., Schoenell W., Gomes J. M., 2006, MNRAS, 370, 721

Mathur S., 2000, MNRAS, 314, L17

Meurs E. J. A., Wilson A. S., 1981, A&AS, 45, 99

Momjian E., Romney J. D., Carilli C. L., Troland T. H., 2003, ApJ, 597, 809

Morganti R., Oosterloo T., Tsvetanov Z., 1998, AJ, 115, 915

Morganti R., Tsvetanov Z. I., Gallimore J., Allen M. G., 1999, A&AS, 137, 457

Morganti R., Holt J., Saripalli L., Oosterloo T. A., Tadhunter C. N., 2007, A&A, 476, 735

Morganti R., Oosterloo T., Oonk J. B. R., Frieswijk W., Tadhunter C., 2015, A&A, 580, A1

Morganti R., Oosterloo T., Schulz R., Tadhunter C., Oonk J. B. R., 2018, preprint, (arXiv:1807.07245)

Morse J. A., Cecil G., Wilson A. S., Tsvetanov Z. I., 1998, ApJ, 505, 159

Moshir M., et al. 1990, in IRAS Faint Source Catalogue, version 2.0 (1990).

Muñoz Marín V. M., González Delgado R. M., Schmitt H. R., Cid Fernandes R., Pérez E., Storchi-Bergmann T., Heckman T., Leitherer C., 2007, AJ, 134, 648

Mulchaey J. S., Wilson A. S., Tsvetanov Z., 1996a, ApJS, 102, 309

Mulchaey J. S., Wilson A. S., Tsvetanov Z., 1996b, ApJ, 467, 197

Mundell C. G., Ferruit P., Nagar N., Wilson A. S., 2009, ApJ, 703, 802

Nagar N. M., Wilson A. S., Mulchaey J. S., Gallimore J. F., 1999, ApJS, 120, 209

Netzer H., 2015, ARA&A, 53, 365

Oshlack A. Y. K. N., Webster R. L., Whiting M. T., 2001, ApJ, 558, 578

Osterbrock D. E., 1989, Astrophysics of gaseous nebulae and active galactic nuclei

Osterbrock D. E., Ferland G. J., 2006, Astrophysics of gaseous nebulae and active galactic nuclei

Osterbrock D. E., Pogge R. W., 1985, ApJ, 297, 166

Ozaki S., 2009, PASJ, 61, 259

Padovani P., 2017, Nature Astronomy, 1, 0194

Panessa F., et al., 2011, MNRAS, 417, 2426

Parma P., Ekers R. D., Fanti R., 1985, A&AS, 59, 511

Penston M. V., et al., 1990, A&A, 236, 53

Perley R. A., Willis A. G., Scott J. S., 1979, Nature, 281, 437

Peterson B. M., 2011, in Narrow-Line Seyfert 1 Galaxies and their Place in the Universe. p. 32

Petrosian A., McLean B., Allen R. J., MacKenty J. W., 2007, ApJS, 170, 33

Pogge R. W., 1988, ApJ, 328, 519

Pogge R. W., 1989, ApJ, 345, 730

Polletta M., et al., 2007, ApJ, 663, 81

Pringle J. E., 1996, MNRAS, 281, 357

Richards J. L., Lister M. L., 2015, ApJ, 800, L8

Robson I., 1996, Active galactic nuclei

Roche N., Humphrey A., Lagos P., Papaderos P., Silva M., Cardoso L. S. M., Gomes J. M., 2016, MNRAS, 459, 4259

Rodríguez-Ardila A., Contini M., Viegas S. M., 2005, MNRAS, 357, 220

Rodríguez-Ardila A., et al., 2017, MNRAS, 465, 906

Romero G. E., Cellone S. A., Combi J. A., 2000, A&A, 360, L47

Roos N., Kaastra J. S., Hummel C. A., 1993, ApJ, 409, 130

Rubinur K., Das M., Kharb P., Honey M., 2017, MNRAS, 465, 4772

Rybicki G. B., Lightman A. P., 1986, Radiative Processes in Astrophysics

Salpeter E. E., 1964, ApJ, 140, 796

Sanders D. B., Soifer B. T., Elias J. H., Madore B. F., Matthews K., Neugebauer G., Scoville N. Z., 1988, ApJ, 325, 74

Sani E., Lutz D., Risaliti G., Netzer H., Gallo L. C., Trakhtenbrot B., Sturm E., Boller T., 2010, MNRAS, 403, 1246

Schawinski K., Treister E., Urry C. M., Cardamone C. N., Simmons B., Yi S. K., 2011, ApJ, 727, L31

Schirmer M., Diaz R., Holhjem K., Levenson N. A., Winge C., 2013, ApJ, 763, 60

Schlafly E. F., Finkbeiner D. P., 2011, ApJ, 737, 103

Schmidt M., 1963, Nature, 197, 1040

Schmitt H. R., Storchi-Bergmann T., Baldwin J. A., 1994, ApJ, 423, 237

Schmitt H. R., Donley J. L., Antonucci R. R. J., Hutchings J. B., Kinney A. L., 2003a, ApJS, 148, 327

Schmitt H. R., Donley J. L., Antonucci R. R. J., Hutchings J. B., Kinney A. L., Pringle J. E., 2003b, ApJ, 597, 768

Schulz R., et al., 2016, A&A, 588, A146

Schwope A., et al., 2000, Astronomische Nachrichten, 321, 1

Seyfert C. K., 1943, ApJ, 97, 28

Shang Z., et al., 2005, The Astrophysical Journal, 619, 41

Shen Y., Ho L. C., 2014, Nature, 513, 210

Shields G. A., 1999, PASP, 111, 661

Shimwell T. W., et al., 2017, A&A, 598, A104

Simpson C., Wilson A. S., Bower G., Heckman T. M., Krolik J. H., Miley G. K., 1997, ApJ, 474, 121

Singh V., Ishwara-Chandra C. H., Wadadekar Y., Beelen A., Kharb P., 2015a, MNRAS, 446, 599

Singh V., Ishwara-Chandra C. H., Sievers J., Wadadekar Y., Hilton M., Beelen A., 2015b, MNRAS, 454, 1556

Steffen W., Gómez J. L., Raga A. C., Williams R. J. R., 1997, ApJ, 491, L73

Stockton A., MacKenty J. W., 1987, ApJ, 316, 584

Sun A.-L., et al., 2018, MNRAS, 480, 2302

Tadhunter C., Tsvetanov Z., 1989, Nature, 341, 422

Tadhunter C., Morganti R., Rose M., Oonk J. B. R., Oosterloo T., 2014, Nature, 511, 440

Tran H. D., 1995, ApJ, 440, 578

Turner T. J., Romano P., George I. M., Edelson R., Collier S. J., Mathur S., Peterson B. M., 2001, ApJ, 561, 131

Ulvestad J. S., Wilson A. S., 1984, ApJ, 278, 544

Ulvestad J. S., Neff S. G., Wilson A. S., 1987, AJ, 93, 22

Ulvestad J. S., Antonucci R. R. J., Goodrich R. W., 1995, AJ, 109, 81

Unger S. W., Pedlar A., Axon D. J., Whittle M., Meurs E. J. A., Ward M. J., 1987, MNRAS, 228, 671

Urry C. M., Padovani P., 1995, PASP, 107, 803

Veilleux S., Osterbrock D. E., 1987, ApJS, 63, 295

Veilleux S., Bland-Hawthorn J., Cecil G., 1999, AJ, 118, 2108

Villar-Martin M., Tadhunter C., Clark N., 1997, A&A, 323, 21

Wasilewski A. J., 1981, PASP, 93, 560

Whalen D. J., Laurent-Muehleisen S. A., Moran E. C., Becker R. H., 2006, AJ, 131, 1948

Whittle M., Wilson A. S., 2004, AJ, 127, 606

Wilson A. S., 1996, Vistas in Astronomy, 40, 63

Wilson A. S., Tsvetanov Z. I., 1994, AJ, 107, 1227

Woltjer L., 1959, ApJ, 130, 38

Wright E. L., et al., 2010, AJ, 140, 1868

Wrobel J. M., 1984, ApJ, 284, 531

Yuan W., Zhou H. Y., Komossa S., Dong X. B., Wang T. G., Lu H. L., Bai J. M., 2008, ApJ, 685, 801

Zel'dovich Y. B., 1964, Soviet Physics Doklady, 9, 195

de Young D. S., 2002, The physics of extragalactic radio sources

A

APPENDIX: LINES PROFILES

IC 5063

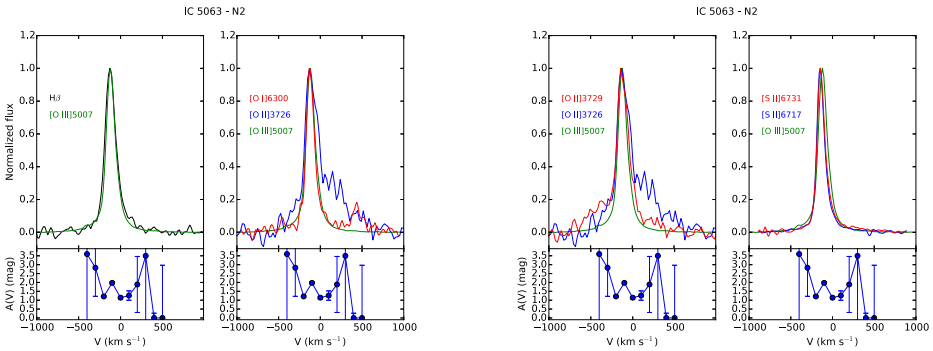

Figure A.1: Comparison of the emission lines of the N2 region of IC 5063. The behaviour of the extinction coefficient as a function of velocity is shown under each plot.

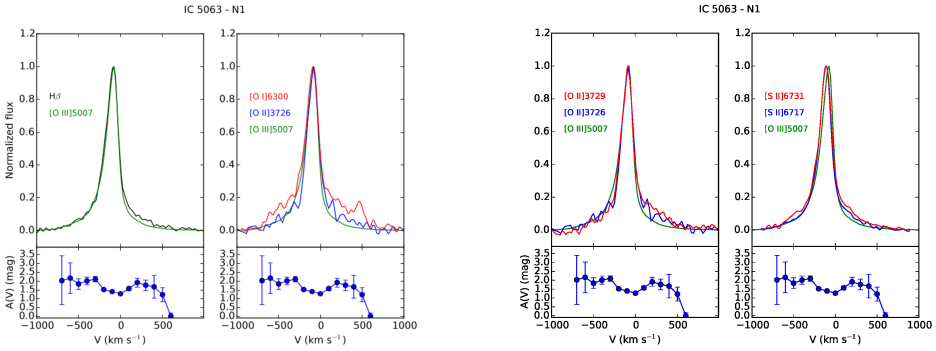

Figure A.2: Comparison of the emission lines of the N1 region of IC 5063. The behaviour of the extinction coefficient as a function of velocity is shown under each plot.

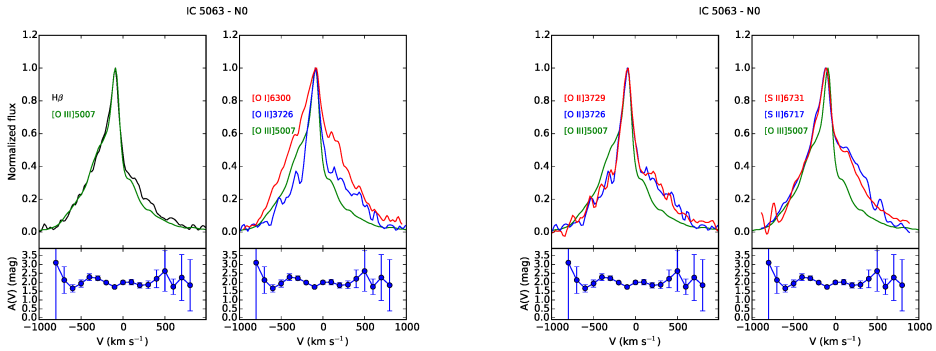

Figure A.3: Comparison of the emission lines of the N0 region of IC 5063. The behaviour of the extinction coefficient as a function of velocity is shown under each plot.

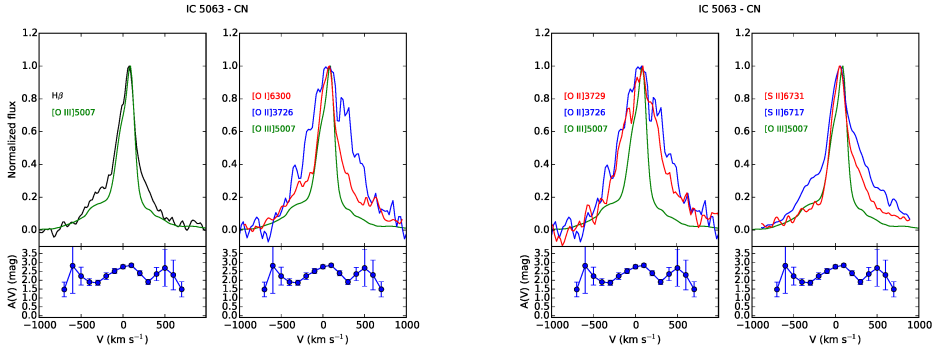

Figure A.4: Comparison of the emission lines of the CN region of IC 5063. The behaviour of the extinction coefficient as a function of velocity is shown under each plot.

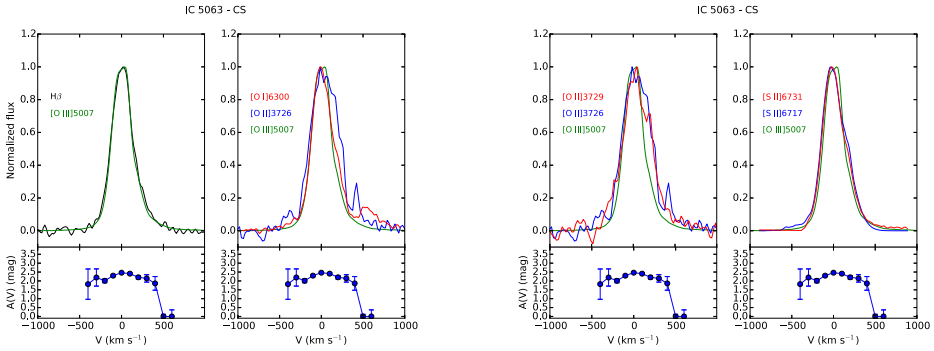

Figure A.5: Comparison of the emission lines of the CS region of IC 5063. The behaviour of the extinction coefficient as a function of velocity is shown under each plot.

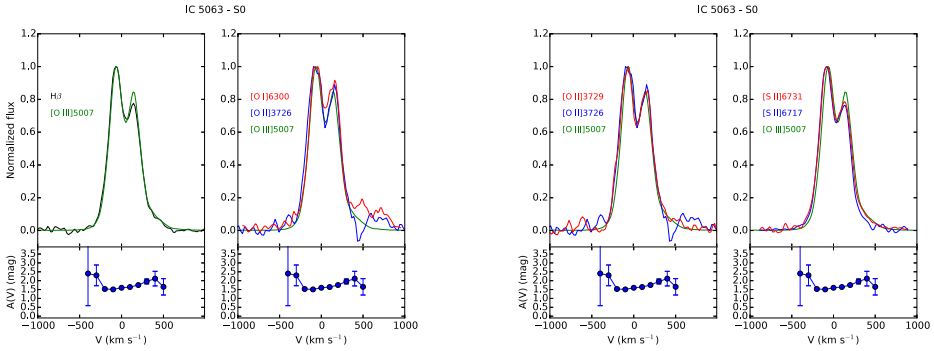

Figure A.6: Comparison of the emission lines of the S0 region of IC 5063. The behaviour of the extinction coefficient as a function of velocity is shown under each plot.

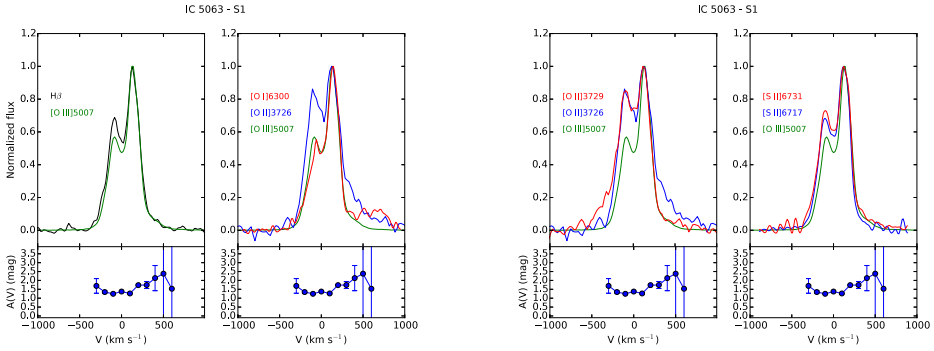

Figure A.7: Comparison of the emission lines of the S1 region of IC 5063. The behaviour of the extinction coefficient as a function of velocity is shown under each plot.

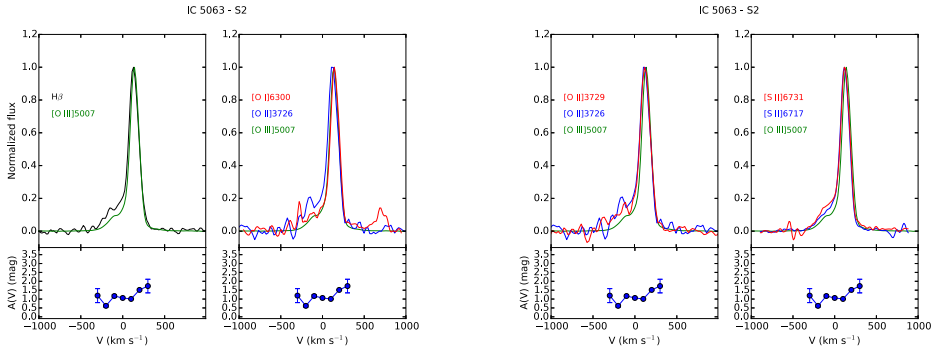

Figure A.8: Comparison of the emission lines of the S2 region of IC 5063. The behaviour of the extinction coefficient as a function of velocity is shown under each plot.

NGC 7212

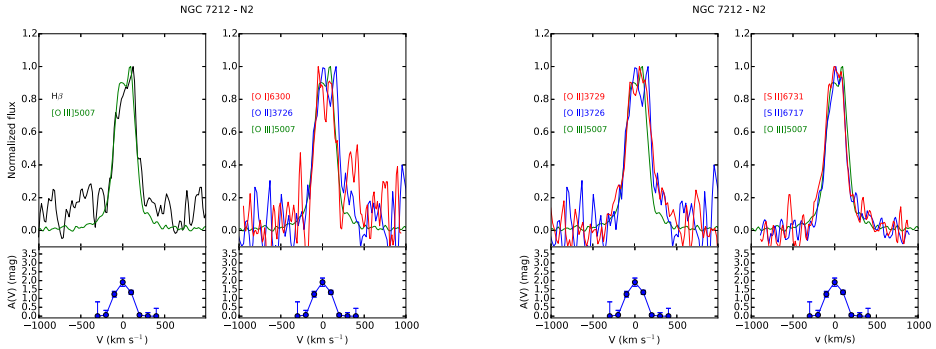

Figure A.9: Comparison of the emission lines of the N2 region of NGC 7212. The behaviour of the extinction coefficient as a function of velocity is shown under each plot.

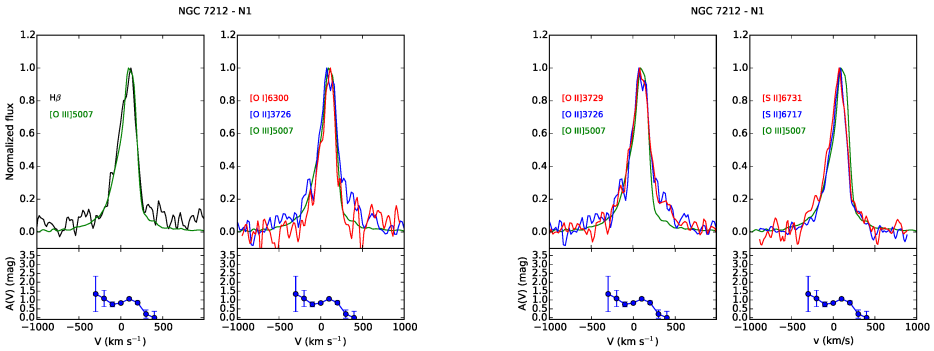

Figure A.10: Comparison of the emission lines of the N1 region of NGC 7212. The behaviour of the extinction coefficient as a function of velocity is shown under each plot.

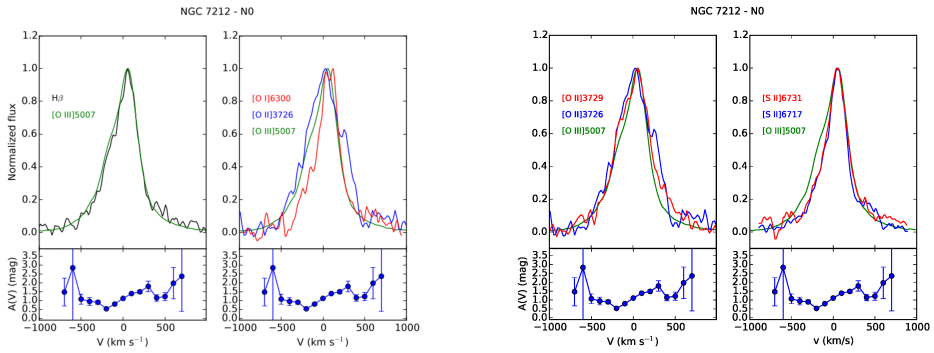

Figure A.11: Comparison of the emission lines of the N0 region of NGC 7212. The behaviour of the extinction coefficient as a function of velocity is shown under each plot.

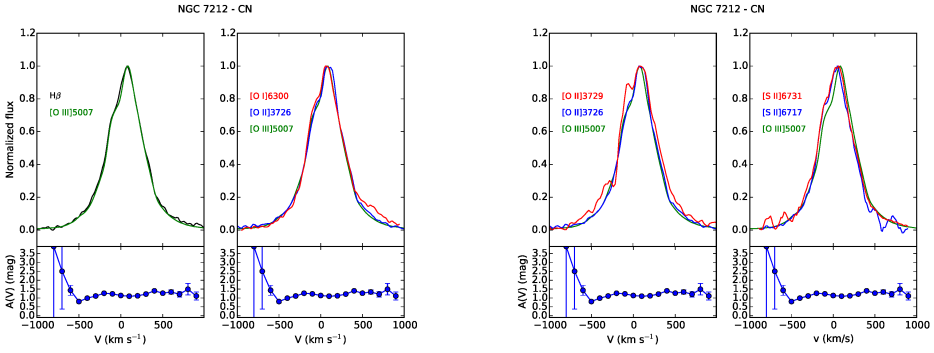

Figure A.12: Comparison of the emission lines of the CN region of NGC 7212. The behaviour of the extinction coefficient as a function of velocity is shown under each plot.

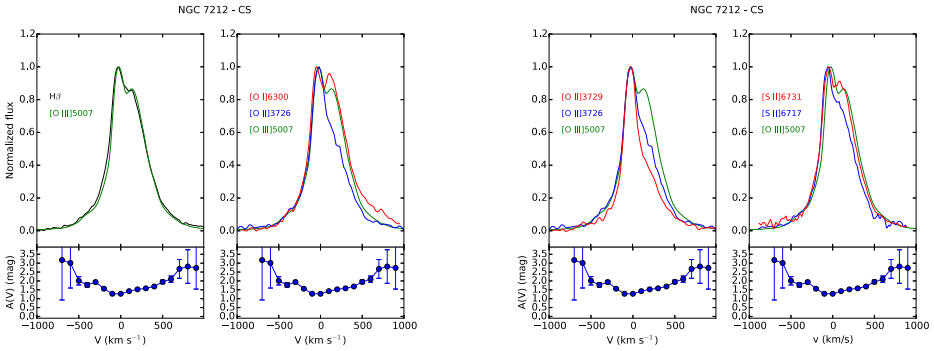

Figure A.13: Comparison of the emission lines of the CS region of NGC 7212. The behaviour of the extinction coefficient as a function of velocity is shown under each plot.

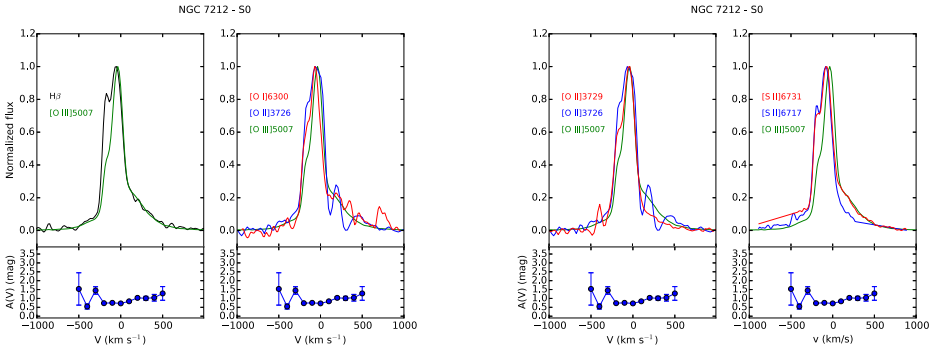

Figure A.14: Comparison of the emission lines of the S0 region of NGC 7212. The behaviour of the extinction coefficient as a function of velocity is shown under each plot.

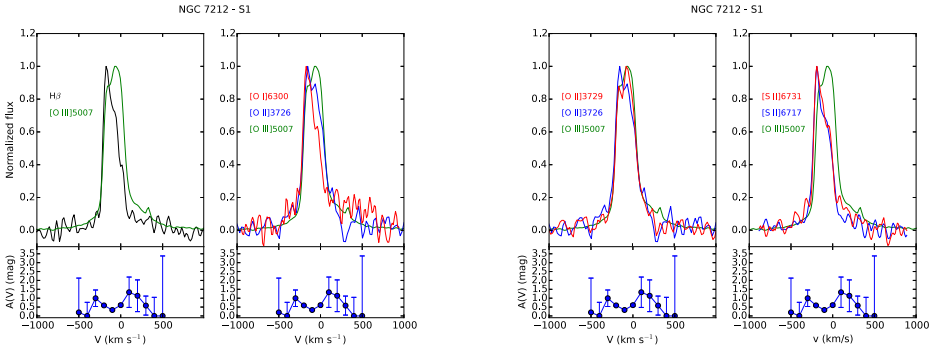

Figure A.15: Comparison of the emission lines of the S1 region of NGC 7212. The behaviour of the extinction coefficient as a function of velocity is shown under each plot.

B

APPENDIX: DIAGNOSTIC DIAGRAMS

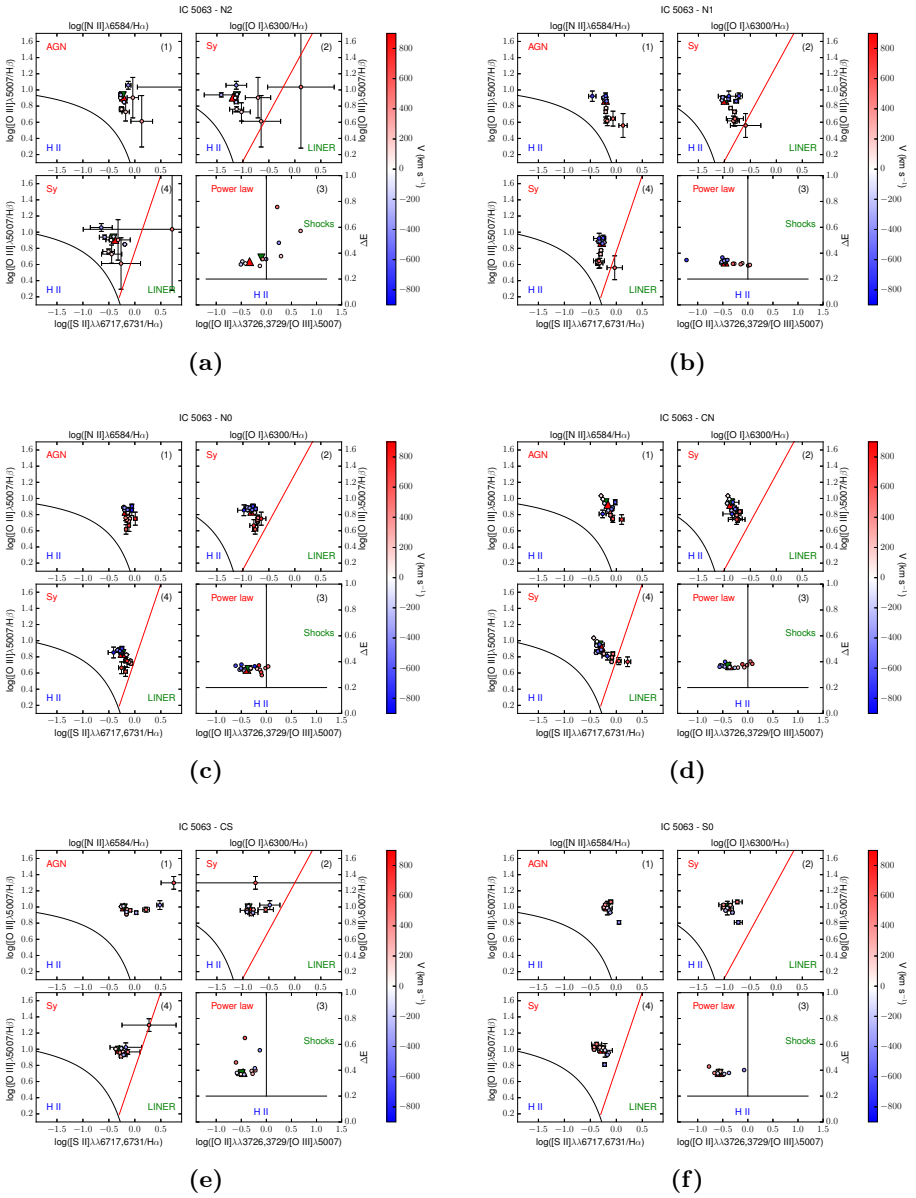

Figure B.1: Diagnostic diagrams of the (a) N2, (b) N1, (c) N0, (d) CN, (e) CS and (f) S0 regions of IC 5063. In each plot we show, from the top left panel clockwise: (1) $\log([O\,III]\mathrm{H}\beta)$ vs $\log([N\,II]/\mathrm{H}\alpha)$, (2) $\log([O\,III]/\mathrm{H}\beta)$ vs $\log([O\,I]/\mathrm{H}\alpha)$, (3) ΔE vs $\log([O\,II]/[O\,III])$, (4) $\log([O\,III]/\mathrm{H}\beta)$ vs $\log([S\,II]/\mathrm{H}\alpha)$ (Baldwin et al., 1981; Veilleux & Osterbrock, 1987). The colorbar shows the velocity of each bin. The black curves in (1), (2), (4) divide power-law ionized regions (top) and H II regions (bottom). The red lines divide Seyfert-like regions (left) and LINER-like regions (right) (Kewley et al., 2006). The black lines in (3) divide H II regions (bottom), power-law ionized region (left) and shock ionized regions (right) (Baldwin et al., 1981).

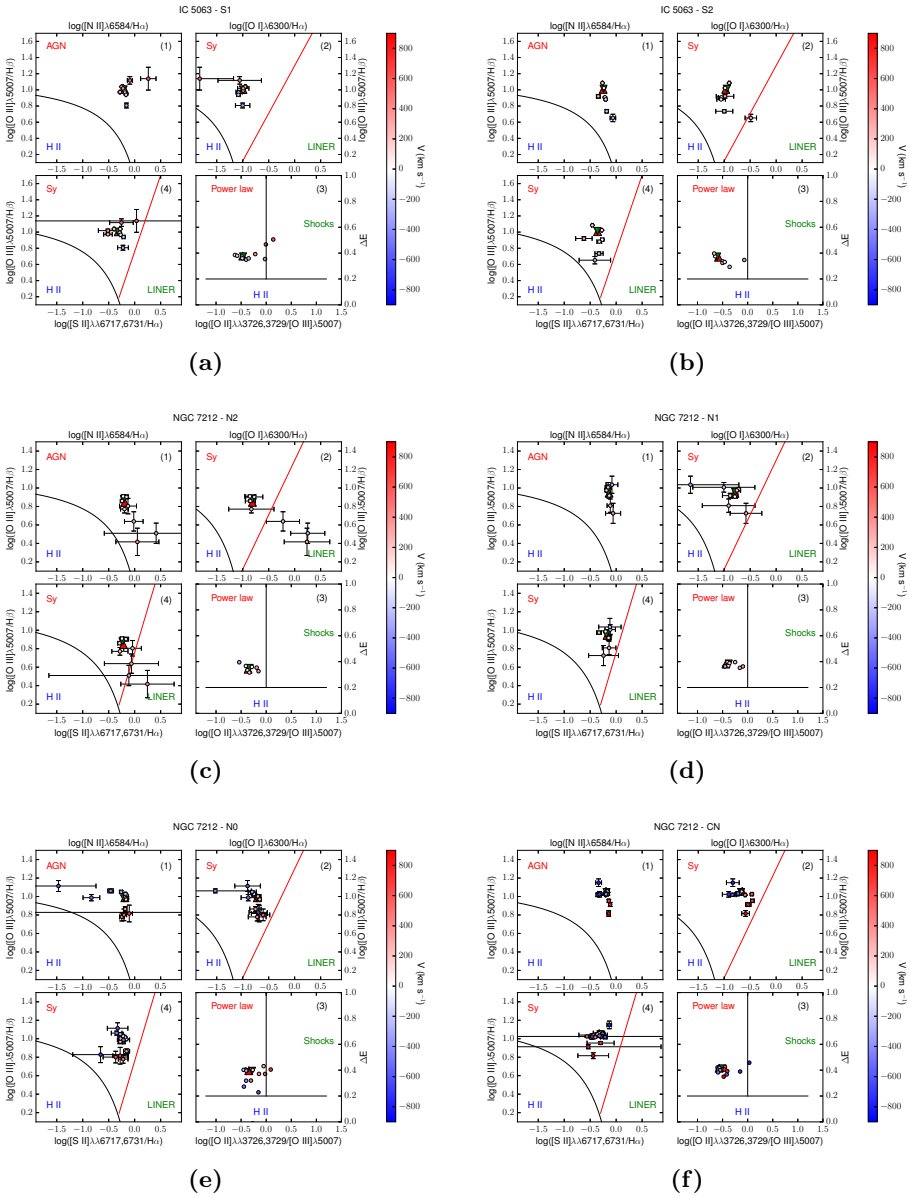

Figure B.2: Diagnostic diagrams of the (a) S1 and (b) S2 regions of IC 5063 and (c) N2, (d) N1, (e) N0 and (f) CN regions of NGC 7212. In each plot we show, from the top left panel clockwise: (1) $\log([O\,III]\mathrm{H}\beta)$ vs $\log([N\,II]/\mathrm{H}\alpha)$, (2) $\log([O\,III]/\mathrm{H}\beta)$ vs $\log([O\,I]/\mathrm{H}\alpha)$, (3) ΔE vs $\log([O\,II]/[O\,III])$, (4) $\log([O\,III]/\mathrm{H}\beta)$ vs $\log([S\,II]/\mathrm{H}\alpha)$ (Baldwin et al., 1981; Veilleux & Osterbrock, 1987). The colorbar shows the velocity of each bin. The black curves in (1), (2), (4) divide power-law ionized regions (top) and H II regions (bottom). The red lines divide Seyfert-like regions (left) and LINER-like regions (right) (Kewley et al., 2006). The black lines in (3) divide H II regions (bottom), power-law ionized region (left) and shock ionized regions (right) (Baldwin et al., 1981).

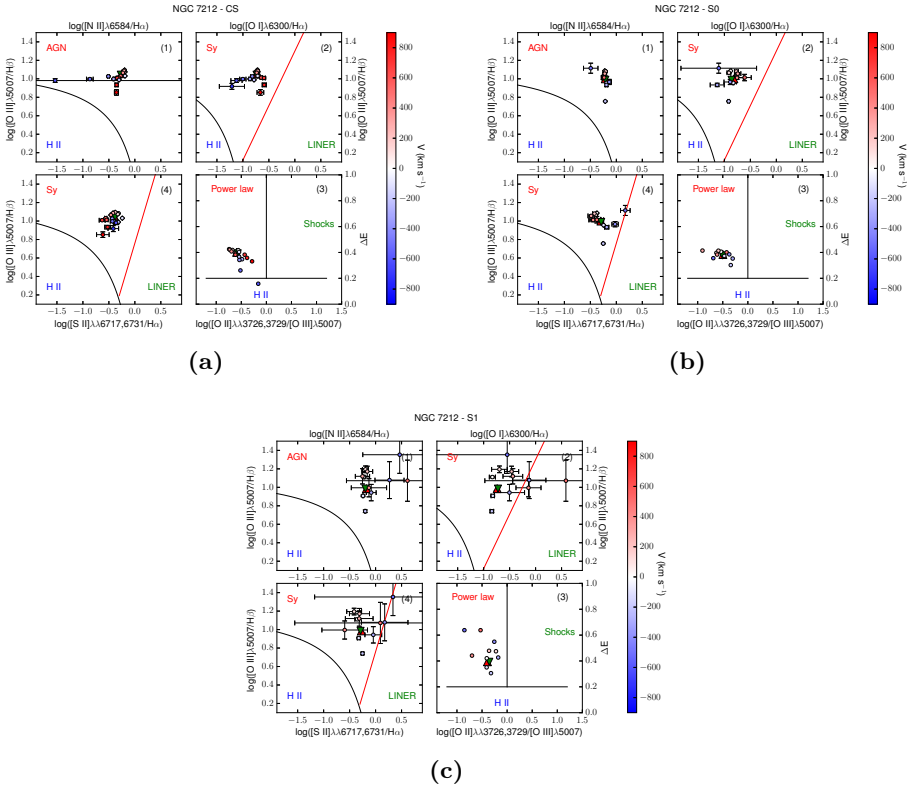

(a) **(b)**

(c)

Figure B.3: Diagnostic diagrams of the (a) CS, (b) S0 and (c) S1 regions of NGC 7212. In each plot we show, from the top left panel clockwise: (1) $\log([O\,III]\mathrm{H}\beta)$ vs $\log([N\,II]/\mathrm{H}\alpha)$, (2) $\log([O\,III]/\mathrm{H}\beta)$ vs $\log([O\,I]/\mathrm{H}\alpha)$, (3) ΔE vs $\log([O\,II]/[O\,III])$, (4) $\log([O\,III]/\mathrm{H}\beta)$ vs $\log([S\,II]/\mathrm{H}\alpha)$ (Baldwin et al., 1981; Veilleux & Osterbrock, 1987). The colorbar shows the velocity of each bin. The black curves in (1), (2), (4) divide power-law ionized regions (top) and H II regions (bottom). The red lines divide Seyfert-like regions (left) and LINER-like regions (right) (Kewley et al., 2006). The black lines in (3) divide H II regions (bottom), power-law ionized region (left) and shock ionized regions (right) (Baldwin et al., 1981).

C

APPENDIX: RESULTS OF SUMA SIMULATIONS

In this appendix we report the flux measurements and the results of SUMA simulations. We produced two tables for each region, the first for $V \geq 0$ and the second for $V < 0$. We numbered the bins according to their velocity, starting from the bin at $V = 0$. For each one of them we compared the observations with the results of the models. In Sec. 1 we show the tables for IC 5063, in Sec. 2 those for NGC 7212.

C.1 IC 5063

Table C.1: Simulation for $v \geq 0$ of the N2 region of IC 5063. For each bin there are the observed quantities and the results of the models. The first nine rows show the comparison between the observed and the synthetic spectra, the remaining rows show the input parameters of each model.

	bin 0		bin 1		bin 2		bin 3		bin 4		bin 5	
line	obs.	mod.	obs.	mod.	obs.	mod.	obs.	mod.	obs.	mod.	obs.	mod.
[O II]λ3727+	3.04	3.3	4.28	4.0	10.46	10.2	38.6	33.3	3.46	3.9	17.8	16.5
[Ne III]λ3869+	1.41	1.34	2.35	1.43	4.23	2.7	11.73	4.3	3.05	2.23	0.0	3.4
[He II]λ4686	0.192	0.3	0.003	0.2	0.05	0.14	0.0	0.07	0.0	0.19	0.0	0.06
[O III]λ5007+	10.58	10.66	7.7	7.68	6.73	7.0	10.35	12.5	5.14	5.2	12.91	9.0
[O I]λ6300,[S II]λ6310	0.2	0.12	0.2	0.1	0.27	0.11	0.56	0.54	0.53	0.54	1.54	0.2
Hα	2.86	3.2	2.86	3.17	2.86	3.2	2.86	4.3	2.38	2.95	3.	4.1
[N II]λ6584	1.51	1.3	1.59	1.78	1.9	1.76	2.61	2.46	3.23	2.1	1.17	2.5
[S II]λ6716	0.53	0.5	0.45	0.48	0.52	0.48	0.58	0.66	0.26	0.25	15.5	0.86
[S II]λ6731	0.46	0.6	0.44	0.74	0.5	0.44	0.78	0.58	1.02	0.47	3.1	1.
FWHM(km s^{-1})	0.0	–	100	–	200	–	300	–	400	–	500	–
V_s (km s^{-1})	–	55	–	100	–	230	–	290	–	400	–	530
n_0(cm^{-3})	–	270	–	250	–	40	–	40	–	210	–	50
D(10^{18} cm)	–	0.0015	–	0.0015	–	0.04	–	0.06	–	0.02	–	0.04
F (units[1])	–	0.25	–	0.3	–	0.02	–	0.002	–	2.0	–	$1. \times 10^{-7}$
O/H (10^{-4})	–	6.6	–	6.6	–	6.0	–	6.6	–	6.6	–	6.0
N/H (10^{-4})	–	1.2	–	0.8	–	0.5	–	0.5	–	0.5	–	1.0
Ne/H(10^{-4})	–	1.4	–	1.6	–	2.	–	2.	–	2.	–	2.0
S/H (10^{-4})	–	0.4	–	0.4	–	0.1	–	0.06	–	0.06	–	0.3
Hβ (erg cm^{-2} s^{-1})	–	3.6×10^{-4}	–	0.003	–	2.3×10^{-4}	–	1.1×10^{-4}	–	0.056	–	3.3×10^{-4}

[1] in 10^{10} phot cm^{-2}s^{-1}eV^{-1} at the Lyman limit ($\alpha_{UV} = -1.5$, $\alpha_X = -0.7$);

Table C.2: Simulation for $V < 0$ of the N2 region of IC 5063. For each bin there are the observed quantities and the results of the models. The first nine rows show the comparison between the observed and the synthetic spectra, the remaining rows show the input parameters of each model.

	bin -1		bin -2		bin -3		bin -4	
line	obs.	mod.	obs.	mod.	obs.	mod.	obs.	mod.
[O II]λ3727+	2.92	2.83	2.2	2.1	8.6	10.2	20.3	24.
[Ne III]λ3869+	1.68	1.6	1.13	1.3	1.53	3.0	0.74	1.5
[He II]λ4686	0.14	0.39	0.1	0.3	0.0	0.8	0.0	0.1
[O III]λ5007+	11.7	11.9	9.4	9.97	11.8	11.2	15.	14.
[O I]λ6300,[S II]λ6310	0.22	0.17	0.21	0.2	0.11	1.0	0.2	0.2
Hα	2.86	3.18	2.86	2.89	2.86	3.9	2.86	4.4
[N II]λ6584	1.5	1.2	1.77	1.8	1.53	3.6	2.13	2.9
[S II]λ6716	0.63	0.5	1.08	0.5	0.42	1.6	0.4	0.5
[S II]λ6731	0.49	0.7	0.75	1.2	0.33	1.2	0.24	0.6
FWHM(km s^{-1})	-100	–	-200	–	-300	–	-400	–
V_s (km s^{-1})	–	100	–	200	–	300	–	400
n_0(cm^{-3})	–	210	–	500	–	16	–	100
D(10^{18} cm)	–	0.0015	–	0.004	–	10.	–	0.09
F (units[1])	–	0.45	–	5.6	–	0.6	–	0.0
O/H (10^{-4})	–	6.6	–	6.6	–	5.6	–	6.6
N/H (10^{-4})	–	0.9	–	0.7	–	0.5	–	0.6
Ne/H(10^{-4})	–	1.6	–	1.2	–	1.0	–	0.6
S/H (10^{-4})	–	0.6	–	0.6	–	0.1	–	0.05
Hβ (erg)	–	7.4×10^{-4}	–	0.09	–	0.004	–	3.8×10^{-4}

[1] in 10^{10} phot cm^{-2}s^{-1}eV^{-1} at the Lyman limit ($\alpha_{UV} = -1.5$, $\alpha_X = -0.7$);

Table C.3: Simulation for $v \geq 0$ of the N1 region of IC 5063. For each bin there are the observed quantities and the results of the models. The first nine rows show the comparison between the observed and the synthetic spectra, the remaining rows show the input parameters of each model.

	bin 0		bin 1		bin 2		bin 3		bin 4		bin 5		bin 6	
line	obs.	mod.	obs.	mod.	obs.	mod.	obs.	mod.	obs.	mod.	obs.	mod.	obs.	mod.
[O II]λ3727+	2.6	2.4	3.20	3.25	4.14	4.4	4.3	4.1	4.54	4.7	3.16	3.1	1.83	1.9
[Ne III]λ3869+	1.26	1.1	2.1	1.1	1.9	2.4	1.17	1.3	1.56	1.2	0.95	1.0	0.5	0.76
[He II]λ4686	0.165	0.4	0.1	0.24	0.04	0.26	0.0	0.2	0.	0.2	0.0	0.17	0.0	0.14
[O III]λ5007+	10.26	10.2	7.91	7.5	7.11	7.1	5.6	5.3	5.48	5.53	5.9	5.9	5.0	5.1
[O I]λ6300,[S II]λ6310	0.31	0.15	0.38	0.15	0.44	0.9	0.46	0.5	0.43	0.45	0.45	0.5	0.66	0.7
Hα	2.86	3.0	2.86	3.2	2.86	2.96	2.86	3.	2.86	3.0	2.86	3.	2.56	3.
[N II]λ6584	1.65	1.7	1.81	1.94	1.8	1.6	1.78	1.5	1.9	2.0	2.47	2.6	3.44	2.4
[S II]λ6716	0.66	0.7	0.74	0.6	0.7	1.0	0.6	0.55	0.72	0.55	0.46	0.42	1.33	0.6
[S II]λ6731	0.61	0.8	0.71	0.84	0.72	1.4	0.64	0.88	0.66	0.84	0.86	0.7	1.05	1.0
FWHM(km s^{-1})	0.0	–	100	–	200	–	300	–	400	–	500	–	600	–
V_s (km s^{-1})	–	50	–	100	–	220	–	300	–	400	–	500	–	600
n_0(cm^{-3})	–	240	–	210	–	300	–	300	–	150	–	140	–	130
D(10^{18} cm)	–	0.0015	–	0.0016	–	0.6	–	0.6	–	1.	–	0.1	–	0.2
F (units[1])	–	0.22	–	0.26	–	2.4	–	2.4	–	1.4	–	2.5	–	4
O/H (10^{-4})	–	6.6	–	6.7	–	6.3	–	6.6	–	6.6	–	6.6	–	6.6
N/H (10^{-4})	–	1.2	–	1.2	–	0.5	–	0.5	–	0.5	–	0.9	–	1.2
Ne/H(10^{-4})	–	1.4	–	1.4	–	1.4	–	1.	–	1.	–	1.	–	1.
S/H (10^{-4})	–	0.6	–	0.6	–	0.07	–	0.07	–	0.07	–	0.1	–	0.2
Hβ(erg cm^{-2} s^{-1})	–	$1. \times 10^{-4}$	–	9.2×10^{-4}	–	0.054	–	0.06	–	0.038	–	0.082	–	0.155

[1] in 10^{10} phot cm^{-2}s^{-1}eV^{-1} at the Lyman limit ($\alpha_{UV} = -1.5$, $\alpha_X = -0.7$);

Table C.4: Simulation for $V < 0$ of the N1 region of IC 5063. For each bin there are the observed quantities and the results of the models. The first nine rows show the comparison between the observed and the synthetic spectra, the remaining rows show the input parameters of each model.

	bin -1		bin -2		bin -3		bin -4		bin -5		bin -6		bin -7	
line	obs.	mod.	obs.	mns1-2	obs.	mod.	obs.	mod.	obs.	mod.	obs.	mod.	obs.	mod.
[O II]λ3727+	2.5	2.56	2.18	2.3	2.44	2.4	2.61	2.9	2.82	2.81	2.62	2.9	0.65	0.82
[Ne III]λ3869+	1.17	1.18	1.1	1.3	1.11	1.4	1.13	1.4	1.32	1.33	1.3	1.4	1.14	0.94
[He II]λ4686	0.127	0.4	0.127	0.38	0.137	0.35	0.129	0.27	0.03	0.29	0.0	0.3	0.0	0.5
[O III]λ5007+	10.84	10.7	10.6	10.5	10.76	10.9	10.2	10.7	9.65	9.8	11.0	10.9	10.6	10.5
[O I]λ6300,[S II]λ6310	0.26	0.15	0.26	0.15	0.26	0.2	0.34	0.22	0.48	0.42	0.55	0.2	0.35	0.05
Hα	2.86	3.1	2.86	2.97	2.86	2.89	2.86	2.88	2.86	2.9	2.86	2.88	2.86	2.9
[N II]λ6584	1.7	1.6	1.72	1.5	1.63	1.8	1.79	2.0	1.86	2.0	1.78	2.0	0.98	0.86
[S II]λ6716	0.85	0.74	0.92	0.4	0.74	0.7	0.68	0.7	0.69	0.61	0.8	0.6	0.75	0.3
[S II]λ6731	0.75	0.63	0.75	0.7	0.66	1.3	0.67	1.5	0.85	1.28	0.78	1.15	0.59	0.65
FWHM(km s^{-1})	-100	–	-200	–	-300	–	-400	–	-500	–	-600	–	-700	–
V_s (km s^{-1})	–	80	–	200	–	300	–	400	–	500	–	600	–	700
n_0(cm^{-3})	–	260	–	250	–	240	–	260	–	280	–	260	–	340
D(10^{18} cm)	–	0.0015	–	0.0025	–	0.011	–	0.011	–	0.011	–	0.011	–	0.0065
F (units[1])	–	0.5	–	1.1	–	3.7	–	5.	–	7.8	–	8.3	–	6.
O/H (10^{-4})	–	6.6	–	6.6	–	6.6	–	6.6	–	6.6	–	6.6	–	6.6
N/H (10^{-4})	–	1.2	–	1.2	–	1.2	–	0.8	–	0.8	–	0.6	–	0.6
Ne/H(10^{-4})	–	1.4	–	1.4	–	1.4	–	1.	–	1.	–	1.	–	1.
S/H (10^{-4})	–	0.6	–	0.6	–	0.6	–	0.3	–	0.3	–	0.3	–	0.3
Hβ (erg cm^{-2} s^{-1})	–	8.7×10^{-4}	–	3.4×10^{-3}	–	0.057	–	0.1	–	0.18	–	0.21	–	0.3

[1] in 10^{10} phot cm^{-2}s^{-1}eV^{-1} at the Lyman limit ($\alpha_{UV} = -1.5$, $\alpha_X = -0.7$);

Table C.5: Simulation for $v \geq 0$ of the N0 region of IC 5063. For each bin there are the observed quantities and the results of the models. The first nine rows show the comparison between the observed and the synthetic spectra, the remaining rows show the input parameters of each model.

	bin 0		bin 1		bin 2		bin 3		bin 4		bin 5		bin 6		bin 7		bin 8	
line	obs.	mod.	obs.	mod.	obs.	mod.	obs.	mod.	obs.	mod.	obs.	mod.	obs.	mod.	obs.	mod.	obs.	mod.
[O II]λ3727+	3.5	3.8	3.25	3.0	3.67	3.3	3.89	4.0	5.2	5.36	6.26	6.3	3.35	3.7	3.64	3.3	3.97	3.96
[Ne III]λ3869+	1.64	1.3	1.58	1.56	1.3	1.58	1.34	1.7	1.81	1.72	1.47	1.6	1.25	1.2	1.23	1.29	0.9	1.2
[He II]λ4686	0.138	0.29	0.11	0.26	0.07	0.2	0.08	0.2	0.1	0.25	0.15	0.3	0.08	0.17	0.11	0.2	0.0	0.2
[O III]λ5007+	9.5	9.4	8.87	8.9	6.48	6.9	6.95	6.84	7.22	7.1	10.7	10.7	5.4	5.48	6.3	6.6	7.6	7.89
[O I]λ6300,[S II]λ6310	0.41	0.32	0.5	0.7	0.57	0.7	0.55	0.7	0.55	0.8	0.56	0.6	0.5	0.3	0.47	0.4	0.64	0.5
Hα	2.86	2.9	2.86	3.0	2.86	2.86	2.86	2.98	2.86	3.0	2.86	2.99	2.86	3.18	2.86	3.18	2.86	3.2
[N II]λ6584	1.85	1.6	2.1	1.7	2.27	2.1	2.18	2.3	2.0	2.2	1.9	2.1	1.93	2.	2.2	2.	2.9	2.8
[S II]λ6716	0.87	0.7	1.1	1.17	1.34	0.8	1.46	0.24	1.33	1.43	1.1	1.0	0.98	0.6	0.63	0.86	0.83	1.
[S II]λ6731	0.72	1.0	0.86	1.76	1.0	1.34	0.97	1.82	0.88	1.9	0.4	1.2	0.91	0.9	0.95	1.2	1.19	1.3
FWHM(km s^{-1})	0.0	–	100	–	200	–	300	–	400	–	500	–	600	–	700	–	800	–
V_s (km s^{-1})	–	58	–	100	–	210	–	280	–	380	–	490	–	600	–	700	–	800
n_0(cm^{-3})	–	420	–	580	–	440	–	300	–	120	–	60	–	80	–	67	–	50
D(10^{18} cm)	–	0.1	–	0.95	–	0.95	–	1.0	–	2.0	–	2.0	–	2.5	–	2.5	–	2.5
F (units[1])	–	2.1	–	5.	–	4.	–	3.	–	1.2	–	0.9	–	1.3	–	2.	–	2.3
O/H (10^{-4})	–	6.6	–	6.6	–	6.6	–	6.6	–	6.6	–	6.6	–	6.6	–	6.6	–	6.6
N/H (10^{-4})	–	0.5	–	0.5	–	0.5	–	0.5	–	0.5	–	0.5	–	0.7	–	0.8	–	0.9
Ne/H(10^{-4})	–	1.2	–	1.2	–	1.2	–	1.2	–	1.2	–	1.0	–	1.3	–	1.3	–	1
S/H (10^{-4})	–	0.12	–	0.12	–	0.12	–	0.12	–	0.12	–	0.08	–	0.1	–	0.16	–	0.16
Hβ (erg cm^{-2} s^{-1})	–	0.068	–	0.12	–	0.09	–	0.07	–	0.028	–	0.017	–	0.041	–	0.07	–	0.5

[1] in 10^{10} phot cm^{-2}s^{-1}eV^{-1} at the Lyman limit ($\alpha_{UV} = -1.5$, $\alpha_X = -0.7$);

Table C.6: Simulation for $V < 0$ of the N0 region of IC 5063. For each bin there are the observed quantities and the results of the models. The first nine rows show the comparison between the observed and the synthetic spectra, the remaining rows show the input parameters of each model.

	bin -1		bin -2		bin -3		bin -4		bin -5		bin -6		bin -7		bin -8	
line	obs.	mns01	obs.	mod.	obs.	mod.	obs.	mod.	obs.	mod.	obs.	mod.	obs.	mod.	obs.	mod.
[O II]λ3727+	2.83	2.84	2.52	2.5	2.27	2.25	2.44	2.6	2.25	2.3	1.81	1.76	2.55	2.4	4.18	4.
[Ne III]λ3869+	1.54	1.3	1.4	1.2	1.2	1.28	1.14	1.3	1.03	1.47	1.11	1.15	1.0	1.37	1.6	1.4
[He II]λ4686	0.09	0.3	0.11	0.36	0.11	0.36	0.09	0.3	0.12	0.26	0.1	0.3	0.0	0.5	0.0	0.6
[O III]λ5007+	10.43	10.5	9.64	9.85	10.33	10.54	10.2	10.5	9.66	9.84	9.97	10.	10.72	10.8	9.64	9.5
[O I]λ6300,[S II]λ6310	0.33	0.15	0.35	0.14	0.35	0.16	0.38	0.17	0.43	0.5	0.5	0.45	0.45	0.5	0.3	0.5
Hα	2.86	3.2	2.86	2.9	2.86	2.9	2.86	2.9	2.86	3.	2.86	3.	2.86	3.2	2.86	3.3
[N II]λ6584	1.75	1.74	1.8	1.9	1.72	2.	1.8	1.95	2.07	2.3	2.49	2.74	2.5	2.5	2.5	2.7
[S II]λ6716	.0.83	0.46	0.89	0.67	0.77	0.57	0.73	0.73	0.85	0.3	0.95	0.5	0.88	0.4	0.64	0.4
[S II]λ6731	0.68	0.680.7	1.16	0.6	1.1	0.6	0.48	0.69	0.6	0.53	0.97	0.73	0.8	0.47	0.77	
FWHM(km s^{-1})	-100	–	-200	–	-300	–	-400	–	-500	–	-600	–	-700	–	-800	–
V$_s$ (km s^{-1})	–	100	–	200	–	300	–	400	–	500	–	600	–	700	–	800
n$_0$(cm^{-3})	–	230	–	200	–	200	–	200	–	260	–	247	–	240	–	170
D(10^{18} cm)	–	0.0015	–	0.012	–	0.012	–	0.012	–	0.05	–	0.05	–	0.06	–	0.11
F (units[1])	–	0.45	–	1.5	–	2.5	–	3.	–	12.2	–	19.	–	53.	–	53.
O/H (10^{-4})	–	6.6	–	6.6	–	6.6	–	6.6	–	6.4	–	6.4	–	6.4	–	6.4
N/H (10^{-4})	–	1.2	–	1.0	–	1.0	–	0.8	–	0.7	–	0.9	–	0.7	–	0.6
Ne/H(10^{-4})	–	1.4	–	1.4	–	1.4	–	1.3	–	1.0	–	0.8	–	0.8	–	0.8
S/H (10^{-4})	–	0.6	–	0.62	–	0.6	–	0.6	–	0.1	–	0.2	–	0.2	–	0.2
Hβ (erg cm^{-2} s^{-1})	–	0.001	–	0.02	–	0.035	–	0.05	–	0.29	–	0.43	–	0.87	–	0.78

[1] in 10^{10} phot cm^{-2}s^{-1}eV^{-1} at the Lyman limit ($\alpha_{UV} = -1.5$, $\alpha_X = -0.7$);

Table C.7: Simulation for $v \geq 0$ of the CN region of IC 5063. For each bin there are the observed quantities and the results of the models. The first nine rows show the comparison between the observed and the synthetic spectra, the remaining rows show the input parameters of each model.

	bin 0		bin 1		bin 2		bin 3		bin 4		bin 5		bin 6		bin 7	
line	obs.	mod.	obs.	mod.	obs.	mod.	obs.	mod.	obs.	mod.	obs.	mod.	obs.	mod.	obs.	mod.
[O II]λ3727+	3.3	3.0	3.	3.3	4.4	4.6	4.65	4.5	6.0	5.7	7.75	7.0	6.87	6.5	4.25	4.1
[Ne III]λ3869+	1.4	1.14	1.4	1.47	1.3	1.7	1.6	1.6	1.93	2.0	2.2	1.5	2.58	2.	1.49	1.45
[He II]λ4686	0.22	0.4	0.2	0.3	0.13	0.29	0.08	0.24	0.07	0.29	0.03	0.29	0.0	0.26	0.0	0.2
[O III]λ5007+	13.0	13.3	14.4	14.6	9.2	9.46	7.36	7.2	8.3	8.6	9.2	9.38	7.56	7.8	7.52	7.5
[O I]λ6300,[S II]λ6310	0.36	0.2	0.34	0.36	0.44	0.8	0.53	0.6	0.49	0.7	0.56	0.6	0.51	0.6	0.49	0.65
Hα	2.87	3.0	2.86	3.4	2.86	2.9	2.86	2.94	2.86	2.86	2.86	2.95	2.86	2.95	2.86	2.95
[N II]λ6584	1.58	1.87	1.45	1.54	1.91	1.85	2.40	2.89	2.2	2.13	2.17	2.2	2.17	2.16	3.62	3.2
[S II]λ6716	0.66	0.62	0.57	0.57	0.98	0.7	1.44	0.6	1.53	0.68	1.65	0.87	1.65	0.8	3.25	1.35
[S II]λ6731	0.54	0.8	0.48	0.95	0.66	1.4	0.88	1.0	0.80	1.0	0.8	1.1	0.8	1.0	1.46	2.
FWHM(km s^{-1})	0.0	–	100	–	200	–	300	–	400	–	500	–	600	–	700	–
V_s (km s^{-1})	–	60	–	150	–	220	–	240	–	440	–	510	–	600	–	700
n_0(cm^{-3})	–	270	–	250	–	240	–	310	–	100	–	60	–	58	–	70
D(10^{18} cm)	–	0.0013	–	0.001	–	0.1	–	0.1	–	0.13	–	0.13	–	0.13	–	0.08
F (units[1])	–	0.36	–	0.74	–	2.6	–	2.6	–	1.8	–	0.7	–	0.68	–	1.5
O/H (10^{-4})	–	6.6	–	6.6	–	5.9	–	6.1	–	5.0	–	6.6	–	6.6	–	6.6
N/H (10^{-4})	–	1.2	–	1.2	–	0.4	–	0.6	–	0.4	–	0.5	–	0.5	–	0.1
Ne/H(10^{-4})	–	1.	–	1.	–	1.	–	1.	–	1.	–	1.	–	1.55	–	1.4
S/H (10^{-4})	–	0.6	–	1.	–	0.08	–	0.08	–	0.08	–	0.1	–	0.1	–	0.3
Hβ (erg cm^{-2} s^{-1})	–	$3.5e-4$	–	$6.4e-4$	–	0.05	–	0.0564	–	0.04	–	0.014	–	0.015	–	0.036

[1] in 10^{10} phot cm^{-2}s^{-1}eV^{-1} at the Lyman limit ($\alpha_{UV} = -1.5$, $\alpha_X = -0.7$);

Table C.8: Simulation for $V < 0$ of the CN region of IC 5063. For each bin there are the observed quantities and the results of the models. The first nine rows show the comparison between the observed and the synthetic spectra, the remaining rows show the input parameters of each model.

	bin -1		bin -2		bin -3		bin -4		bin -5		bin -6		bin -7	
line	obs.	mod.	obs.	mod.	obs.	mod.	obs.	mod.	obs.	mod.	obs.	mod.	obs.	mod.
[O II]λ3727+	3.76	3.7	3.9	3.6	2.5	2.6	2.3	2.48	2.00	2.17	3.15	3.13	$0.+0.43$	$1.+0.5$
[Ne III]λ3869+	1.78	1.77	1.68	1.57	1.5	1.56	1.34	1.6	1.5	1.5	3.05	2.5	1.3	1.4
[He II]λ4686	0.2	0.3	0.15	0.27	0.1	0.25	0.025	0.28	0.0	0.26	0.0	0.36	0.0	0.3
[O III]λ5007+	11.6	11.8	9.57	9.76	9.8	9.6	10.41	10.67	9.84	9.84	12.1	12.3	8.67	8.6
[O I]λ6300,[S II]λ6310	0.32	0.55	0.39	0.47	0.47	0.5	0.44	0.5	0.46	0.45	0.4	0.4	0.4	0.4
Hα	2.86	2.98	2.86	2.99	2.86	3.0	2.86	3.0	2.86	3.0	2.86	2.97	2.86	2.98
[N II]λ6584	1.7	1.99	2.0	2.13	2.36	2.34	2.42	2.5	2.3	2.3	2.72	2.7	1.56	1.89
[S II]λ6716	0.73	0.57	0.83	0.4	0.97	0.4	1.	0.4	0.89	0.3	0.88	0.4	0.9	0.5
[S II]λ6731	0.45	0.82	0.34	0.67	0.37	0.7	0.46	0.7	0.37	0.6	0.47	0.74	1.0	1.0
FWHM(km s^{-1})	-100	–	-200	–	-300	–	-400	–	-500	–	-600	–	-700	–
V$_s$ (km s^{-1})	–	100	–	200	–	300	–	400	–	500	–	600	–	700
n$_0$(cm^{-3})	–	480	–	420	–	420	–	290	–	260	–	200	–	200
D(10^{18} cm)	–	0.68	–	0.68	–	0.68	–	0.05	–	0.05	–	0.047	–	0.042
F (units[1])	–	5.	–	5.	–	10.	–	11.	–	12.2	–	17.	–	19.
O/H (10^{-4})	–	6.	–	6.6	–	6.6	–	6.4	–	6.4	–	6.5	–	6.6
N/H (10^{-4})	–	0.5	–	0.5	–	0.6	–	0.7	–	0.7	–	0.7	–	0.7
Ne/H(10^{-4})	–	1.	–	1.	–	1.	–	1.	–	1.	–	1.5	–	1.3
S/H (10^{-4})	–	0.04	–	0.06	–	0.07	–	0.1	–	0.1	–	0.14	–	0.3
Hβ (erg cm^{-2} s^{-1})	–	0.09	–	0.1	–	0.21	–	0.24	–	0.29	–	0.33	–	0.5

[1] in 10^{10} phot cm^{-2}s^{-1}eV^{-1} at the Lyman limit ($\alpha_{UV} = -1.5$, $\alpha_X = -0.7$);

Table C.9: Simulation for $v \geq 0$ of the CS region of IC 5063. For each bin there are the observed quantities and the results of the models. The first nine rows show the comparison between the observed and the synthetic spectra, the remaining rows show the input parameters of each model.

	bin 0		bin 1		bin 2		bin 3		bin 4		bin 5		bin 6	
line	obs.	mod.	obs.	mod.	obs.	mod.	obs.	mod.	obs.	mod.	obs.	mod.	obs.	mod.
[O II]λ3727+	2.7	2.4	3.13	3.2	4.72	4.9	4.33	4.0	5.5	5.6	2.29	2.6	7.4	7.
[Ne III]λ3869+	1.31	1.37	1.48	1.23	1.9	1.6	2.17	1.17	2.5	2.16	1.22	1.5	4.7	3.7
[He II]λ4686	0.18	0.45	0.17	0.32	0.18	0.21	0.13	0.26	0.1	0.38	0.094	0.45	0.0	0.9
[O III]λ5007+	13.6	13.8	13.42	12.8	12.34	12.36	10.82	10.2	12.12	12.13	12.43	12.2	25.7	24.3
[O I]λ6300,[S II]λ6310	0.27	0.35	0.34	0.3	0.45	0.37	0.5	0.3	0.34	0.6	0.74	1.0	0.44	0.44
Hα	2.86	2.95	2.86	3.3	2.86	3.4	2.86	3.2	2.86	2.98	2.69	3.	2.5	3.8
[N II]λ6584	1.58	1.36	1.56	1.58	2.03	1.9	1.97	2.13	2.32	2.0	4.44	4.2	14.1	11.
[S II]λ6716	0.65	0.6	0.62	0.64	0.9	0.87	0.82	0.95	0.66	0.61	0.48	0.43	0.31	0.24
[S II]λ6731	0.64	0.75	0.59	1.0	0.79	1.3	0.73	1.58	0.80	0.76	1.49	0.8	4.4	0.5
FWHM(km s^{-1})	0.0	–	100	–	200	–	300	–	400	–	500	–	600	–
V_s (km s^{-1})	–	60	–	150	–	180	–	300	–	410	–	500	–	600
n_0(cm^{-3})	–	320	–	220	–	180	–	140	–	70	–	220	–	210
D(10^{18} cm)	–	1.0	–	0.001	–	0.002	–	0.007	–	1.	–	0.1	–	0.17
F (units[1])	–	1.0	–	0.6	–	0.32	–	0.4	–	1.5	–	16.	–	253.
O/H (10^{-4})	–	5.8	–	6.6	–	6.4	–	6.7	–	5.2	–	6.9	–	7.
N/H (10^{-4})	–	0.7	–	1.2	–	1.2	–	1.2	–	0.7	–	0.9	–	2.2
Ne/H(10^{-4})	–	1.	–	1.	–	1.	–	1.	–	1.	–	1.2	–	1.
S/H (10^{-4})	–	0.04	–	1.	–	1.	–	1.	–	0.04	–	0.1	–	0.3
Hβ (erg cm^{-2} s^{-1})	–	0.136	–	7×10^{-4}	–	5×10^{-4}	–	9.2×10^{-4}	–	0.023	–	0.3	–	2.59

[1] in 10^{10} phot cm^{-2}s^{-1}eV^{-1} at the Lyman limit ($\alpha_{UV} = -1.5$, $\alpha_X = -0.7$);

Table C.10: Simulation for $v < 0$ of the CS region of IC 5063. For each bin there are the observed quantities and the results of the models. The first nine rows show the comparison between the observed and the synthetic spectra, the remaining rows show the input parameters of each model.

	bin 1		bin 2		bin 3		bin 4	
line	obs.	mod.	obs.	mod.	obs.	mod.	obs.	mod.
[O II]λ3727+	2.65	2.8	3.14	3.2	5.	5.2	7.8	8.3
[Ne III]λ3869+	1.58	1.3	1.31	1.13	1.37	1.47	0.59	1.3
[He II]λ4686	0.17	0.4	0.08	0.3	0.0	0.23	0.0	0.5
[O III]λ5007+	14.67	14.89	11.6	11.3	11.5	11.9	14.63	14.7
[O I]λ6300,[S II]λ6310	0.36	0.34	0.34	0.3	0.45	0.37	0.94	1.
Hα	2.86	3.3	2.86	3.2	2.86	3.3	2.86	3.
[N II]λ6584	1.73	1.37	1.98	1.6	3.	2.6	8.67	7.
[S II]λ6716	0.8	0.6	0.95	0.8	1.	1.1	1.7	1.1
[S II]λ6731	0.76	1.88	0.85	1.16	0.72	1.8	1.2	1.2
FWHM(km s^{-1})	-100	–	-200	–	-300	–	-400	–
V_s (km s^{-1})	–	150	–	200	–	300	–	410
n_0(cm^{-3})	–	220	–	140	–	140	–	50
D(10^{18} cm)	–	0.001	–	0.004	–	0.007	–	0.7
F (units[1])	–	0.8	–	0.42	–	0.33	–	2.1
O/H (10^{-4})	–	6.6	–	6.4	–	6.6	–	5.5
N/H (10^{-4})	–	1.2	–	1.2	–	1.3	–	1.2
Ne/H(10^{-4})	–	1.	–	1.	–	1.	–	0.5
S/H (10^{-4})	–	1.	–	1.	–	1.	–	0.1
Hβ (erg cm^{-2} s^{-1})	–	6.6×10^{-4}	–	6.3×10^{-4}	–	7×10^{-4}	–	0.029

[1] in 10^{10} phot cm^{-2}s^{-1}eV^{-1} at the Lyman limit ($\alpha_{UV} = -1.5$, $\alpha_X = -0.7$);

Table C.11: Simulation for $v \geq 0$ of the S0 region of IC 5063. For each bin there are the observed quantities and the results of the models. The first nine rows show the comparison between the observed and the synthetic spectra, the remaining rows show the input parameters of each model.

	bin 0		bin 1		bin 2		bin 3		bin 4		bin 5	
line	obs.	mod.	obs.	mod.	obs.	mod.	obs.	mod.	obs.	mod.	obs.	mod.
[O II]λ3727+	2.37	2.4	2.52	3.0	2.98	2.6	3.23	2.9	2.3	2.8	2.07	2.5
[Ne III]λ3869+	1.4	1.34	1.46	2.0	1.59	2.0	1.9	1.7	2.7	2.4	1.5	1.6
[He II]λ4686	0.16	0.44	0.2	0.4	0.2	0.38	0.22	0.3	0.21	0.35	0.25	0.4
[O III]λ5007+	13.2	13.3	13.85	13.5	14.0	14.0	13.2	13.67	14.4	14.46	15.4	14.6
[O I]λ6300,[S II]λ6310	0.33	0.33	0.35	0.7	0.37	0.7	0.28	0.3	0.27	0.21	0.5	0.2
Hα	2.87	2.98	2.86	3.0	2.86	3.0	2.86	2.9	2.86	2.89	2.86	2.88
[N II]λ6584	1.84	1.5	1.88	2.0	1.86	1.98	1.65	1.76	1.74	1.77	2.23	1.9
[S II]λ6716	1.5	0.7	0.83	0.6	0.69	0.44	0.49	0.38	0.44	0.35	0.42	0.47
[S II]λ6731	0.7	0.93	0.76	0.86	0.68	0.74	0.58	0.8	0.63	0.75	0.77	1.0
FWHM(km s^{-1})	0.0	–	100	–	200	–	300	–	400	–	500	–
V_s (km s^{-1})	–	60	–	100	–	180	–	290	–	400	–	500
n_0(cm^{-3})	–	320	–	620	–	620	–	430	–	340	–	300
D(10^{18} cm)	–	1.0	–	0.7	–	0.5	–	0.008	–	0.01	–	0.012
F (units[1])	–	0.95	–	11.	–	23.	–	10.	–	12.	–	15.
O/H (10^{-4})	–	5.8	–	5.8	–	6.6	–	6.6	–	6.1	–	6.5
N/H (10^{-4})	–	0.8	–	0.7	–	0.5	–	0.5	–	0.5	–	0.6
Ne/H(10^{-4})	–	1.	–	1.	–	1.	–	1.	–	1.3	–	1.0
S/H (10^{-4})	–	0.05	–	0.04	–	0.06	–	0.18	–	0.18	–	0.3
Hβ (erg cm^{-2} s^{-1})	–	0.135	–	0.17	–	0.35	–	0.19	–	0.2	–	0.3

[1] in 10^{10} phot cm^{-2}s^{-1}eV^{-1} at the Lyman limit ($\alpha_{UV} = -1.5$, $\alpha_X = -0.7$);

Table C.12: Simulation for $v < 0$ of the S0 region of IC 5063 For each bin there are the observed quantities and the results of the models. The first nine rows show the comparison between the observed and the synthetic spectra, the remaining rows show the input parameters of each model.

	bin 1		bin 2		bin 3		bin 4	
line	obs.	mod.	obs.	mod.	obs.	mod.	obs.	mod.
[O II]λ3727+	2.43	2.68	3.06	2.8	3.58	3.5	5.43	5.47
[Ne III]λ3869+	1.27	1.4	1.35	1.6	2.2	1.6	0.12	1.0
[He II]λ4686	0.15	0.37	0.12	0.3	0.02	0.28	0.0	0.2
[O III]λ5007+	12.97	13.0	12.0	12.0	11.4	11.1	8.98	8.88
[O I]λ6300,[S II]λ6310	0.32	0.46	0.3	0.3	0.41	0.46	0.53	0.4
Hα	2.86	2.9	2.86	2.9	2.86	2.9	2.86	2.96
[N II]λ6584	1.9	1.9	2.07	2.2	2.18	2.	3.22	3.86
[S II]λ6716	0.9	0.53	1.09	0.54	0.92	0.5	0.98	0.82
[S II]λ6731	0.8	1.1	0.9	1.1	1.0	1.0	0.72	1.3
FWHM(km s^{-1})	-100	–	-200	–	-300	–	-400	–
V_s (km s^{-1})	–	100	–	170	–	300	–	400
n_0(cm^{-3})	–	850	–	600	–	370	–	130
D(10^{18} cm)	–	0.007	–	0.01	–	0.008	–	0.08
F (units[1])	–	9.2	–	7.	–	6.	–	2.2
O/H (10^{-4})	–	5.	–	6.6	–	6.6	–	6.1
N/H (10^{-4})	–	0.5	–	0.6	–	0.5	–	0.8
Ne/H(10^{-4})	–	0.7	–	1.	–	1.	–	0.7
S/H (10^{-4})	–	0.2	–	0.2	–	0.18	–	0.12
Hβ (erg cm^{-2} s^{-1})	–	0.14	–	0.168	–	0.12	–	0.054

[1] in 10^{10} phot cm^{-2}s^{-1}eV^{-1} at the Lyman limit ($\alpha_{UV} = -1.5$, $\alpha_X = -0.7$);

Table C.13: Simulation for $v \geq 0$ of the S1 region of IC 5063. For each bin there are the observed quantities and the results of the models. The first nine rows show the comparison between the observed and the synthetic spectra, the remaining rows show the input parameters of each model.

	bin 0		bin 1		bin 2		bin 3		bin 4		bin 5		bin 6	
line	obs.	mod.	obs.	mod.	obs.	mod.	obs.	mod.	obs.	mod.	obs.	mod.	obs.	mod.
[O II]λ3727+	3.26	3.0	2.5	2.86	2.88	3.1	4.7	4.2	6.3	6.8	13.9	12.2	19.	18.
[Ne III]λ3869+	1.7	1.3	1.6	1.8	1.7	1.7	2.6	2.1	3.3	3.0	4.9	3.9	1.4	3.
[He II]λ4686	0.15	0.4	0.2	0.44	0.22	0.4	0.22	0.34	0.12	0.9	0.0	0.84	0.0	0.6
[O III]λ5007+	13.22	13.2	14.64	14.7	14.65	14.5	12.54	13.0	14.0	13.86	17.7	17.0	19.97	19
[O I]λ6300,[S II]λ6310	0.29	0.2	0.33	0.7	0.32	0.7	0.24	0.7	0.29	1.0	0.25	0.4	0.04	0.2
Hα	2.87	3.0	2.86	3.0	2.86	3.0	2.86	3.0	2.86	3.8	2.86	3.4	2.86	3.5
[N II]λ6584	1.82	1.85	1.7	2.0	1.6	1.97	1.49	2.3	1.71	2.8	2.3	2.77	1.87	2.7
[S II]λ6716	0.77	0.62	0.82	0.6	0.59	0.33	0.4	0.38	0.31	0.46	0.6	0.5	0.8	0.7
[S II]λ6731	0.7	0.8	0.69	0.8	0.55	0.55	0.5	0.6	0.56	0.87	0.97	1.0	0.7	1.
FWHM(km s^{-1})	0.0	–	100	–	200	–	300	–	400	–	500	–	600	–
V$_s$ (km s^{-1})	–	60	–	90	–	200	–	320	–	430	–	510	–	600
n$_0$(cm^{-3})	–	270	–	810	–	420	–	250	–	230	–	150	–	80
D(10^{18} cm)	–	0.0013	–	0.5	–	0.22	–	0.6	–	0.13	–	0.3	–	0.92
F (units[1])	–	0.36	–	15.	–	18.	–	11.	–	70.	–	90.	–	65.
O/H (10^{-4})	–	6.6	–	5.8	–	6.6	–	6.6	–	6.5	–	6.9	–	7.1
N/H (10^{-4})	–	1.2	–	0.5	–	0.5	–	0.5	–	0.4	–	1.2	–	0.4
Ne/H(10^{-4})	–	1.2	–	0.8	–	0.8	–	1.	–	1.0	–	1.2	–	1.
S/H (10^{-4})	–	0.6	–	0.04	–	0.04	–	0.04	–	0.2	–	0.4	–	0.3
Hβ (erg cm^{-2} s^{-1})	–	$3.5e-4$	–	0.21	–	0.26	–	0.166	–	0.6	–	1.16	–	0.79

[1] in 10^{10} phot cm^{-2}s^{-1}eV^{-1} at the Lyman limit ($\alpha_{UV} = -1.5$, $\alpha_X = -0.7$);

Table C.14: Simulation for $V < 0$ of the S1 region of IC 5063. For each bin there are the observed quantities and the results of the models. The first nine rows show the comparison between the observed and the synthetic spectra, the remaining rows show the input parameters of each model.

	bin 1		bin 2		bin 3		bin 4	
line	obs.	mod.	obs.	mod.	obs.	mod.	obs.	mod.
[O II]λ3727+	3.1	2.93	3.88	3.7	6.06	6.3	284.4	70.
[Ne III]λ3869+	1.55	1.55	1.55	1.4	1.81	2.0	–	–
[He II]λ4686	0.14	0.37	0.09	0.3	0.0	0.3	0.0	–
[O III]λ5007+	12.5	12.55	11.7	11.7	8.57	8.8	23.55	42.
[O I]λ6300,[S II]λ6310	0.24	0.6	0.23	0.5	0.28	2.0	0.31	0.2
Hα	2.86	3.0	2.86	2.97	2.86	3.0	2.86	5.9
[N II]λ6584	1.87	2.0	1.95	2.1	1.98	1.8	2.8	2.
[S II]λ6716	0.8	0.5	0.9	0.5	0.75	0.97	0.48	0.4
[S II]λ6731	0.73	0.74	0.84	0.84	0.96	1.07	0.37	0.3
FWHM(km s^{-1})	-100	–	-200	–	-300	–	-400	–
V_s (km s^{-1})	–	96	–	200	–	300	–	400
n_0(cm^{-3})	–	760	–	400	–	130	–	20
D(10^{18} cm)	–	0.5	–	0.22	–	3.	–	0.186
F (units[1])	–	9.5	–	6.	–	1.2	–	0.0
O/H (10^{-4})	–	5.8	–	6.6	–	6.5	–	6.5
N/H (10^{-4})	–	0.5	–	0.5	–	0.3	–	0.2
Ne/H(10^{-4})	–	0.8	–	0.8	–	0.8	–	0.1
S/H (10^{-4})	–	0.04	–	0.06	–	0.04	–	0.01
Hβ (erg cm^{-2} s^{-1})	–	0.16	–	0.11	–	0.026	–	2.6×10^{-5}

[1] in 10^{10} phot cm^{-2}s^{-1}eV^{-1} at the Lyman limit ($\alpha_{UV} = -1.5$, $\alpha_X = -0.7$);

Table C.15: Simulation for $V \geq 0$ of the S2 region of IC 5063. For each bin there are the observed quantities and the results of the models. The first nine rows show the comparison between the observed and the synthetic spectra, the remaining rows show the input parameters of each model.

	bin 0		bin 1		bin 2		bin 3	
line	obs.	mod.	obs.	mod.	obs.	mod.	obs.	mod.
[O II]λ3727+	2.54	2.4	2.38	2.5	2.6	2.8	2.53	2.0
[Ne III]λ3869+	1.87	1.3	1.6	1.5	1.9	2.4	1.5	1.75
[He II]λ4686	0.09	0.4	0.15	0.49	0.19	0.5	0.05	0.28
[O III]λ5007+	11.0	11.7	14.2	14.2	16.15	16.16	11.0	11.5
[O I]λ6300,[S II]λ6310	0.25	0.2	0.3	0.24	0.36	0.7	0.3	0.6
Hα	2.86	3.0	2.86	3.0	2.86	3.1	2.86	3.0
[N II]λ6584	1.74	1.64	1.66	1.4	1.66	2.1	1.3	1.7
[S II]λ6716	0.87	0.6	0.87	0.53	0.87	0.37	0.3	0.3
[S II]λ6731	0.69	0.7	0.65	0.75	0.55	0.67	0.4	0.5
FWHM(km s^{-1})	0.0	–	100	–	200	–	300	–
V_s (km s^{-1})	–	55	–	100	–	200	–	300
n_0(cm^{-3})	–	270	–	220	–	520	–	520
D(10^{18} cm)	–	0.0015	–	0.0014	–	0.1	–	0.1
F (units[1])	–	0.34	–	0.6	–	33.	–	23.
O/H (10^{-4})	–	6.6	–	6.6	–	6.6	–	6.6
N/H (10^{-4})	–	1.2	–	1.2	–	0.5	–	0.5
Ne/H(10^{-4})	–	1.4	–	1.4	–	1.0	–	1.0
S/H (10^{-4})	–	0.6	–	0.8	–	0.06	–	0.06
Hβ (erg cm^{-2} s^{-1})	–	3.2×10^{-4}	–	$6.6e-4$	–	0.39	–	0.44

[1] in 10^{10} phot cm^{-2}s^{-1}eV^{-1} at the Lyman limit ($\alpha_{UV} = -1.5$, $\alpha_X = -0.7$);

Table C.16: Simulation for $V < 0$of the S2 region of IC 5063. For each bin there are the observed quantities and the results of the models. The first nine rows show the comparison between the observed and the synthetic spectra, the remaining rows show the input parameters of each model.

	bin -1		bin -2		bin -3	
line	obs.	mod.	obs.	mod.	obs.	mod.
[O II]λ3727+	2.66	2.8	2.37	2.4	3.85	3.87
[Ne III]λ3869+	1.84	1.54	1.2	1.4	1.54	1.46
[He II]λ4686	0.09	0.3	0.0	0.2	0.0	0.2
[O III]λ5007+	10.2	10.2	7.36	7.33	7.1	7.3
[O I]λ6300,[S II]λ6310	0.25	0.5	0.29	0.4	0.93	0.8
Hα	2.86	3.0	2.86	2.98	2.86	2.95
[N II]λ6584	1.88	1.7	1.88	1.98	2.47	2.6
[S II]λ6716	0.69	0.66	0.69	0.5	0.57	0.4
[S II]λ6731	0.64	0.99	0.65	0.815	0.54	0.6
FWHM(km s^{-1})	-100	–	-200	–	-300	–
V_s (km s^{-1})	–	100	–	200	–	300
n_0(cm^{-3})	–	600	–	600	–	280
D(10^{18} cm)	–	1.0	–	0.2	–	0.32
F (units[1])	–	6.9	–	7.0	–	3.2
O/H (10^{-4})	–	6.0	–	6.0	–	6.0
N/H (10^{-4})	–	0.5	–	0.8	–	1.
Ne/H(10^{-4})	–	1.0	–	1.0	–	1.
S/H (10^{-4})	–	0.06	–	0.08	–	0.05
Hβ (erg cm^{-2} s^{-1})	–	0.14	–	0.16	–	0.07

[1] in 10^{10} phot cm^{-2}s^{-1}eV^{-1} at the Lyman limit ($\alpha_{UV} = -1.5$, $\alpha_X = -0.7$);

C.2 NGC 7212

Table C.17: Simulations for $V \geq 0$ of the N2 region of NGC 7212. For each bin there are the observed quantities and the results of the models. The first nine rows show the comparison between the observed and the synthetic spectra, the remaining rows show the input parameters of each model.

	bin 0		bin 1		bin 2		bin 3		bin 4	
line	obs.	mod.	obs.	mod.	obs.	mod.	obs.	mod.	obs.	mod.
[O II]λ3727+	4.2	4.6	3.06	3.07	2.72	2.76	2.8	2.7	1.83	1.6
[O III]λ5007+	10.8	10.9	9.5	9.11	7.88	7.7	6.0	6.2	3.99	4.5
[O I]λ6300+,[S II]λ6310	0.39	0.3	0.4	0.5	0.42	0.4	1.26	1.3	1.8	0.7
Hα	2.86	2.9	2.86	3.0	2.86	3.0	2.12	3.0	1.05	3.4
[N II]λ6584	1.72	1.75	1.63	1.68	1.8	2.0	2.0	1.96	1.18	0.84
[S II]λ6716	0.93	0.9	0.85	0.69	0.87	0.6	1.11	0.7	1.03	0.5
[S II]λ6731	0.7	1.13	0.61	1.	0.62	1.	0.72	1.1	0.8	0.85
FWHM(km s^{-1})	0.0	–	100	–	200	–	300	–	400	–
V_s (km s^{-1})	–	55	–	100	–	200	–	300	–	400
n_0(cm^{-3})	–	220	–	580	–	530	–	430	–	200
D(10^{18}cm)	–	0.12	–	0.95	–	0.85	–	0.85	–	0.85
F (units[1])	–	0.25	–	0.89	–	4.0	–	5.0	–	2.5
O/H (10^4)	–	6.6	–	6.6	–	6.6	–	6.6	–	6.6
N/H (10^4)	–	0.6	–	0.5	–	0.5	–	0.5	–	0.5
Ne/H(10^4)	–	1.	–	1.2	–	1.2	–	1.2	–	1.2
S/H (10^4)	–	0.15	–	0.07	–	0.1	–	0.12	–	0.16
Hβ (erg cm^{-2} s^{-1})	–	0.019	–	0.12	–	0.14	–	0.156	–	0.255

[1] in 10^{10} phot cm^{-2}s^{-1}eV^{-1} at the Lyman limit ($\alpha_{UV} = -1.5$, $\alpha_X = -0.7$);

Table C.18: Simulations for $V < 0$ of the N2 region of NGC 7212. For each bin there are the observed quantities and the results of the models. The first nine rows show the comparison between the observed and the synthetic spectra, the remaining rows show the input parameters of each model.

	bin -1		bin -2		bin -3	
line	obs.	mod.	obs.	mod.	obs.	mod.
[O II]λ3727+	3.14	3.1	2.05	2.2	0.94	0.91
[O III]λ5007+	10.7	10.4	8.6	8.3	4.84	4.53
[O I]λ6300+,[S II]λ6310	0.48	0.5	–	–	0.66	0.5
Hα	2.86	3.	2.86	3.06	0.37	3.37
[N II]λ6584	2.	1.7	2.12	1.6	0.96	0.96
[S II]λ6716	1.04	0.76	1.2	1.1	0.1	0.24
[S II]λ6731	0.89	1.13	1.4	1.9	0.19	0.4
FWHM(km s^{-1})	-100	–	-200	–	-300	–
V_s (km s^{-1})	–	100	–	200	–	300
n_0(cm^{-3})	–	580	–	600	–	500
D(10^{18}cm)	–	0.95	–	0.92	–	0.93
F (units[1])	–	6.0	–	9	–	18
O/H (10^4)	–	6.6	–	6.6	–	6.6
N/H (10^4)	–	0.5	–	0.7	–	1.0
Ne/H(10^4)	–	1.2	–	1.2	–	1.2
S/H (10^4)	–	0.07	–	0.2	–	0.1
Hβ (erg cm^{-2} s^{-1})	–	0.13	–	0.2	–	0.7

[1] in 10^{10} phot cm^{-2}s^{-1}eV^{-1} at the Lyman limit ($\alpha_{UV} = -1.5$, $\alpha_X = -0.7$);

Table C.19: Simulations for $V \geq 0$ of the N1 region of NGC 7212. For each bin there are the observed quantities and the results of the models. The first nine rows show the comparison between the observed and the synthetic spectra, the remaining rows show the input parameters of each model.

	bin 0		bin 1		bin 2		bin 3		bin 4	
line	obs.	mod.	obs.	mod.	obs.	mod.	obs.	mod.	obs.	mod.
[O II]λ3727+	3.33	3.3	3.85	3.6	4.10	4.37	4.49	4.32	4.28	4.36
[Ne III]λ3869+	1.3	1.34	1.47	1.5	1.5	1.6	1.7	1.74	2.	1.54
He II λ4686	0.13	0.33	0.18	0.4	0.15	0.3	0.0	0.26	0.0	0.22
[O III]λ5007+	10.75	10.7	12.9	13.0	12.48	12.45	8.74	8.9	7.3	7.46
[O I]λ6300+,[S II]λ6310	0.46	0.12	0.54	0.13	0.5	0.6	0.35	0.5	0.63	0.7
Hα	2.86	3.2	2.86	2.9	2.86	2.95	2.86	2.99	2.38	2.94
[N II]λ6584	2.05	2.15	1.95	2.4	1.86	2.0	2.2	2.1	2.08	1.7
[S II]λ6716	1.16	0.5	1.06	0.85	0.75	0.5	1.18	0.5	0.7	0.42
[S II]λ6731	0.9	0.6	0.73	1.1	0.6	0.9	0.91	0.93	0.66	0.78
FWHM(km s^{-1})	0.0	–	100	–	200	–	300	–	400	–
V_s (km s^{-1})	–	55	–	100	–	200	–	300	–	400
n_0(cm^{-3})	–	270	–	170	–	300	–	320	–	200
D(10^{18}cm)	–	0.0015	–	0.045	–	0.03	–	0.03	–	0.02
F (units[1])	–	0.25	–	0.89	–	4.0	–	5.0	–	2.5
O/H (10^4)	–	6.6	–	6.6	–	6.6	–	6.6	–	6.6
N/H (10^4)	–	1.2	–	1.2	–	0.5	–	0.4	–	0.4
Ne/H(10^4)	–	1.4	–	1.4	–	1.0	–	1.0	–	1.2
S/H (10^4)	–	0.4	–	0.4	–	0.1	–	0.1	–	0.1
Hβ (erg cm^{-2} s^{-1})	–	3.6×10^{-4}	–	0.011	–	0.07	–	0.12	–	0.06

[1] in 10^{10} phot cm^{-2}s^{-1}eV^{-1} at the Lyman limit ($\alpha_{UV} = -1.5$, $\alpha_X = -0.7$);

Table C.20: Simulations for $V < 0$ of the N1 region of NGC 7212. For each bin there are the observed quantities and the results of the models. The first nine rows show the comparison between the observed and the synthetic spectra, the remaining rows show the input parameters of each model.

	bin -1		bin -2		bin -3	
line	obs.	mod.	obs.	mod.	obs.	mod.
[O II]λ3727+	2.85	2.76	5.7	5.9	3.85	4.1
[Ne III]λ3869+	1.9	1.45	2.84	2.8	3.4	2.2
He II λ4686	0.15	0.4	0.27	0.47	0.0	0.4
[O III]λ5007+	11.	11.1	13.8	14.	14.14	14.
[O I]λ6300+,[S II]λ6310	0.37	0.22	0.28	0.5	0.06	0.1
Hα	2.86	3.0	2.86	2.97	2.86	2.9
[N II]λ6584	2.1	1.73	2.	2.7	2.37	2.2
[S II]λ6716	1.09	0.63	1.	1.3	0.93	0.82
[S II]λ6731	0.96	0.85	1.16	1.4	1.24	1.35
FWHM(km s^{-1})	-100	–	-200	–	-300	–
V_s (km s^{-1})	–	90	–	200	–	300
n_0(cm^{-3})	–	200	–	80	–	140
D(10^{18}cm)	–	0.0016	–	0.48	–	0.05
F (units[1])	–	0.37	–	1.1	–	3.3
O/H (10^4)	–	6.6	–	6.6	–	6.6
N/H (10^4)	–	1.4	–	1.2	–	1.2
Ne/H(10^4)	–	1.6	–	1.6	–	1.6
S/H (10^4)	–	0.8	–	0.1	–	0.2
Hβ (erg cm^{-2} s^{-1})	–	5.2×10^{-4}	–	0.015	–	0.055

[1] in 10^{10} phot cm^{-2}s^{-1}eV^{-1} at the Lyman limit ($\alpha_{UV} = -1.5$, $\alpha_X = -0.7$);

Table C.21: Simulations for $v \geq 0$ of the region N0 of NGC 7212. For each bin there are the observed quantities and the results of the models. The first nine rows show the comparison between the observed and the synthetic spectra, the remaining rows show the input parameters of each model.

	bin 0		bin 1		bin 2		bin 3		bin 4		bin 5		bin 6		bin 7	
line	obs.	mod.	obs.	mod.	obs.	mod.	obs.	mod.	obs.	mod.	obs.	mod.	obs.	mod.	obs.	mod.
[O II]λ3727+	3.85	3.82	3.9	4.18	5.0	5.0	8.93	8.6	5.26	5.4	2.98	3.27	6.	5.9	8.1	8.3
[Ne III]λ3869+	2.0	1.9	1.85	1.84	2.05	2.09	3.6	3.22	2.79	2.33	3.1	2.2	2.6	2.5	0.4	1.3
He II λ4686	0.21	0.36	0.2	0.3	0.17	0.4	0.25	0.4	0.14	0.28	0.19	0.2	0.0	0.27	0.0	0.3
[O III]λ5007+	13.2	13.78	12.6	12.5	12.43	12.58	13.44	13.3	9.89	10.0	7.98	7.99	8.59	8.5	9.2	9.2
[O I]λ6300+,[S II]λ6310	0.56	0.22	0.6	0.3	0.61	0.60	0.56	0.51	0.5	0.5	0.54	0.7	0.71	0.9	0.59	0.6
Hα	2.86	3.2	2.86	3.2	2.86	2.9	2.86	3.02	2.86	2.98	2.86	3.13	2.86	3.	2.86	3.
[N II]λ6584	2.0	2.15	2.05	1.7	1.95	2.4	1.88	1.6	1.88	1.7	1.62	1.4	1.78	2.	2.25	2.4
[S II]λ6716	1.0	0.9	0.91	0.87	0.73	1.0	0.73	0.78	1.07	0.85	1.04	0.6	0.4	0.68	0.52	0.7
[S II]λ6731	0.95	1.0	0.83	1.1	0.8	1.5	0.81	1.0	0.93	1.2	0.67	0.74	0.83	0.89	0.98	0.6
FWHM(km s^{-1})	0.0	–	100	–	200	–	300	–	400	–	500	–	600	–	700	–
V_s (km s^{-1})	–	53	–	100	–	200	–	300	–	400	–	500	–	600	–	700
n_0(cm^{-3})	–	250	–	180	–	120	–	100	–	100	–	100	–	60	–	20
D(10^{18}cm)	–	0.0013	–	0.0027	–	0.17	–	0.28	–	0.5	–	0.5	–	0.25	–	1.1
F (units[1])	–	0.21	–	0.26	–	2.6	–	2.7	–	1.7	–	3.0	–	0.9	–	0.2
O/H (10^4)	–	6.6	–	6.6	–	6.6	–	6.6	–	6.6	–	6.6	–	6.6	–	6.6
N/H (10^4)	–	1.2	–	1.2	–	0.7	–	0.3	–	0.4	–	0.5	–	0.5	–	0.5
Ne/H(10^4)	–	1.5	–	1.5	–	1.5	–	1.5	–	1.5	–	1.9	–	1.7	–	0.8
S/H (10^4)	–	0.6	–	0.9	–	0.2	–	0.08	–	0.08	–	0.08	–	0.08	–	0.05
Hβ (erg cm^{-2} s^{-1})	–	1.7×10^{-4}	–	3.6×10^{-4}	–	0.048	–	0.047	–	0.033	–	0.077	–	0.02	–	0.004

[1] in 10^{10} phot cm^{-2}s^{-1}eV^{-1} at the Lyman limit ($\alpha_{UV} = -1.5$, $\alpha_X = -0.7$);

Table C.22: Simulations for $V < 0$ of the region N0 of NGC 7212. For each bin there are the observed quantities and the results of the models. The first nine rows show the comparison between the observed and the synthetic spectra, the remaining rows show the input parameters of each model.

	bin -1		bin -2		bin -3		bin -4		bin -5		bin -6		bin -7	
line	obs.	mod.	obs.	mod.	obs.	mod.	obs.	mod.	obs.	mod.	obs.	mod.	obs.	mod.
[O II]λ3727+	4.04	4.4	3.78	3.8	4.5	4.1	4.58	4.9	3.5	3.57	9.1	9.3	3.65	30
[Ne III]λ3869+	1.94	1.95	1.5	2.	1.78	1.9	2.16	2.	1.7	1.89	7.5	3.1	6.95	1.8
He II λ4686	0.25	0.3	0.2	0.39	0.18	0.39	0.3	0.4	0.57	0.32	0.0	0.7	0.0	0.25
[O III]λ5007+	13.7	13.3	14.	14.2	14.7	14.7	14.98	15.	13.	12.83	17.4	17.	9.5	9.4
[O I]λ6300+,[S II]λ6310	0.47	0.32	0.47	0.32	0.43	0.35	0.08	0.2	0.56	0.67	0.35	0.6	0.57	0.5
Hα	2.86	3.16	2.86	2.89	2.86	2.9	2.86	2.9	2.86	2.93	2.86	3.1	2.86	3.
[N II]λ6584	1.99	1.8	1.9	2.	1.57	1.5	0.99	1.2	0.42	0.6	0.1	2.	0.013	0.6
[S II]λ6716	0.95	0.91	0.88	0.74	0.74	0.73	0.74	0.62	0.73	0.5	0.48	0.8	0.5	0.57
[S II]λ6731	0.92	1.2	0.83	1.2	0.77	1.26	0.55	1.0	1.0	0.93	0.86	0.8	0.12	0.9
FWHM(km s^{-1})	-100	–	-200	–	-300	–	-400	–	-500	–	-600	–	-700	–
V_s (km s^{-1})	–	100	–	200	–	300	–	400	–	500	–	600	–	700
n_0(cm^{-3})	–	180	–	220	–	160	–	120	–	150	–	30	–	64
D(10^{18}cm)	–	0.0013	–	0.04	–	0.043	–	0.052	–	0.05	–	1.7	–	1.
F (units[1])	–	0.26	–	4.5	–	4.7	–	3.6	–	6.8	–	3.0	–	2.7
O/H (10^4)	–	6.6	–	6.6	–	6.6	–	6.6	–	6.6	–	6.6	–	6.6
N/H (10^4)	–	1.2	–	0.7	–	0.8	–	0.6	–	0.6	–	0.6	–	0.6
Ne/H(10^4)	–	1.5	–	1.5	–	1.3	–	1.3	–	1.3	–	1.3	–	1.3
S/H (10^4)	–	0.3	–	0.2	–	0.2	–	0.15	–	0.15	–	0.15	–	0.1
Hβ (erg cm^{-2} s^{-1})	–	$3.4e-4$	–	0.08	–	0.07	–	0.06	–	0.13	–	0.03	–	0.06

[1] in 10^{10} phot cm^{-2}s^{-1}eV^{-1} at the Lyman limit ($\alpha_{UV} = -1.5$, $\alpha_X = -0.7$);

Table C.23: Simulations for $V \geq 0$ of the region CN of NGC 7212, part 1. For each bin there are the observed quantities and the results of the models. The first nine rows show the comparison between the observed and the synthetic spectra, the remaining rows show the input parameters of each model.

	bin 0		bin 1		bin 2		bin 3		bin 4		bin 5	
line	obs.	mod.	obs.	mod.	obs.	mod.	obs.	mod.	obs.	mod.	obs.	mod.
[O II]λ3727+	2.82	2.65	2.93	3.01	3.04	3.17	3.18	3.05	3.61	3.56	3.39	3.7
[Ne III]λ3869+	1.96	1.94	2.0	2.1	2.09	2.08	2.22	2.3	2.07	2.74	2.54	2.4
He II λ4686	0.24	0.56	0.24	0.4	0.24	0.4	0.23	0.49	0.25	0.52	0.24	0.5
[O III]λ5007+	14.8	14.9	15.6	15.1	15.34	15.0	14.9	14.9	14.65	14.5	13.87	13.4
[O I]λ6300,[S II]λ6310	0.61	0.75	0.62	0.74	0.61	0.64	0.6	1.0	0.60	0.8	0.72	0.85
Hα	2.86	2.92	2.86	3.04	2.86	3.03	2.86	3.2	2.86	3.24	2.86	3.33
[N II]λ6584	1.99	2.12	1.94	1.98	1.91	2.0	1.88	2.14	1.79	2.3	1.79	2.28
[S II]λ6716	0.72	0.68	0.64	0.67	0.61	0.5	0.55	0.44	0.41	0.37	0.49	0.34
[S II]λ6731	0.85	0.78	0.78	1.0	0.72	0.81	0.69	0.76	0.61	0.66	0.64	1.61
FWHM(km s^{-1})	0.0	–	100	–	200	–	300	–	400	–	500	–
V_s (km s^{-1})	–	60	–	90	–	200	–	300	–	400	–	510
n_0(cm^{-3})	–	230	–	800	–	450	–	350	–	240	–	190
D(10^{18}cm)	–	1.0	–	0.7	–	1.5	–	0.2	–	0.16	–	0.14
F (units[1])	–	0.97	–	15.	–	14.	–	30.	–	26.	–	25.
O/H (10^4)	–	5.8	–	6.5	–	6.5	–	6.6	–	6.6	–	6.6
N/H (10^4)	–	0.8	–	0.5	–	0.5	–	0.5	–	0.5	–	0.5
Ne/H(10^4)	–	1.2	–	1.0	–	1.0	–	1.0	–	1.2	–	1.1
S/H (10^4)	–	0.04	–	0.05	–	0.05	–	0.06	–	0.06	–	0.07
Hβ (erg cm^{-2} s^{-1})	–	0.06	–	0.22	–	0.21	–	0.37	–	0.32	–	0.33

[1] in 10^{10} phot cm^{-2}s^{-1}eV^{-1} at the Lyman limit ($\alpha_{UV} = -1.5$, $\alpha_X = -0.7$);

Table C.24: Simulations for $V \geq 0$ of the region CN of NGC 7212, part 2. For each bin there are the observed quantities and the results of the models. The first nine rows show the comparison between the observed and the synthetic spectra, the remaining rows show the input parameters of each model.

	bin 6		bin 7		bin 8		bin 9	
line	obs.	mod.	obs.	mod.	obs.	mod.	obs.	mod.
[O II]λ3727+	3.73	4.0	3.11	3.3	3.21	3.	2.12	2.6
[Ne III]λ3869+	2.61	0.94	2.0	2.17	2.1	1.8	1.26	1.3
He II λ4686	0.18	0.4	0.26	0.4	0.29	0.37	0.18	0.26
[O III]λ5007+	14.1	13.2	12.1	11.8	11.2	11.86	9.2	9.2
[O I]λ6300,[S II]λ6310	0.97	1.0	0.99	0.77	0.83	0.72	0.73	0.7
Hα	2.86	3.1	2.86	3.04	2.86	2.97	2.86	2.99
[N II]λ6584	1.96	2.2	2.07	1.93	2.2	1.65	2.06	1.8
[S II]λ6716	0.15	0.24	0.74	0.52	0.18	0.38	0.44	0.4
[S II]λ6731	0.63	0.45	0.69	1.0	0.65	0.76	0.6	0.67
FWHM(km s^{-1})	600	–	700	–	800	–	900	–
V_s (km s^{-1})	–	580	–	700	–	800	–	900
n_0(cm^{-3})	–	190	–	170	–	150	–	92.
D(10^{18}cm)	–	0.08	–	0.07	–	0.06	–	0.1
F (units[1])	–	22.	–	22.	–	21.	–	8.
O/H (10^4)	–	6.6	–	6.6	–	6.6	–	6.5
N/H (10^4)	–	0.6	–	0.5	–	0.5	–	1.
Ne/H(10^4)	–	1.3	–	1.3	–	1.3	–	1.2
S/H (10^4)	–	0.07	–	0.2	–	0.2	–	0.15
Hβ (erg cm^{-2} s^{-1})	–	0.35	–	0.4	–	0.42	–	0.2

[1] in 10^{10} phot cm^{-2}s^{-1}eV^{-1} at the Lyman limit ($\alpha_{UV} = -1.5$, $\alpha_X = -0.7$);

Table C.25: Simulations for $V < 0$ of the region CN of NGC 7212. For each bin there are the observed quantities and the results of the models. The first nine rows show the comparison between the observed and the synthetic spectra, the remaining rows show the input parameters of each model.

	bin -1		bin -2		bin 3		bin -4		bin -5		bin -6		bin -7		bin -8	
line	obs.	mod.	obs.	mod.	obs.	mod.	obs.	mod.	obs.	mod.	obs.	mod.	obs.	mod.	obs.	mod.
[O II]λ3727+	3.05	3.	2.75	2.78	2.74	2.7	3.	3.17	2.77	2.87	3.97	4.0	7.5	7.4	15.2	14.
[Ne III]λ3869+	2.0	2.1	1.76	2.	1.72	2.83	1.77	1.5	1.66	1.67	2.8	2.6	2.9	2.74	3.96	3.0
He II λ4686	0.23	0.43	0.21	0.38	0.23	0.47	0.2	0.37	0.12	0.3	0.18	0.46	0.11	0.6	0.0	0.79
[O III]λ5007+	15.	15.1	14.5	14.3	14.3	14.5	14.2	14.2	14.4	14.36	14.	14.3	15.2	14.8	21.56	15.2
[O I]λ6300,[S II]λ6310	0.62	0.8	0.56	0.7	0.5	0.9	0.52	0.5	0.53	0.4	0.41	0.5	0.35	0.4	0.42	0.3
Hα	2.86	3.	2.86	3.	2.86	3.2	2.86	2.9	2.86	2.93	2.86	3.	2.86	2.97	2.86	4.2
[N II]λ6584	1.93	1.98	1.85	2.0	1.78	1.7	1.83	2.	1.4	1.75	1.26	1.77	1.36	1.5	1.31	1.5
[S II]λ6716	0.72	0.67	0.71	0.61	0.63	0.55	0.62	0.5	0.67	0.44	0.58	0.35	0.43	0.41	0.18	0.48
[S II]λ6731	0.85	1.0	0.85	1.	0.876	0.96	0.82	1.0	0.69	0.89	1.27	1.13	0.63	0.74	1.7	0.47
FWHM(km s^{-1})	-100	–	-200	–	-300	–	-400	–	-500	–	-600	–	-700		-800	
V_s (km s^{-1})	–	90	–	200	–	300	–	400	–	500	–	600	–	700	–	870
n_0(cm^{-3})	–	800	–	530	–	400	–	300	–	280	–	180	–	95	–	20
D(10^{18}cm)	–	0.7	–	1.4	–	0.17	–	0.03	–	0.018	–	0.07	–	0.13	–	8.3
F (units[1])	–	15.	–	17.	–	35.	–	19.	–	12.5	–	23.	–	17.	–	26.6
O/H (10^4)	–	6.5	–	6.5	–	6.5	–	6.5	–	6.6	–	6.6	–	6.6	–	6.7
N/H (10^4)	–	0.5	–	0.5	–	0.5	–	0.5	–	0.5	–	0.4	–	0.3	–	0.3
Ne/H(10^4)	–	1.0	–	1.0	–	0.8	–	0.8	–	1.	–	1.3	–	1.4	–	1.3
S/H (10^4)	–	0.05	–	0.07	–	0.086	–	0.2	–	0.2	–	0.2	–	0.2	–	0.4
Hβ (erg cm^{-2} s^{-1})	–	0.2	–	0.26	–	0.45	–	0.36	–	0.23	–	0.35	–	0.21	–	0.23

[1] in 10^{10} phot cm^{-2}s^{-1}eV^{-1} at the Lyman limit ($\alpha_{UV} = -1.5$, $\alpha_X = -0.7$);

Table C.26: Simulations for $V \geq 0$ of the region CS of NGC 7212, part 1. For each bin there are the observed quantities and the results of the models. The first nine rows show the comparison between the observed and the synthetic spectra, the remaining rows show the input parameters of each model.

	bin 0		bin 1		bin 2		bin 3		bin 4		bin 5		bin 6	
line	obs.	mod.	obs.	mod.	obs.	mod.	obs.	mod.	obs.	mod.	obs.	mod.	obs.	mod.
[O II]λ3727+	3.34	3.3	2.5	3.1	2.24	2.3	2.26	2.46	2.34	2.67	2.58	2.5	2.5	2.7
[Ne III]λ3869+	1.95	2.0	1.81	1.75	1.85	1.9	1.9	1.9	2.08	1.9	2.44	1.7	2.56	2.3
He II λ4686	0.23	0.59	0.23	0.4	0.23	0.5	0.22	0.49	0.23	0.5	0.23	0.5	0.17	0.24
[O III]λ5007+	16.2	16.1	15.85	15.7	16.6	16.8	16.25	16.0	15.5	15.3	14.3	14.3	13.8	14.
[O I]λ6300+	0.2	0.12	0.2	0.1	0.27	0.11	0.56	0.54	0.53	0.54	1.54	0.2	0.64	0.1
Hα	2.86	2.95	2.86	2.97	2.86	3.0	2.86	3.2	2.86	3.2	2.86	3.2	2.86	2.87
[N II]λ6584	1.8	1.86	1.85	1.77	1.8	1.7	1.77	1.82	1.68	1.86	1.52	1.7	1.4	1.67
[S II]λ6716	0.67	0.63	0.6	0.42	0.53	0.3	0.5	0.3	0.43	0.3	0.32	0.22	0.38	0.34
[S II]λ6731	0.72	0.71	0.73	0.77	0.66	0.6	0.6	0.6	0.55	0.6	0.46	0.46	0.44	0.78
FWHM(km s^{-1})	0.0	–	100	–	200	–	300	–	400	–	500	–	600	–
V$_s$ (km s^{-1})	–	60	–	100	–	200	–	300	–	400	–	530	–	600
n$_0$(cm^{-3})	–	220	–	900	–	700	–	500	–	400	–	360	–	300
D(10^{18}cm)	–	1.0	–	0.05	–	0.05	–	0.05	–	0.05	–	0.04	–	0.008
F (units[1])	–	1.2	–	15.	–	42.	–	46.	–	46.	–	47.	–	7.2
O/H (10^4)	–	6.6	–	6.6	–	6.6	–	6.6	–	6.6	–	6.6	–	6.6
N/H (10^4)	–	0.6	–	0.4	–	0.4	–	0.4	–	0.4	–	0.4	–	0.5
Ne/H(10^4)	–	1.2	–	0.8	–	0.8	–	0.8	–	0.8	–	0.8	–	1.4
S/H (10^4)	–	0.04	–	0.07	–	0.07	–	0.08	–	0.09	–	0.09	–	0.2
Hβ (erg cm^{-2} s^{-1})	–	0.054	–	0.22	–	0.53	–	0.59	–	0.6	–	0.73	–	0.17

[1] in 10^{10} phot cm^{-2}s^{-1}eV^{-1} at the Lyman limit ($\alpha_{UV} = -1.5$, $\alpha_X = -0.7$);

Table C.27: Simulations for $V \geq 0$ of the region CS of NGC 7212, part 2. For each bin there are the observed quantities and the results of the models. The first nine rows show the comparison between the observed and the synthetic spectra, the remaining rows show the input parameters of each model.

	bin 7		bin 8		bin 9	
line	obs.	mod.	obs.	mod.	obs.	mod.
[O II]λ3727+	3.77	3.3	3.54	3.9	3.69	3.0
[Ne III]λ3869+	3.23	3.	3.18	2.4	2.23	2.2
He II λ4686	0.23	0.33	0.19	0.3	0.22	0.26
[O III]λ5007+	14.	15.	11.6	11.6	9.77	9.83
[O I]λ6300+	0.73	0.1	0.73	0.4	0.62	0.76
Hα	2.86	2.87	2.86	2.92	2.86	2.98
[N II]λ6584	1.3	1.5	1.27	1.6	1.26	1.44
[S II]λ6716	0.3	0.4	0.48	0.45	0.38	0.3
[S II]λ6731	0.37	0.8	0.37	0.8	0.31	0.49
FWHM(km s^{-1})	700	–	800	–	900	–
V_s (km s^{-1})	–	690	–	800	–	900
n_0(cm^{-3})	–	180	–	105	–	92
D(10^{18}cm)	–	0.02	–	0.06	–	0.1
F (units[1])	–	8.5	–	9.1	–	7.9
O/H (10^4)	–	6.7	–	6.6	–	6.7
Ne/H(10^4)	–	0.5	–	0.5	–	0.5
Ne/H(10^4)	–	1.9	–	1.9	–	1.9
S/H (10^4)	–	0.2	–	0.2	–	0.1
Hβ (erg cm^{-2} s^{-1})	–	0.2	–	0.19	–	0.19

[1] in 10^{10} phot cm^{-2}s^{-1}eV^{-1} at the Lyman limit ($\alpha_{UV} = -1.5$, $\alpha_X = -0.7$);

Table C.28: Simulations for $V < 0$ of the region CS of NGC 7212. For each bin there are the observed quantities and the results of the models. The first nine rows show the comparison between the observed and the synthetic spectra, the remaining rows show the input parameters of each model.

	bin -1		bin -2		bin -3		bin -4		bin -5		bin -6		bin -7	
line	obs.	mod.	obs.	mod.	obs.	mod.	obs.	mod.	obs.	mod.	obs.	mod.	obs.	mod.
[O II]λ3727+	2.06	2.06	2.8	2.7	3.27	3.	3.07	3.22	3.	3.	6.58	6.4	5.93	5.7
[Ne III]λ3869+	1.64	1.63	1.36	1.45	1.8	1.7	1.62	1.77	2.22	2.1	1.34	1.68	1.52	1.5
He II λ4686	0.19	0.37	0.19	0.38	0.21	0.3	0.23	0.36	0.19	0.3	0.15	0.4	0.0	0.3
[O III]λ5007+	14.4	14.2	14.	14.5	13.4	13.2	14.25	14.47	13.4	13.1	12.93	13.2	11.33	11.8
[O I]λ6300,[S II]λ6310	0.55	0.6	0.47	0.4	0.39	0.4	0.43	0.42	0.28	0.26	0.21	0.6	0.8	1.2
Hα	2.86	2.96	2.86	2.98	2.86	2.9	2.86	2.9	2.86	2.9	2.86	3.13	2.86	2.95
[N II]λ6584	1.85	1.63	1.42	1.4	1.11	1.0	0.88	1.0	0.39	0.6	0.08	0.6	0.0	0.6
[S II]λ6716	0.83	0.6	0.66	0.5	0.5	0.4	0.57	0.4	0.54	0.4	0.4	0.8	0.44	0.5
[S II]λ6731	0.81	1.0	0.71	0.99	0.58	0.8	0.47	0.76	0.52	0.76	0.8	1.3	0.66	0.87
FWHM(km s^{-1})	-100	–	-200	–	-300	–	-400	–	-500	–	-600	–	-700	–
V_s (km s^{-1})	–	120	–	200	–	300	–	400	–	500	–	600	–	700
n_0(cm^{-3})	–	1200	–	500	–	350	–	290	–	270	–	100	–	100
D(10^{18}cm)	–	0.02	–	0.024	–	0.024	–	0.0247	–	0.0245	–	0.2	–	0.54
F (units[1])	–	23.	–	14.	–	14.	–	16.	–	16.	–	1.	–	0.34
O/H (10^4)	–	6.6	–	6.6	–	6.6	–	6.6	–	6.6	–	6.6	–	6.6
N/H (10^4)	–	0.4	–	0.4	–	0.4	–	0.4	–	0.3	–	0.2	–	0.2
Ne/H(10^4)	–	0.8	–	0.8	–	1.0	–	1.0	–	1.2	–	0.8	–	0.8
S/H (10^4)	–	0.16	–	0.16	–	0.16	–	0.16	–	0.16	–	0.15	–	0.07
Hβ (erg cm^{-2} s^{-1})	–	0.37	–	0.23	–	0.3	–	0.31	–	0.33	–	0.146	–	0.02

[1] in 10^{10} phot cm^{-2}s^{-1}eV^{-1} at the Lyman limit ($\alpha_{UV} = -1.5$, $\alpha_X = -0.7$);

Table C.29: Simulations for $V \geq 0$ of the region S0 of NGC 7212. For each bin there are the observed quantities and the results of the models. The first nine rows show the comparison between the observed and the synthetic spectra, the remaining rows show the input parameters of each model.

	bin 0		bin 1		bin 2		bin 3		bin 4		bin 5	
line	obs.	mod.	obs.	mod.	obs.	mod.	obs.	mod.	obs.	mod.	obs.	mod.
[O II]λ3727+	3.57	3.3	2.75	2.73	3.1	3.3	1.4	2.1	2.5	2.78	3.9	4.1
[Ne III]λ3869+	1.8	2.0	2.27	2.68	2.1	2.2	2.1	2.3	2.	2.2	2.2	2.38
He II λ4686	0.22	0.59	0.2	0.4	0.22	0.5	0.22	0.46	0.18	0.5	0.0	0.6
[O III]λ5007+	16.3	16.1	15.5	16.2	16.1	15.3	15.2	15.1	13.63	13.65	13.75	13.43
[O I]λ6300+,[S II]λ6310	0.38	0.5	0.35	0.8	0.5	0.8	0.51	0.7	0.7	0.9	0.7	0.8
Hα	2.86	2.95	2.86	3.	2.86	3.13	2.86	3.13	2.86	3.2	2.86	3.36
[N II]λ6584	1.7	1.86	1.72	1.7	1.78	1.65	1.71	1.6	1.67	1.84	1.67	2.1
[S II]λ6716	0.63	0.63	0.51	0.4	0.42	0.3	0.35	0.4	0.6	0.4	0.6	0.3
[S II]λ6731	0.58	0.71	0.64	0.5	0.67	0.5	0.59	0.8	0.6	0.7	0.6	0.54
FWHM(km s^{-1})	0.0	–	100	–	200	–	300	–	400	–	500	–
V_s (km s^{-1})	–	60	–	110	–	200	–	280	–	400	–	500
n_0(cm^{-3})	–	220	–	920	–	420	–	550	–	350	–	260
D(10^{18}cm)	–	1.	–	0.18	–	0.12	–	0.1	–	0.1	–	0.075
F (units[1])	–	1.2	–	20.	–	25.	–	45.	–	48.	–	46.
O/H (10^4)	–	6.6	–	6.6	–	6.6	–	6.6	–	6.6	–	6.6
N/H (10^4)	–	0.6	–	0.4	–	0.4	–	0.4	–	0.4	–	0.4
Ne/H(10^4)	–	1.2	–	1.2	–	1.0	–	1.0	–	1.0	–	1.0
S/H (10^4)	–	0.04	–	0.04	–	0.04	–	0.08	–	0.08	–	0.09
Hβ (erg cm^{-2} s^{-1})	–	0.054	–	0.28	–	0.31	–	0.6	–	0.61	–	0.58

[1] in 10^{10} phot cm^{-2}s^{-1}eV^{-1} at the Lyman limit ($\alpha_{UV} = -1.5$, $\alpha_X = -0.7$);

Table C.30: Simulations for $V < 0$ of the region S0 of NGC 7212. For each bin there are the observed quantities and the results of the models. The first nine rows show the comparison between the observed and the synthetic spectra, the remaining rows show the input parameters of each model.

	bin -1		bin -2		bin -3		bin -4		bin -5	
line	obs.	mod.	obs.	mod.	obs.	mod.	obs.	mod.	obs.	mod.
[O II]λ3727+	3.06	2.9	2.6	2.7	4.28	4.7	3.94	3.6	3.9	4.2
[Ne III]λ3869+	1.3	1.6	0.78	1.2	1.7	1.6	0.77	0.87	4.8	1.1
He II λ4686	0.16	0.3	0.09	0.2	0.18	0.3	0.16	0.3	0.03	0.4
[O III]λ5007+	12.1	12.4	7.66	7.53	11.5	11.4	12.26	12.5	17.63	17.
[O I]λ6300+,[S II]λ6310	0.42	0.6	0.34	0.4	0.21	0.6	0.37	0.3	0.22	0.2
Hα	2.86	2.97	2.86	3.	2.86	2.95	2.86	2.92	2.86	2.89
[N II]λ6584	1.85	1.5	1.75	1.6	1.85	1.6	2.1	2.1	0.92	0.75
[S II]λ6716	0.9	0.53	0.9	0.86	1.0	1.5	1.26	0.6	1.87	0.9
[S II]λ6731	0.72	0.88	0.7	1.5	0.86	2.2	1.44	1.2	2.39	1.8
FWHM(km s^{-1})	-100	–	-200	–	-300	–	-400	–	-500	–
V_s (km s^{-1})	–	100	–	200	–	300	–	400	–	500
n_0(cm^{-3})	–	900	–	550	–	200	–	200	–	170
D(10^{18}cm)	–	0.2	–	0.35	–	0.25	–	0.03	–	0.03
F (units[1])	–	10.	–	6.	–	3.4	–	6.	–	10.
O/H (10^4)	–	6.6	–	6.6	–	6.6	–	6.6	–	6.6
N/H (10^4)	–	0.6	–	0.6	–	0.6	–	0.6	–	0.4
Ne/H(10^4)	–	0.9	–	0.9	–	0.9	–	0.6	–	0.6
S/H (10^4)	–	0.06	–	0.15	–	0.13	–	0.18	–	0.4
Hβ (erg cm^{-2} s^{-1})	–	0.18	–	0.14	–	0.06	–	0.12	–	0.14

[1] in 10^{10} phot cm^{-2}s^{-1}eV^{-1} at the Lyman limit ($\alpha_{UV} = -1.5$, $\alpha_X = -0.7$);

Table C.31: Simulations for $V \geq 0$ of the region S1 of NGC 7212. For each bin there are the observed quantities and the results of the models. The first nine rows show the comparison between the observed and the synthetic spectra, the remaining rows show the input parameters of each model.

	bin 0		bin 1		bin 2		bin 3		bin 4		bin 5	
line	obs.	mod.	obs.	mod.	obs.	mod.	obs.	mod.	obs.	mod.	obs.	mod.
[O II]λ3727+	5.1	5.0	4.4	4.3	6.48	6.9	0.52	3.5$*$	1.9	2.	3.5	3.5
[Ne III]λ3869+	1.9	1.76	5.6	3.1	1.0	1.7$*$	0.0	1.47	0.	1.37	0.0	1.67
He II λ4686	0.30	0.8	0.67	0.9	0.26	0.8	0.0	0.4	0.0	0.35	0.0	0.5
[O III]λ5007+	17.25	17.7	20.5	22.3	19.1	20.	16.5	16.9	14.	13.7	16.0	15.83
[O I]λ6300+,[S III]λ6312	0.42	0.32	0.57	0.2	0.99	0.95	1.04	0.7	1.5	0.5	2.7	1.0
Hα	2.86	2.87	2.86	2.9	2.86	3.	2.86	2.9	2.0	2.9	2.89	2.97
[N II]λ6584	1.7	1.44	1.82	1.74	1.98	2.12	1.6	1.73	1.5	1.6	2.89	2.14
[S II]λ6716	0.71	0.67	0.44	0.35	0.7	0.85	0.67	0.53	0.0	0.25	–	0.3
[S II]λ6731	0.55	0.62	0.66	0.43	0.7	1.1	0.7	1.0	0.54	0.56	0.0	0.7
FWHM(km s^{-1})	0.0	–	100	–	200	–	300	–	400	–	500	–
V_s (km s^{-1})	–	60	–	100	–	190	–	300	–	400	–	500
n_0(cm^{-3})	–	110	–	150	–	120	–	300	–	500	–	280
D(10^{18}cm)	–	0.7	–	0.16	–	0.16	–	0.018	–	0.0064	–	0.035
F (units[1])	–	1.3	–	4.3	–	5.7	–	10.	–	20.	–	40.
O/H (10^4)	–	6.6	–	6.6	–	6.6	–	6.6	–	6.6	–	6.6
N/H (10^4)	–	0.6	–	1.0	–	0.6	–	0.5	–	0.5	–	0.5
Ne/H(10^4)	–	1.2	–	1.8	–	0.8	–	0.8	–	0.8	–	0.8
S/H (10^4)	–	0.35	–	0.4	–	0.35	–	0.2	–	0.2	–	0.2
Hβ (erg cm^{-2} s^{-1})	–	0.012	–	0.024	–	0.039	–	0.15	–	0.4	–	0.6

[1] in 10^{10} phot cm^{-2}s^{-1}eV^{-1} at the Lyman limit ($\alpha_{UV} = -1.5$, $\alpha_X = -0.7$);

Table C.32: Simulations for $V < 0$ of the region S1 of NGC 7212. For each bin there are the observed quantities and the results of the models. The first nine rows show the comparison between the observed and the synthetic spectra, the remaining rows show the input parameters of each model.

	bin -1		bin -2		bin -3		bin -4		bin -5	
line	obs.	mod.	obs.	mod.	obs.	mod.	obs.	mod.	obs.	mod.
[O II]λ3727+	3.16	3.5	2.63	2.8	5.8	5.7	6.65	6.6	3.17	3.5
[Ne III]λ3869+	1.	1.5	0.73	1.1	1.45	1.62	0.75	1.7	0.0	2.7
He II λ4686	0.07	0.39	0.08	0.2	0.0	0.3	0.0	0.4	0.0	0.3
[O III]λ5007+	10.73	10.22	7.3	7.5	11.6	11.66	15.	14.83	30.73	25.
[O I]λ6300+,[S II]λ6310	0.43	0.5	0.4	0.4	0.9	1.0	1.9	1.7	0.81	0.1
Hα	2.86	2.97	2.86	3.	2.86	2.97	2.53	3.2	2.86	3.8
[N II]λ6584	1.64	1.6	1.81	2.1	2.35	2.4	4.7	2.34	8.32	1.8
[S II]λ6716	0.76	1.	0.91	0.6	1.34	1.62	1.73	1.56	3.12	0.3
[S II]λ6731	0.59	1.6	0.69	1.	1.25	2.1	2.05	1.9	3.05	0.5
FWHM(km s^{-1})	-100	–	-200	–	-300	–	-400	–	-500	–
V_s (km s^{-1})	–	110	–	200	–	300	–	400	–	500
n_0(cm^{-3})	–	580	–	580	–	140	–	70	–	100
D(10^{18}cm)	–	0.36	–	0.36	–	1.6	–	1.6	–	0.126
F (units[1])	–	4.4	–	6.	–	2.	–	2.	–	30.
O/H (10^4)	–	6.6	–	6.6	–	6.6	–	6.6	–	6.6
N/H (10^4)	–	0.5	–	0.5	–	0.5	–	0.5	–	1.
Ne/H(10^4)	–	1.0	–	0.8	–	0.8	–	0.8	–	0.8
S/H (10^4)	–	0.1	–	0.1	–	0.1	–	0.1	–	0.8
Hβ (erg cm^{-2} s^{-1})	–	0.09	–	0.14	–	0.036	–	0.027	–	0.12

[1] in 10^{10} phot cm^{-2}s^{-1}eV^{-1} at the Lyman limit ($\alpha_{UV} = -1.5$, $\alpha_X = -0.7$);

RINGRAZIAMENTI

Vorrei ringraziare i miei genitori, mia sorella e tutto il resto della mia famiglia per il supporto che mi hanno dato durane questi anni di studi. Inoltre vorrei ringraziare gli amici che mi hanno sopportato in tutti questi anni, in particolare Denise, Ugo, Bianca e Ilaria. Un ringraziamento speciale va a Stefano, il mio relatore dai temi della triennale, che mi ha guidato durante i miei primi passi nel mondo della ricerca, e a tutto il gruppo di ricerca qua a Padova.